

State Resolved Measurements of Methane  
Reactivity on Ni(111) and Ir(111) Surfaces

A dissertation

Submitted by

Eric K. Dombrowski

In partial fulfillment of the requirements for the degree of

Doctor of Philosophy

In

Chemistry

**Tufts University**

May, 2018

© 2018, Eric K. Dombrowski

Adviser: Arthur L. Utz



# State Resolved Measurements of Methane Reactivity on Ni(111) and Ir(111) Surfaces

By

Eric K. Dombrowski

Submitted to the Department of Chemistry at Tufts University on May 1, 2017 in  
partial fulfillment of the requirements for the Degree of Doctor of Philosophy in  
Chemistry

## **Abstract**

The initial sticking probability for methane dissociation on Ir(111) and Ni(111) surfaces are measured using molecular beam surface scattering techniques. State-resolved measurements coupling infrared laser excitation to the incident methane beam allowed for the reactivity of a single ro-vibrational state to be probed. A precursor-mediated reaction pathway is highlighted on Ir(111) demonstrating the first mode-selective behavior for a physisorbed molecule leading to dissociation. Despite the different interaction times between the molecule and surface, the direct dissociative and precursor-mediated mechanisms had identical vibrational efficacies for the ( $\nu_3$ ,  $v=1$ ) vibrational state. The reaction

of  $\text{CHD}_3$  on Ni(111) in the  $(\nu_1, \nu=1)$  vibrational state was used as a model system for direct comparison with ab-initio molecular dynamics simulations to obtain the first chemically accurate description of a polyatomic molecule-surface reaction.

Surface temperature effects for the dissociative chemisorption of methane on Ni(111) are explored for both the initial sticking probability and diffusion of carbon into the nickel lattice. It was observed that methane dissociation was insensitive to surface temperatures at and above 800 K and exciting the methane to the  $(\nu_3, \nu=1)$  vibrational state enhanced reactivity even at the highest methane internal energies. Diffusion of carbon into the nickel bulk was observed to turn on rapidly around a surface temperature of 780 K under the conditions studied. Under these conditions the studied reactivities and diffusivities were much closer to those used in industrial steam reforming reactors.

# Acknowledgments

It is an interesting task to look back at what is now 24 years of schooling and try to appreciate the many people, places, and events that have led me here. The most appropriate place to start is where all my curiosity, motivation, and support are derived from; my family. I am truly blessed to have such wonderful, devoted, and understanding parents. I attribute my love for all things technical to my father, Scott. No matter the project I conceived in my young mind, he always embraced them and encouraged me to approach them from my own naïve understanding. When they failed, as most do, his example of commitment and his guiding hand left me both empowered and enamored. However, his technical abilities are dwarfed by his heart. His love for my mother, Karen, shines as bright today as I can only imagine it did the day they met. He has taught me that showing that love and never being stingy with it is the most rewarding way to live. I spent countless hours with my mom when I was younger, always at her side whether it was during her aerobics classes in the local church, at the salon where she cut hair, or coloring at a table while she finished her waitressing duties. Her example in how to treat other people, always with kindness and compassion, showed me at this ripe young age the benefits of charisma and charm. I am grateful for that time and for the thousands upon thousands of sporting events that she so devotedly attended even when I was hours away in another state. These two are the best people I have, and will ever meet. I am certain of that.

As with all sibling relationships mine with my brother, Greg, is dotted with love, physical and mental pain, and an unrivaled sharing of our lives. Luckily the love has been dominant since High School where he took me in and embraced me in his group of friends. I received invaluable lessons in how to party from the best of them and am glad to still call them all friends. We were partners in developing our ability to work on mechanical systems starting with his first lobster boat, to our first Jeep, to the myriad projects that we currently work on together. To a more practical point, I am grateful that he opened his home to me for the final leg of this dissertation, even with him starting his life with his wonderful fiancée, Amy. I have truly enjoyed spending as much time as we have been afforded recently and cannot wait for Amy to be part of the Dombrowski clan.

To my second family, the Utz lab, I couldn't have completed these long and arduous years without the great people I have had the pleasure to work with. My advisor, Art Utz, has been a tremendous inspiration and help in completing this work. Never once have I felt inadequate under your tutelage despite the shadow you cast. I am thankful for your patience and truly allowing me to pursue the work in your lab that I find most rewarding, sometimes spending weeks on teaching myself programming that hasn't always produced the most useful outcomes. You have been my mentor throughout these years, but I think of Dr. Deno Del Sesto as a close second. Thank you for the beautiful chamber you built and mostly, for the knowledge you instilled upon me which still guides my experimental approach to this day. And to Eric Peterson, who spent many late

nights with me scratching our heads as to why experiments weren't always working properly. Finally, to round out the Eric trifecta, is Eric High. I have truly enjoyed the time we have spent in lab together the last four years. It is one thing to have a lab mate but another altogether to spend all that time with a friend. Thank you for always having high spirits when mine are low and being able to just turn the music up and forget we are actually doing work.

Lastly, I would like to thank my two committee members from Tufts for helping me navigate the graduate lifestyle, Dr. Charlie Sykes and Dr. Samuel Thomas. You are both amazing people with wonderful teaching styles. The students at Tufts are lucky to have the both of you. Also, to my outside committee member, Dr. Bret Jackson, from UMass Amherst. Our work has always had heavy overlap and I am thankful that you have always done the hard part so that I could stick to the experimental aspects!

# TABLE OF CONTENTS

ABSTRACT.....	III
ACKNOWLEDGMENTS .....	V
TABLE OF CONTENTS .....	VIII
LIST OF FIGURES .....	XI
LIST OF TABLES .....	XIV
CHAPTER 1 : INTRODUCTION.....	1
CHAPTER 2 : EXPERIMENTAL APPARATUS AND METHODS.....	26
2.1 GENERAL EXPERIMENTAL APPROACH.....	28
2.2 MOLECULAR BEAM FORMATION AND CHARACTERIZATION .....	30
2.2.1 Methane molecular beam formation.....	30
2.2.2 Time-of-Flight Measurements.....	34
2.2.3 Flux Measurements.....	42
2.3 SUBSTRATE CONTROL AND CLEANING PROCEDURES .....	44
2.3.1 Cleaning Ir(111) .....	44
2.3.2 Cleaning Ni(111) .....	45
2.4 MEASURING INITIAL STICKING PROBABILITIES .....	47
2.4.1 King and Wells Reflectivity Method.....	48
2.4.2 King and Wells Reflectivity with Laser Modulation .....	50
2.4.3 Auger electron spectroscopy.....	56
2.5 LASER SYSTEM AND STATE-RESOLVED TECHNIQUES .....	61
2.5.1 General laser setup and operation .....	62
2.5.2 Excitation of CH <sub>4</sub> at low Nozzle Temperature .....	65
2.5.3 Excitation of CHD <sub>3</sub> and CH <sub>4</sub> at high Nozzle Temperatures .....	70
2.6 REFERENCES .....	75
CHAPTER 3 : PRECURSOR-MEDIATED REACTIVITY OF VIBRATIONALLY HOT MOLECULES: METHANE ON IR(111).....	78
3.1 INTRODUCTION.....	78

3.2 EXPERIMENTAL APPROACH.....	92
3.3 RESULTS AND DISCUSSION.....	98
3.3.1 <i>Direct Dissociative Chemisorption</i> .....	100
3.3.2 <i>Low <math>E_{trans}</math> Channel</i> .....	103
3.4 CONCLUSIONS .....	113
3.5 REFERENCES .....	115
<b>CHAPTER 4 : CHEMICALLY ACCURATE SIMULATION OF A POLYATOMIC MOLECULE-METAL SURFACE REACTION.....</b>	<b>121</b>
4.1 INTRODUCTION.....	121
4.2 EXPERIMENTAL METHODS .....	125
4.3 RESULTS AND DISCUSSION.....	139
4.4 CONCLUSION AND FUTURE DIRECTIONS .....	147
4.5 REFERENCES .....	149
<b>CHAPTER 5 :... STATE-RESOLVED REACTIVITY (<math>N_3</math>, <math>V=1</math>) OF <math>CH_4</math> ON NI(111) AT ELEVATED SURFACE TEMPERATURES.....</b>	<b>153</b>
5.1 INTRODUCTION.....	153
5.2 EXPERIMENTAL METHODS .....	160
5.3 RESULTS AND DISCUSSION.....	168
5.4 CONCLUSIONS AND FUTURE DIRECTIONS.....	178
5.5 REFERENCES .....	180
<b>CHAPTER 6 :..... CARBON UPTAKE INTO NI(111) DURING <math>CH_4</math> MOLECULAR BEAM DEPOSITION .....</b>	<b>185</b>
6.1 INTRODUCTION.....	185
6.2 EXPERIMENTAL METHODS .....	194
6.3 RESULTS AND DISCUSSION.....	198
6.4 CONCLUSION AND FUTURE DIRECTIONS .....	213
6.5 REFERENCES .....	215
<b>APPENDIX A   LABVIEW CRYSTAL TEMPERATURE CONTROLLER .....</b>	<b>220</b>

<b>APPENDIX B IGOR - MODULATION FIT WALKTHROUGH.....</b>	<b>239</b>
<b>APPENDIX C IGOR – DISSOLUTION STARTUP .....</b>	<b>253</b>

# List of Figures

<b>FIGURE 1.1</b> GLOBAL AMMONIA PRODUCTION .....	5
<b>FIGURE 1.2</b> LEYNARD-JONES POTENTIAL FOR METHANE .....	7
<b>FIGURE 1.3</b> COMPARISON OF $E_{\text{TRANS}}$ , $E_{\text{VIB}}$ , AND $E_{\text{TRANS}}$ AS A FUNCTION OF $T_{\text{SURF}}$ .....	10
<b>FIGURE 1.4</b> SIMULATED STICKING PROBABILITY CURVES .....	12
<b>FIGURE 1.5</b> METHANE $E_{\text{TRANS}}$ VALUES OVER A RANGE OF BEAM CONDITIONS.....	14
<b>FIGURE 2.1</b> MOLECULAR BEAM SURFACE SCATTERING CHAMBER SCHEMATIC .....	32
<b>FIGURE 2.2</b> SCHEMATIC OF ROTATING CHOPPER WHEEL. ....	37
<b>FIGURE 2.3</b> DEMONSTRATION OF A METHANE TIME-OF-FLIGHT MEASUREMENT. ..	38
<b>FIGURE 2.4</b> MEASURED HE AND H <sub>2</sub> TIME-OF-FLIGHTS .....	40
<b>FIGURE 2.5</b> EXAMPLE OF A KING AND WELLS EXPERIMENT .....	49
<b>FIGURE 2.6</b> EXAMPLE OF A KING AND WELLS MODULATION EXPERIMENT.....	51
<b>FIGURE 2.7</b> CALCULATED STICKING PROBABILITIES FROM FIGURE 2.6.....	53
<b>FIGURE 2.8</b> FITTING TO K&W MODULATION DATA .....	55
<b>FIGURE 2.9</b> AES CARBON DEPOSITION MAP FOR LASER OFF DOSE. ....	58
<b>FIGURE 2.10</b> AES CARBON DEPOSITION MAP FOR LASER ON DOSE .....	60
<b>FIGURE 3.1</b> DIRECT & PRECURSOR MEDIATED REACTION PATHWAYS ON Ir(111). 91	
<b>FIGURE 3.2</b> $S_0^{\text{OFF}}$ AND $S_0^{\text{V}3}$ INITIAL STICKING PROBABILITIES ON Ir(111). ....	99
<b>FIGURE 3.3</b> CONTRIBUTIONS FROM PRECURSOR MEDIATED AND DIRECT DISSOCIATION TO $S_0$ .....	104
<b>FIGURE 4.1</b> VIBRATIONAL AND ROTATIONS FACTORS FOR CALCULATING $F_{\text{EXC}}$ ....	135
<b>FIGURE 4.2</b> $S_0^{\text{OFF}}$ AND $S_0^{\text{V}1}$ FOR CHD <sub>3</sub> ON Ni(111) .....	141
<b>FIGURE 4.3</b> COMPARISON OF MEASURED VALUES WITH AIMD $S_0$ VALUES.....	143
<b>FIGURE 5.1</b> $S_0^{\text{OFF}}$ AND $S_0^{\text{V}3}$ FOR CH <sub>4</sub> ON Ni(111) AT DIFFERENT SURFACE TEMPERATURES.....	169

<b>FIGURE 5.2</b>	RELATIVE FRACTIONAL CHANGE IN $S_0^{\text{OFF}}$ COMPARED TO $S_0^{\text{V3}}$ .....	171
<b>FIGURE 5.3</b>	SURFACE TEMPERATURE DEPENDENCE FOR $S_0^{\text{OFF}}$ .....	172
<b>FIGURE 5.4</b>	SURFACE TEMPERATURE DEPENDENCE FOR $S_0^{\text{V3}}$ .....	173
<b>FIGURE 5.5</b>	CALCULATED ACTIVATION ENERGIES AS A FUNCTION OF $E_{\text{TRANS}}$ .....	176
<b>FIGURE 6.1</b>	CARBON SOLUBILITY AND DIFFUSION ON NICKEL.....	189
<b>FIGURE 6.2</b>	EXAMPLE OF KING AND WELLS MEASURING UPTAKE OF CARBON. ..	196
<b>FIGURE 6.3</b>	KING AND WELLS MEASUREMENTS FOR $T_{\text{SURF}} = 685 - 750 \text{ K}$ .....	199
<b>FIGURE 6.4</b>	METHANE UPTAKE AS A FUNCTION OF $S_0$ . .....	200
<b>FIGURE 6.5</b>	KING AND WELLS MEASUREMENTS FOR $T_{\text{SURF}} = 780 - 850 \text{ K}$ .....	201
<b>FIGURE 6.6</b>	STEADY-STATE CARBON ACCUMULATION RATES .....	204
<b>FIGURE 6.7</b>	TOTAL CALCULATED METHANE ACCUMULATION FOR ALL CONDITIONS.	206
<b>FIGURE 6.8</b>	CHANGING CARBON DEPOSITION AREA AND ITS EFFECT ON DISSOLUTION.....	208
<b>FIGURE 6.9</b>	CARBON DIFFUSION MODEL ON Ni(111).....	209
<b>FIGURE 6.10</b>	INSENSITIVITY OF $V_3$ VIBRATION ON METHANE DISSOCIATION. ....	210
<b>FIGURE A. 1</b>	SCHEMATIC FOR CRYSTAL HEATER ASSEMBLY.....	222
<b>FIGURE A. 2</b>	FRONT PANEL FOR “PID TEMPERATURE CONTROLLER.VI” .....	227
<b>FIGURE A. 3</b>	.....BLOCK DIAGRAM FOR “PID TEMPERATURE CONTROLLER.VI”	228
<b>FIGURE A. 4</b>	BLOCK DIAGRAM FOR “SIMPLIFIED PID WITH NORMALIZED OUTPUT.VI” .....	230
<b>FIGURE A. 5</b>	BLOCK DIAGRAM FOR “SIMPLE PID.VI” .....	231
<b>FIGURE A. 6</b>	BLOCK DIAGRAM FOR “PID TEMP READING.VI” .....	232
<b>FIGURE A. 7</b>	BLOCK DIAGRAM FOR “CONV TYPE E, MV-K.VI” .....	233
<b>FIGURE A. 8</b>	BLOCK DIAGRAM FOR “SETPOINT CALCULATOR.VI “ .....	234
<b>FIGURE A. 9</b>	BLOCK DIAGRAM FOR “SWITCHING BETWEEN SETPOINTS.VI” .....	235
<b>FIGURE A. 10</b>	BLOCK DIAGRAM FOR “PLAY SOUND.VI” .....	236

<b>FIGURE B. 1</b> KING AND WELLS MODULATION EXPERIMENT IN IGOR ANALYSIS PROGRAM.....	242
<b>FIGURE B. 2</b> OUTPUT FROM IGOR MACRO FOR MODULATION ANALYSIS.....	243
<b>FIGURE B. 3</b> OUTPUT FROM IGOR MACRO FOR MODULATION ANALYSIS.....	244
<b>FIGURE B. 4</b> FINAL RESULTS FROM IGOR MACRO WITH CALCULATED STICKING PROBABILITIES. ....	245
<b>FIGURE C. 1</b> FRONT PANEL FOR CHANGING CONSTANTS USED IN THE MODEL .....	256
<b>FIGURE C. 2</b> CALCULATED ENERGETIC FACTORS FOR THE DIFFERENT PROCESSES IMPACTING CARBON ALLOCATION.....	257
<b>FIGURE C. 3</b> AN EXAMPLE OF THE OUTPUT FROM THE FITTING PROGRAM. ....	258
<b>FIGURE C. 4</b> FUNCTIONAL DEPENDENCE FOR THE DIFFERENT PATHWAYS ON CARBON CONCENTRATIONS IN THEIR RESPECTIVE LAYERS .....	259

# List of Tables

<b>TABLE 1.1</b> EIGENSTATE RESOLVED STUDIES FOR CH <sub>4</sub> DISSOCIATION .....	18
<b>TABLE 2.1</b> CALCULATED E <sub>vib</sub> VALUES FOR CH <sub>4</sub> TEMPERATURES 300 – 1000 K.....	35
<b>TABLE 2.2</b> MEASURED METHANE ROTATIONAL TEMPERATURES.....	68
<b>TABLE 2.3</b> NORMAL VIBRATIONAL MODES OF CH <sub>4</sub> AND CHD <sub>3</sub> .....	72
<b>TABLE 3.1</b> METHANE BEAM CONDITIONS ON Ir(111).....	93
<b>TABLE 3.2</b> MEASURED VIBRATIONAL EFFICACIES AND CALCULATED C-H BOND LENGTHS AT THEIR TRANSITION STATE.....	102
<b>TABLE 4.1</b> CHD <sub>3</sub> /Ni(111) BEAM CONDITIONS FOR EXPERIMENTS. ....	128
<b>TABLE 4.2</b> C <sub>3v</sub> CHARACTER TABLE .....	132
<b>TABLE 4.3</b> ROTATIONAL CONSTANTS FOR CHD <sub>3</sub> .....	132
<b>TABLE 4.4</b> ... EQUATIONS FOR CALCULATING THE SPIN WEIGHTS FOR THE DIFFERENT SYMMETRY SPECIES OF CHD <sub>3</sub> AND THEIR ASSOCIATED <i>K</i> VALUES. ....	133
<b>TABLE 4.5</b> CALCULATED VIBRATIONAL AND ROTATIONAL FACTORS FOR F <sub>exc</sub> ...	136
<b>TABLE 4.6</b> S <sub>0</sub> <sup>OFF</sup> AND S <sub>0</sub> <sup>v1</sup> FOR CHD <sub>3</sub> ON Ni(111). ....	140
<b>TABLE 4.7</b> FITTING PARAMETERS FOR S <sub>0</sub> <sup>OFF</sup> AND S <sub>0</sub> <sup>v1</sup> .....	144
<b>TABLE 5.1</b> SURFACE COUPLING PARAMETERS CALCULATED THROUGH DFT TECHNIQUES.(40).....	158
<b>TABLE 5.2</b> CH <sub>4</sub> /Ni(111) BEAM CONDITIONS FOR EXPERIMENTS. ....	161
<b>TABLE 5.3</b> CALCULATED VIBRATIONAL AND ROTATIONAL FACTORS FOR F <sub>exc</sub> . ..	164
<b>TABLE 5.4</b> MEASURED CH <sub>4</sub> INITIAL STICKING PROBABILITIES FOR S <sub>0</sub> <sup>OFF</sup> & S <sub>0</sub> <sup>v3</sup> . 170	
<b>TABLE 5.5</b> CALCULATED COEFFICIENTS FROM THE BEST FIT LINES FOR S <sub>0</sub> .. .....	175

State Resolved Measurements of Methane  
Reactivity on Ni(111) and Ir(111) Surfaces

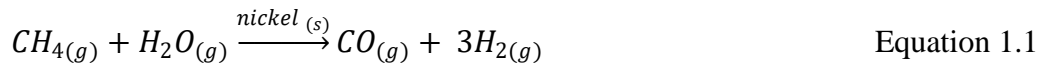
# Chapter 1 Introduction

Surfaces provide a rich environment for processing chemicals. Wolfgang Pauli, a man familiar with surfaces and boundaries, was quoted as saying, "God made the bulk; the surface was invented by the devil."<sup>(1)</sup> This demonic nature stems from the diversity of chemical interactions that occur at surfaces. Bulk materials have a largely uniform distribution of structural and molecular moieties that tempers the possible outcomes resulting from chemical interactions. Atoms on or near an interface are in anisotropic environments where their lowest energy state differs significantly from their bulk counterparts. The lack of a full complement of neighbors for a surface atom oftentimes makes it more reactive than any other part of the material.

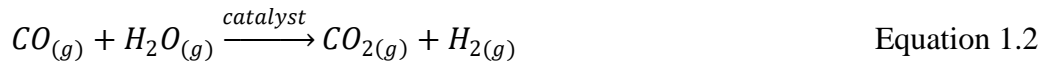
Heterogeneous reactions at interfaces between solids and gases are a class of reaction that is heavily exploited in industrial application due to the favorable energetics and ease of generating separable products. In 2015 the global market for chemical sales was valued at \$3.5 trillion corresponding to every individual on earth consuming \$500 worth of chemicals during the same time period.<sup>(2)</sup> The study of surfaces and how their structure and energetics influence the conversion of gases is paramount for the design of new catalysts for industrial use. As we move into a future with increasing energy demands we must find processing techniques that limit unwanted byproducts and while maximizing the return on energy input.

For a surface, the two dimensional structure contains many fewer atoms than the three dimensional bulk substrate. This limits the number of reactive events that can take place based on the available surface area of the catalyst. Industrial reactions are performed under elevated pressures and temperatures to increase the number of surface collisions that results in a reactive encounter. High pressures complicate analysis because they limit the path length that electrons and photons can travel before experiencing a destructive event. Surface analysis techniques rely heavily on the use of electrons to determine the structure of the surface and the atomic or molecular composition of surface bound species. Additionally, catalysts typically contain microcrystalline surfaces that include many different facets that contribute differently to reactivity, or, in the extreme, produce completely different products. Surface science techniques bypass these complications by performing experiments 1) under vacuum where stray collisions are minimized, 2) on well defined surfaces containing a single crystalline face, and 3) for gaseous reagents with well defined energetics. This process is similar to taking apart an already functioning machine in an effort to understand and improve its operation; the machine is working but are there components of the machine that could be better designed?

The chemical reaction system that is detailed in the following chapters is the **steam reforming of methane**. Steam reforming takes methane in the presence of hyper-thermal steam and a metal catalyst, usually nickel, to produce carbon monoxide and the industrially relevant gas, hydrogen (Equation 1.1).



The undesirable carbon monoxide is further reacted in the presence of steam and a catalyst to produce more hydrogen gas and the by-product carbon dioxide (Equation 1.2).



Demand for hydrogen comes from many sources ranging from the petrochemical industry, fuel cell applications, and further processing in the Haber-Bosch process to produce ammonia.(3) Ammonia is important for the use as fertilizer in agriculture.(4) In 2015 the United States consumed 88% of its nearly 140,000 metric tons of produced and imported ammonia as fertilizer. The global demand for ammonia is well above one hundred thousand metric tons annually and has been increasing for years, as shown in Figure 1.1.(5)

The first catalytic step for producing hydrogen from methane is the rate limiting initial C-H bond cleavage on the metal surface.(6) After the initial CH bond is broken, subsequent C-H bond cleavage proceeds more rapidly and recombination of hydrogen atoms on the surface leads to H<sub>2(g)</sub> desorption and a surface bound CH<sub>x</sub> (x = 0-3) fragment, where x is surface temperature dependent.(7) From a fundamental standpoint, methane is an ideal molecule for study since it is more complex than surface reactions with diatomic molecules, but the system is still amenable to high-level theoretical calculations. The initial C-H bond cleavage of methane on metal surfaces has been the scrutiny of many

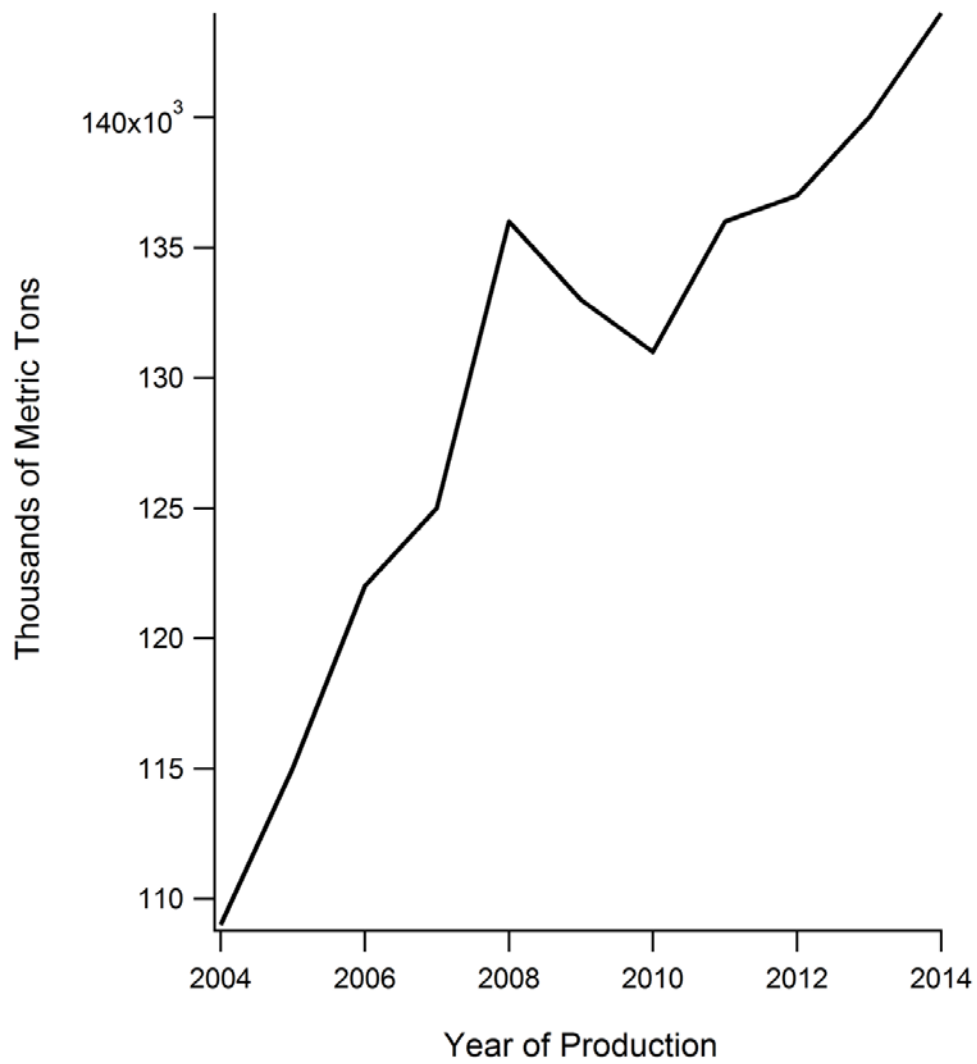


**Figure 1.1** Global ammonia production from 2004 – 2014 collected by the United States Geological Survey.<sup>5</sup>

experimental and theoretical studies in an effort to characterize the important energetic coordinates that promote dissociation. A variety of surfaces have been studied with a focus on the low index faces of Ni, Pt, and Ir metals.(8) Data has also been collected on W(9), Ru(10), Pd(11), and several mixed alloy systems.(12-14) The topic of this thesis focuses on two metallic surfaces in particular, namely the Ir(111) surface discussed in Chapter 3, and the Ni(111) surface discussed in Chapters 4-6. These two surfaces provide strikingly different reaction dynamics due to their largely different methane dissociation barriers, ca. 39(15) and 97(16) kJ/mol, respectively. Using the tools of surface science we aim to separate the energetic components that describe the complicated potential energy surface for methane dissociation.

The methane-surface interaction can be modeled using a one-dimensional Lennard-Jones potential.(17) This is a useful depiction when assessing how translational energy,  $E_{trans}$ , influences dissociative chemisorption for an activated process. The curves shown in Figure 1.2 represent the total energy of the methane – surface system. As methane approaches the surface possessing one of the three translational energies,  $E_{trans}$ , the molecule encounters a repulsive energetic barrier (B or C). Methane molecules that have sufficient  $E_{trans}$  overcome this barrier leading to C-H bond cleavage on the surface. The potential described by curve B corresponds to the lower barrier reaction on Ir(111), and curve C represents Ni(111). A methane molecule that has sufficient  $E_{trans}$  to overcome the barrier dissociates and ends up in the chemisorption well, D, where it becomes bound as a methyl radical and hydrogen atom on the surface. Molecules with insufficient

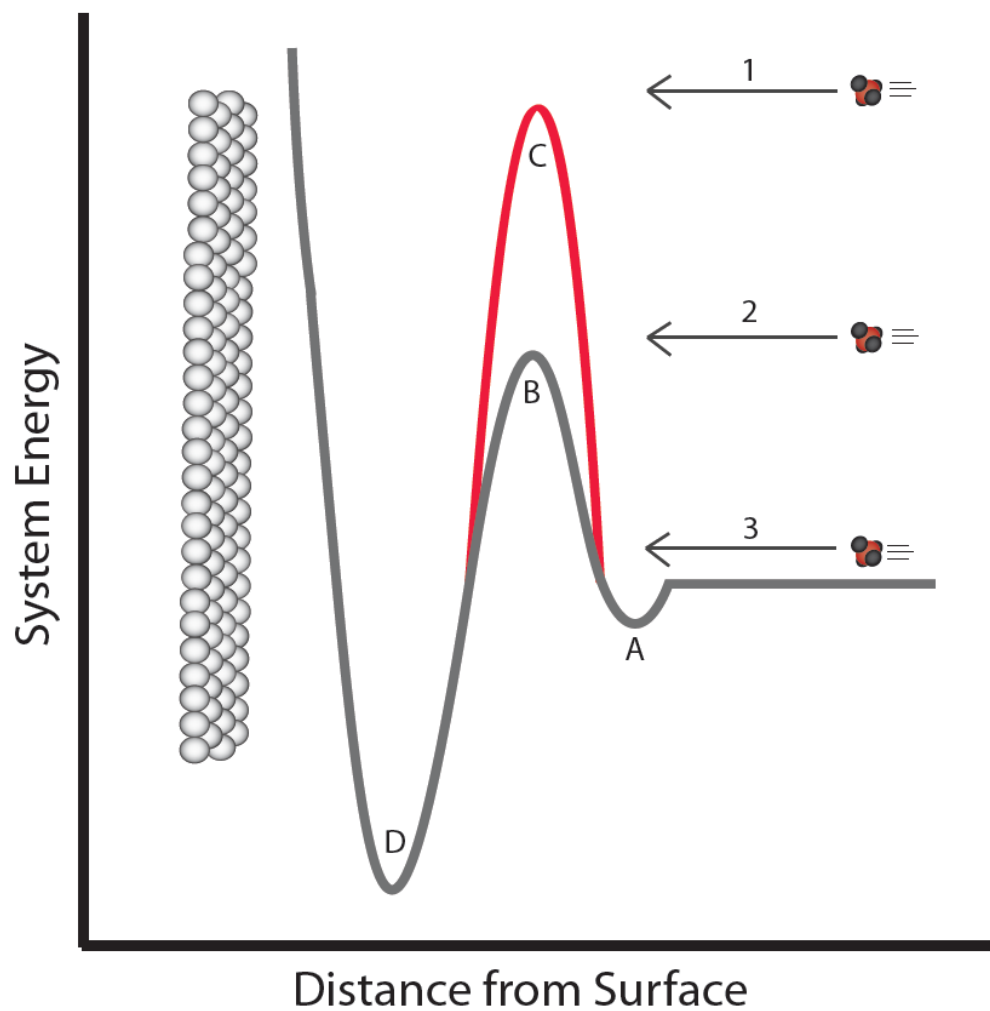


**Figure 1.2** Lennard-Jones potential showing the relative barrier heights for methane reacting on Ir(111) [B] and Ni(111) [C]. The potential well [A] corresponds to the trapping channel and [D] the chemisorption well. The three cases for incident methane correspond to decreasing translational energy,  $E_{trans}$ , from 1-3 as described in the text.

$E_{trans}$  scatter from the surface in non-reactive collisions. For methane reacting on Ni(111) (potential C) only molecules with the highest  $E_{trans}$ , as in Case 1, will dissociate. On Ir(111) molecules with  $E_{trans}$  described by Cases 1 and 2 both react because their incident energy is above the activation barrier of potential B. This type of reaction is considered a *direct dissociative mechanism* because there is direct conversion of the incident reagent into product during a single collision with no surface accommodation or additional steps. For a molecule reacting via a direct dissociative mechanism the initial sticking probability,  $S_0$ , defined as the sticking probability on a clean surface, increases approximately exponentially with  $E_{trans}$ . If the molecule has sufficiently low  $E_{trans}$  it can access a different reaction pathway. As the molecule approaches the surface it can lose  $E_{trans}$  during an inelastic collision with the surface and become molecularly physisorbed in the physisorption well, A, depicted by Case 3. If the methane still possesses, or can acquire, enough *internal energy* it can overcome the chemisorption barrier leading to molecular dissociation into the potential well, D.

A methane molecule trapped in the physisorption well, A, may desorb non-reactively back into the gas phase or the physisorbed complex may overcome the chemisorption barrier leading to C-H bond cleavage. The branching ratio of molecules that successfully overcome the chemisorption barrier compared to the molecules that desorb non-reactively is the quotient of the rate constants for the two processes, Equation 1.3.

$$Branching\ Ratio = \frac{k_{chemisorption}}{k_{desorption}} = A_c \exp\left(\frac{-E_{a,c}}{RT}\right) / A_d \exp\left(\frac{-E_{a,d}}{RT}\right) \quad Eq. 1.3$$

In this way surfaces with lower chemisorption barriers have the potential to exhibit a low  $E_{trans}$  pathway for dissociation that is not observed on surfaces with a higher barrier. This lower energy pathway is present for methane dissociation on Ir(111). As  $E_{trans}$  decreases a secondary *trapping mediated reaction mechanism* becomes dominant and the reaction probability increases. The presence of a low  $E_{trans}$  mechanism leads to several questions. Why does trapping on the surface increase the likelihood for dissociation? Do energetic coordinates aside from  $E_{trans}$  promote dissociation for a physisorbed molecule, or does the methane molecule transfer its available internal energy to the surface before reacting? These questions and a host of other considerations are discussed in Chapter 3 for the dissociative chemisorption of methane on Ir(111) using techniques described below.

As discussed above, the industrial conversion of methane to hydrogen requires high temperatures within a reactor. This means methane molecules have more  $E_{trans}$  to overcome the dissociation barrier through a direct mechanism; however, it is insufficient to assume that the increased dissociation rate is solely due to increased translational energy. Increased temperatures also lead to methane molecules with additional vibrational,  $E_{vib}$ , and rotational energy,  $E_{rot}$ , as well as a more energetic surface,  $E_{surf}$ . As a point of comparison between the available energetic coordinates, Figure 1.3 shows  $E_{trans}$ ,  $E_{vib}$ , and  $E_{surf}$  from 300 – 1000 K for CH<sub>4</sub> and Ni(111). The exclusion of  $E_{rot}$  is intentional at this point and is discussed in greater detail in the following chapters. At low temperatures the available energy in the system is dominated by  $E_{trans}$  and  $E_{surf}$ , however,  $E_{vib}$

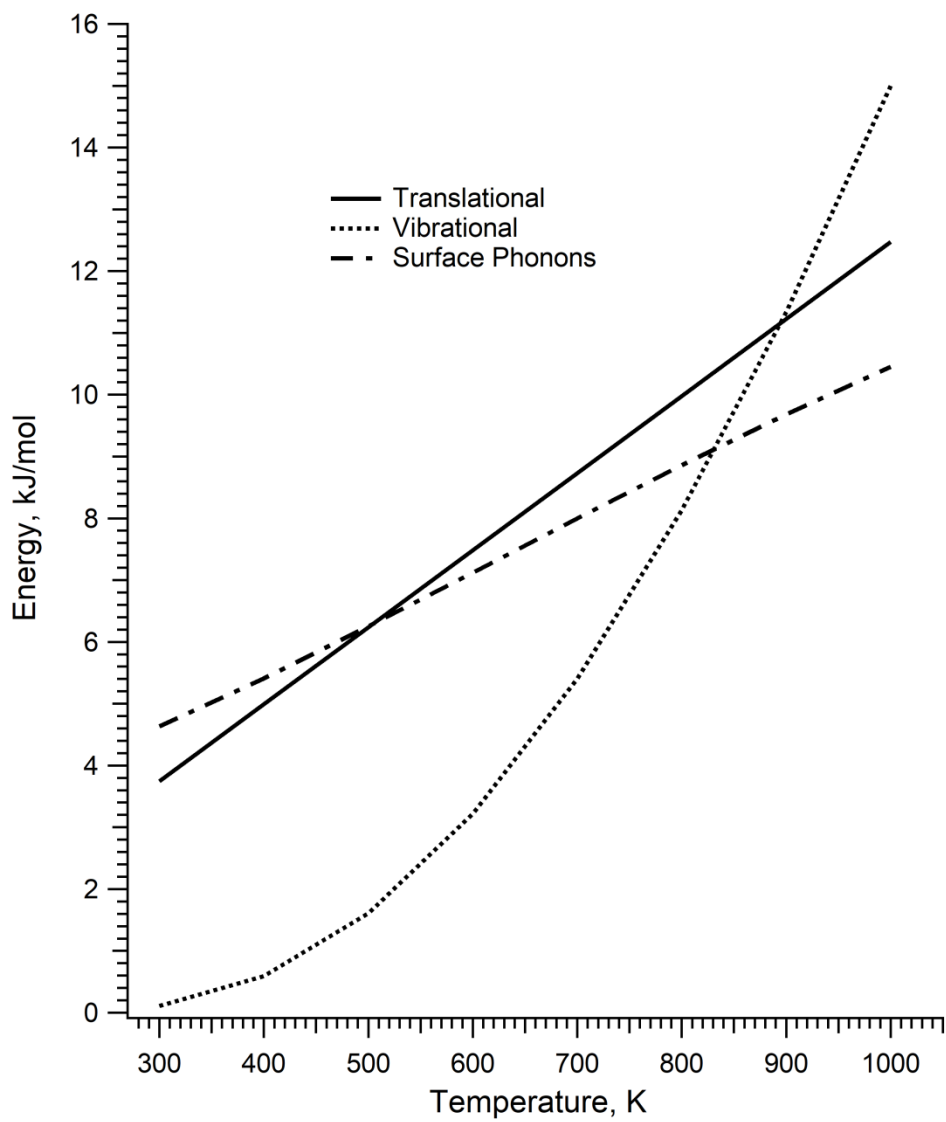


**Figure 1.3** Calculated methane translational ( $E_{trans}$ ), vibrational ( $E_{vib}$ ), and Ni(111) surface vibrational ( $E_{surf}$ ) energies from 300 – 1000 K. The methane translational energy is calculated as an ideal gas, the vibrational energy calculation is described in more detail in Chapter 2, and the surface vibrational energy is based on a simple harmonic oscillator approximation.

rapidly increases around 700 K. Steam reforming reactors are typically operated at internal temperatures exceeding 900 K(18) where these different modes of energy have appreciable effects. It also highlights the inherent difficulty in separating contributions from the different energetic coordinates under thermal conditions. A commonly used comparison for how the different energetic coordinates contribute to reactivity is the *energetic efficacy*,  $\eta$ . Comparing  $E_{vib}$  to  $E_{trans}$  as an example,  $\eta$  is a measure of how much  $E_{vib}$  reduces the amount of  $E_{trans}$  needed to obtain a given sticking probability. An efficacy of one means that the added  $E_{vib}$  promotes dissociation equally well as the same amount of  $E_{trans}$ ; values above one means  $E_{vib}$  is better at promoting dissociation and the inverse is true for values below one. The calculation of  $\eta$  is demonstrated in Equation 1.4 where  $\Delta E_{trans}$  is the reduction in  $E_{trans}$  and  $E_{vib}$  is the amount of vibrational energy added to the system.

$$n_{vib} = \frac{\Delta E_{trans}}{E_{vib}} \quad \text{Equation 1.4}$$

Let us imagine a surface-molecule system in which  $E_{trans}$ ,  $E_{vib}$ , and  $E_{surf}$  are easily separable with three knobs for independent control of each energetic coordinate. In this case, assume that the molecules only react via a direct dissociative mechanism. Therefore,  $S_0$  increases exponentially with  $E_{trans}$ . Consider an experiment that keeps  $E_{vib}$  and  $E_{surf}$  constant and increases  $E_{trans}$  continuously while recording  $S_0$ . The resulting plot of  $S_0(E_{trans})$  is simulated in Figure 1.4. As in Equation 1.4, let us compare how  $E_{vib}$  promotes dissociation relative to  $E_{trans}$ . To do this, a known amount of  $E_{vib}$  is added to the reactant

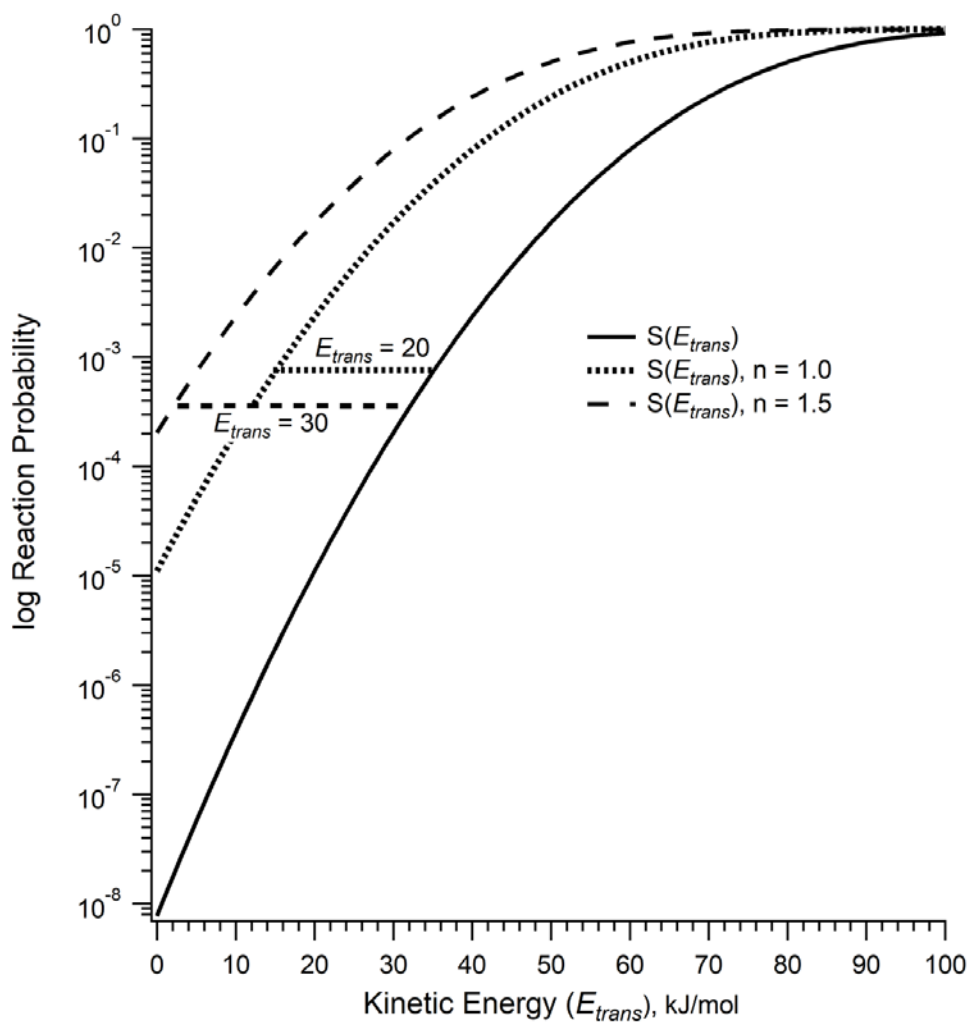


**Figure 1.4** Simulated sticking probability curves for methane dissociation as a function of translational energy,  $E_{trans}$ . The two dotted lines are hypothetical cases where added vibrational energy,  $E_{vib}$ , contribute to reaction probability, as described in the text.

molecules and  $S_0(E_{trans})$  is reevaluated; the result of which is a shift in the sticking curve, quantified as  $\Delta E_{trans}$ . If 20 kJ/mol of  $E_{vib}$  is added to the molecules and the  $S_0(E_{trans})$  curve shifts by  $\Delta E_{trans} = 20$  kJ/mol the efficacy of the added vibrational energy is  $\eta = 1 \left( \frac{\Delta E_{trans}}{E_{vib}} = \frac{20 \text{ kJ/mol}}{20 \text{ kJ/mol}} \right)$ . In this case vibrational energy is equally as effective at promoting dissociation when compared to  $E_{trans}$ . Alternatively, a  $\Delta E_{trans} = 30$  kJ/mol shift for the same  $E_{vib}$  leads to an efficacy of  $\eta = 1.5$  and the vibrational energy is *more* effective at promoting the reaction. These two cases are depicted graphically in Figure 1.4 showing the offset  $\Delta E_{trans}$ .

Here we see the importance in separating out the contributions from the various modes of energy for a clean comparison, but, the act of separating these variables is inherently difficult with the controls routinely available during experiments. Early gas-bulb experiments looked at how conversion rates changed with reactor temperature but as shown in Figure 1.3 the energy content of multiple energetic coordinates are coupled to temperature. Control over  $E_{trans}$  is drastically improved through the use of a supersonically expanded nozzle source in which the reagent gas is expanded through a small orifice into a low pressure vacuum environment. Heating the nozzle produces molecules with more  $E_{trans}$  and  $E_{vib}$ , however, seeding the reagent gas in different carrier gases produces a completely different set of  $E_{trans}$  values at the same nozzle temperature,  $T_{nozzle}$ . Figure 1.5 shows calculated  $E_{trans}$  values for methane supersonically expanded through a heated nozzle source with different seed gas identities. Taking a vertical slice down the four curves depicted in Figure 1.5 corresponds to methane molecules that have different  $E_{trans}$  but the same  $E_{vib}$  content as set by  $T_{nozzle}$ . With these

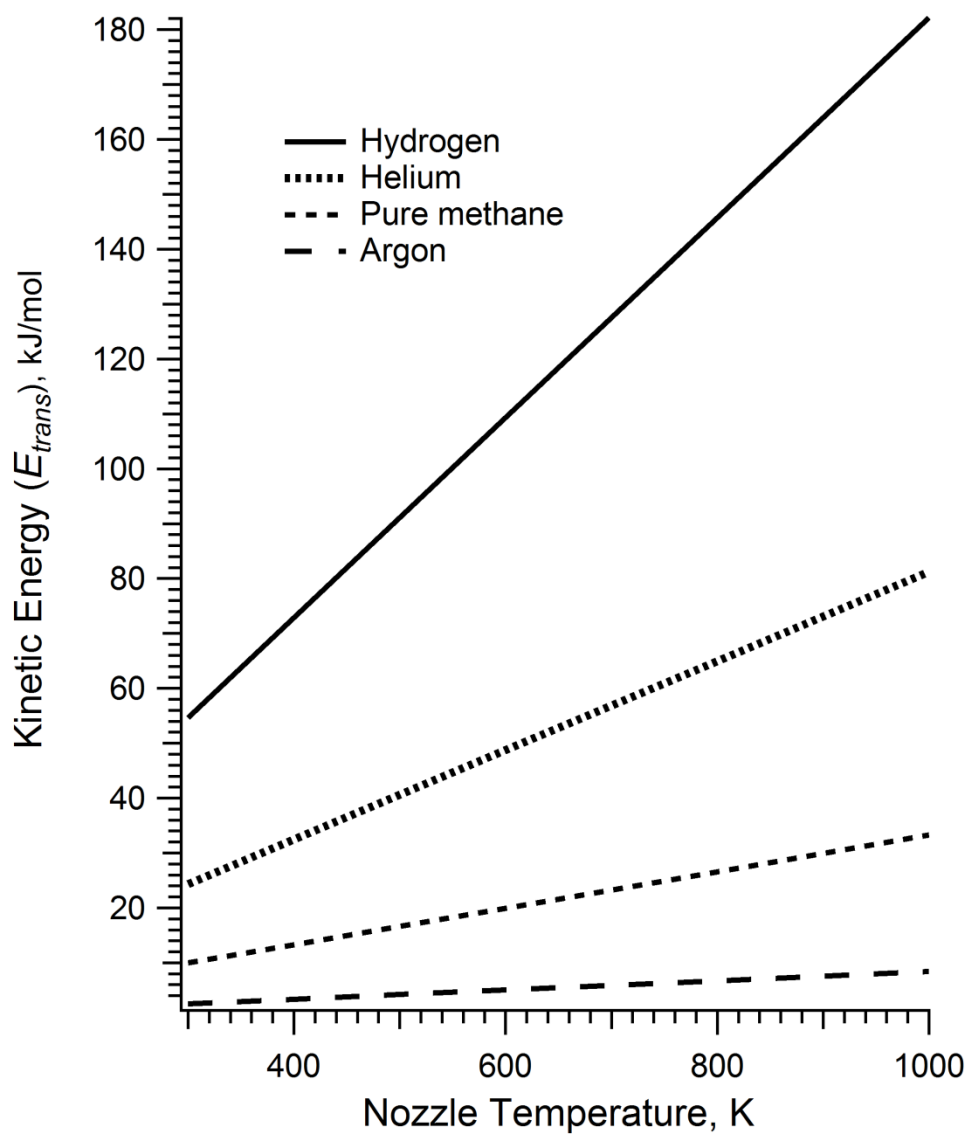


**Figure 1.5** Calculated translational energies,  $E_{trans}$ , for supersonically expanded methane mixes. The beams consist of 1% methane seeded in the carrier gases hydrogen, helium, and argon, with a pure methane beam for comparison.

techniques it is possible to have a constant nozzle temperature over a wide range of  $E_{trans}$ , effectively isolating  $E_{trans}$  from  $E_{vib}$ . It has been widely observed for methane reactivity on single crystals metal surfaces that molecules that possess more  $E_{vib}$  are more likely to react.(19) The question that arises from this observation is: how exactly does  $E_{vib}$  couple to the reaction coordinate to enhance reactivity?

A single atom does not contain any vibrational energy because it lacks the bonding structure that exists even in the simplest diatomic molecules. For a diatomic molecule, an increase in the gas temperature populates the single  $R_1$ - $R_2$  stretch vibration. Any observed change in reactivity as a function of  $E_{vib}$  must then be derived from variation in the  $R_1$ - $R_2$  bond length. For example, the heavily studied dissociation of  $H_2$  on metal surfaces is strongly influenced by molecular vibrational energy.(20) Moving to more complex molecules, such as methane, expands the range of possible vibrational identities. Methane possesses four vibrational modes: two bending modes,  $\nu_2$  and  $\nu_4$ , and two stretching modes,  $\nu_1$  and  $\nu_3$ . Under thermal conditions these four vibrational modes are populated as gas temperature increases. This is very similar to the problem demonstrated above where it was impossible to separate  $E_{trans}$  and  $E_{vib}$  under thermal conditions because they are inherently linked by gas temperature. If the same trick is applied here as above, a horizontal line can be drawn in Figure 1.5 to give constant  $E_{trans}$  with different degrees of  $E_{vib}$  set by  $T_{nozzle}$ . At the same  $E_{trans}$  value  $S_0$  increases with  $E_{vib}$ ; however, the broad thermal  $E_{vib}$  distributions make it nearly impossible to separate contributions from the four normal modes. To measure the effect of

each vibrational mode it is then necessary to preferentially populate one mode relative to the other three.

Recent advances in experimental technique couple infrared laser excitation with supersonic molecular beam sources to produce molecules with a non-thermal distribution of vibrational states. The laser, tuned to a frequency resonant with a single methane ro-vibrational state, intersects the molecular beam path where it excites a fraction of the incident methane molecules from the vibrational ground state to the  $v_i$  state. The state-resolved initial sticking probability,  $S_0^{vi}$ , quantifies the reactivity for methane molecules only residing in the excited state.

Contributions to  $S_0^{vi}$  from thermally populated states are removed by taking the difference in reactivity for methane molecules with,  $S_0^{On}$ , and without,  $S_0^{Off}$ , laser excitation and dividing by the fraction of molecules excited by the laser,  $f_{exc}$ . This term is then added to the ground state sticking probability,  $S_0^{v=0}$ , to give  $S_0^{vi}$  as in Equation 1.5.

$$S_0^{vi} = \frac{S_0^{On} - S_0^{Off}}{f_{exc}} + S_0^{v=0} \quad \text{Equation 1.5}$$

Now, instead of comparing how well the different modes of energy couple to the reaction coordinate, it is possible to assess how *individual* vibrational states compare to  $E_{trans}$  and to other vibrational modes. Let us now define the efficacy from Equation 1.4 as the efficacy for individual vibrational modes where  $E_{vib}^{vi}$  is the energy of the vibrationally excited state,  $v_i$ .

$$n(v_i) = \frac{\Delta E_{trans}}{E_{vib}^{vi}} \quad \text{Equation 1.6}$$

The first methane state-resolved initial sticking measurements were performed by Juurlink et al.(21) for the  $\nu_3$  anti-symmetric C-H stretching mode of methane dissociating on Ni(100). This study was followed by experiments performed by Higgins et al.(22) and Schmid et al.(23) for  $2\nu_3$  reactivity on Pt(111) and Ni(100), respectively. Since then there have been a host of metal surfaces and vibrational modes probed through this technique, outlined in Table 1.1. These initial studies showed that methane dissociation was sensitive to the identity of the vibrational mode, and not just the total amount of added  $E_{vib}$ .

The overall observations from these experiments has been that the  $\nu_1$  symmetric C-H stretch has the largest vibrational efficacy, followed by the  $\nu_3$  antisymmetric C-H stretch, with the  $\nu_2$  and  $\nu_4$  bending modes showing the lowest. Additionally, excitation to the overtones does not lead to a purely additive effect, with the second quanta promoting the reaction to a lesser degree than the first.(24) With the large quantities of experimental evidence there is definitive proof that that dissociation does not occur through a statistical process in which dissociation is driven by the total energy available to the reacting methane molecule. The reaction depends on more complicated dynamical processes that must be described for accurate modeling. This brings us back to a question posed above: how exactly does  $E_{vib}$  couple to the reaction coordinate to produce the observed increase in reactivity?

For methane dissociation to demonstrate mode-selectivity there must be differential access to the transition state based on the selected vibrational mode. Molecular dissociation is best described by a multi-dimensional potential energy

Surface Identity	Vibrational Mode	Reference
Ni(111)	$v_3$ $2v_3$ $3v_4$ $v_2 + v_4$	Smith(25) Bisson(24) Juurlink(26) Chen(27)
Ni(100)	$v_3$ $2v_3$ $v_1$ $3v_4$	Juurlink(21) Schmid(23) Maroni(28) Juurlink(26)
Pt(111)	$v_3$ $2v_3$	Ueta(29) Bisson(24), Higgins(22)
Pt(110)-(1x2)	$2v_3$ $v_1 + v_4$ $v_3 + v_4$ $2v_2 + v_4$	Bisson(30) Bisson(30) Bisson(30) Bisson(30)
Ir(111)	$v_3$	Dombrowski(31)

**Table 1.1** Eigenstate resolved studies for CH<sub>4</sub> dissociation

surface (PES) incorporating how the molecular and energetic degrees of freedom couple into the C-H bond cleavage channel. Distortion of intra-molecular coordinates at the transition state through vibrational motion can provide better access to the reaction channel for a late-barrier process, as described by Polanyi.(32) For the first time in history density functional theory has recently been able to account for all the molecular degrees of freedom and surface properties impacting methane dissociation on metallic single crystals. The calculated transition state geometry for atoms in the methane-surface complex differs significantly from their pre-reaction equilibrium positions. Two significant distortions are the C-H bond length of the dissociating H atom and the displacement of the metal atom beneath the dissociating methane, the latter of which will be discussed in the following paragraph. Looking at the (111) facet of Ni, Pt, and Ir single crystals the calculated C-H bond elongation at the transition state are 1.59,(33) 1.47,(33) and 1.43(34) Å, respectively, compared to the equilibrium C-H bond length in the gas phase of 1.09 Å. Methane molecules possessing more C-H stretching characteristic,  $\nu_1$  or  $\nu_3$ , should provide better access to the dissociation channel with the effect greatest on Ni, followed by Pt, and then Ir. That is indeed the case, with the measured efficacy being greatest for the former and lowest for the latter.(29, 31, 35)

The above focus on  $E_{trans}$  and  $E_{vib}$  coupling to the reaction coordinate has been intentional as those two energetic coordinates have been the most extensively studied. The effects of  $E_{rot}$  have been proven to be negligible in beam-surface scattering experiments(36) and the use of supersonic molecular beams

leads to rotationally cool reactant methane molecules. Therefore, the effects of  $E_{rot}$  will be largely ignored in the following chapters. The contribution from surface vibrations, or phonons, however, cannot be ignored. As mentioned above the calculated transition state geometry on Ni, Pt, and Ir show displacement of the metal atom at the adsorption site away from the lattice. This implicates phonon motion in enhanced access to the transition state. Generally, it has been observed that higher surface temperatures lead to higher dissociation probabilities but the impact of surface temperature is more subtle than for  $E_{trans}$  or  $E_{vib}$ .

Early molecular beam surface-scattering studies on Ni(111)(37), Ni(100)(38), and Pt(111)(39) were minimally influenced by surface temperature. The experiments were carried out with molecular beams containing a broad thermal distribution of vibrationally excited states, which decreased the impact of surface temperature on the  $E_{trans}$  threshold for reaction. Campbell performed state-resolved molecular beam experiments for the  $v_3 v=1$  excited state of methane on Ni(111).(40) The surface temperature was held at 90 K where surface phonon populations are minimal, effectively freezing the surface vibrational motion. Methane molecules that impinged on the 90 K surface were substantially less reactive than under the same conditions at 475 K because of their inability to access the minimum energy pathway. In Chapter 5 the same system is studied but at elevated surface temperatures up to 1000 K and much higher methane internal energies to assess how dissociation proceeds when the system is saturated with available energy.

Understanding how molecular dissociation is activated on surfaces has been the goal of surface scientists for many decades. Methane dissociation on metal surfaces is an ideal system to study in the next big leap in this understanding. The methods outlined above give a framework to deconstruct the complicated potential energy surface that governs dissociation. Here, we present experimental data for methane dissociation on Ir(111) and Ni(111). With this information we expand upon the existing knowledge base and provide important thermodynamic and kinetic factors that lead to more robust methods for predictive modeling.

## References

1. B. Jamtveit, P. Meakin, *Growth, Dissolution, and Pattern Formation in Geosystems*. (Kluwer Academic Publishers, Dordrecht ; Boston, 1999), vol. xviii, pp. 309.
2. CEFIC. (The European Chemical Industry Council, <http://www.cefic.org/>, 2016).
3. J. Emsley, *Nature's Building Blocks: An A-Z Guide to the Elements*. (Oxford University Press, New York, 2011).
4. R. Nehring, "Fertilizer Use & Markets," (United States Department of Agriculture, <https://www.usda.gov/>, 2016).
5. L. Apodaca, "Mineral Commodity Summaries: Nitrogen (Fixed) -- Ammonia," *Mineral Commodity Summaries* (US Department of Agriculture, 2016).
6. A. C. Luntz, J. Harris, CH<sub>4</sub> dissociation on metals: a quantum dynamics model. *Surface Science* **258**, 397-426 (1991).
7. S. T. Ceyer, Q. Y. Yang, M. B. Lee, J. D. Beckerle, A. D. Johnson, The Mechanism for the Dissociation of Methane on a Nickel Catalyst. *Studies in Surface Science and Catalysis* **36**, 51-66 (1988).
8. H. Chadwick, R. D. Beck, Quantum State-Resolved Studies of Chemisorption Reactions. *Annual Review of Physical Chemistry* **68**, 39-61 (2017).
9. C. T. Rettner, H. E. Pfnür, D. J. Auerbach, Dissociative Chemisorption of CH<sub>4</sub> on W(110): Dramatic Activation by Initial Kinetic Energy. *Physical Review Letters* **54**, 2716-2719 (1985).
10. J. H. Larsen, P. M. Holmblad, I. Chorkendorff, Dissociative Sticking of CH<sub>4</sub> on Ru(0001). *J. Chem. Phys.* **110**, 2637-2642 (1999).
11. M. Valden, J. Pere, M. Hirsimaki, S. Suhonen, M. Pessa, Activated adsorption of methane on clean and oxygen-modified Pt(111) and Pd(110). *Surf. Sci.* **377**, 605-609 (1997).
12. J. H. Larsen, I. Chorkendorff, Increased dissociation probability of CH<sub>4</sub> on Co/Cu(111). *Surf. Sci.* **405**, 62-73 (1998).
13. T. Kondo, T. Sasaki, S. Yamamoto, Dissociative chemisorption of CH<sub>4</sub> on a cesiated Pt(111) surface studied by supersonic molecular beam scattering techniques. *J. Chem. Phys.* **116**, 7673-7684 (2002).
14. P. M. Holmblad, J. H. Larsen, I. Chorkendorff, Modification of Ni(111) Reactivity Toward CH<sub>4</sub>, CO, and D<sub>2</sub> by Two-Dimensional Alloying. *J. Chem. Phys.* **104**, 7289-7295 (1996).
15. H. L. Abbott, I. Harrison, Dissociative Chemisorption and Energy Transfer for Methane on Ir(111). *The Journal of Physical Chemistry B* **109**, 10371-10380 (2005).
16. S. Nave, A. K. Tiwari, B. Jackson, Methane dissociation and adsorption on Ni(111), Pt(111), Ni(100), Pt(100), and Pt(110)-(1×2): Energetic study. *The Journal of Chemical Physics* **132**, 054705 (2010).

17. J. E. Lennard-Jones, Processes of adsorption and diffusion on solid surfaces. *Transactions of the Faraday Society* **28**, 333-359 (1932).
18. J. F. Xu, F. Froment, Methane steam reforming, methanation and water-gas shift: I. Intrinsic kinetics. *AiChE Journal* **35**, 88-96 (1989).
19. A. C. Luntz, R. D. Beck, Review Article: Dynamics of methane dissociation on transition metals. *Journal of Vacuum Science & Technology A: Vacuum, Surfaces, and Films* **35**, 05C201 (2017).
20. B. Hammer, M. Scheffler, K. W. Jacobsen, J. K. Nørskov, Multidimensional Potential Energy Surface for H<sub>2</sub> Dissociation over Cu(111). *Physical Review Letters* **73**, 1400-1403 (1994).
21. L. B. F. Juurlink, P. R. McCabe, R. R. Smith, C. L. DiCologero, A. L. Utz, Eigenstate-Resolved Studies of Gas-Surface Reactivity: CH<sub>4</sub>( $\nu_3$ ) Dissociation on Ni(100). *Physical Review Letters* **83**, 868-871 (1999).
22. J. Higgins, A. Conjusteau, G. Scoles, S. L. Bernasek, State selective vibrational ( $2\nu_3$ ) activation of the chemisorption of methane on Pt (111). *The Journal of Chemical Physics* **114**, 5277-5283 (2001).
23. M. P. Schmid, P. Maroni, R. D. Beck, T. R. Rizzo, Surface reactivity of highly vibrationally excited molecules prepared by pulsed laser excitation: CH<sub>4</sub> ( $2\nu_3$ ) on Ni(100). *The Journal of Chemical Physics* **117**, 8603-8606 (2002).
24. R. Bisson, M. Sacchi, T. T. Dang, B. Yoder, P. Maroni, R. D. Beck, State-Resolved Reactivity of CH<sub>4</sub>( $2\nu_3$ ) on Pt(111) and Ni(111): Effects of Barrier Height and Transition State Location. *The Journal of Physical Chemistry A* **111**, 12679-12683 (2007).
25. R. R. Smith, D. R. Killelea, D. F. DelSesto, A. L. Utz, Preference for Vibrational over Translational Energy in a Gas-Surface Reaction. *Science* **304**, 992-995 (2004).
26. L. B. F. Juurlink, R. R. Smith, D. R. Killelea, A. L. Utz, Comparative Study of C-H Stretch and Bend Vibrations in Methane Activation on Ni(100) and Ni(111). *Physical Review Letters* **94**, 208303 (2005).
27. N. Chen, Y. Huang, A. L. Utz, State-Resolved Reactivity of Methane ( $\nu_2 + \nu_4$ ) on Ni(111). *The Journal of Physical Chemistry A* **117**, 6250-6255 (2013).
28. P. Maroni, D. C. Papageorgopoulos, M. Sacchi, T. T. Dang, R. D. Beck, T. R. Rizzo, State-resolved gas-surface reactivity of methane in the symmetric C-H stretch vibration on Ni(100). *Physical Review Letters* **94**, 246104 (2005).
29. H. Ueta, L. Chen, R. D. Beck, I. Colon-Diaz, B. Jackson, Quantum state-resolved CH<sub>4</sub> dissociation on Pt(111): coverage dependent barrier heights from experiment and density functional theory. *Physical Chemistry Chemical Physics* **15**, 20526-20535 (2013).
30. R. Bisson, M. Sacchi, R. Beck, Mode-specific reactivity of CH<sub>4</sub> on Pt(110)-(1 $\times$ 2): The concerted role of stretch and bend excitation. *Physical Review -Series B-* **82**, 121404(R) (2010).

31. E. Dombrowski, E. Peterson, D. Del Sesto, A. L. Utz, Precursor-mediated reactivity of vibrationally hot molecules: Methane activation on Ir(1 1 1). *Catalysis Today* **244**, 10-18 (2015).
32. J. C. Polanyi, Concepts in reaction dynamics. *Accounts of Chemical Research* **5**, 161-168 (1972).
33. S. Nave, B. Jackson, Methane dissociation on Ni(111) and Pt(111): Energetic and dynamical studies. *The Journal of Chemical Physics* **130**, 054701 (2009).
34. G. Henkelman, H. Jonsson, Theoretical Calculations of Dissociative Adsorption of CH<sub>4</sub> on an Ir(111) Surface. *Physical Review Letters* **86**, 664-667 (2001).
35. R. R. Smith, PhD Thesis, Rovibrational State-Resolved Studies of Methane Dissociation on Ni(111), *Tufts University* (2003).
36. L. B. F. Juurlink, R. R. Smith, A. L. Utz, The role of rotational excitation in the activated dissociative chemisorption of vibrationally excited methane on Ni(100). *Faraday Discussions* **117**, 147-160 (2000).
37. M. B. Lee, Q. Y. Yang, S. T. Ceyer, Dynamics of the activated dissociative chemisorption of CH<sub>4</sub> and implication for the pressure gap in catalysis: A molecular beam-high resolution electron energy loss study. *The Journal of Chemical Physics* **87**, 2724-2741 (1987).
38. P. M. Holmblad, J. Wambach, I. Chorkendorff, Molecular beam study of dissociative sticking of methane on Ni(100). *The Journal of Chemical Physics* **102**, 8255-8263 (1995).
39. A. C. Luntz, D. S. Bethune, Activation of methane dissociation on a Pt(111) surface. *The Journal of Chemical Physics* **90**, 1274-1280 (1989).
40. V. L. Campbell, PhD Thesis, State Resolved Measurement of Surface Temperature Dependence and Isotopically Selective Reactivity of Methane on Ni(111), *Tufts University* (2011).



## Chapter 2 : **Experimental Apparatus and Methods**

The experimental studies described in this thesis explore how energy deposited into specific energetic coordinates of the reactants, may, or may not, influence the probability of a gas-surface reaction, the reaction mechanism, and the identity of reaction products. These experiments aim to simulate conditions that exist in an industrial reactor, but with control, or knowledge of, each contributing factor to reaction probability. This makes analysis of the complicated system and underlying processes more meaningful. The apparatus and associated experimental methods are vital to the success of the studies in this thesis, and they are described in this chapter.

Two supersonic molecular beam surface scattering chambers were used. The two chambers are similar in their implementation but the design and specific instrumentation varies. Results in Chapter 3 were collected on the newly constructed, more compact, apparatus(1) housing the Ir(111) single crystal; while, Chapters 4-6 were collected using the existing chamber, which is described extensively in previous publications(2-8), on Ni(111).

A tunable infrared laser source on an independent laser table supplies either chamber with the photons necessary to perform state-resolved initial sticking probability measurements. Section 2.1 gives an overview of the experimental approach. Details of the molecular beam formation,

characterization, and experimental procedures for measuring reaction probability are described in Sections 2.2 – 2.4. The laser system and details related to state-resolved infrared excitation are described in Section 2.5.

## 2.1 General experimental approach

These experiments were performed in one of two triply differentially pumped supersonic molecular beam surface scattering chamber. Gas-phase methane reagents were entrained in a supersonic molecular beam that provided hyperthermal reagents with large amounts of narrowly distributed translational energy,  $E_{trans}$ . The beam terminated in the Main Chamber where the molecules impacted the metal surface and the gas-surface reaction occurred. The initial reaction probability, or sticking probability,  $S_0$ , for methane was measured for selected amounts of  $E_{trans}$ , vibrational population, and surface temperature,  $T_{surf}$ , to assess how these factors influenced dissociation. Excitation of the methane in the molecular beam with a tunable infrared laser excited a fraction of the  $v=0$  ground state methane molecules to a vibrationally excited state,  $v_i$ . The enhancement in reactivity for the beam with laser excited molecules compared to the beam without laser excitation is then due solely to the fraction of molecules now in that excited state. In this way we can measure the initially sticking probability for molecules in the  $v_i$  vibrational state, or the state-resolved sticking probability,  $S_0^{v_i}$ .(9)

The methane translational energy and energy distribution are quantified through time-of-flight techniques (Section 2.2.1) and the incident fluxes are measured (Section 2.2.2) to obtain the absolute coverage of methane after reactive doses. Preparation and characterization of the Ir and Ni single crystal surfaces is described in Section 2.3. Experimental methods for measuring  $S_0$  are described in

Section 2.4. The measurement of  $S_0$  was performed with real time King and Wells reflectivity techniques (Sections 2.4.1 and 2.4.2), or by measuring the quantity of dissociation products after a set dose time (Section 2.4.3). These techniques provide the means to separate the various energetic coordinates that impact reactivity for methane on two different metal surfaces, Ir(111) and Ni(111). Characterization of vibrational state populations in the beam and our modification of those populations by infrared laser excitation is the topic of Section 2.5. The thermal vibrational energy,  $E_{vib}$ , of the methane molecules exiting the nozzle orifice are measured directly (Section 2.5.2) or inferred from the nozzle temperature,  $T_{nozzle}$  (Section 2.5.3). The fraction of molecules excited by the laser to the  $v_i$  vibrational state is dependent on the number of molecules available in the  $v=0$  ground state; therefore, it is inherently linked to the thermal  $E_{vib}$  distribution. General laser techniques are also described in Section 2.5.

## **2.2 Molecular beam formation and characterization**

A generalized schematic of the methane molecular beam line is depicted in Figure 2.1. Gas expands from the molecular beam nozzle (2) in the Source chamber and passes through a skimmer (3) before entering the first differentially pumped chamber (FDC). Here, the infrared laser (4) intersects the beam then passes through a second collimating aperture (5). A rotating chopper wheel (6) housed in the second differential chamber (SDC) can rotate at 300 Hz to produce pulses of gas for time-of-flight characterization of the beam, or the slot can be positioned to allow the beam to continue on its path. A room-temperature pyroelectric bolometer (7) can be inserted into the beam path to monitor the extent of infrared laser absorption by the beam, or be retracted to then pass through an electromechanical shutter(8), which controls dose duration. The beam then passes through the beam valve (9) with three size limiting apertures that define the beam image on the surface (11) in the Main chamber (MC). An inert beam flag (10) can also be inserted into the beam path for molecular beam reflectivity measurements. This section of the chapter will highlight the use of each component of the beam line to produce and characterize the supersonic molecular beams used in the experiments detailed in Chapters 3-6.

### **2.2.1 Methane molecular beam formation**

The methane supersonic molecular beam was prepared by expanding a high pressure source ( $>10$  PSIG) into a low pressure environment ( $<1 \times 10^{-4}$  torr) through a roughly  $25 \mu\text{m}$  diameter nozzle orifice. Pure methane, or seeded beams

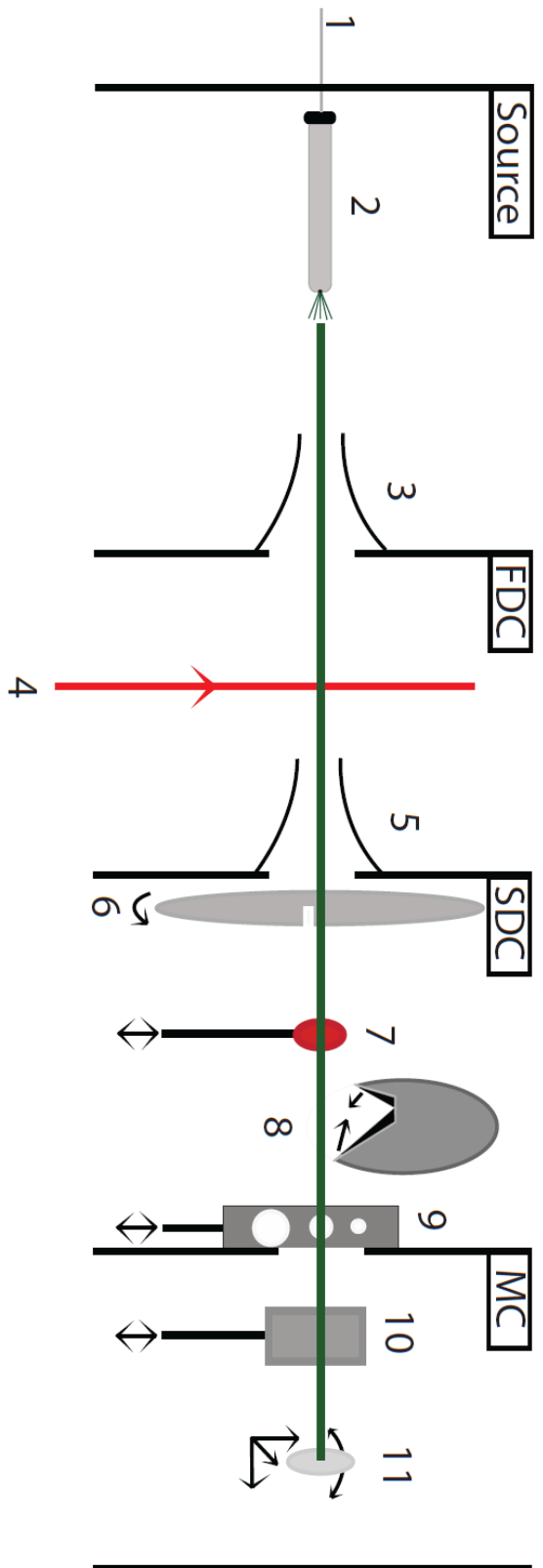


**Figure 2.1** Schematic of the molecular beam line in the differentially pumped surface scattering apparatus. The molecular beam is formed in the **Source** chamber and passes through the first and second differentially pumped chamber (**FDC**, **SDC**, respectively) where it intersects the single crystal (**11**) in the main chamber (**MC**). Many of the components are attached to motion stages or actuators as expressed by the black arrows in the figure.

1. External gas feed
2. Molecular beam nozzle
3. Beam skimmer
4. Infrared excitation source
5. Secondary beam skimmer
6. Rotating chopper wheel
7. Pyroelectric bolometer
8. Beam shutter
9. Beam selector
10. Beam flag
11. Single crystal metal surface

consisting of a dilute mixture of methane in He or H<sub>2</sub> provided access to a wide range of  $E_{trans}$ . Molecules thermalize with the nozzle walls and experience multiple collisions before exiting through the nozzle orifice.<sup>(10)</sup> The nozzle assembly is water cooled and can be resistively heated from 290 - 1050 ± 1 K. The nozzle temperature,  $T_{nozzle}$ , was monitored with a type-K thermocouple spot welded to the face of the nozzle in close proximity to the nozzle orifice. For the reasons mentioned above it is assured the thermocouple temperature gave an accurate reading for the gas temperature as it exits the nozzle.

Contaminants were removed from the reagent gas before passing through the molecular beam nozzle. First, the reagent gas passed through a dry ice (solid CO<sub>2</sub>) / acetone slurry to trap water or other condensable impurities that may be present. Second, a Supelpure O-Trap (Supelco) removed any molecular oxygen, remaining water vapor, or reactive carbonaceous species. To verify that all contaminants had been removed a non-reactive methane beam ( $T_{nozzle}, T_{surf} = 300$  K) was dosed onto the surface for several times longer than the experimental doses being performed. Under these conditions methane is not expected to react and adsorb to the surface, but any larger hydrocarbons, water, or other reactive impurities would adsorb to the surface. After the dose the surface was analyzed with Auger electron spectroscopy, AES, to detect any products resulting from contamination in the beam. No adsorbates were detected, so these methods confirmed that our methane reagents are contaminant free.

The methane  $E_{trans}$  was controlled through heating the nozzle or seeding the methane in a carrier gas at different mix percentages. Higher nozzle

temperatures,  $T_{nozzle}$ , produced faster reagents with inherently more  $E_{trans}$ .<sup>(11)</sup> In addition to adding  $E_{trans}$ , the resulting reagents possessed a nearly Maxwell-Boltzmann distribution of vibrational states set by  $T_{nozzle}$ .<sup>(12)</sup> In most cases, a broad thermal vibrational population complicates our experiments because we often look to separate the individual energetic effects leading to reaction. Table 2.1 demonstrates the effect of increasing  $T_{nozzle}$  on the methane  $E_{vib}$  content. It also shows how  $T_{nozzle}$  affects the resulting  $v=0$  ground state population, which is discussed in greater detail in Section 2.5. Seeding techniques allowed for  $E_{trans}$  to be controlled independent of  $E_{vib}$ . Gases with a lower molecular weight exited the nozzle at a higher velocity relative to heavier gases. Collisions between the reactant and seed gases (He, H<sub>2</sub>, Ar, and Kr in our case) and between themselves produced reactants with highly directional and uniformly distributed speeds. These controls, temperature and seed identity/ratio, allowed access to a wide range of methane reagent translational energies ranging from 3 - 190 kJ mol<sup>-1</sup>.

A skimmer placed after the nozzle selected the inner-most part of the expansion where uniformity is highest. There are a total of four chambers making up the differentially pumped beam line starting in the Source and ending with the experimental stage, the Main Chamber. This setup allows us to maximize directional flux to the crystal while minimizing effusive load during experiments.

### 2.2.2 Time-of-Flight Measurements

The average  $E_{trans}$  and  $E_{vib}$  distributions were characterized through time-of-flight quadrupole mass spectrometry (TOF-QMS) measurements utilizing

<b>Gas Temperature, K</b>	<b><math>E_{vib}</math> (kJ/mol)</b>	<b>Percent in ground state, <math>v=0</math></b>
300	0.114	99.3
450	1.02	94.0
700	5.40	73.4
850	9.68	58.9
1000	15.00	45.5

**Table 2.1** Calculated thermal vibrational energy,  $E_{vib}$ , for CH<sub>4</sub> at temperatures between 300 – 1000 K and the percentage of methane molecules remaining in the  $v=0$  ground state at the given temperatures.

a mechanical chopper wheel rotating at 300 Hz and in-line quadrupole mass spectrometer (QMS, UTI 100C). The chopper wheel in the chamber used for Ir(111) measurements, Fig. 2.2, contained slots for modulating the beam and separate slots for a light-emitting photodiode (LED) trigger to synchronize the chopper wheel position with QMS detection. The generated TOF trace (Figure 2.3) was the sum of 20,000 gas pulses produced by chopping the methane beam. The trace was then fit to a density-weighted Gaussian distribution function.<sup>(11, 13)</sup> The functional form of the fit defines the stream velocity,  $v_0$ , and velocity width,  $\alpha$ , for the gas pulse with  $N_v$  being a normalization constant.

$$f(v) = N_v v^3 \exp\left(-\left[\frac{v-v_0}{\alpha}\right]^2\right) \quad \text{Equation 2.1}$$

In the fitting procedure it was necessary to account for the chopper wheel gating function, ion flight time, and delays that exist between the LED trigger and QMS detection. Microsecond inaccuracies can produce large differences in  $E_{trans}$ . The gating function for Chamber 1(6) and Chamber 2(1) have been described elsewhere and the methodology for calculating the ion flight time and electronic delays for Chamber 2 were followed closely to those outlined in Ref. 1. The delays for Chamber 1 will be briefly described below.

A new nozzle was installed on Chamber 1 in spring of 2014 and a divergence from past behavior was observed. The velocities for CH<sub>4</sub> and CHD<sub>3</sub> molecular beams were less than predicted for all beam conditions but were markedly slower at elevated  $T_{nozzle}$ . To investigate the cause of this deviation TOFs were conducted for pure He and H<sub>2</sub> molecular beams for similar nozzle

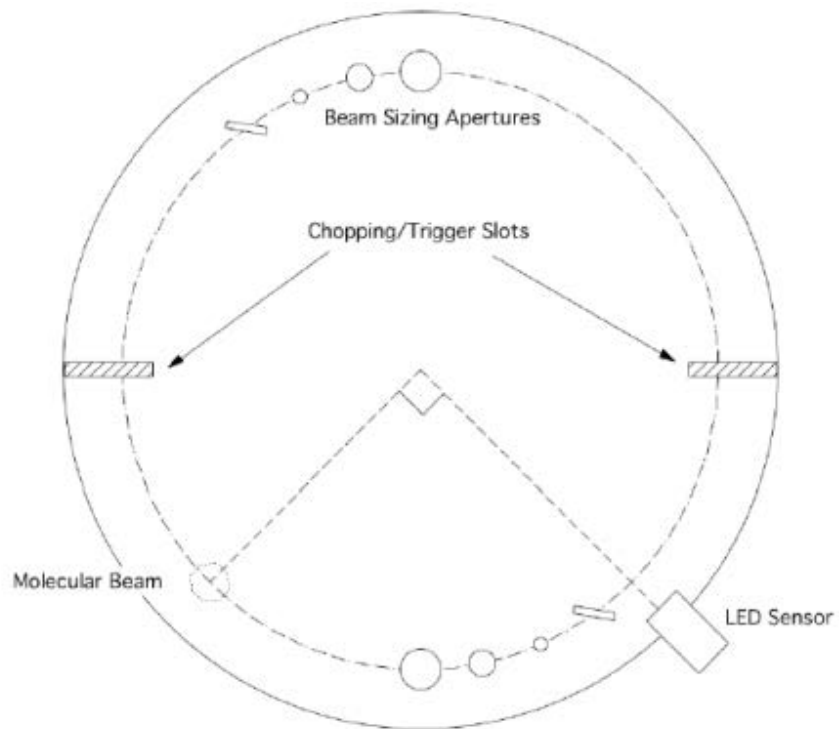


**Figure 2.2** Rotating chopper wheel for the Ir(111) experiments, reproduced from Ref. 1. The wheel is housed in the SDC for time-of-flight measurements. The chopper wheel used for Ni(111) experiments has similar features, but has four slots, two large and two small, spaced at  $90^\circ$  intervals around the wheel. Triggering for the LED occurs off one of the big slots instead of an independent triggering slot.

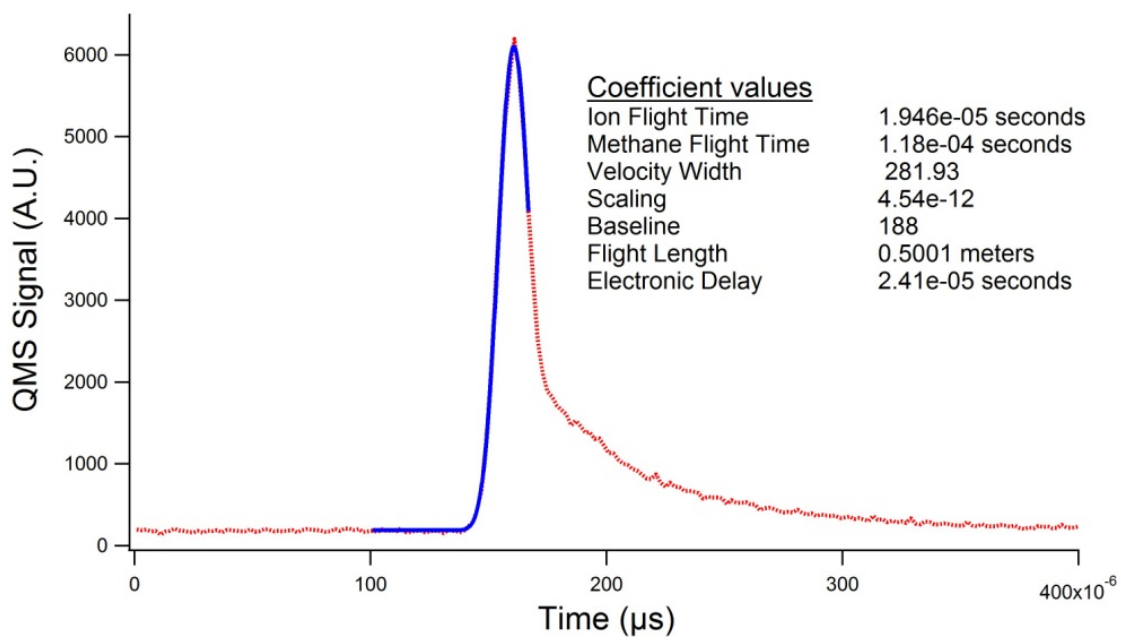


**Figure 2.3** Example of a typical time-of-flight residual and the resulting fitting parameters as described in the text.

temperatures. The TOFs were measured with and without a 0.210 m long extender on the QMS assembly. This eliminated the need for accurate determination of electronic delays as the difference in arrival times was solely due to the difference in length of the extender. The measured He translational energies were consistent with predicted values; however, the H<sub>2</sub> beam deviated at higher nozzle temperatures, as shown in Figure 2.4. This effect was also dependent on the gas backing pressure with lower pressures producing slower velocities for the same gas conditions. The difference the beams was the presence of rotational and vibrational levels in H<sub>2</sub>, and not in He. Accurate determination of the heat capacity for H<sub>2</sub> is complicated by rotational cooling ( $E_{rot} \rightarrow E_{trans}$ ) during expansion. As previously demonstrated by Smith(14) the heat capacity for H<sub>2</sub> can be calculated by fitting to an unconstrained three-term polynomial where  $E_{trans}$  is the translational energy,  $T_{nozzle}$  is the nozzle temperature and the  $k_i$  coefficients are the fitting parameters.

$$E_{trans} = k_0 + k_1 T_n + k_2 T_n^2 \quad \text{Equation 2.2}$$

Through this analysis we found that the calculated heat capacity varied from  $(5.56/2) \times R$  to  $(5.67/2) \times R$  for the  $T_{nozzle} = 288 - 1000$  K range, slightly lower than the  $(5.83/2) \times R$  to  $(5.90/2) \times R$  calculated in Ref 5 over a similar  $T_{nozzle}$  range. This can possibly be explained by a decrease in size of the nozzle orifice leading to a decrease in the  $E_{rot} \rightarrow E_{trans}$  energy transfer. The fact that higher nozzle pressures led to an increase in  $E_{trans}$  supports this idea. With a greater number density of molecules leaving the nozzle, there were more opportunities for collisions between molecules and an increased likelihood for energy transfer.

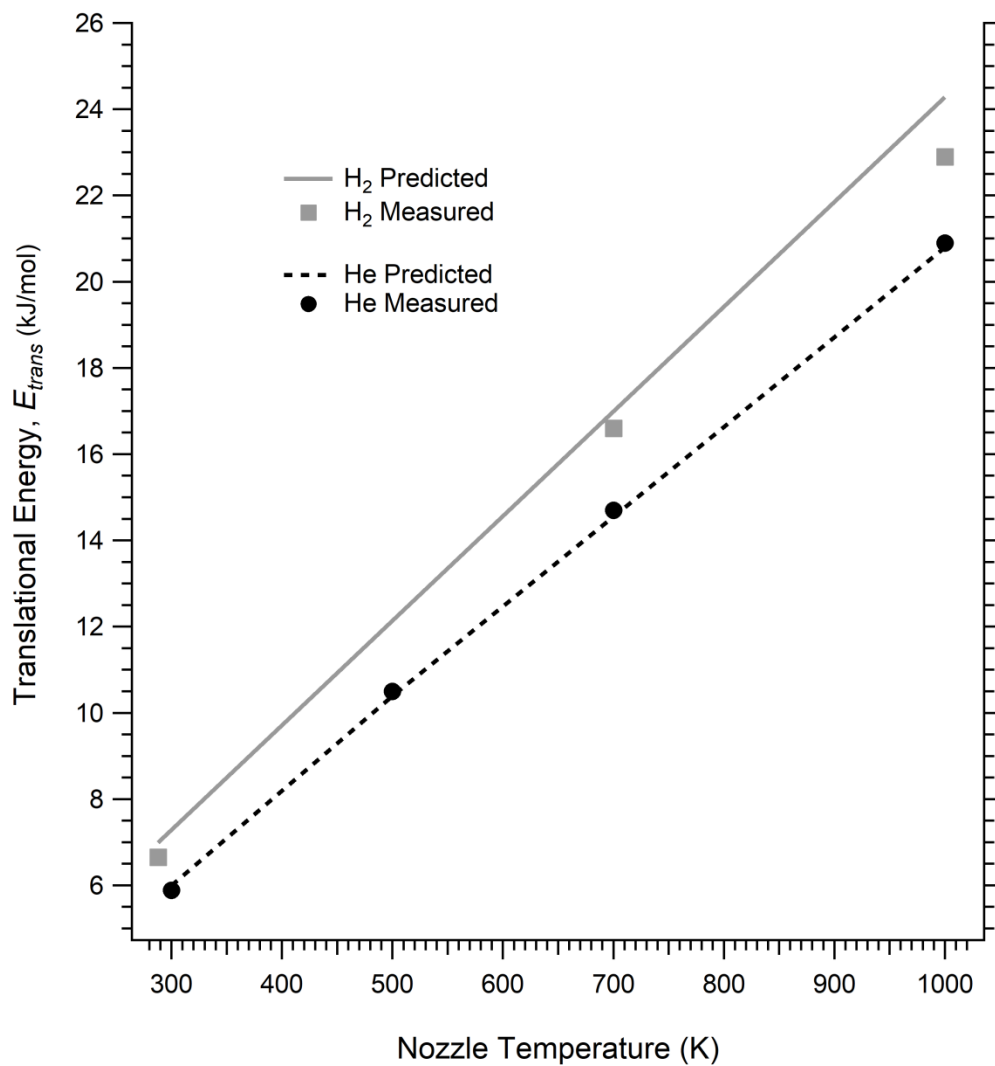


**Figure 2.4** Measured and predicted translational energies,  $E_{trans}$ , for pure He and H<sub>2</sub> molecular beams. Backing pressures were 180 and 60 psig respectively.

The same extender based TOF measurements were performed for the CH<sub>4</sub> and CHD<sub>3</sub> molecular beams since we could not trust that they were relatable to predicted values. The He TOFs were unaffected by incomplete rotational cooling; therefore, they were used to determine the delays associated with syncing the chopper wheel with QMS detection. The velocity in Equation 2.1 was measured for the CH<sub>4</sub> and CHD<sub>3</sub> beams using the extender but this did not yield the velocity distribution because that quantity is dependent on the delays. The electronic delays,  $t_{electronic}$ , for He and CH<sub>4</sub>/CHD<sub>3</sub> were the same but the ion flight time,  $t_{ion}$ , through the QMS rod assembly are different because  $t_{ion}$  is inversely proportional to the square root of the ion mass. The neutral ion flight time,  $t_{neutral}$ , or the time it took for the gas pulse generated by the chopper wheel to reach the QMS ionization zone, was then expressed in Equation 2.3 where  $t_{tot}$  was the measured arrival time.

$$t_{neutral} = t_{tot} - (t_{ion} + t_{electronic}) = t_{tot} - t_{delay} \quad \text{Equation 2.3}$$

The ion flight time and electronic delays were pooled to represent the total timing delay,  $t_{delay}$ . For each beam condition the velocity,  $v_0$ , was constrained to the value obtained using the extender and  $t_{delay}$  as determined using the He beam, the normalization constant  $N_v$ , and  $\alpha$  were determined through a non-linear least squares fit to Equation 2.1 using the TOF residuals obtained with and without the extender.

### 2.2.3 Flux Measurements

It was important to know the number density of methane molecules that hit the surface per unit time, denoted as the flux. The initial sticking probability was calculated using the flux of incident methane molecules as described in section 2.4.2 and flux also affects the uptake of methane on the surface during an extended dose. The flux of reactant molecules was quantified for each set of beam conditions. Since the gas mixes we used were seeded in a carrier gas, pressure readouts in the main chamber are a convolution of the methane reagent and seed gas. The procedure for experimentally determining the flux in  $\text{ML s}^{-1}$  is outlined below.

First the partial pressure of methane for a given set of beam conditions was measured using the QMS to monitor  $m/z = 16$  amu with the beam entering the main chamber and scattering off an inert beam flag. The methane beam was then blocked using the beam shutter (#8, Figure 2.1) and pure methane was introduced via a leak valve (Varian, 951-5106) into the main chamber until the QMS signal matched that obtained from the beam. Next the QMS ionizer was turned off (so as not to interfere with the ionization gauge reading), and the pressure was recorded. This recorded pressure was corrected for the ion gauge sensitivity factor for methane,  $\frac{N_2}{CH_4} = \frac{1}{1.4}$  to obtain the steady state partial pressure of methane in the chamber during the beam exposure. The partial pressure of methane introduced by the beam was much greater than the base pressure of the chamber; therefore, the resulting pressure reading represented the steady state

methane pressure introduced by the reagent beam. Using the ideal gas law this value was converted to the number of methane molecules leaving the chamber through the pump per second.

$$\frac{CH_4 \text{ molecules}}{\text{second}} = P_{CH_4} \times \frac{3.21E^{19} CH_4 \text{ molecules}}{\text{Torr} \times L} \quad \text{Equation 2.4}$$

This quantity was then converted to the flux per  $\text{cm}^2$ , where  $V_{chamber} = 26.3 \text{ L}$  is the chamber volume,  $A_{overlap} = 0.12 \text{ cm}^2$  is the area of the methane beam on the crystal for the small beam valve hole, and  $PS = 80 \text{ L/s}$  is the methane pumping speed under dose conditions.(6)

$$\frac{CH_4 \text{ molecules}}{\text{cm}^2} = \frac{CH_4 \text{ molecules}}{\text{second}} \times \frac{V_{chamber}}{A_{overlap} \times PS} \quad \text{Equation 2.5}$$

The resulting value is calibrated to represent the flux in monolayers per second, ML/s, by dividing by the density of surface atoms for each surface. For Ir(111) and Ni(111) these quantities are  $1.57 \times 10^{15}$  and  $1.90 \times 10^{15}$  atoms/ $\text{cm}^2$ , respectively. We obtain flux values ranging from 0.05 to 2 ML/s for beams used.

## 2.3 Substrate control and cleaning procedures

A single crystal of known structure and orientation was located in the ultra high vacuum (UHV) Main Chamber. The crystal was spot welded to tantalum legs which were mechanically fastened to a liquid nitrogen cooled XYZ-rotatable manipulator. The manipulator allowed the crystal to be manually positioned for exposure to the molecular beam, argon ion sputtering, auger electron spectroscopy (AES), or be raised out of the molecular beam path for TOF-QMS measurements.

Surface temperatures from 90 - 300 K were achieved by adding liquid nitrogen or dry ice coolant in the cryostat. A tungsten filament behind the single crystal provided resistive heating up to 700 K and electron bombardment with a positive bias applied to the crystal heated the crystal to temperatures exceeding 1500 K. A newly developed computer controlled PID algorithm (Appendix A) controlled the surface temperature within  $\pm 1$  K. Since the temperature range and cleaning procedures were different for Ir(111) and Ni(111) they used different thermocouple materials, type-R and type-E, respectively. The use of type-R thermocouple materials (Pt/Rh) were compatible with the higher temperatures required for cleaning Ir(111) and also provided oxidative stability from the repetitive use of oxygen cleaning cycles.

### 2.3.1 Cleaning Ir(111)

The surface was first sputtered with an ion sputter gun (Phi 04-191) at an incident angle of  $45^\circ$  relative to the surface normal for 5 minutes in the presence of  $1 \times 10^{-4}$  Torr Ar (500 eV) at approximately 100 K crystal temperature.

Sputtering the surface removed any adsorbed contaminants in addition to several layers of Ir atoms. The surface was then annealed for 45 minutes at 1300 K to rearrange the atoms to the ordered (111) surface. To eliminate any possible carbon on the surface the crystal was heated to 1100 K in the presence of  $1 \times 10^{-7}$  Torr  $O_2$  for 15 minutes and subsequently flashed to 1500 K to desorb any remaining oxygen. After this process the crystal was verified for cleanliness by looking for any carbon or oxygen remaining on the surface through AES. Sputtering was carried out once in the morning and the oxidation cycle after each experimental dose of methane. Calcium contaminants were occasionally seen by AES at an electron energy about 270 eV but repeated sputtering was sufficient to eliminate this feature.

### **2.3.2 Cleaning Ni(111)**

The Ni surface was sputtered in the same manner as above but since the cryogen used in the Ni(111) experiments was dry ice as opposed to liquid nitrogen the crystal temperature during sputtering was around 230 K. The surface was then annealed for 45 minutes at 1100 K. Removing carbon contaminants on Ni was much easier than on Ir(111); however, removing oxygen was much more difficult. Annealing for 5 minutes at 1000 K removed all C via dissolution into the crystal bulk. No carbon remains on the surface after this annealing cycle. Oxidative titration of carbon on the surface were performed by introducing  $O_{2(g)}$  into the chamber while monitoring the CO and  $CO_2$  desorption products via QMS. No C was detected on the surface by this sensitive method following annealing. Oxygen contamination on the surface was fairly rare because of the highly

reducing environment used in these experiments, but its presence was occasionally observed by AES at an electron energy of 550 eV. If there was oxygen on the surface it was removed with a 5 minute reduction by  $1 \times 10^{-6}$  Torr  $\text{H}_{2(g)}$  while holding  $T_{surf} = 1000$  K.

## 2.4 Measuring initial sticking probabilities

The initial sticking probability ( $S_0$ ) is a measure of the reaction probability for a given gaseous species on a solid substrate in the zero coverage limit. We measured  $S_0$  spanning 6-8 orders of magnitude, which required a variety of analysis techniques. Each method for measuring  $S_0$  was developed with some understanding of the surface-bound intermediates formed, the identity of thermal stable products, and if surface adsorbates alter subsequent probabilities for methane dissociation and adsorption. The two methods used in the following chapters were post-dose detections of the adsorbed products on the surface using AES, and the real-time monitoring of adsorption through King and Wells (K&W) molecular beam reflectivity techniques.<sup>(15)</sup> AES detection was useful under conditions when  $S_0 < 0.01$  and experimental doses up to 4 hours might be required to accumulate a detectable quantity of reaction products. It does require that reaction products accumulate on the surface and do not desorb or dissolve into the metal lattice prior to detection. Therefore, the AES method is unable to measure  $S_0$  if the surface product had any mobility into the crystal lattice, which removed the detectable product. The K&W method relied on detecting the change in partial pressure of the reacting gas as it adsorbed on the surface. For example, if half of the methane molecules entering the main chamber reacted on the surface the corresponding methane pressure would decrease by 50%. The ability to measure small changes in the partial pressure of methane in the chamber sets the detection limit for this approach.

Chen(16) described the use of laser modulation techniques coupled with K&W reflectivity to simultaneously obtain sticking values for both  $S_0^{\text{Off}}$  and  $S_0^{\text{On}}$ .(16) Section 2.4.2 expands and refines this work and data obtained through this technique are presented in Chapters 5-6.

### 2.4.1 King and Wells Reflectivity Method

The K&W method is a convenient way of quantifying the sticking probability of gaseous molecules reacting irreversibly with a solid substrate. This method was used at higher reaction probabilities, typically  $S_0 > 1\%$ , as smaller changes in pressure were within the noise limit of the instrument. In addition to  $S_0$ , the coverage dependent sticking probability  $S(\theta)$  could be acquired when  $\theta$  increased with exposure.

The K&W method involved measuring the change partial pressure of methane before and after exposure to the crystal surface. The sticking probability,  $S_0$ , is represented as:

$$S_0 = \frac{\text{\# reacting molecules}}{\text{total \# of molecules striking surface}} \quad \text{Equation 2.6}$$

The partial pressure of the methane in the Main Chamber was measured using the QMS when the molecular beam was (1) completely blocked from going into the chamber, (2) introduced into the chamber but blocked from hitting the crystal by an inert beam flag, and (3) impinging the single crystal. A representative trace of these three regions is shown in Figure 2.5. The drop in counts, and correspondingly pressure, at region (3) was a relative measure of the number of

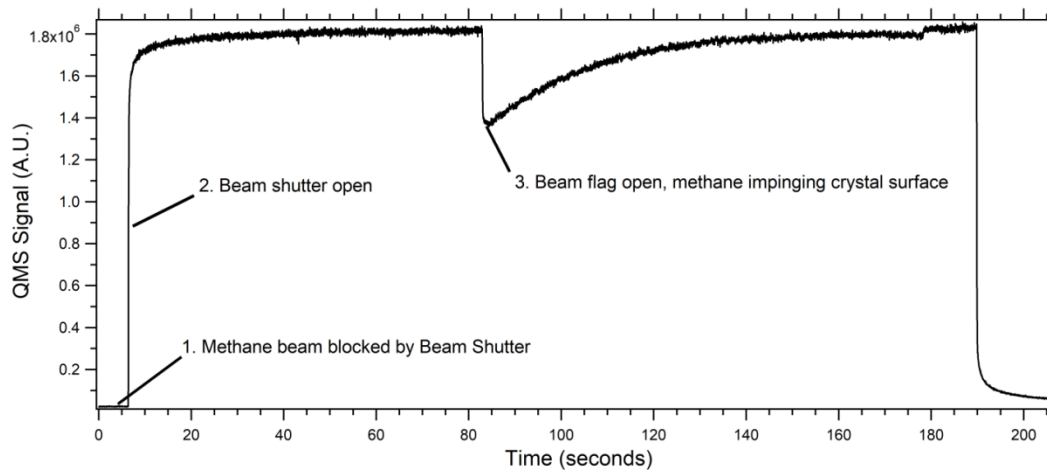


**Figure 2.5** Representative King and Wells experiment for a 0.25% CH<sub>4</sub>/H<sub>2</sub> mix reacting on Ni(111). The nozzle and surface temperatures for this dose were 900 K and 700 K, respectively.

reacting molecules, and when taken with the total number of molecules in the asymptote of region (2),  $S_0$  was determined as in Equation 2.6.

Maximizing pumping speed of the reacting gas was important as slower pumping speeds cause longer tails when transitioning between the three regions outlined above. Liquid nitrogen cooled surfaces in the diffusion pump trap and the crystal cryostat can act as a cryogenic getter for partially condensable gases. Those gases accumulate on the surface when pressure rises, and desorb when the pressure falls, or when cryogen levels drop. To minimize these effects it is a good idea to maintain constant cryogen fill levels to decrease the fluctuation caused by the adsorption/desorption equilibrium. Using dry ice as a coolant in the crystal cryostat eliminates this effect for most gases on cryostat surfaces.

#### **2.4.2 King and Wells Reflectivity with Laser Modulation**

An electro-mechanical shutter placed in the laser beam line (#4, Figure 2.1) modulated the infrared laser, and therefore infrared excitation within the molecular beam. We used this modulation to measure the laser-on,  $S_0^{On}$ , and laser-off,  $S_0^{Off}$ , initial sticking probabilities. The shutter was placed 10 cm from a sapphire window leading into the chamber and operated with a square wave driven power supply operating between 0.5-1 Hz. The shutter drive signal was recorded along with the K&W partial pressure QMS data using a custom built Labview program. More details about the laser system are discussed in Section 2.5. A typical K&W laser modulation experiment is displayed in Figure 2.6 and shows the resulting QMS signal for methane at  $m/z = 15$  amu. Laser modulation

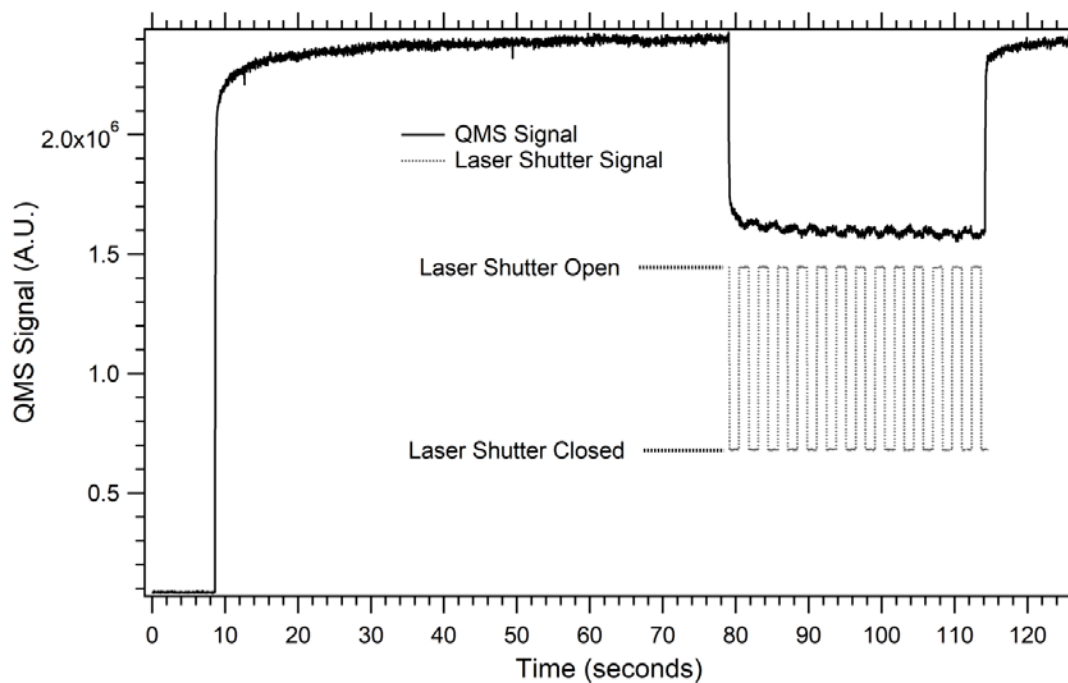


**Figure 2.6** King and Wells reflectivity modulation measurements for  $\text{CH}_4$  excited to the  $\nu_3 \nu=1$  vibrational mode on Ni(111). The  $\text{CH}_4$  conditions for this dose were  $T_{\text{nozzle}} = 900 \text{ K}$ ,  $T_{\text{surf}} = 1000 \text{ K}$ . The Laser Shutter Signal shows the effect of when the shutter is open versus closed on the recorded QMS signal.

modulates the reactivity of the methane molecules in the beam, and the trace shows the effect of this modulation during deposition.

There were several advantages to performing K&W experiments with laser modulation. First, at elevated nozzle temperatures the fraction of excited molecules was small (<10%) which led to small differences in  $S_0^{Off}$  and  $S_0^{On}$  (between 0.1-1%). To obtain adequate statistics without modulation, each experimental dose yielded a single measurement of  $S_0^{Off}$  or  $S_0^{On}$ . Independent doses needed to be carried out with 3+ repetitions each for molecules with and without laser excitation. By modulating the excitation source at, for example, 1 Hz, independent measurements of  $S_0^{Off}$  and  $S_0^{On}$  were acquired each second, and tens of independent measurements could be acquired in a single 1-minute K&W experiment. This drastically improved counting statistics dramatically reduced time for data acquisition.

Second, any instrumental drift (e.g. part-per thousand drifts in QMS sensitivity) during the experiment was minimized by taking the difference of paired adjacent sticking measurements. The time between adjacent  $S_0^{Off}$  and  $S_0^{On}$  measurements, as defined by the shutter frequency, was at most 2 seconds. We find that main sources of instrument drift in our experiments occur over a time scale of 10 seconds or more. The calculated results from Figure 2.6 are visualized in Figure 2.7 with the difference in  $S_0^{On}$  and  $S_0^{Off}$  values represented by the blue trace (right axis). A custom macro written for the data analysis program IGOR pro facilitated data processing and is included in Appendix B. Pooling the data in this way decreases our measured variance by more than two-fold.

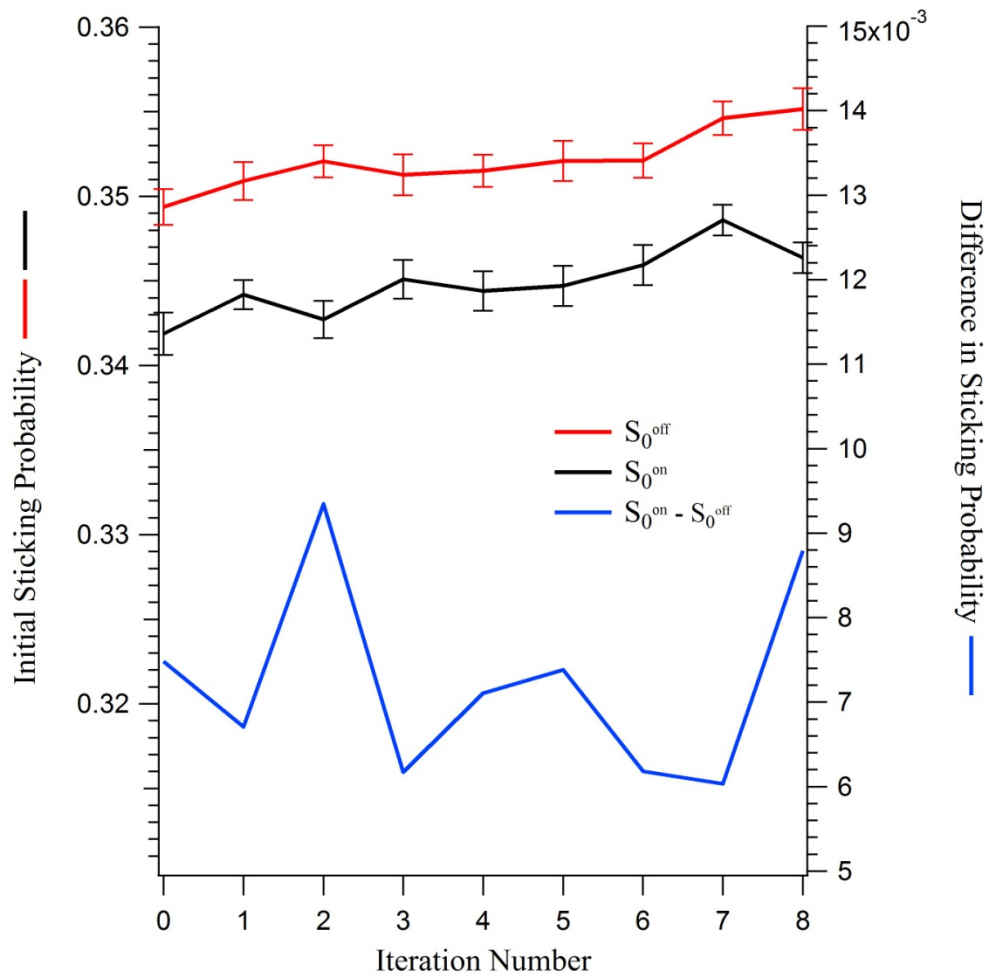


**Figure 2.7** Displayed are the results calculated from King and Wells experiment in Figure 2.6 with the left axis being the calculated initial sticking probabilities with and without laser excitation,  $S_0^{\text{on}}$ , and  $S_0^{\text{off}}$ , respectively. The right axis is the difference in these two values used in the calculation of the state resolved sticking probability  $S_0^{v_3, v=1}$ .

Lastly, note the difference between the K&W traces in Figures 2.5 and 2.6; in Figure 2.5 the sticking probability decreased as methane was deposited on the surface but it stayed constant in Figure 2.6. The cause of this observation is discussed in detail in Chapter 6, but briefly, this was because the surface temperature in Figure 2.6 was such that the carbon product rapidly dissolved into the bulk nickel lattice. For surface temperatures where dissolution is slow, carbon products of methane dissociation remain on the surface and block or inhibit subsequent reactivity during the duration of the dose. The pairing of adjacent sticking measurements discussed above is then not applicable under these conditions. To more accurately determine  $S_0^{Off}$  and  $S_0^{On}$  the adsorption isotherm,  $S(\theta)$ , for methane adsorption was collected during laser modulation and fit to the Temkin isotherm(17) where  $S(\theta)$  is the coverage dependent sticking probability,  $S_0$  is the initial sticking probability,  $\alpha_T$  is a fitting parameter, and  $\theta$  is carbon coverage in ML.

$$S(\theta) = S_0 \times (1 - \alpha_T \theta) \quad \text{Equation 2.7}$$

An example of this procedure is shown in Figure 2.8, as described in the caption. The effects of rapid site blocking were minimized by extrapolating the isotherm back to the zero coverage limit where  $S_0$  was derived from the y-intercept of the fit. The Temkin isotherm was chosen because it matched the empirically determined straight line relationship between sticking,  $S$ , and  $\theta$ . The coverage values ranged from a clean surface,  $\theta = 0$ , to a maximum of around  $\theta = 0.5$ .

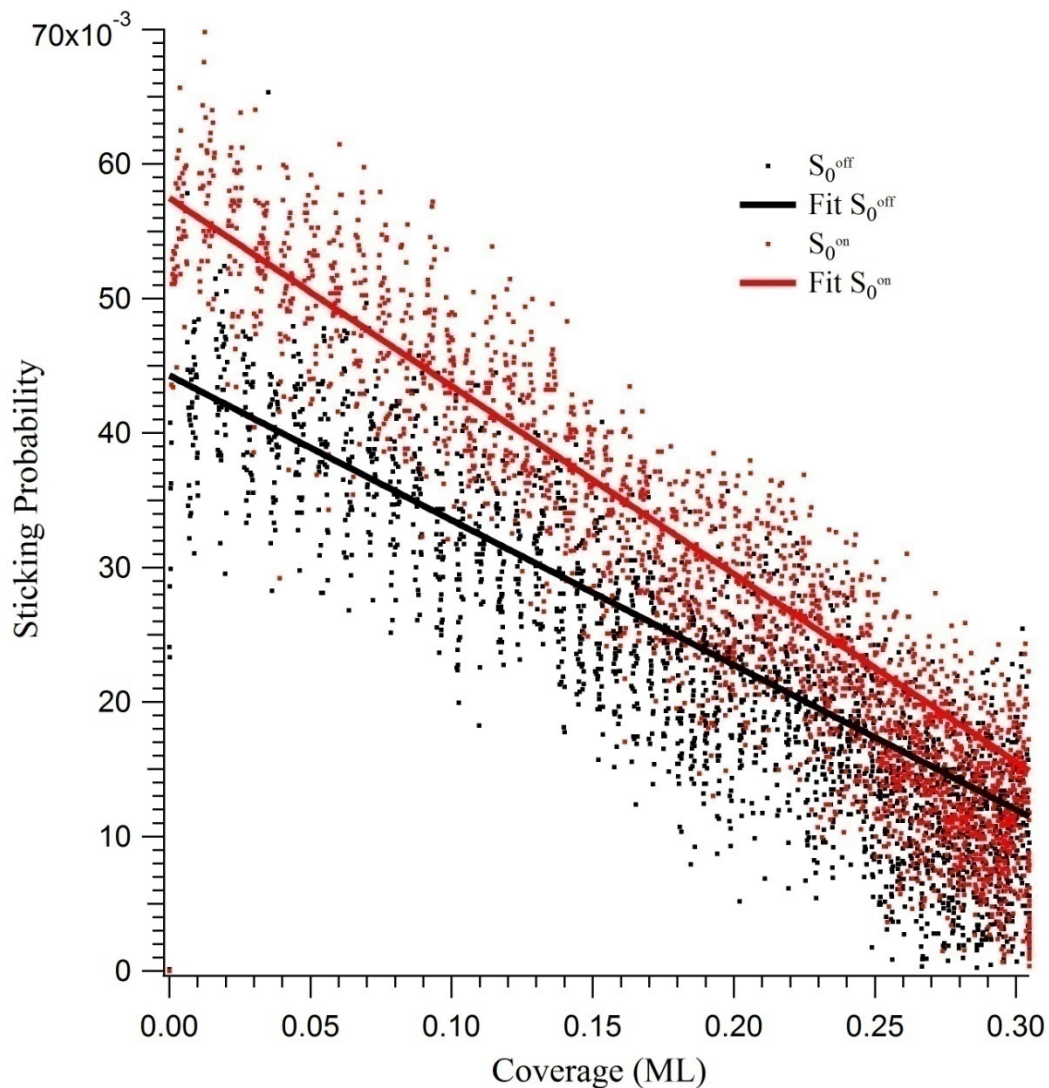


**Figure 2.8** Measured initial sticking probabilities for  $\text{CH}_4$  on Ni(111) with  $T_{\text{nozzle}} = 600 \text{ K}$  and  $T_{\text{surf}} = 600 \text{ K}$  as a function of surface coverage. The initial sticking probabilities  $S_0^{\text{off}}$  and  $S_0^{\text{on}}$  are determined by extrapolation back to zero coverage limit of the fit lines as described in the text.

### 2.4.3 Auger electron spectroscopy

We used Auger electron spectroscopy (AES) to determine cleanliness of the surface before deposition with the methane beam and to quantify the amount of carbon left on the surface after deposition. Since data from Chapter 4-6 were collected using K&W techniques to measure  $S_0$ , the focus of this section will be on determining the carbon monolayer (ML) coverage on Ir(111) as presented in Chapter 3.

AES is a post-dose analysis technique so the monolayer coverage must be kept below 10% to ensure that  $S_0$  is representative of methane sticking on a clean surface. On the chamber used for the Ir(111) experiments, the current output from the AES (Phi Electronics Model 15-110) cylindrical mirror analyzer was processed by a lock in amplifier to yield the derivative plot of electron intensity,  $dN/dE$ , since a small dither was applied to the pass voltage of the CMA. The AES signal was recorded for electron energies 200 - 300 eV. Iridium atoms produced a large signal at 229 eV and the surface bound carbon appeared at 272 eV, both being easily separated for analysis. The peak to peak magnitudes for both signals were quantified and the ratio was taken to give the C:Ir ratio. The value of this ratio was then related to carbon ML coverage in the following way. King and Wells measurements using a beam with an energy that results in  $S_0 \approx 0.10$  were performed for a range of dose times. After each dose, the C:Ir ratio was measured using AES. The ML coverage was calculated as in Equation 2.8 where  $\theta$  is the carbon coverage (as related to the C:Ir ratio),  $S_0$  is the sticking probability, as

determined by the K&W method, flux is as determined as described in Section 2.2.3, and time is the duration for that specific dose.

$$\theta = S_0 \times flux \times time \quad \text{Equation 2.8}$$

The AES spectrum and resulting C:Ir ratio is then calibrated to this absolute sticking coverage and used for doses to determine  $S_0$ .

We also needed to verify that the molecular beam was aligned with the ca. 10 mm diameter Ir(111) crystal, and that AES measurements were quantifying C deposition in the region of the surface dosed by the beam. To verify the correct area on the Ir(111) crystal was analyzed we performed spatially resolved measurements by translating the crystal in front of the AES after dosing with the methane beam *without* laser excitation. A demonstration of this analysis is displayed in Figure 2.9 showing the clear top-hat shape resulting from the dose. For subsequent doses a single spot in the middle of the deposition map was chosen and measured five times for C:Ir ratio determination.

Doses where the methane molecules were excited with the infrared laser required additional mapping of the deposited carbon after each dose, as described in Ref. (18). Doppler shifts in the IR adsorption frequency of the molecules in different portions of the gently diverging molecular beam result in a laser-frequency-dependent mapping of state-selected molecules to the surface. When the laser intersects the molecular beam exactly perpendicular to the beam path, molecules travelling along the beam center are preferentially excited. We therefore needed to ensure that the molecules being excited within the molecular

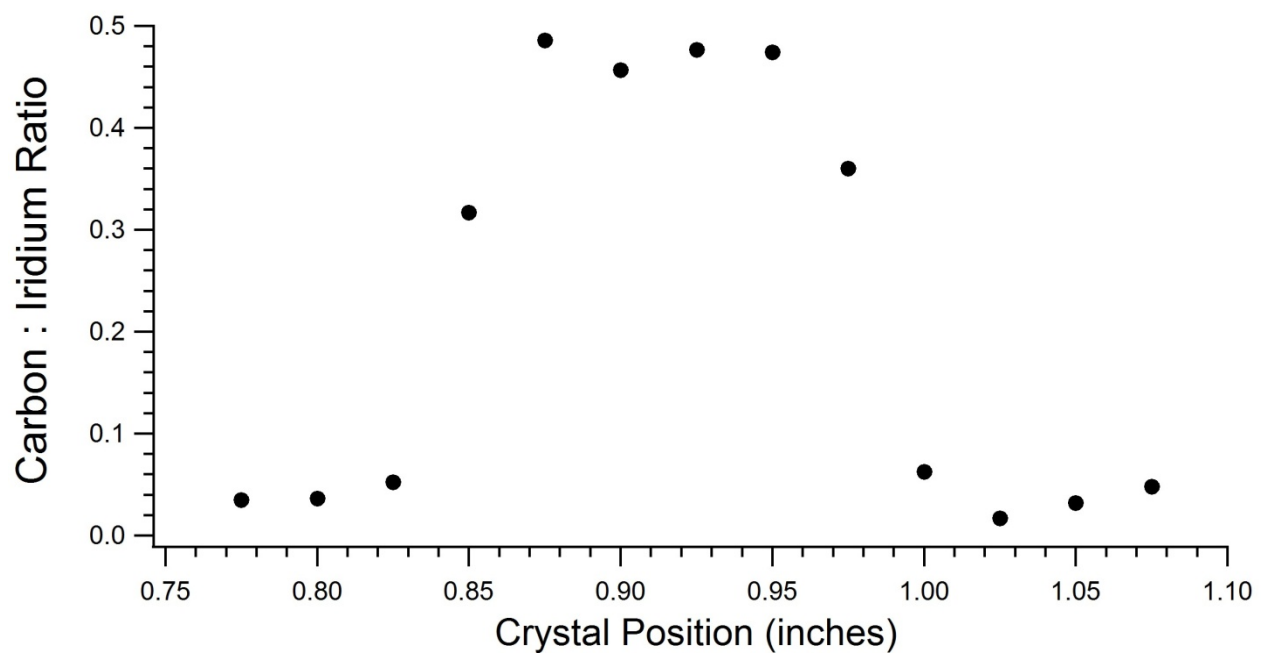


**Figure 2.9** Carbon deposition map on Ir(111) after exposure to a 5% CH<sub>4</sub>/He beam at  $T_{nozzle} = 1000$  K and  $T_{surf} = 1000$  K. This dose was performed using the small beam valve hole (SBVH) as selected using the beam selector (#9 Figure 2.1).

beam were impacting the correct area of the crystal. The resulting AES spectrum in Figure 2.10 is similar to that in Figure 2.9 with two major differences. First, the doses were performed using the large beam valve hole (LBVH) so the molecular 11 mm diameter molecular beam image completely overlapped the 10 mm diameter crystal surface and carbon was detected across the entire face of the Ir(111) crystal. This ensured that we were not clipping any of the excited molecules with the chopper wheel / beam selector before impact with the surface. Second, the resulting shape is consistent with the expected Gaussian profile across the face of the surface. This was a result of the single pass excitation of the molecular beam with the infrared laser used in this setup. On either side of the Gaussian feature, there was significant carbon accumulation from molecules that are not resonant with the laser. Therefore, by measuring C coverage in the crystal center we can obtain  $S_0^{On}$  for the laser excited beam, and the C coverage on the sides of the Gaussian feature gave a measure of  $S_0^{Off}$ .

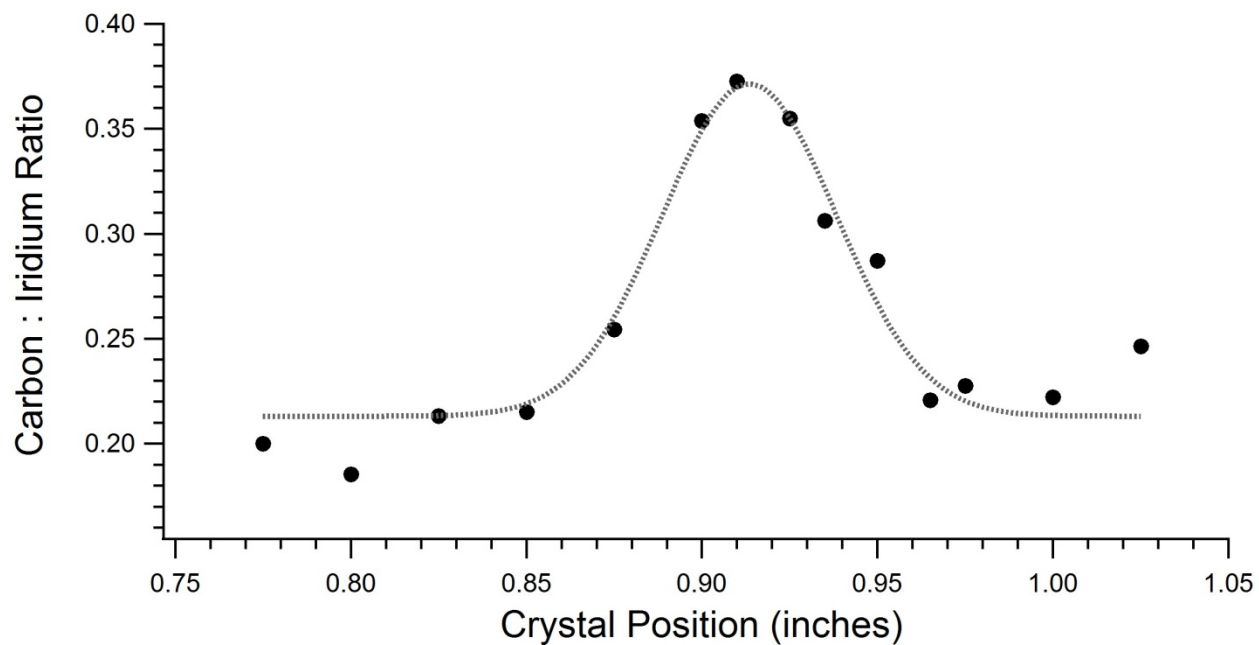


**Figure 2.10** Carbon deposition map on Ir(111) *with* laser excitation of the incident methane beam. The methane dose was performed using a 3% CH<sub>4</sub>/H<sub>2</sub> mix at  $T_{nozzle} = 300$  K and  $T_{surf} = 1000$  K. The black circles correspond to the C:Ir ratio at different positions along the crystal and the dotted silver line is a Gaussian fit to these points.

## 2.5 Laser system and state-resolved techniques

As discussed in Chapter 1, vibrational energy within the reacting methane promotes C-H bond cleavage. Increasing the gas temperature increases the population of vibrationally excited reactants. The distribution of vibrational states is inherently thermal and both stretching ( $\nu_1, \nu_3$ ) and bending ( $\nu_2, \nu_4$ ) vibrations are thermally populated according to their degeneracies, vibrational frequencies, and the temperature. Distinguishing the reactivity of these four characteristically different vibrational modes is difficult when using thermal energy as the excitation source. To understand how specific vibrational motion promotes reaction, state-resolved measurements were performed with a narrow bandwidth laser source, exciting a large fraction of the incident methane to a single ro-vibrational state with sufficient energy to impact the aggregate reactivity. The state-resolved sticking probability,  $S_0^{v_i}$ , for methane excited to the  $\nu_i$  vibrational state is calculated as in Equation 2.9, where  $f_{exc}$  is the fraction of all methane molecules excited and  $S_0^{v=0}$  is the  $v=0$  ground state sticking probability. The methods used for determining these quantities are outlined in the sections below.

$$S_0^{v_i} = \frac{S_0^{On} - S_0^{Off}}{f_{exc}} + S_0^{v=0} \quad \text{Equation 2.9}$$

This general approach to obtaining state-resolved reaction probabilities has been used, and described, extensively in previous publications(8, 16); the general techniques used in these experiments are summarized below with any changes highlighted. Values of  $S_0^{v_i}$  are partially sensitive to  $f_{exc}$ , so our procedure for

estimating  $f_{exc}$  at both lower and elevated nozzle temperatures will be a particular focus.

### **2.5.1 General laser setup and operation**

The laser system used in these studies was a periodically-poled Lithium Niobate optical parametric oscillator (OPO) made by Aculight (Model 2400 Module C). A seed laser (IPG Photonics, YAR-15K) feeds the OPO with a single mode and singly-resonant laser beam, which the OPO splits into two beams of different energies. One of these beams (the non-resonant and less energetic idler) was used for experiments, while the other beam was terminated into a beam dump outside the OPO module. Fine tuning was accomplished by tuning the pump laser frequency while maintaining the resonance condition for the complementary signal photon. The ca. 3.3  $\mu\text{m}$  photons needed for this experiment then tune synchronously as the pump laser frequency is tuned. The system produced ca. 1 W of single mode infrared light at this wavelength.

Stability of the laser frequency was important because some experiments require multiple hours of deposition before the quantity of surface products were sufficiently high enough to be detected. Small fractional beam splitters allowed most of the laser intensity to be used for excitation of the molecular beam. The remainder was used for both frequency stabilization and spectral analysis of the single mode infrared light. The output wavenumber was measured with a wavemeter (Burleigh, WA20-IR) and single mode generation was verified with a 7.5 GHz spectrum analyzer (Burleigh). Adjustments to the output frequency were

made through each of the following adjustments: changing the OPO crystal angle with respect to the incident seed laser, or the feedback-controlled temperature of the OPO crystal assembly, provided coarse control over the output wavelength over the tuning range of the laser. Changing the OPO etalon angle suppressed spurious cavity modes and ensured stable single mode operation. Computer controlled tuning of the 0-90 V programmable piezoelectric on the seed laser effected very small changes ( $<0.001 \text{ cm}^{-1}$ ) over a total range of several tenths of a  $\text{cm}^{-1}$  and was used to fine tune the laser into resonance with the methane absorption feature. In actuality, the first three adjustments are intimately linked. One must be careful when adjusting the first two controls as they may induce a rapid temperature increase of the crystal assembly in the worst of scenarios.

To ensure the laser stayed tuned to the transition of interest during deposition a temperature-stabilized vacuum jacketed Fabry-Pérot etalon was used as a frequency reference. The laser was tuned to the desired frequency and a piezoelectric controlled mirror adjusted the etalon cavity length to maximize laser transmission through the etalon and into a photodetector. When this condition was achieved a feedback loop is maintained between the Fabry-Pérot and the seed laser piezoelectric control, discussed above. A small dither was placed on the laser frequency (ca. 100 kHz or less), and the in-phase derivative signal for transmission through the etalon was locked to its zero-crossing, which corresponded to the maximum transmission. Once the laser frequency is actively locked and stabilized to the Fabry-Pérot transmission fringe, the laser can be tuned by slowly tuning the Fabry-Pérot cavity mirror. The photodetector signal is

kept maximized through manipulation of the seed laser piezo drive, keeping the laser "locked" at the desired frequency with high reliability.

The high intensity output of infrared light, between 500 - 1400 mW with < 1MHz line-width directed into the molecular beam apparatus, was sufficient to saturate the investigated CH<sub>4</sub> and CHD<sub>3</sub> transitions. For accurate state-resolved measurements we needed to quantify the fraction of excited molecules within the methane molecular beam,  $f_{exc}$ . A lithium tantalate, LiTaO<sub>3</sub>, pyroelectric bolometer inside the second differentially pumped vacuum chamber (#7 Figure 2.1) and quantified changes in the energy content of molecules impinging on its surface. We used the bolometer to measure the relative vibrational population of the methane molecules with and without laser excitation. Laser excitation of the beam was interrupted with a square-wave driven electromechanical shutter. When the laser was off resonance with the desired transition molecules impinged on the bolometer with a steady heat content, and the bolometer signal was zero because there was no net change in the energy transfer to the detector. As the laser was tuned into resonance with a methane ro-vibrational transition, the change in vibrational energy within the methane beam varied with actuation of the electromechanical shutter. The bolometer signal changed in response to the modulated infrared laser excitation, and its preamplified output was fed into a lock-in amplifier set at the frequency of the shutter drive. The bolometer and associated preamplifier was attached to a linear feedthrough that inserted the sensor element into the methane beam path for IR absorption measurements and retracted it for dosing the vibrationally excited molecules onto the surface. To

ensure full saturation of the transition was achieved, we measured the pyroelectric signal while attenuating the laser source with a tunable rotatable zero order half-wave plate (Alphas, PO-TWP-L2-25-IR). Decreasing laser fluence by 50% produced no observable decrease in bolometer signal, indicating we have sufficient photons to achieve maximum population in the desired excited states. While the same laser is used for experiments on both chambers there are differences in methane excitation methods, therefore, the exact method for calculating the value of  $f_{exc}$  to use in Eq. 2.9 will be discussed in more detail below.

### 2.5.2 Excitation of CH<sub>4</sub> at low Nozzle Temperature

For state-resolved experiments of methane dissociation on Ir(111) and presented in Chapter 3, the infrared laser excited CH<sub>4</sub> molecules from the ground vibrational state ( $v''=0, J''=1$ ) to the  $\nu_3$  anti-symmetric stretch ( $v'=1, J'=2$ ) via the R(1) transition at 3038.485 cm<sup>-1</sup>. To maximize the population of  $v''=0, J''=1$  initial state for the transition, the nozzle temperature was held at 300 K for all but one measurement, where a 400 K nozzle temperature was used to access a higher  $E_{trans}$ . The laser intersected the molecular beam with a single pass, which required the deposition on the surface to be mapped through AES techniques as discussed in Section 2.4.3.

The fraction of excited molecules,  $f_{exc}$ , within the beam was important when calculating the state-resolved sticking probability because we were interested in separating the effects from the excited and non-excited methane

reacting on the surface. Exciting more of the molecules to the  $v_1$  excited state led to a larger difference in  $S_0^{On} - S_0^{Off}$  (Equation 2.9) so  $f_{exc}$  is a scaling factor to account for these differences. The quantity,  $f_{exc}$ , is the product of the fraction of all methane molecules that are in the  $v''=0, J''=1$  ground state accessible for excitation, which we denote  $f_{pop}$ , and the experimentally determined fraction of those molecules in the beam that are excited,  $f_2$ .

$$f_{exc} = f_{pop} \times f_2 \quad \text{Equation 2.9}$$

The Acculite Argos laser system produces 700 mW or more of single mode, narrow bandwidth output power for resonant excitation of the  $v_3$  transition. This much power is sufficient to saturate this transition. At saturation the excitation rate is equal to the stimulated emission rate, and the steady-state fractional population of the excited state is given by Eq. 2.10.

$$f_2 = \frac{g_1}{g_1 + g_2} = 1/2 \quad \text{Equation 2.10}$$

The laser is linearly polarized, which leads to the selection rules of  $\Delta m_J = 0$  for the  $m_J$  sublevels of each rotational state. For an R-branch infrared transition, this results in the degeneracy of the lower and upper states being equal, so  $f_2 = 1/2$  in the limit of a fully saturated transition. For each set of molecular beam conditions, saturation of the transition was verified by monitoring the pyroelectric bolometer signal as the laser power was varied using the half-wave plate located in the laser path. The absorption signal reached a plateau corresponding to saturation at power levels less than 500 mW, and remained constant as laser power increased up to the maximum available. Therefore, we were confident that the laser's photon

density was sufficient to completely saturate absorption for available CH<sub>4</sub> molecules. The fraction of molecules in the correct ground ro-vibrational state,  $f_{pop}$ , is the product of the fraction of molecules in the correct vibrational state (the  $v''=0$  vibrational state),  $f_{vib}$ , and the fraction of those molecules in the correct rotational state ( $J''=1$ ),  $f_{rot}$ .

$$f_{pop} = f_{vib} \times f_{rot} \quad \text{Equation 2.11}$$

Juurlink et al. measured the rotational distribution for the  $v=0$  vibrational ground state for  $J=0 \rightarrow 5$  in CH<sub>4</sub> molecular beams at  $T_{nozzle} < 500$  K(2, 6) and found that there was significant rotational cooling within the rotational state distribution. To verify we were observing similar cooling dynamics for the different nozzle assembly(1) used in Chamber 2 we measured the rotational state distribution for  $J=0 \rightarrow 3$  for a variety of CH<sub>4</sub> mixes at  $T_{nozzle} = 300$  K. The maximum pyroelectric bolometer signal for molecules in the  $v''=0$  vibrational state was recorded as the laser was tuned to the desired rotational branch. These values were normalized to the statistical weight for each rotational level as described by Campbell(8) to give an estimate of the rotational temperature for each gas composition. Table 2.2 contains the mix identities and calculated rotational temperature  $T_{rot}$  for several of the mixes used in Chapter 3. This analysis yielded  $T_{rot} < 10$  K which only decreases our  $f_{exc}$  values by 1-2% relative to the populations predicted in the limit of complete rotational cooling. However, this does not mean that 98-99% of the molecules are in the  $J''=1$  rotational state. As CH<sub>4</sub> rotations cool during supersonic expansion, the  $J$  state to which each molecule cools is dictated by the rotational wavefunction symmetry and nuclear

<b>Mix Identity</b>	<b>Rotational Temperature, K</b>
75% CH <sub>4</sub> / Kr	7.73
100% CH <sub>4</sub>	9.04
50% CH <sub>4</sub> / He	7.19

**Table 2.2** Measured rotational temperatures at  $T_{nozzle} = 300$  K as described in the text and by Campbell.(19)

spin statistics.(20-22) Methane has three rotational symmetry species A, F, and E which must be conserved during collisional relaxation. Among the  $J''=0$  to 6 rotational states, sublevels with a symmetry species of A are  $J=(0,3,4)$ ; species F is present for  $J=(1,2,3,4)$ ; and species E is present for  $J=(2,4)$ . For a case where rotational cooling is virtually complete, each rotational sublevel will cool to the lowest lying J state that possesses a sublevel with that symmetry. So all rotations of species A will cool to  $J=0$ , species F cools to  $J=1$ , and E species cool to  $J=2$ . In a thermal sample, the relative population of these three species for A, F, and E are 5:9:2. Therefore, the highest fraction (9/16) of molecules are species F, and they will relax into  $J=1$  when cooling is complete. Considering there was significant cooling during expansion as discussed above, the fraction of molecules in the  $J''=1$  rotational state used in further calculations was  $f_{rot} = 9/16$ .

When  $T_{nozzle} = 300$  K the vibrational energy content of the methane beam was very low. Bronnikov showed that under these conditions, the vibrational ground state population was not significantly altered by vibrational cooling upon supersonic expansion. Therefore,  $f_{vib}$  is well approximated by a Boltzmann distribution of vibrational states and the resulting ground state vibrational population,  $f_{vib}$ , exceeds 0.99. At our highest  $T_{nozzle}$  of 400 K this value drops to  $f_{vib} = 0.96$ . Since these values differ from 1.00 by far less than the error in measuring  $S_0$ , we approximated  $f_{vib} \approx 1$  for the purpose of calculating  $f_{exc}$  in experiments with low  $T_{nozzle}$ .

Due to the minimal population of excited vibrational states and the nearly complete cooling in the beams at these low nozzle temperatures, the overall calculation for  $f_{exc}$  was greatly simplified to be represented as:

$$f_{exc} = f_{vib} \times f_{rot} \times f_2 = 1 \times \frac{9}{16} \times \frac{1}{2} \quad \text{Equation 2.12}$$

For the calculations presented in Chapter 3 the fraction of excited molecules for each beam was then taken as 28% (9/32).

### 2.5.3 Excitation of CHD<sub>3</sub> and CH<sub>4</sub> at high Nozzle Temperatures

Results presented in Chapters 4-6 explored the reactivity of methane with  $E_{trans} > 80$  kJ/mol. Accessing these higher values of  $E_{trans}$  required seeding low percentages of CH<sub>4</sub> and CHD<sub>3</sub> in H<sub>2</sub> (0.05 - 3%) at elevated  $T_{nozzle}$ . The dynamic range of the pyroelectric detector becomes an issue for these low flux and high state-dilution gas conditions. This prevented the direct measurement of the rotational temperature through characterization of the rotational state distributions as described above. Additionally, the contributions from vibrational state dilution can no longer be ignored as even at  $T_{nozzle} = 500$  K, there is significant population in the lower lying bending modes for both CH<sub>4</sub> and CHD<sub>3</sub> molecular beams.

The laser setup was also slightly different in comparison to Section 2.5.2 as there was a multi-pass mirror assembly located in the first differentially pumped chamber. The use of the multi-pass allowed for spatially uniform carbon deposition on the surface because the mirror assembly was adjusted so the laser crossed the molecular beam path multiple times, each at a slightly different angle

of intersection. This ensured that the Doppler shifted molecules that had divergent paths within the multi-pass still encountered resonant photons.(3) The methods for determining  $f_{vib}$  and  $f_{rot}$  under these conditions are described below.

Vibrational cooling of methane during expansion is much less efficient than for rotational or translational degrees of freedom, especially in cases where the energy difference between transitions is greater than  $kT$ .(23) This leaves a significant portion of vibrational energy that is not converted into translational energy. The vibrational state distribution of  $CH_4$  contains clumps of closely spaced vibrational modes, or polyads. This spacing is due to the bending modes ( $v_2$  and  $v_4$ ) having vibrational energies that are almost exactly half the energy of the stretching modes ( $v_1$  and  $v_3$ ) in  $CH_4$  as shown in Table 2.3. The polyad structure is not as pronounced for  $CHD_3$  due to the addition of C-D bonds which lower the vibrational frequency for both the stretching and bending modes, however, it also exhibits polyad structuring.

Bronnikov et al. measured the vibrational state populations for supersonic beams of  $CH_4$  and found that while there was some vibrational cooling within polyads, relaxation to different polyads was unlikely.(10) For example, because there is a significant energy gap between the ground state  $v=0$  vibrational state and any of the  $v=1$  bending vibrational states, it was unlikely for collisional energy transfer during expansion to relax a bending vibration to  $v=0$ . Therefore, the fraction of molecules in the ground state represents  $f_{vib}$ , can be assumed to have a thermal distribution unaffected by expansion through the nozzle. For  $CH_4$ , the vibrational state distribution was calculated(6, 8, 14) at each nozzle

Mode	Band Center (cm <sup>-1</sup> ) CH <sub>4</sub>	Band Center (cm <sup>-1</sup> ) CHD <sub>3</sub>
v <sub>1</sub>	2914	2993
v <sub>2</sub>	1524	2142
v <sub>3</sub>	3020	1003
v <sub>4</sub>	1306	2263
v <sub>5</sub>	-	1282
v <sub>6</sub>	-	1036

**Table 2.3** Vibrational normal modes of CH<sub>4</sub> and CHD<sub>3</sub>(24, 25)

temperature for all vibrational states having  $E_{vib} \leq 16,000 \text{ cm}^{-1}$  by calculating degeneracy-weighted Boltzmann factors for all possible harmonic combinations of the four normal modes listed in Table 2.3, summing those factors to obtain a vibrational partition function, and then calculating the fraction of molecules in each vibrational state. The fraction of molecules in the ground state,  $f_{v=0}$ , represents the fraction of molecules that exist in the  $v=0$  vibrational state that we excite from.

$$f_{v=0} = \frac{n_{v=0}}{\sum_{i=1}^{i=4} n_{vi}} = f_{vib} \quad \text{Equation 2.13}$$

The calculations for  $\text{CHD}_3$  are performed in a similar fashion including all vibrational states at  $E_{vib} \leq 16,000 \text{ cm}^{-1}$  for all harmonic combinations of the 6 normal modes. The energy gap between the  $v=0$  and  $v=1$  bending vibrational states is still large enough to prevent significant collisional relaxation between these vibrational states, so making the assumptions of ground state population asserted above is still valid.

As mentioned above it was not possible for us to explicitly determine the rotational temperature for both  $\text{CH}_4$  and  $\text{CHD}_3$  at these elevated nozzle temperatures. Previously, the rotational state distribution of  $\text{CH}_4$  molecular beams seeded in  $\text{H}_2(14)$  and  $\text{He}(7)$  were measured on the same apparatus in the  $v=0$  vibrational state with  $J \leq 5$  over the  $T_{nozzle} = 300$  to  $500 \text{ K}$  range. The rotational temperature,  $T_{rot}$ , was determined for each of the gas conditions and related to  $T_{nozzle}$  to find that  $T_{rot} \approx 0.0247 \times T_{nozzle}$ . This relationship was also shown to be consistent with observed excitation fractions for IR absorption at higher nozzle

temperature. We assumed the rotational cooling dynamics are similar for CHD<sub>3</sub> and used this relationship between nozzle temperature and rotational temperature for both CH<sub>4</sub> and CHD<sub>3</sub> beams. We then reconstructed the distribution of rotational states from the calculated  $T_{rot}$  value to include higher values of J. The fraction of molecules that were in J", the initial rotational level for IR excitation, was calculated from the population weighted Boltzmann factor for J" divided by the rotational partition function, where  $g_J$  is the statistical weight for the rotational levels, and  $E_J$  is the energy of the individual rotational states. Values of  $E_J$  were calculated from spectroscopic constants for the symmetric top CHD<sub>3</sub> molecule and the spherical top CH<sub>4</sub>.

$$f_{rot,J''} = \frac{g_{J''} \times \exp\left(\frac{-hcE_{J''}}{T_{rot}}\right)}{\sum g_J \times \exp\left(\frac{-hcE_J}{T_{rot}}\right)} \quad \text{Equation 2.14}$$

As in Section, 2.4.2, the overall fraction of excited molecules for these experiments is expressed by Equation 2.12. We measure or calculate  $f_{vib}$  and  $f_{rot}$  for each unique set of beam conditions (gas mix, nozzle temperature, backing pressure) and use these quantities in Equation 2.12, along with  $f_2 = 9/32$  for saturated excitation from the  $v''=0, J''=1$  state to obtain  $f_{exc}$ . For specific  $f_{exc}, f_{vib}$ , and  $f_{rot}$  values obtained in a particular experiment, see the applicable Chapters 4-6, which also contain more molecule specific considerations.

## 2.6 References

1. D. Del Sesto, PhD Thesis, The Role of Thermally Excited Vibrations in Gas-Surface Reactions: Methane on Ni(111) and Ir(111), *Tufts University* (2011).
2. P. R. McCabe, L. B. F. Juurlink, A. L. Utz, A molecular beam apparatus for eigenstate-resolved studies of gas-surface reactivity. *Review of Scientific Instruments* **71**, 42-53 (2000).
3. L. B. F. Juurlink, R. R. Smith, A. L. Utz, Controlling Surface Chemistry with Light: Spatially Resolved Deposition of Rovibrational-State-Selected Molecules. *The Journal of Physical Chemistry B* **104**, 3327-3336 (2000).
4. L. B. F. Juurlink, R. R. Smith, A. L. Utz, The role of rotational excitation in the activated dissociative chemisorption of vibrationally excited methane on Ni(100). *Faraday Discussions* **117**, 147-160 (2000).
5. L. B. F. Juurlink, P. R. McCabe, R. R. Smith, C. L. DiCologero, A. L. Utz, Eigenstate-Resolved Studies of Gas-Surface Reactivity: CH<sub>4</sub>(v<sub>3</sub>) Dissociation on Ni(100). *Physical Review Letters* **83**, 868-871 (1999).
6. L. B. F. Juurlink, PhD Thesis, Eigenstate-resolved measurements of methane dissociation on Ni(100), *Tufts University* (2000).
7. D. R. Killelea, PhD Thesis, Bond-Selective Control of a Gas-Surface Reaction, *Tufts University* (2007).
8. V. L. Campbell, PhD Thesis, State Resolved Measurement of Surface Temperature Dependence and Isotopically Selective Reactivity of Methane on Ni(111), *Tufts University* (2011).
9. L. B. F. Juurlink, R. R. Smith, D. R. Killelea, A. L. Utz, Comparative Study of C-H Stretch and Bend Vibrations in Methane Activation on Ni(100) and Ni(111). *Physical Review Letters* **94**, 208303 (2005).
10. D. K. Bronnikov, D. V. Kalinin, V. D. Rusanov, Y. G. Filimonov, Y. G. Selivanov, J. C. Hilico, Spectroscopy and non-equilibrium distribution of vibrationally excited methane in a supersonic jet. *Journal of Quantitative Spectroscopy and Radiative Transfer* **60**, 1053-1068 (1998).
11. D. J. Auerback, in *Atomic and Molecular Beam Methods*, G. Scoles, Ed. (Oxford University Press, New York, 1988), vol. 1, pp. 362-379.
12. D. K. Bronnikov, D. V. Kalinin, V. D. Rusanov, Y. G. Filimonov, Y. G. Selivanov, J. C. Hilico, Spectroscopy and Non-Equilibrium Distribution of Vibrationally Excited Methane in a Supersonic Jet. *J. Quant. Spectrosc. Radiat. Transfer* **60**, 1053-1068 (1998).
13. H. A. Michelsen, D. J. Auerbach, A critical examination of data on the dissociative adsorption and associative desorption of hydrogen at copper surfaces. *The Journal of Chemical Physics* **94**, 7502-7520 (1991).
14. R. R. Smith, PhD Thesis, Rovibrational State-Resolved Studies of Methane Dissociation on Ni(111), *Tufts University* (2003).
15. M. G. W. D.A. King, Reaction mechanism in chemisorption kinetics: nitrogen on the {100} plane of tungsten. *Proceedings of the Royal Society of London. A. Mathematical and Physical Sciences* **339**, 245-269 (1974).

16. N. Chen, PhD Thesis, State-resolved Reactivity and Bond selective Control of Methane Dissociation on Ni(111), *Tufts University* (2013).
17. R. I. Masel, *Principles of adsorption and reaction on solid surfaces.*, Wiley series in Chemical Engineering (Wiley, New York, 1996), pp. 804.
18. L. B. F. Juurlink, R. R. Smith, A. L. Utz, Controlling Surface Chemistry with Light: Spatially Resolved Deposition of Rovibrational-State-Selected Molecules. *J.Phys.Chem.B* **104**, 3327-3336 (2000).
19. V. L. Campbell, N. Chen, H. Guo, B. Jackson, A. L. Utz, Substrate Vibrations as Promoters of Chemical Reactivity on Metal Surfaces. *The Journal of Physical Chemistry A* **119**, 12434-12441 (2015).
20. H. Herzberg, *Molecular spectra and molecular structure.*, (Krieger Publishing Co., Malabar, ed. 2nd, 1991).
21. E. B. Wilson, The Statistical Weights of the Rotational Levels of Polyatomic Molecules, Including Methane, Ammonia, Benzene, Cyclopropane and Ethylene. *The Journal of Chemical Physics* **3**, 276-285 (1935).
22. E. B. Wilson, Symmetry Considerations Concerning the Splitting of Vibration-Rotation Levels in Polyatomic Molecules. *The Journal of Chemical Physics* **3**, 818-821 (1935).
23. J. T. Yardley, *Introduction to molecular energy transfer.*, (Academic Press, New York, 1980).
24. S. Albert, S. Bauerecker, V. Boudon, L. R. Brown, J. P. Champion, M. Loëte, A. Nikitin, M. Quack, Global analysis of the high resolution infrared spectrum of methane  $^{12}\text{CH}_4$  in the region from 0 to  $4800\text{cm}^{-1}$ . *Chemical Physics* **356**, 131-146 (2009).
25. O. N. Ulenikov, E. S. Bekhtereva, S. Albert, S. Bauerecker, H. Hollenstein, M. Quack, High resolution infrared spectroscopy and global vibrational analysis for the  $\text{CH}_3\text{D}$  and  $\text{CHD}_3$  isotopomers of methane. *Molecular Physics* **108**, 1209-1240 (2010).

Chapter 3 is reprinted from Catalysis Today, 244, Dombrowski, E., Peterson, E.  
Del Sesto, D., Utz, A.L, Precursor-mediated reactivity of vibrationally hot  
molecules: Methane activation on Ir(111), with permission from Elsevier.

<https://doi.org/10.1016/j.cattod.2014.10.025>

# Chapter 3 : Precursor-Mediated Reactivity of Vibrationally Hot Molecules: Methane on Ir(111)

## 3.1 Introduction

The activated dissociative chemisorption of methane into adsorbed methyl and H on catalytically active transition metals has been a target of surface science studies for decades due to its role as the rate-limiting step in the industrial steam-reforming reaction.<sup>(1-4)</sup> This reaction is typically run at very high temperatures and pressures to maximize the number and reaction probability of methane-catalyst collisions. In addition to its importance in heterogeneous catalysis, methane activation has also emerged as a key model system for understanding the mechanistic details of dissociative chemisorption. As a small polyatomic molecule, methane possesses nearly all of the features of chemically complex reaction systems while remaining amenable to high-level theoretical and experimental investigation. The potential energy surface governing reactivity includes coordinates derived from C-H bond stretching and bending, molecule-surface distances and angles, and surface atom distortions. A large body of work now suggests that many of these coordinates influence reaction probability.

The high activation energy for methane dissociation makes it a particularly attractive system for study with supersonic molecular beam sources, which provide an intense source of hyperthermal reagents.<sup>(5, 6)</sup> Collisions that occur

during supersonic expansion lead to efficient translational and rotational cooling and resultantly narrow translational ( $E_{trans}$ ) and rotational ( $E_{rot}$ ) energy distributions among the incident reagents. Seeding techniques create beams of methane reagents with high  $E_{trans}$  to mimic the most energetic and reactive molecules in the tail of the thermal Maxwell-Boltzmann  $E_{trans}$  distribution. Vibrational cooling is much less efficient, however, and the vibrational state distribution in the beam is similar to that of a thermal distribution at the molecular beam nozzle source temperature.<sup>(7)</sup> Molecular beam studies have provided a wealth of insight into dynamical factors that impact reactivity.<sup>(8, 9)</sup>

More recently, experiments that pair supersonic molecular beams with direct infrared laser excitation of methane have provided the ability to quantify the reaction probability,  $S_0$ , for methane molecules in select rotational and vibrational quantum states.<sup>(4, 10, 11)</sup> Laser excitation occurs in the gas phase prior to surface impact, and surface science techniques quantify reaction products and their identity. The coupling of laser excitation and molecular beam methods provides the experimental tools necessary to deconvolute the complicated potential energy surface (PES) that describes the methane - surface interaction. Methane vibrations and surface phonons have both been identified as important energetic coordinates that influence reaction probability. State-resolved beam-surface scattering experiments also highlight the limited extent of vibrational energy scrambling that occurs during the reactive collision. Examples of vibrational mode-selective chemistry, in which the identity of the vibrational

motion affects reaction probability, and bond selective chemistry, in which vibrational motion influences product identity, are widespread. (10, 11)

The earliest beam-surface scattering study of methane activation explored dissociative chemisorption on a W(100) surface.(12) Shortly thereafter, Ceyer and coworkers investigated CH<sub>4</sub> and CD<sub>4</sub> dissociation on Ni(111).(13, 14) Both studies reported a monotonic and exponential increase in reaction probability with increasing  $E_{trans}$ , which pointed to the importance of translational energy in activating the reaction. At a fixed  $E_{trans}$ , beams with hotter vibrational state distributions were more reactive, which pointed to the importance of methane's vibrations in promoting reactivity. Observation of a collision-induced reaction pathway implicated methane's bending vibrations in promoting reaction.(15) Since that time, the range of surfaces explored with conventional beam-surface scattering techniques has expanded to include Pt(111)(16-18), Pt(110)-(1x2)(19-21), Pt(533)(22), Ni(100)(23), Ru(0001)(24, 25), Ir(111)(26, 27), Ir(110)(28, 29) Pd(110)(30) and mixed metal systems such as Cs/Pt(111),(31) Co/Cu(111)(32) and Au/Ni(111).(33) The majority of these studies reveal that  $S_0$  increases monotonically and nearly exponentially with increasing  $E_{trans}$  over the range of  $E_{trans}$  explored. Such behavior is consistent with a direct reaction mechanism, in which the incident methane molecule undergoes a single collision with the surface. Killelea pointed out that the timescale for interaction of these hyperthermal molecules with the surface is short relative to the rotational period of methane and the vibrational period of the surface – an affect that has repercussions for the dynamics of reaction.(34) Transition state calculations

suggest a relatively tight transition state geometry for methane dissociation.(35, 36) Consequently, many incident methane molecules impact the surface in an unfavorable geometry that results in an  $E_{trans}$  threshold for reaction significantly higher than the transition state energy. Given the limited time available for molecular reorientation, these molecules scatter non-reactively back into the gas phase. As  $E_{trans}$  increases, a greater fraction of the incident molecules have sufficient energy to surmount their effective energy threshold for reaction, and reactivity increases.

Among the many prior beam-surface scattering studies of methane activation, several identified a low- $E_{trans}$  reaction channel in which  $S_0$  decreased with increasing  $E_{trans}$ . Seets and coworkers first identified this channel for methane dissociation on Ir(110)-(1x2)(28, 29, 37), and Ir(111).(26, 27) Their experiments used a room temperature molecular beam nozzle source, preparing methane molecules that were predominantly in the ground vibrational state. At a fixed  $E_{trans}$ , raising  $T_{surf}$  led to a significant increase in  $S_0$  in this low  $E_{trans}$  channel. They attributed the low- $E_{trans}$  reactivity to a precursor-mediated reaction mechanism. In a plot of  $S_0$  vs.  $E_{trans}$ , precursor mediated reactivity typically dominates at low  $E_{trans}$  where dissociation via the direct channel is low due to the high activation barrier. Direct dissociation dominates at high  $E_{trans}$  where the trapping probability is least. The presence of these two channels results in an overall reaction probability curve that resembles a check mark.

The precursor-mediated mechanism is depicted and contrasted with the direct mechanism in Fig. 1. In a precursor-mediated reaction, the incident

molecule first loses a portion of its normal momentum and becomes trapped near the surface in the physisorption well. The molecule can then tumble and diffuse on the surface before it desorbs or reacts. Since trapping requires dissipation of normal momentum, trapping probabilities are greatest at  $E_{trans} = 0$  kJ/mol and decrease as  $E_{trans}$  increases. Once the molecule's normal momentum is thermalized, its reaction probability reduces to a kinetic competition between dissociation over the reaction barrier and desorption, and the fraction of trapped molecules reacting is independent of initial  $E_{trans}$ . The  $E_{trans}$  dependence of trapping and subsequent reaction contrasts with the direct reaction mechanism where reactivity increases with increasing  $E_{trans}$ . When the product of the trapping probability and the reaction probability for the trapped molecule exceeds the corresponding reaction probability for the direct channel, precursor-mediated reactivity dominates and  $S_0$  decreases with increasing  $E_{trans}$ . Corrugated surfaces, which more effectively couple normal to parallel momentum, typically enhance trapping probabilities and extend the range of  $E_{trans}$  over which trapping probabilities are significant. Molecular dynamics code predicts trapping dynamics well.(38, 39) A detailed study provides trapping probabilities and lifetimes of the physisorbed molecules on the Ir(111) and Ir(110)-(1x2) surfaces over a wide range of  $E_{trans}$  and  $T_{surf}$ .(40) The energetic barrier to methane dissociation on Ir surfaces is lower than that of other catalytically active metals, resulting in a more favorable branching ratio for reaction relative to desorption for those molecules that do trap. The precursor-mediated mechanism is potentially important in thermally activated reactions such as steam reforming because a large number of

methane molecules in an industrial reactor possess kinetic energies that fall within this low-energy regime.

Walker and coworkers observed a low  $E_{trans}$  reaction channel in their studies of methane dissociation on Pt(110)-(1x2) that was similar to that reported by Seets et al., but they suggested an alternate mechanistic origin for this effect.(19, 20) In analogy to studies of H<sub>2</sub> dissociation on Pd and Cu surfaces,(41) they proposed that angular anisotropy in the methane/surface potential might lead to significant reorientation forces on the incident methane molecule. The ability of those forces to reorient, or “steer” methane into a lower energy and more reactive geometry might be greatest at low incident energies where the molecule-surface interaction persists for the longest time. The  $E_{trans}$  dependence of this effect would therefore be qualitatively similar to that predicted for precursor-mediated reactivity. They noted that their data did not rule out the possibility of a precursor-mediated reaction channel involving vibrationally hot methane molecules, but suggested that at low  $E_{trans}$ , CH<sub>4</sub> molecules might be steered into a particularly low-barrier or barrier-less reaction path that could dramatically enhance reactivity. More recent state-resolved experiments of CH<sub>4</sub> dissociation on Pt(110)-(1x2) confirm the low- $E_{trans}$  reactivity reported by Walker and coworkers for molecules without laser excitation, but  $S_0$  for molecules in the  $2\nu_3$  vibrational state (2 quanta of C-H stretch) appear to react via a direct reaction mechanism at all  $E_{trans}$  between 4 and 62 kJ/mol.(21)

Theoretical(42) and molecular beam(43) studies of H<sub>2</sub> dissociation on Pd(100) and state-resolved beam-surface scattering studies(44) of H<sub>2</sub> dissociation

on Pd(111) found that a key signature of the “steering-assisted” mechanism was the dependence of  $S_0$  on the molecule’s rotational angular momentum,  $J$ . Viewed classically, the torque resulting from angular anisotropy in the molecule-surface PES more easily leads to molecular orientation when angular momentum is low – a behavior borne out by experiment in this system. As  $J$  increases,  $S_0$  initially decreases until the benefits of additional rotational energy outweigh the propensity for angular momentum to inhibit reorientation, at which point  $S_0$  begins to increase.

Juurlink and coworkers used rotational-state-resolved measurements of  $\text{CH}_4$  dissociation on Ni(111) to assess the role of dynamical steering in methane activation.<sup>(45)</sup> The studies spanned an  $E_{trans}$  range from 9 kJ/mol, where low- $E_{trans}$  reaction channels on Pt(110)-(1x2), Ir(110)-(1x2), and Ir(111) were present, up to 49 kJ/mol where reactivity via the direct channel dominates. The experiments quantified reactivity in  $v=1$  of the  $\nu_3$  C-H stretching vibration, and rotational quantum numbers ranged from  $J=0$  to 3 - values expected to be most sensitive to potential steering effects. At a given  $E_{trans}$ ,  $S_0$  varied by no more than a factor of 2 among rotational states and showed little or no systematic variation with  $J$ , in contrast to the systematic  $J$ -dependence expected if a steering mechanism were dominant. More significantly, the observed dependence of  $S_0$  on  $J$  was essentially independent of  $E_{trans}$  over the full range of  $E_{trans}$  investigated, suggesting that molecular reorientation during surface approach is either negligible, or occurs to a similar degree over a wide range of incident  $E_{trans}$ . Neither interpretation of the data is consistent with the dynamical steering

mechanism described by Walker and coworkers, in which strong steering effects dominate at low  $E_{trans}$  but become negligible at  $E_{trans} > 20$  kJ/mol.

Additional computational work by the King group searched for, but did not find evidence for a barrier-less reaction path for methane dissociation, and Anghel et al. concluded that of the two mechanisms that Walker et al. identified to describe their low- $E_{trans}$  experimental data, the precursor-mediated mechanism was most likely.<sup>(46)</sup> Since that time, electronic structure calculations have more thoroughly and accurately characterized the methane-surface PES for a range of catalytically active metals. Ab initio molecular dynamics calculations of trideutero methane ( $\text{CHD}_3$ ) dissociation on Pt(111) found no evidence for steering of the vibrationally excited C-H stretching state.<sup>(47)</sup> Those calculations are consistent with state-resolved beam-surface scattering measurements of  $\text{CHD}_3$  and  $\text{CH}_4$  dissociation on Ni(100), in which laser polarization aligned the transition dipole of the excited C-H stretching vibration relative to the surface.<sup>(48, 49)</sup> The data revealed up to a 40% change in  $S_0$  when the polarization direction was rotated from parallel to perpendicular alignment. Calculations that compare the rotationally adiabatic and rotationally sudden approximations for methane dissociation on Ni(111)<sup>(50)</sup> and Ni(100)<sup>(51)</sup> found modest differences in reactivity that are far smaller than the 3-4 order of magnitude enhancements in  $S_0$  (relative to the direct channel) that would be necessary to reconcile a steering mechanism with the reactivity reported by Walker et al. in the low- $E_{trans}$  regime. The absence of zero-barrier reaction paths for methane dissociation on Ni and Ir surfaces, and the similarity in angular anisotropy of the PES for many of these

systems suggest that the conclusions of Anghel et al. are very likely to be relevant for methane activation on Ni and Ir surfaces as well.

The work presented here is motivated by the question of whether precursor-mediated reactions can play an important role in catalytic processing conditions that involve highly activated reactions. While precursor-mediated reactions are relatively common for systems with low activation barriers, their importance in highly activated reactions, such as methane dissociation, is less clear. This is because the need for significant trapping probabilities (and therefore low  $E_{trans}$ ) conflicts with the need for energy to activate the reaction, of which  $E_{trans}$  can play an important role.

Traditionally, the surface has been seen as providing the required energy to activate precursor-mediated reactions through energy exchange with the physisorbed reagents. In an attempt to address this point, kinetic measurements in the presence of a static gas pressure (bulb experiments) that provided independent control over the surface and gas temperatures were performed.(26, 28, 52) Those reactions whose reactivity scaled strongly with gas temperature were interpreted to follow a direct mechanism due to the increasing  $E_{trans}$  of the incident molecules, while reactions that showed a more dominant dependence on surface temperature were thought to proceed via a precursor mediated mechanism due to the enhanced ability of the surface to exchange vibrational energy with the physisorbed molecule.

Three recent developments cloud this interpretation of the data. First, state-resolved beam-surface scattering studies have demonstrated that vibrationally excited methane molecules can exhibit significant reactivity, even at low  $E_{trans}$ . Therefore, significant internal energy can compensate for the absence of  $E_{trans}$  in a highly activated reaction. Second, theoretical studies have shown a significant role for surface atom motion (and thus surface temperature) in enhancing transition state access.<sup>(35, 53, 54)</sup> Thus, surface temperature can lead to enhanced reactivity via a direct reaction channel, which complicates the “conventional wisdom” interpretation of a strong surface temperature dependence correlating with trapping-mediated reactivity. Third, the time constants for vibrational damping, which range from 1ps for strongly chemisorbed CO on Pt(111)<sup>(55, 56)</sup> to more than 10 ps for more weakly bound adsorbates,<sup>(57)</sup> are now understood to be much longer than the few 100-fs interaction time in a direct hyperthermal molecule-surface encounter.<sup>(34)</sup> In fact, vibrational lifetimes may be comparable to or longer than physisorption lifetimes at elevated surface temperatures. As a result, a vibrational ground state molecule that traps on the surface may desorb before acquiring significant vibrational energy due to energy exchange with the surface. On the other hand, a vibrationally excited gas phase molecule could trap, retain its internal energy for many picoseconds, and sample a range of molecular orientations, vibrational phases, and surface sites before it is quenched or desorbs.

Therefore, an alternate pathway for precursor-mediated reactivity involving vibrationally excited methane molecules emerges.<sup>(19, 20, 46)</sup> A

vibrationally excited methane molecule that physisorbs onto a metal surface can either accommodate to the thermal temperature of the metal through electron-hole-pair coupling or phonon-coupling with the metal, or its added vibrational energy can be used to overcome the activation energy for CH bond cleavage. In the former case the surface temperature will entirely describe the methane molecules' propensity to react or desorb, however in the latter case added vibrational energy can lead to a higher measured reaction probability. Enhanced precursor-mediated reactivity has been reported before for a vibrationally excited molecule, but not on a metal surface. Bisson et al. observed precursor-mediated reactivity of vibrationally excited silane on Si(100).(58)

It is important to consider whether the internal vibrational energy of a methane molecule significantly alters its physisorption probability. Several studies suggest the role of internal energy on trapping is modest. In studies of H<sub>2</sub>O sticking on H<sub>2</sub>O ice, internal vibrational energy does not explain why the sticking probability is not unity at low incident  $E_{trans}$ .(59) Wodtke et al. reported that internal energy does not significantly impact the trapping of NO ( $v=2$ ) on Au(111).(60) Beck and coworkers studied the state-resolved precursor mediated dissociation of SiH<sub>4</sub> on Si(100).(58) They demonstrated that the  $|2000\rangle$  Si-H stretching vibration was more reactive than the  $|1100\rangle$  vibration, both of which were more reactive than the ground state SiH<sub>4</sub> molecules. This was the first observed case of a physisorbed precursor showing state-resolved specificity, and it established that vibrationally excited silane trapped sufficiently well on the semiconducting Si(100) surface to permit reaction. Sibener and Lee looked at the

effect of thermal vibrational energy on the condensation of  $\text{CCl}_4$  and  $\text{SF}_6$  on their respective ice structures.<sup>(61)</sup> In contrast to the other studies discussed above, at the lowest  $E_{trans}$ , internal energy inhibited sticking by about a factor of 5, but that effect vanished at higher values of  $E_{trans}$ . Therefore, there is good evidence that vibrationally excited molecules can efficiently trap on semiconductor and metal surfaces. This can be understood when one moves away from the simple 1-D picture of potential energy in Fig. 3.1. The full methane-surface potential includes far more degrees of freedom. The high frequency internal vibrations of methane couple well to the reaction coordinate for dissociation, but couple poorly to the much lower frequency methane-surface vibrations that are more strongly coupled to the desorption channel.

In this study, we describe vibrational state-resolved reactivity measurements of  $\text{CH}_4$  dissociation on Ir(111). We report results for molecules predominantly in the vibrational ground state ( $v=0$ ) and for those excited to  $v=1$  of the antisymmetric C-H stretching vibration,  $\nu_3$ .

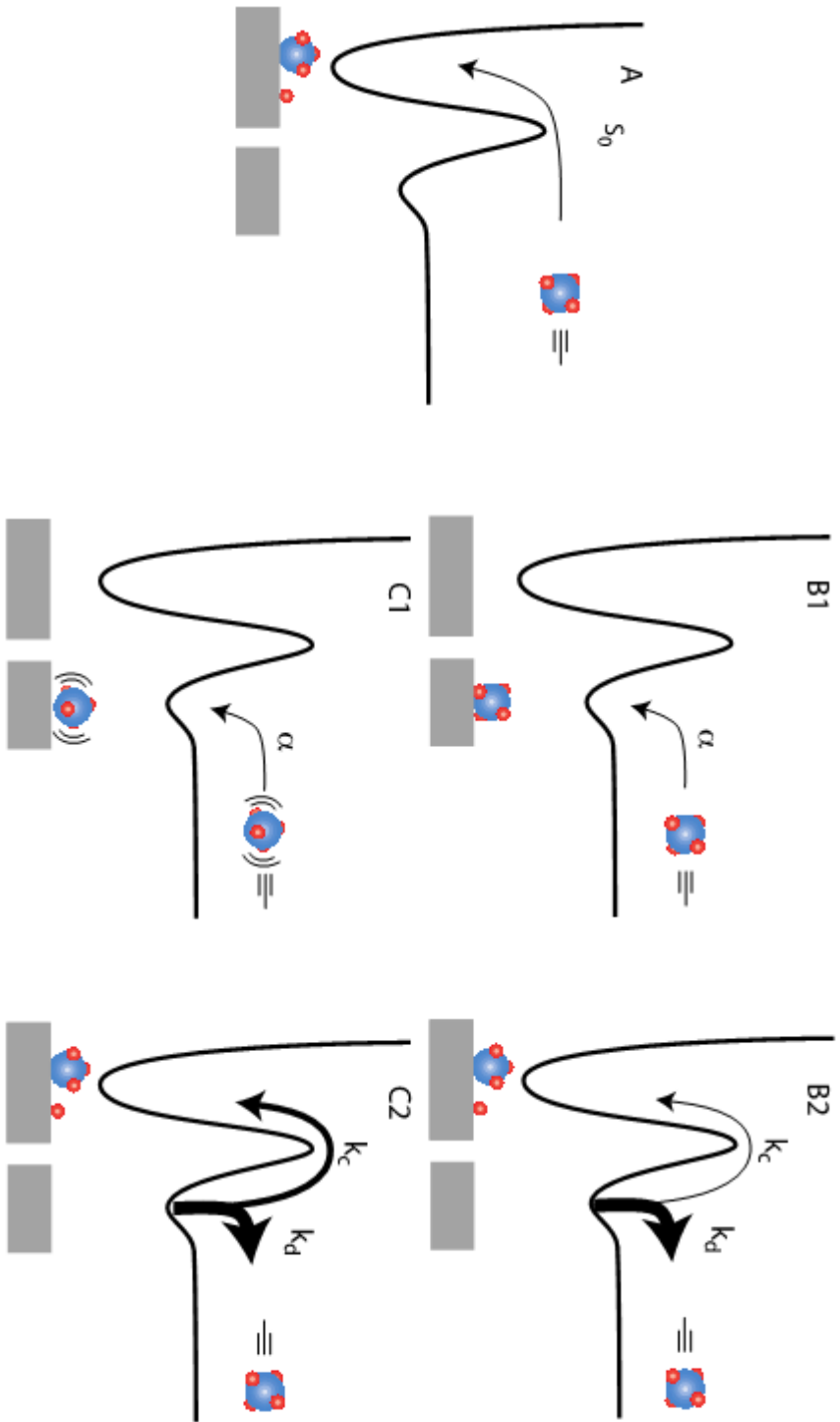


**Figure 3.1** Direct (panel A) and precursor-mediated (panels B and C) reaction mechanisms. In A, methane approaches the surface with energy greater than the effective barrier to reaction and proceeds to form surface bound methyl and H reaction products. In B1, methane approaches the surface with energy less than the effective barrier height and traps in the molecular physisorption well. In B2, the physisorbed molecule either desorbs with rate constant  $k_d$ , or chemisorbs with rate constant  $k_c$ . Panel C illustrates the situation for a vibrationally excited reagent. In C1 the vibrating molecule (vibration denoted by parentheses) approaches the surface and traps. In C2, as in B2, methane also desorbs or chemisorbs, but its additional internal energy increases the relative rate of chemisorption. Depending on whether vibrational quenching precedes desorption, it may desorb in  $v=0$  or an excited vibrational state.

## 3.2 Experimental Approach

The experiments were performed in a supersonic molecular beam surface scattering apparatus made up of four differentially pumped chambers. While this chamber is not the one used in prior studies in our lab, its design, and our procedures are very similar to those reported in the past.<sup>(4, 10, 62)</sup> The molecular beam terminated in the main chamber where the gas – surface reactions occurred. Gas mixtures of methane in Kr, Ar, He, or H<sub>2</sub> (all Airco, reagent grade) passed through a getter trap (SupelPure-O, Supelco) to remove trace impurities of reactive gases and unsaturated hydrocarbons and then expanded through a temperature controlled molecular beam nozzle with a 25 μm orifice. Skimming and collimation produced well-defined supersonic methane beams. A chopper wheel and quadrupole mass spectrometer located on the beamline allowed us to perform time-of-flight analysis of the beam. The carrier gas identity, seed ratio, and gas temperature were varied to obtain the necessary translational energies, as detailed in Table 3.1. Incident fluxes were obtained by using the experimentally measured partial pressure of CH<sub>4</sub> in the chamber under dosing conditions, the experimentally determined pumping speed of the chamber, and the known area of the beam image on the surface.

Experiments performed without laser excitation provide a good estimate of the reactivity of methane's  $v=0$  vibrational ground state. We used a nozzle temperature of 300 K for all but one  $E_{trans}$  measured, as shown in Table 3.1. If we assume that there is no vibrational cooling in the molecular beam, at least 99.3% of all methane molecules in the beam are in the vibrational ground state, 0.7%

% Methane	Carrier Gas	$T_{nozzle}$ , K	$E_{trans}$ , kJ/mol
10%	Ar	300	2.8
75%	Kr	300	4.0
80%	Ar	300	6.5
100%	-	300	8.7
50%	He	300	12.4
50%	He	400	16.4
1%	He	300	23.9
10%	H <sub>2</sub>	300	32.7
3%	H <sub>2</sub>	300	48.5

**Table 3.1** Nominal gas compositions, molecular beam nozzle temperatures, and measured  $E_{trans}$  for supersonic beams used in this study.

have one quantum of C-H bend excitation, and the fractional population of higher-lying excited states is less than  $2 \times 10^{-5}$  when  $T_{nozzle} = 300$  K. Those fractions change to 96.5% ( $v=0$ ), 3.4% ( $v=1$  bending states), and 0.08% (higher lying states) at  $T_{nozzle} = 400$  K. In our prior studies of  $\text{CH}_4$  dissociation on Ni(111), we have studied the effect of nozzle temperature on reactivity. By estimating the state-resolved reactivity of each vibrationally excited state, weighting that reactivity by the state's population at a given nozzle temperature, and summing over all states, we can assess the contribution of thermally excited vibrational states in the beam to our laser-off reactivity measurements.<sup>(63)</sup> We find that at  $T_{nozzle} = 300$  K on Ni(111), the  $S_0$  we measure is a tight upper limit on the inherent reactivity of the  $v=0$  ground state. We can make an analogous assessment for methane dissociation on Ir(111). We assume a vibrational efficacy of 1 for the  $v=1$  bending states in methane. This efficacy is nearly 2.5 times greater than we observe for the  $v_3$  C-H stretching state on Ir(111) (see Section 3.3) and more than twice the maximum efficacy observed for methane bending states on Ni or Pt surfaces, so it serves as a generous upper limit on the contribution of bending states to laser-off beam measurements.<sup>(64-66)</sup> We predict that when  $T_{nozzle} = 300$  K, our measurements of  $S_0$  without laser excitation are about 15% higher than the inherent reactivity of methane in its  $v=0$  state – well within the error bars on our measurements. At  $T_{nozzle} = 400$  K, this worst-case estimate suggests that the measured laser-off reactivity is no more than a factor of 2 greater than that of the vibrational ground state. Assuming a more realistic vibrational efficacy for the bending states of 0.4 that is consistent with observations on Ni and Pt surfaces

suggests that laser-off reactivity at  $T_{nozzle} = 400$  K is no more than 10% greater than the vibrational ground state reactivity. Therefore, we feel confident in approximating the reactivity of methane's  $v=0$  ground state with our laser-off reactivity in this study.

For state-resolved reactivity measurements of excited vibrational states, light from an infrared (IR), continuous wave laser (Aculight Argos) intersected the molecular beam in a collision-free region 14.5 cm upstream from the surface. We excited methane molecules to  $v_3, v=1$  via the R(1) transition at  $3038.4985\text{ cm}^{-1}$ . The radiative lifetime of the vibrationally excited molecules is much longer than their flight time from excitation region to the surface, so the methane molecules impinge on the surface in their laser-prepared state. The laser power dependence of absorption was measured with a lithium tantalate pyroelectric bolometer with integrated preamplifier (Eltec). Those measurements verified that we saturated the selected optical transition under the conditions of our experiment. The bolometer was mounted on a manipulator and was retracted from the beam line during reaction probability experiments.

The crystal used in these experiments was an iridium single crystal polished within  $0.1^\circ$  of the (111) face (Surface Preparation Laboratory). The crystal was attached to a liquid nitrogen cooled rotatable XYZ manipulator. A temperature controller using a combination of radiative and electron bombardment heating provided  $\pm 1$  K control over surface temperature from 100 K to 1600 K. A sequence consisting of 7 minutes of  $\text{Ar}^+$  sputtering, 50 minutes of annealing at 1200 K, 10 minutes of oxidation at 1100 K in the presence of  $1.0 \times$

$10^{-7}$  Torr  $O_2$  and a quick flash to 1600 K resulted in a clean surface, as determined by Auger Electron Spectroscopy (AES). The surface was held at 1000 K during the dose. At that temperature, methyl reaction products rapidly dehydrogenate, H recombinatively desorbs, and carbon remains bound to the surface, but does not dissolve into the bulk. Following a timed exposure to a molecular beam of known flux, carbon coverage was quantified using the C/Ir ratio from AES measurements. We used molecular beam reflectivity measurements to quantify  $S_0$  for a high-energy  $CH_4$  molecular beam whose reactivity had previously been reported in the literature.<sup>(26)</sup> We then used that known value of  $S_0$  and our flux measurements to obtain an absolute calibration of carbon coverage for our AES method. Based on this calibration we were able to measure carbon coverage as low as 0.01ML (one percent of a monolayer) with this approach. The ratio of the carbon coverage remaining after the dose to the integrated flux during the beam exposure yielded the reaction probability,  $S_0$ .

Laser excitation allows us to measure the reaction probability of methane molecules whose internal energy is precisely defined, unlike thermally excited sources. Since we are not able to prepare 100% of the molecular beam in the desired state, we compare the reactivity of the beam with and without laser excitation to obtain the inherent reactivity of the laser-excited  $v_3$  state. Equation 3.1 relates the inherent reaction probability of the  $v_3$  laser excited state to the measured quantities  $S_0^{On}$  and  $S_0^{Off}$ , which are the average reaction probabilities of the molecular beam with and without laser excitation, respectively, and  $f_{exc}$ , which is the experimentally measured excitation fraction.<sup>(4)</sup> At the relatively low nozzle

temperatures employed in this study, rotational cooling in the beam was nearly complete, as verified by direct IR absorption measurements of rotational state populations in our beam. Nuclear spin statistics limited the fractional population of the initial state for our IR transition (the  $v=0, J=1$  level) to 56%, so we excited approximately 28% of all methane molecules in the beam to  $v=1, J=2$  of  $\nu_3$ , and  $f_{exc} = 0.28$ . As discussed above, the vibrational ground state reactivity,  $S_0^{v=0}$ , is very nearly equal to the laser-off reactivity due to the low thermal population of vibrationally excited states at the nozzle temperatures used here.

$$S_0^{v_i} = \frac{S_0^{off} - S_0^{0n}}{f_{exc}} + S_0^{v=0} \quad \text{Equation 3.1}$$

### 3.3 Results and Discussion

Measurements of the initial reaction probability of CH<sub>4</sub> for both ground and vibrationally excited methane appear in Figure 3.2. Each point represents the average of 3 or more measurements, and the error bars show  $\pm 2\sigma$ . All measurements were performed with the molecular beam impinging on the surface at normal incidence, and the surface temperature was  $1000 \pm 1$  K. The laser-off data are in excellent agreement with the previously reported results from Seets et al.(26)

The additional 36 kJ/mol of vibrational energy in the  $\nu_3$  antisymmetric C-H stretch contributed significantly to  $S_0$  over the entire translational energy range. This is not surprising, as Seets et al. report an apparent activation energy for CH<sub>4</sub> dissociation on Ir(111) of 27 kJ/mol based on their measurements in a thermal (bulb) experiment.(26) Therefore, vibrationally excited molecules impinge on the surface with an internal energy greater than the apparent activation energy for reaction. For both ground and excited vibrational states,  $S_0$  initially decreases with increasing  $E_{trans}$  – a clear signature for a trapping mediated reaction channel. As  $E_{trans}$  increases above ca. 12 kJ/mol, the direct reaction mechanism begins to dominate as  $S_0$  increases monotonically with increasing  $E_{trans}$ . We next discuss results for the high and low  $E_{trans}$  regimes in greater detail.

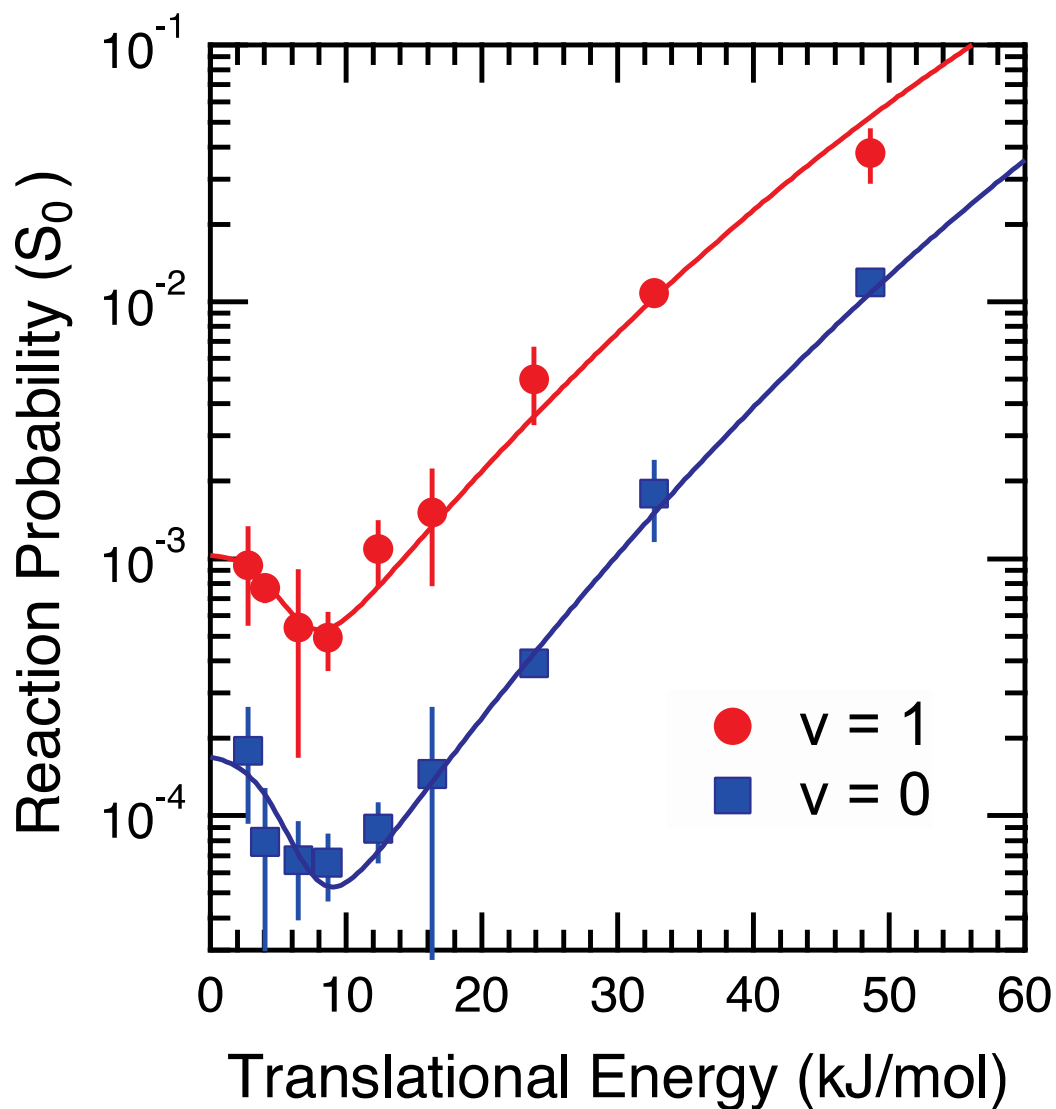


**Figure 3.2** State-resolved reaction probabilities for methane in the vibrational ground (blue squares) and laser excited  $v_3, v=1, J=2$  states (red circles). The lines passing through the data represent the sum of precursor-mediated and direct reaction channels, as described in Sections 3.3.1 and 3.3.2.

### 3.3.1 Direct Dissociative Chemisorption

At incident translational energies above about 15 kJ/mol, reactivity increases monotonically and nearly exponentially with increasing  $E_{trans}$ . This behavior is a common feature of methane activation on a wide range of catalytically active transition metals, and it is consistent with a direct (single collision) mechanism for reaction. In this mechanism, an incident molecule impinges on the surface with a particular internal and translational energy, orientation, impact site, and collection of vibrational phases. The geometric factors result in a threshold energy for reaction that could be much higher than the minimum energy threshold for reaction if the approach geometry is unfavorable.<sup>(67)</sup> If the molecule's energetics project favorably on the reaction coordinate and exceed the energy threshold for the molecule's particular geometric configuration, the molecule dissociates. Otherwise, it scatters non-reactively from the surface. As  $E_{trans}$  increases, the range of energetically accessible approach geometries increases leading to an increase in  $S_0$ . If the distribution of effective barriers is approximately Gaussian in shape, then  $S_0$  has the shape of an error function with a functional form given by Eq. 3.2. Here,  $A$  defines the asymptotic reactivity at high  $E_{trans}$ ,  $E_0$  and  $W$  are the center and width of the Gaussian function that defines the error function,  $erf$ , and the  $v$  labels the vibrational state of interest.

$$S_0(E_{trans}, v) = \frac{A(v)}{2} \left( 1 + erf \left( \frac{E_{trans} - E_0}{W(v)} \right) \right) \quad \text{Equation 3.2}$$

When comparing state-resolved measurements of the vibrational ground state and an excited vibrational state, it is common to find that the shape of the  $S_0$  curve is similar for the two states ( $A$  and  $W$  match), but the curve for the excited state is offset along the  $E_{trans}$  axis. This offset,  $\Delta E_{trans} = E_0^{v=0} - E_0^v$  is a quantitative and  $E_{trans}$ -independent measure of how much  $E_{vib}$  reduces the amount of  $E_{trans}$  needed to obtain a given reaction probability. The vibrational efficacy, defined as  $\eta(v) = \Delta E_{trans} / E_{vib}$  is a convenient measure of the ability of a particular vibration to promote dissociative chemisorption. When  $\eta(v) < 1$ ,  $E_{vib}$  is less effective than an equivalent amount of  $E_{trans}$  in promoting reactivity. Within the context of Polanyi's rules, this would be the expected case for an "early" barrier.<sup>(68)</sup> When  $\eta(v) > 1$ , the vibration is more effective than an equivalent amount of  $E_{trans}$  (late barrier case), and the situation where  $\eta(v) = 1$  would be expected for a fully statistical model of reactivity where all energetic modes are equivalent in their ability to promote dissociation or complete internal vibrational mode scrambling occurs before reaction. Figure 3.3 shows error function fits that describe the  $v=0$  and  $v_3$  reactivity data in the direct region well. Both curves share the same width ( $W=36$ ) and asymptote ( $A=1$ ) parameters, but differ in their shift ( $E_0$ ) along the  $E_{trans}$  axis ( $E_0 = 113.5$  and  $98$  kJ/mol for the  $v=0$  and  $v_3, v=1$  states, respectively). Based on the difference in  $E_0$  values for the two states and the known value of  $E_{vib} = 36$  kJ/mol for the  $v_3, v=1$  state, we calculate  $\eta = 0.43$  for  $\text{CH}_4$  ( $v_3, v=1$ ) on Ir(111).

The efficacy of  $\text{CH}_4$  ( $v_3, v=1$ ) on Ir(111) is less than that reported for other close-packed catalytically active metal surfaces. Table 3.2 summarizes the results.

Surface	Vib. State	$\eta$ , Efficacy	Ref.	r, CH
Ni(111)	$\nu_3$	1.25	(69)	1.59Å(36)
Pt(111)	$\nu_3$	0.71	(70)	1.47Å(36)
Ir(111)	$\nu_3$	0.43	This Work	1.43Å(35)

**Table 3.2** Measured vibrational efficacies and calculated C-H bond lengths at the transition state for three close-packed fcc metals.

The trend observed in vibrational efficacy tracks the extent of C-H bond extension in the calculated transition state geometry. While other factors, including the details of the gas-surface interaction potential and its influence over surface-induced intramolecular vibrational redistribution (IVR) during the reactive encounter will also play a role in determining the efficacy of any particular vibrational state,<sup>(34)</sup> it does make sense that the most distorted transition state geometry benefits most from vibrational activation along the distorted coordinate. The low efficacy of  $v_3$  on Ir(111) also explains in part why the reaction probabilities in Fig 3.3 are low, given that the internal energy of the state, 36 kJ/mol, exceeds the nominal activation energy for the reaction. It is likely that the reaction coordinate includes significant contributions from other degrees of freedom, such as surface atom motion, angular deformations, and motion along the surface normal, and that excitation in the  $v_3$  coordinate alone is not sufficient to promote reaction.

### 3.3.2 Low $E_{trans}$ Channel

At low incident  $E_{trans}$ , we observe that  $S_0$  initially decreases with increasing  $E_{trans}$ . For reasons outlined in Section 3.1, we feel this behavior most likely arises from a precursor-mediated reaction mechanism. A precursor-mediated reaction can be viewed to occur in two steps. In the first, the incident molecule loses sufficient normal momentum to become trapped in the physisorption potential well at the surface. The trapping probability,  $\alpha(E_n)$  depends on the molecule's incident translational energy along the surface normal ( $E_n$ ), momentum transfer and surface corrugation. Once on the surface, the

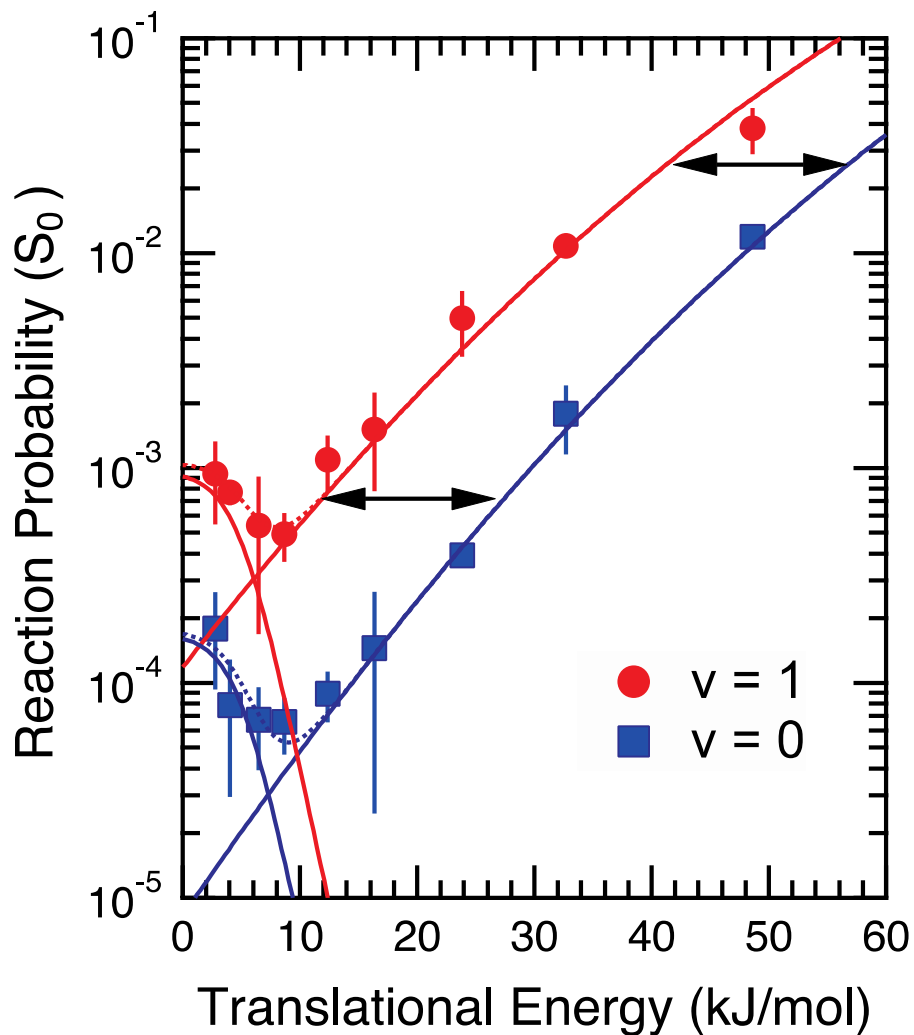


**Figure 3.3** Contribution of precursor-mediated and direct reaction mechanisms (solid lines) to the overall reaction probability of methane in its vibrational ground (blue) and vibrationally excited ( $v_3, v=1$ , red) states (dotted lines). The black arrows show the constant  $E_{trans}$  offset between the direct reaction probability curves for  $v=0$  and  $v=1$ . The offset of 15.5 kJ/mol corresponds to a vibrational efficacy of 0.43 for the  $v_3$  vibrational fundamental.

molecule can tumble and diffuse while sampling different geometric orientations that may have lower energetic thresholds to reaction. It could also diffuse to a step or defect site where the reaction barrier is lower than on a terrace. Translational degrees of freedom thermalize most quickly, with rotational and vibrational degrees of freedom taking progressively longer. If at some time the molecule possesses sufficient energy along the reaction coordinate to exceed the reaction threshold, it can go on to dissociatively chemisorb. The dissociative chemisorption channel ( $k_c(T)$ ) is in kinetic competition with desorption ( $k_d(T)$ ). For methane on Ir(111), the activation energy to desorption has been estimated to be 0.129 eV,<sup>(40)</sup> which is less than half of the activation energy for reaction. Therefore, the probability for an incident molecule reacting via a precursor state is the product of the probability that it traps,  $\alpha(E)$ , and the kinetic branching ratio for chemisorption via the physisorbed state, as shown in Eq. 3.3.

$$S_0(E, T_{surf}) = \alpha(E) \frac{k_c(T)}{k_c(T) + k_d(T)} = \alpha(E) S_0(0, T_{surf}) \quad \text{Equation 3.3}$$

Since the ratio of rate constants is independent of initial  $E_{trans}$ , the translational energy dependence of  $S_0$  for precursor-mediated reactivity is completely determined by  $\alpha(E)$ .

If our low- $E_{trans}$  reaction channel corresponds to a precursor-mediated mechanism, it will have the same  $E_{trans}$  dependence as  $\alpha(E)$ . Sitz and Mullins performed classical molecular dynamics trajectory calculations in a detailed study of methane trapping on Ir(110)-(1x2) and Ir(111).<sup>(40)</sup> They calculated  $\alpha(E)$  on both surfaces over a range of surface temperatures. They first confirmed that their

calculations accurately reproduced experimental measurements of  $\alpha(E)$  on Ir(110)-(1x2) at  $T_{surf} = 65$  K (28, 37). They then investigated how  $\alpha(E)$  changes as  $T_{surf}$  increases. On Ir(111), they found that  $\alpha(E_{trans}=5 \text{ kJ/mol}) = 0.4$ , and is nearly independent of  $T_{surf}$  from 100 to 1500 K. At  $E_{trans} = 10 \text{ kJ/mol}$ ,  $\alpha(E)$  increases from about 0.15 to 0.3 between  $T_{surf} = 300$  K and 1200 K (thermally induced surface atom motion leads to a modest increase in  $\alpha$  at higher  $E_{trans}$  where trapping probabilities are low). Once trapped, the residence times for  $\text{CH}_4$  physisorbed on Ir(111) were calculated to be 8 ps at  $T_{surf} = 1000$  K and 30 ps at  $T_{surf} = 500$  K.

When one compares Sitz and Mullins' molecular dynamics calculations of  $\alpha(E)$  to prior measurements of  $S_0(E, T_{surf})$  for methane dissociation on Ir(111)(2 $\times$ 6), the calculated trapping probabilities quantitatively reproduce the  $E_{trans}$  dependence of  $S_0$  over a range of surface temperatures that include 1000 K, the surface temperature used in our study. The excellent agreement between a quantitative prediction of trapping probability and the experimentally measured  $E_{trans}$  dependence of  $S_0$  further supports the interpretation that a precursor-mediated mechanism is responsible for the low- $E_{trans}$  reaction channel. Seets et al. used Eq. 3.4 with the parameters of  $x=31.0$ ,  $E_y=1.89$ , and  $N=0.83$  as an empirical function that accurately reproduced  $\alpha(E_n)$  in their experiments, and we used this functional form in the analysis of our data in Fig. 3.3.

$$\alpha(E_n) = \frac{1}{\exp(E_n x - E_y) + N} \quad \text{Equation 3.4}$$

To model our data, we summed contributions from the precursor-mediated (Eq. 3.3) and direct reaction channels (Eq. 3.2) to obtain a total reaction

probability. We then compared the total reaction probability to our measured data. When  $E_{trans} > 20$  kJ/mol, the direct mechanism dominated and the data tightly constrained the parameters in Eq. 3.2. We then turned to the low- $E_{trans}$  regime. We constrained  $\alpha(E_n)$  to the functional form reported by Seets et al. (Eq. 3.4) and treated  $S_0(0, T_{surf})$  in Eq. 3.3, as the single adjustable parameter for each vibrational state ( $v=0$  and  $v_3, v=1$ ). The fit yielded values of  $S_0(0, T_{surf})$  equal to  $1.6 \pm 0.4 \times 10^{-4}$  and  $9.2 \pm 0.6 \times 10^{-4}$  for  $v=0$  and  $v_3, v=1$ , respectively. In the limit of  $E_n=0$ ,  $\alpha(E_n)$  approaches unity, so we can equate  $S_0(E_{trans} = 0, T_{surf})$  to the ratio of rate constants in Eq. 3.3. Given our measured values for  $S_0(0, T_{surf})$ , it is clear that  $k_d \gg k_c$ , so the ratio of  $S_0(0, T_{surf})$  values points to a nearly six-fold increase in  $k_c$  for  $v_3, v=1$  relative to  $v=0$ . The solid lines in Fig. 3.3 illustrate the  $E_{trans}$ -dependent contribution of both trapping-mediated (negative slopes) and direct channels (positive slopes) to overall reactivity while the dashed lines show their sum for comparison to the data.

We can use the values of  $S_0(0, T_{surf} = 1000$  K) from the analysis of our data, the relationship between  $S_0(0, T_{surf})$ ,  $k_c$  and  $k_d$  in Eq. 3.3, prefactors from the kinetic analysis of Seets et al.,(26) and the reported activation energy for desorption to estimate the activation energy for chemisorption,  $E_{a,c}$  for both the vibrational ground state and the  $v_3$  vibrationally excited state. We approximate the vibrational ground state reactivity with our laser off data. Seets et al. measured  $S_0$  over a range of surface temperatures. Their analysis of data in the low- $E_{trans}$  regime yielded a ratio of the prefactors for chemisorption and desorption of  $v_c / v_d = 1.8 \times 10^{-3}$ .(26) We use that ratio, our own measurement of  $S_0(E_{trans} = 0, T_{surf} =$

$1000 \text{ K}) = 1.6 \times 10^{-4}$  for the  $v=0$  state, and the reported activation energy for desorption,  $E_{a,d} = 0.129 \text{ eV}$ , (40) to calculate  $E_{a,c} (v=0) = 33 \text{ kJ/mol}$ . This value compares very well with the value of  $32 \text{ kJ/mol}$  that Seets et al. obtained for their molecular beam data. For  $v=1$  of the  $\nu_3$  C-H stretching state, if we assume the same values for  $E_{a,d}$  and the prefactor ratio  $\nu_c / \nu_d$ , and we use our measured value of  $S_0(E_{trans} = 0, T_{surf} = 1000 \text{ K}) = 9.2 \times 10^{-4}$ , we calculate  $E_{a,c} (v=1) = 18 \text{ kJ/mol}$ . Therefore, adding  $36 \text{ kJ/mol}$  of internal energy to the incident methane molecule reduces the effective activation energy for reaction, as viewed through the surface temperature dependence of reactivity, by  $33 - 18 = 15 \text{ kJ/mol}$ . The ratio of this difference to  $E_{vib} = 36 \text{ kJ/mol}$  gives an efficacy for the  $\nu_3$  vibration in promoting dissociative chemisorption via a precursor state of  $0.42$  – nearly identical to the efficacy of  $0.43$  that we observed for the direct reaction channel. Since the values of vibrational efficacy relate to how well energy in a particular vibrational state evolves into motion along the reaction coordinate, it is perhaps not surprising that the  $\nu_3$  vibration is similarly effective in promoting dissociative chemisorption via a direct or precursor-mediated reaction mechanism.

The ability of vibrationally hot gas phase molecules to exhibit enhanced reactivity via a physisorbed state is significant. It establishes that even in the presence of the highly efficient electronically mediated vibrational quenching channels on a metal surface, trapped molecules can retain their vibrational energy long enough to influence reactivity. Anghel and coworkers suggested this mechanism was most likely responsible for the low- $E_{trans}$  reaction channel for methane dissociation on Pt(110)-(1x2), and noted that it is consistent with what is

known about the lifetime of vibrations in chemisorbed species, which range from 1 to a few 10's of ps.(55, 57) Given that physisorbed species are generally more weakly coupled to the electronic structure of the surface, we would expect their vibrational lifetimes to even longer than those of chemisorbed species.

Figure 3.3 also shows that near  $E_{trans} = 0$ , the reactivity of the precursor channel is an order of magnitude or more greater than our model predicts for a direct reaction of the same vibrational state. This is true even though the energy content of the incident molecule and surface are essentially identical for the two reaction channels. The enhanced reactivity of the physisorbed molecules likely results from their ability to sample a wider range of geometric configurations during their surface encounter. The 8-ps physisorption lifetime at  $T_{surf} = 1000$  K is much longer than molecules experience during a direct encounter (typically a few 100's of fs). It is also longer than the classical vibrational periods of surface atoms and internal methane vibrations, and the classical rotational period for a methane molecule. The transition state geometry for methane is relatively tight. Therefore, many molecules initially encounter the surface in an unfavorable geometry where the  $E_{trans}$  threshold for reaction is relatively high. During the few 100 fs of a direct encounter, the molecules do not have sufficient time to reorient and sample more favorable geometries, so they scatter non-reactively. On the other hand, if they first trap into a precursor state, they can reorient, diffuse, sample different vibrational phases (particularly of the surface atoms) and find a lower barrier path to reaction.

In addition to providing enhanced geometric sampling of phase space, physisorption can alter the electronic structure of the adsorbate and potentially impact reaction energetics. Ostom et al. reported a physisorption-induced C-H bond elongation in methane on a Pt surface.<sup>(71)</sup> Calculations by Henkelman et al. predicted particularly strong, molecularly bound states of methane at kink and adatom defect sites on an Ir(111) surface, but they did not find evidence that these more strongly bound methane molecules would dissociate with higher probability.<sup>(35)</sup>

Prior studies of precursor mediated reactions focused on gas phase molecules approaching the surface in their ground vibrational state. Upon physisorbing to a hot surface, thermalization will drive a transfer of vibrational energy into the physisorbed molecule's vibrational degrees of freedom. The resulting flow of energy into the reaction complex has been seen as a primary means for the surface to activate the precursor molecules and drive reaction. In our experiments, the physisorbed molecules are all initially in the  $\nu_3$  vibrational state – a non-equilibrium situation where the average  $E_{vib}$  of the physisorbed methane molecules is much greater than  $kT_{surface}$ , so thermalization will tend to reduce the average vibrational energy content of methane. Nonetheless, we still observe a pronounced physisorption reaction channel for the vibrationally excited molecules. Our observation of enhanced reactivity for physisorbed methane molecules makes clear that precursor mediated reactivity on a metal can still occur even when there is not significant energy flow from surface to adsorbate.

The ability of a vibrationally hot precursor molecule to retain its internal energy for a period of time suggests other kinetic mechanisms that might occur on surfaces. Depending on the excited molecule's vibrational lifetime and desorption kinetics, it could diffuse from a terrace site where it may have initially landed on the surface to nearby step, kink, or defect sites where local energetic threshold for reaction is lower. Such a mechanism results in complicated kinetics involving trapping, diffusion, desorption, quenching, and reaction at sites with different activation energies.(72)

Finally, we comment on why prior state resolved studies might have failed to detect precursor-mediated reactivity metal surfaces. A significant contributor to enhanced precursor reactivity is the ability of the precursor state to expand the range of geometric configurations that can undergo reaction. In situations where the internal energy of the molecule is already significant relative to the reaction barrier, reaction probabilities for a direct channel at low  $E_{trans}$  may already be high, and additional geometric sampling will have a minimal effect on opening additional reaction channels. In the other extreme, the internal energy of the incident molecule (and the efficacy of that excitation in promoting reaction) must be sufficiently high to overcome effective barriers to reaction. If the internal energy of the molecule is much less than the minimum barrier to reaction, the dissipation of normal kinetic energy upon trapping could leave the molecule far short of the energy requirement for reaction. Nonetheless, under high temperature thermal processing conditions, a preponderance of molecules has translational energies consistent with very high trapping probabilities. At the same time, the

presence of multiple low-frequency vibrational modes in polyatomic molecules can lead to significant populations of vibrationally hot molecules in the gas phase. Therefore, we suggest it is prudent to consider the importance of vibrationally hot precursor molecules in heterogeneously catalyzed processes involving highly activated chemical reactions.

### 3.4 Conclusions

State-resolved beam-surface scattering studies that prepare a high flux of vibrationally excited molecules at low incident  $E_{trans}$  reveal that a gas-phase vibrational excitation of the  $\nu_3$  C-H stretching fundamental can survive to enhance the dissociative chemisorption probability of a physisorbed methane molecule by nearly a factor of six relative to the vibrational ground state. This observation suggests that prior assessments of the role of precursor mediated channels in thermal reactions, which primarily relied on the measured reactivity of vibrational ground state molecules, significantly underestimate the importance of precursor-mediated reactivity in thermal processes. Our results also cloud the conventional interpretation of kinetic bulb studies, where it has been assumed that when reactivity scales with gas temperature, a direct mechanism prevails. We have demonstrated an alternative interpretation of that observation – raising the gas temperature increases the number of vibrationally hot molecules in the gas phase that are available to trap and react with enhanced probability relative to vibrational ground state molecules.

In the higher  $E_{trans}$  regime, we observe methane dissociation via a direct mechanism. In this regime, we are able to extract a vibrational efficacy for reaction of 0.43, which indicates that the  $\nu_3$  C-H stretching vibration is only modestly effective in promoting reactivity on the Ir(111) surface relative to the (111) surfaces of Pt or Ni. A kinetic analysis of reactivity via the precursor-mediated channel suggests a nearly identical efficacy for  $\nu_3$  excitation in promoting the reaction via a precursor-mediated pathway. The observed trend in

efficacy is consistent with extent of C-H bond extension at the transition state to dissociation on these three surfaces.

### 3.5 References

1. J. R. Rostrup-Nielsen, J. Sehested, J. K. Nørskov, in *Advances in Catalysis, Vol 47*, H. Knöppfer, B. C. Gates, Eds. (Academic Press, San Diego, 2002), vol. 47, pp. 65-139.
2. J. H. Larsen, I. Chorkendorff, From fundamental studies of reactivity on single crystals to the design of catalysts. *Surf. Sci. Rep.* **35**, 165-222 (1999).
3. T. V. Choudhary, E. Aksoylu, D. W. Goodman, Nonoxidative activation of methane. *Catal. Rev.-Sci. Eng.* **45**, 151-203 (2003).
4. L. B. F. Juurlink, D. R. Killelea, A. L. Utz, State-Resolved Probes of Methane Dissociation Dynamics. *Prog. Surf. Sci.* **84**, 69-134 (2009).
5. S. T. Ceyer, Dissociative Chemisorption: Dynamics and Mechanisms. *Annu. Rev. Phys. Chem.* **39**, 479-510 (1988).
6. C. T. Rettner, D. J. Auerbach, Molecular Beam Studies of Vibrational Energy Transfer and Vibrational Activation in Molecule-Surface Collisions. *J. Elect. Spectrosc. Rel. Phenom.* **45**, 335-350 (1987).
7. D. K. Bronnikov, D. V. Kalinin, V. D. Rusanov, Y. G. Filimonov, Y. G. Selivanov, J. C. Hilico, Spectroscopy and Non-Equilibrium Distribution of Vibrationally Excited Methane in a Supersonic Jet. *J. Quant. Spectrosc. Radiat. Transfer* **60**, 1053-1068 (1998).
8. C. T. Rettner, D. J. Auerbach, J. C. Tully, A. W. Kleyn, Chemical Dynamics at the Gas-Surface Interface. *Journal of Physical Chemistry* **100**, 13021-13033 (1996).
9. A. W. Kleyn, Molecular Beams and Chemical Dynamics at Surfaces. *Chem. Soc. Rev.* **32**, 87-95 (2003).
10. R. D. Beck, A. L. Utz, in *Dynamics of Gas-Surface Interactions: Atomic-level Understanding of Scattering processes at Surfaces*, R. D. Muiño, H. F. Busnago, Eds. (Springer-Verlag, Berlin, 2013), chap. 8.
11. A. L. Utz, Mode-Selective Chemistry at Surfaces. *Current Opinion in Solid State & Materials Science* **13**, 4-12 (2009).
12. C. T. Rettner, H. E. Pfnür, D. J. Auerbach, Dissociative Chemisorption of CH<sub>4</sub> on W(110): Dramatic Activation by Initial Kinetic Energy. *Physical Review Letters* **54**, 2716-2719 (1985).
13. M. B. Lee, Q. Y. Yang, S. T. Ceyer, Dynamics of the Activated Dissociative Chemisorption of CH<sub>4</sub> and Implication for the Pressure Gap in Catalysis: A Molecular Beam-High Resolution Electron Energy Loss Study. *J. Chem. Phys.* **87**, 2724-2741 (1987).
14. M. B. Lee, Q. Y. Yang, S. L. Tang, S. T. Ceyer, Activated Dissociative Chemisorption of CH<sub>4</sub> on Ni(111): Observation of a methyl radical and implication for the pressure gap in catalysis. *J. Chem. Phys.* **85**, 1693 (1986).
15. J. D. Beckerle, A. D. Johnson, Q. Y. Yang, S. T. Ceyer, Collision induced dissociative chemisorption of CH<sub>4</sub> on Ni(111) by inert gas atoms: The

- mechanism for chemistry with a hammer. *J. Chem. Phys.* **91**, 5756-5777 (1989).
16. A. C. Luntz, D. S. Bethune, Activation of Methane Dissociation on a Pt(111) Surface. *J. Chem. Phys.* **90**, 1274-1280 (1989).
  17. G. R. Schoofs, C. R. Arumainayagam, M. C. McMaster, R. J. Madix, Dissociative Chemisorption of Methane on Pt(111). *Surf. Sci* **215**, 1-28 (1989).
  18. D. J. Oakes, M. R. S. McCoustra, M. A. Chesters, Dissociative Adsorption of Methane on Pt(111) Induced by Hyperthermal Collisions. *Faraday Discuss.*, 325-336 (1993).
  19. A. V. Walker, D. A. King, Dynamics of the dissociative adsorption of methane on Pt{110}(1 x 2). *Physical Review Letters* **82**, 5156-5159 (1999).
  20. A. V. Walker, D. A. King, Dynamics of Dissociative Methane Adsorption on Metals: CH<sub>4</sub> on Pt{110}(1x2). *J. Chem. Phys.* **112**, 4739-4748 (2000).
  21. R. Bisson, M. Sacchi, R. D. Beck, State-Resolved Reactivity of CH<sub>4</sub> on Pt (110) - (1x2): The Role of Surface Orientation and Impact Site. *J. Chem. Phys.* **132**, 094702 (2010).
  22. A. T. Gee, B. E. Hayden, C. Mormiche, A. W. Kleyn, B. Riedmuller, The Dynamics of the Dissociative Adsorption of Methane on Pt(533). *J. Chem. Phys.* **118**, 3334-3341 (2003).
  23. P. M. Holmblad, J. Wambach, I. Chorkendorff, Molecular-Beam Study of Dissociative Sticking of Methane On Ni(100). *J. Chem. Phys.* **102**, 8255-8263 (1995).
  24. J. H. Larsen, P. M. Holmblad, I. Chorkendorff, Dissociative Sticking of CH<sub>4</sub> on Ru(0001). *J. Chem. Phys.* **110**, 2637-2642 (1999).
  25. H. Mortensen, L. Diekhoner, A. Baurichter, A. C. Luntz, CH<sub>4</sub> dissociation on Ru(0001): A view from both sides of the barrier. *J. Chem. Phys.* **116**, 5781-5794 (2002).
  26. D. C. Seets, C. T. Reeves, B. A. Ferguson, M. C. Wheeler, C. B. Mullins, Dissociative Chemisorption of Methane on Ir(111): Evidence for Direct and Trapping-Mediated Mechanisms. *J. Chem. Phys.* **107**, 10229-10241 (1997).
  27. T. A. Jachimowski, C. J. Hagedorn, W. H. Weinberg, Direct and trapping-mediated dissociative chemisorption of methane on Ir(111). *Surf. Sci.* **393**, 126-134 (1997).
  28. D. C. Seets, M. C. Wheeler, C. B. Mullins, Trapping-Mediated and Direct Dissociative Chemisorption of Methane on Ir(110): A Comparison of Molecular Beam and Bulb Experiments. *J. Chem. Phys.* **107**, 3986-3998 (1997).
  29. R. W. Verhoef, D. Kelly, C. B. Mullins, W. H. Weinberg, Direct dissociative chemisorption of methane and ethane on Ir(110): Isotope effects and vibrationally assisted chemisorption. *Surf. Sci.* **311**, 196-213 (1994).

30. M. Valden, J. Pere, M. Hirsimaki, S. Suhonen, M. Pessa, Activated adsorption of methane on clean and oxygen-modified Pt{111} and Pd{110}. *Surf. Sci.* **377**, 605-609 (1997).
31. T. Kondo, T. Sasaki, S. Yamamoto, Dissociative chemisorption of CH<sub>4</sub> on a cesiated Pt(111) surface studied by supersonic molecular beam scattering techniques. *J. Chem. Phys.* **116**, 7673-7684 (2002).
32. J. H. Larsen, I. Chorkendorff, Increased dissociation probability of CH<sub>4</sub> on Co/Cu(111). *Surf. Sci.* **405**, 62-73 (1998).
33. P. M. Holmblad, J. H. Larsen, I. Chorkendorff, Modification of Ni(111) Reactivity Toward CH<sub>4</sub>, CO, and D<sub>2</sub> by Two-Dimensional Alloying. *J. Chem. Phys.* **104**, 7289-7295 (1996).
34. D. R. Killelea, A. L. Utz, On the origin of mode- and bond-selectivity in vibrationally mediated reactions on surfaces. *Phys. Chem. Chem. Phys.* **15**, 20545-20554 (2013).
35. G. Henkelman, H. Jonsson, Theoretical Calculations of Dissociative Adsorption of CH<sub>4</sub> on an Ir(111) Surface. *Physical Review Letters* **86**, 664-667 (2001).
36. S. Nave, B. Jackson, Methane Dissociation on Ni(111) and Pt(111): Energetic and Dynamical Studies. *J. Chem. Phys.* **130**, 054701 (2009).
37. D. C. Seets, M. C. Wheeler, C. B. Mullins, Mechanism of the dissociative chemisorption of methane over Ir(110): Trapping-mediated or direct? *Chemical Physics Letters* **266**, 431-436 (1997).
38. J. C. Tully, Dynamics of Gas-Surface Interactions - 3D Generalized Langevin Model Applied to FCC and BCC Surfaces. *J. Chem. Phys.* **73**, 1975-1985 (1980).
39. C. W. Muhlhausen, L. R. Williams, J. C. Tully, Dynamics of Gas-Surface Interactions - Scattering and Desorption of NO from Ag(111) and Pt(111). *J. Chem. Phys.* **83**, 2594-2606 (1985).
40. G. O. Sitz, C. B. Mullins, Molecular dynamics simulations of the influence of surface temperature on the trapping of methane on iridium single- crystalline surfaces. *J. Phys. Chem. B* **106**, 8349-8353 (2002).
41. G. O. Sitz, Gas Surface Interactions Studied with State-Prepared Molecules. *Rep. Progr. Phys.* **65**, 1165-1193 (2002).
42. A. Gross, S. Wilke, M. Scheffler, 6-Dimensional Quantum Dynamics of Adsorption and Desorption of H<sub>2</sub> At Pd(100) - Steering and Steric Effects. *Physical Review Letters* **75**, 2718-2721 (1995).
43. K. D. Rendulic, G. Anger, A. Winkler, Wide Range Nozzle Beam Adsorption Data for the systems H<sub>2</sub>/Nickel and H<sub>2</sub>/Pd(100). *Surface Sci.* **208**, 404-424 (1989).
44. M. Gostein, G. O. Sitz, Rotational state-resolved sticking coefficients for H<sub>2</sub> on Pd(111): Testing dynamical steering in dissociative adsorption. *J. Chem. Phys.* **106**, 7378-7390 (1997).
45. L. B. F. Juurlink, R. R. Smith, A. L. Utz, Controlling Surface Chemistry with Light: Spatially Resolved Deposition of Rovibrational-State-Selected Molecules. *The Journal of Physical Chemistry B* **104**, 3327-3336 (2000).

46. A. T. Anghel, D. J. Wales, S. J. Jenkins, D. A. King, Pathways for dissociative methane chemisorption on Pt{110}-(1x2). *Phys. Rev. B* **71**, 209902 (2005).
47. F. Nattino, H. Ueta, H. Chadwick, M. E. van Reijzen, R. D. Beck, B. Jackson, M. C. van Hemert, G. J. Kroes, Ab Initio Molecular Dynamics Calculations versus Quantum-State-Resolved Experiments on CHD<sub>3</sub> + Pt(111): New Insights into a Prototypical Gas-Surface Reaction. *J. Phys. Chem. Lett.* **5**, 1294-1299 (2014).
48. B. L. Yoder, R. Bisson, R. D. Beck, Steric Effects in the Chemisorption of Vibrationally Excited Methane on Ni(100). *Science* **329**, 553-556 (2010).
49. B. L. Yoder, R. Bisson, P. M. Hundt, R. D. Beck, Alignment Dependent Chemisorption of Vibrationally Excited CH(4)(v<sub>3</sub>) on Ni(100), Ni(110), and Ni(111). *Journal of Chemical Physics* **135**, 224703 (2011).
50. B. Jackson, S. Nave, The dissociative chemisorption of methane on Ni(111): The effects of molecular vibration and lattice motion. *Journal of Chemical Physics* **138**, 174705 (2013).
51. B. Jackson, S. Nave, The dissociative chemisorption of methane on Ni(100): Reaction path description of mode-selective chemistry. *Journal of Chemical Physics* **135**, (2011).
52. B. Ølgaard Nielsen, A. C. Luntz, P. M. Holmblad, I. Chorkendorff, Activated Dissociative Chemisorption of Methane On Ni(100) - a Direct Mechanism Under Thermal Conditions? *Catalysis Letters* **32**, 15-30 (1995).
53. S. Nave, B. Jackson, Methane Dissociation on Ni(111): The Role of Lattice Reconstruction. *Physical Review Letters* **98**, 173003 (2007).
54. A. K. Tiwari, S. Nave, B. Jackson, Methane Dissociation on Ni(111): A New Understanding of the Lattice Effect. *Physical Review Letters* **103**, 253201 (2009).
55. J. D. Beckerle, R. R. Cavanagh, M. P. Casassa, E. J. Heilweil, J. C. Stephenson, Subpicosecond transient infrared spectroscopy of adsorbates: Vibrational dynamics of CO/Pt(111). *J. Chem. Phys.* **95**, 5403-5418 (1991).
56. J. D. Beckerle, M. P. Casassa, R. R. Cavanagh, E. J. Heilweil, J. C. Stephenson, Ultrafast Infrared Response of Adsorbates on Metal-Surfaces - Vibrational Lifetime of Co/Pt(111). *Physical Review Letters* **64**, 2090-2093 (1990).
57. V. Krishna, J. C. Tully, Vibrational lifetimes of molecular adsorbates on metal surfaces. *J. Chem. Phys.* **125**, (2006).
58. R. Bisson, T. T. Dang, M. Sacchi, R. D. Beck, Vibrational Activation in Direct and Precursor-Mediated Chemisorption of SiH<sub>4</sub> on Si(100). *J. Chem. Phys.* **129**, 081103 (2008).
59. K. D. Gibson, D. R. Killelea, H. Yuan, J. S. Becker, S. J. Sibener, Determination of the sticking coefficient and scattering dynamics of water on ice using molecular beam techniques. *J. Chem. Phys.* **134**, (2011).

60. A. M. Wodtke, H. Yuhui, D. J. Auerbach, Insensitivity of trapping at surfaces to molecular vibration. *Chemical Physics Letters* **413**, 326-330 (2005).
61. S. J. Sibener, Y. T. Lee, The Internal and Translational Energy-Dependence of Molecular Condensation Coefficients - SF<sub>6</sub> and CCl<sub>4</sub>. *J. Chem. Phys.* **101**, 1693-1703 (1994).
62. P. R. McCabe, L. B. F. Juurlink, A. L. Utz, A Molecular Beam Apparatus for Eigenstate-Resolved Studies of Gas-Surface Reactivity. *Rev. Sci. Instrum.* **71**, 42-53 (2000).
63. D. F. DelSesto, Ph.D., The role of Thermally Excited Vibrations in Gas-Surface Reactions: Methane on Ni(111) and Ir(111), *Tufts University Medford, MA* (2011).
64. L. B. F. Juurlink, R. R. Smith, D. R. Killelea, A. L. Utz, Comparative Study of C-H Stretch and Bend Vibrations in Methane Activation on Ni(100) and Ni(111). *Physical Review Letters* **94**, 208303 (2005).
65. R. Bisson, M. Sacchi, R. D. Beck, Mode-Specific Reactivity of CH<sub>4</sub> on Pt (110) - (1×2): The Concerted Role of Stretch and Bend Excitation. *Phys. Rev. B* **82**, 121404 (2010).
66. N. Chen, Y. Huang, A. L. Utz, State-Resolved Reactivity of Methane (v<sub>2</sub> + v<sub>4</sub>) on Ni(111). *J. Phys. Chem. A* **117**, 6250-6255 (2013).
67. A. C. Luntz, A Simple Model for Associative Desorption and Dissociative Chemisorption. *J. Chem. Phys.* **113**, 6901-6905 (2000).
68. J. C. Polanyi, Some Concepts in Reaction Dynamics. *Acct. Chem. Res.* **5**, 161-168 (1972).
69. R. R. Smith, D. R. Killelea, D. F. DelSesto, A. L. Utz, Preference for Vibrational over Translational Energy in a Gas-Surface Reaction. *Science* **304**, 992-995 (2004).
70. H. Ueta, L. Chen, R. D. Beck, I. Colon-Diaz, B. Jackson, Quantum state-resolved CH<sub>4</sub> dissociation on Pt(111): coverage dependent barrier heights from experiment and density functional theory. *Phys. Chem. Chem. Phys.* **15**, 20526-20535 (2013).
71. H. Ostrom, H. Ogasawara, L. A. Naslund, K. Andersson, L. G. M. Pettersson, A. Nilsson, Geometric and electronic structure of methane adsorbed on a Pt surface. *J. Chem. Phys.* **127**, (2007).
72. H. Mortensen, L. Diekhoner, A. Baurichter, E. Jensen, A. C. Luntz, Dynamics of ammonia decomposition on Ru(0001). *J. Chem. Phys.* **113**, 6882-6887 (2000).



# Chapter 4 : Chemically Accurate Simulation of a Polyatomic Molecule-Metal Surface Reaction

## 4.1 Introduction

Predictive modeling of dissociative chemisorption for polyatomic molecules on metal surfaces has the potential to drastically improve mechanistic interpretations and guide future studies. The complexity in accurately calculating the potential energy surface for reactions increases exponentially with the number of participating electrons and energetic states. Nearly exact solutions of the Schrödinger equation utilizing full quantum scattering calculations have been demonstrated for three-atom reactions(1) such as the gas phase abstraction reaction of H<sub>2</sub> with F.(2) In contrast to the gas phase, reactions on surfaces require the treatment of molecular degrees of freedom (DOFs) within the gaseous reagent *and* the metal's electronic structure. This increased complexity leads to significant challenges for both density functional theory (DFT)(3) and ab initio(4, 5) electronic structure methods. Current state of the art dynamics calculations for polyatomic dissociation on metal surfaces yield semi-quantitative results when compared to molecular beam experiments.(6-13)

Advancement of theoretical methods for the reaction of polyatomic atoms on metal surfaces is hindered by existing computational and experimental limitations. Previous benchmark DFT gas-phase studies demonstrate the difficulty

in obtaining reaction barrier magnitudes within 1 kcal/mol (4.2 kJ/mol)(14, 15), which is necessary to obtain a chemically accurate description of the reaction. Additionally, for molecules heavier than H<sub>2</sub> the effects of surface atom motion must be included in the dynamics calculations because the surface atom position may modulate the reaction barrier height(7), or alter the energy transfer between the surface and molecule.(16) Equally as important as selecting the correct functional is choosing a system that both builds upon existing knowledge and fills in gaps of misunderstanding while avoiding unnecessary approximations to ensure the accuracy of the model. Previous experimental studies were performed under conditions that require quantum dynamics for an accurate description, leading to excessive approximations and omission(6, 8), or approximation(10, 11) of participating degrees of freedom in the reaction.

An ideal system for the advancement of theoretical methods of polyatomic surface reactions is the dissociative chemisorption of methane on metal surfaces. Methane is more complex than previously studied systems but is still amenable to high level theoretical description with its high level of symmetry and relatively small number of electrons. This system has also been the scrutiny of many experimental and theoretical studies which help guide our qualitative understanding for this specific reaction on a host of different metal surfaces and a variety of methane isotopologues. Its dissociation on metal surfaces constitutes the rate determining step in the steam reforming reaction(17) of methane to produce hydrogen. The reaction of methane on Ni, Pt, and Ir metal surfaces has proven to be non-statistical in nature producing large differences in reactivity

based on the identity of the vibrational state. The C-H stretching modes produce large enhancements in reactivity when compared to bending modes. For example, exciting the C-H stretch vibration ( $\nu_1, \nu=1$ ) in the triply-deuterated methane isotopologue, CHD<sub>3</sub>, leads to a 100-fold increase in the C-H : C-D cracking pattern on Ni(111).<sup>(18)</sup>

With these goals and limitations in mind the CHD<sub>3</sub> + Ni(111) system was selected to demonstrate the joint theoretical-experimental approach to obtain a chemically accurate description for the reaction. Experiments are performed to obtain an observable quantity that is dependent on the reaction barrier height for this specific reaction. Reaction conditions are chosen such that the quasi-classical trajectory (QCT) method utilized in conjunction with Ab Initio Molecular Dynamics (AIMD) allows for comparison between theory and experiment.<sup>(9)</sup> In practice we perform supersonic molecular beam measurements to obtain the initial sticking probability,  $S_0$ , for CHD<sub>3</sub> on a clean Ni(111) surface. To ensure there are minimal quantum dynamical effects methane internal energies are kept above the reaction barrier so the process occurs “over the barrier” with minimal contributions from tunneling. The experiments are performed at surface temperature,  $T_{surf} = 550$  K, to ensure the reaction occurs above the surface Debye temperature of Ni(111) ( $370 \pm 5$  K<sup>(19)</sup>). Under these conditions, energy exchange with the surface phonons can be described through classical mechanics.

Initial sticking probabilities are measured for both thermal and eigen-state resolved ( $\nu_1, \nu=1$ ) CHD<sub>3</sub> molecules with translational energies,  $E_{trans}$ , ranging from  $\approx 100 - 160$  kJ/mol. Using the same CHD<sub>3</sub> conditions as experiment,

AIMD(9, 20) calculations were performed using the ab initio total-energy and molecular-dynamics program, VASP(21, 22). Forces were derived from the potential energy calculated with DFT and a specific reaction parameter (SRP(23)) functional.

## 4.2 Experimental Methods

The experiments performed at Tufts University are described below. For a more detailed description of theoretical calculations performed at Leiden Institute for Chemistry please refer to the published paper and supplemental information there within.<sup>(24)</sup>

Experiments were performed in a triply-differentially pumped supersonic molecular beam surface-scattering chamber which has been extensively described elsewhere with specific details about the apparatus found in Refs (18, 25-30). A dilute mix of 1-2% CHD<sub>3</sub> (Cambridge Isotope Laboratories, isotopic purity = 98%) in H<sub>2</sub> (99.9999%, Airgas) was continuously expanded through a roughly 25 μm diameter molecular beam nozzle source at 25 psig to form the molecular beam. Before expansion the feed gas was purified by passage through a dry-ice in acetone bath to remove condensable contaminants and sequentially passed through a Supelpure O-Trap (Supelco) which removed any remaining oxygen containing species and reactive hydrocarbons.

The nickel single crystal (Surface Preparation Laboratory) was cut and polished to 0.1° of the (111) face and housed in the ultra-high vacuum experimental chamber. The surface was cleaned by heating to 1000 K for 30 seconds to remove any carbon or hydrogen on the surface. At this temperature, carbon dissolved into the Ni bulk, and H recombinationally desorbed. Next, the surface was sputtered with 500 eV Ar<sup>+</sup> ions for 15 minutes to remove any sulfur or oxygen species. The roughened surface was then annealed to 1100 K for 45

minutes to obtain the clean Ni(111) surface as verified through auger electron spectroscopy. This cleaning procedure was performed at the beginning of each day. Between each experimental dose the Ni(111) surface was cleaned by heating the crystal to 1000 K for 5 minutes to dissolve any of the adsorbed carbon into the nickel substrate.

The experiments were carried out at a surface temperature  $T_{surf} = 550$  K. To access the high  $E_{trans}$  needed for these studies, CHD<sub>3</sub> was seeded in H<sub>2</sub>. At 550 K, any carrier gas that dissociated on the surface promptly recombined and desorbed from the surface leading to low steady-state coverages of H (ca. <0.03 ML) during CHD<sub>3</sub> exposure. To verify this assertion the  $T_{surf}$  dependence of the initial sticking probability  $S_0$  was compared for beams seeded in both H<sub>2</sub> and He carriers over a  $T_{surf}$  range of 400 - 700 K. The desorption temperature for H<sub>2</sub> on Ni(111) is between 338 and 373 K<sup>(31)</sup> but H may be present on the surface at higher temperatures under conditions that continually expose the surface to a reactive source of H<sub>2</sub>. This is in contrast to He beams where He does not accommodate to the surface and the atoms scatter non-reactively. For a 1% CH<sub>4</sub> in He beam  $S_0$  steadily decreased from 0.030 to 0.025 when  $T_{surf}$  decreased from 700 to 400 K. Two H<sub>2</sub> carrier beams (11% CH<sub>4</sub>/H<sub>2</sub>, 0.25% CH<sub>4</sub>/H<sub>2</sub>) both showed a sharp drop off in  $S_0$  when  $T_{surf}$  was dropped below 500 K. Measurements of  $S_0$  decreased from 0.07 to 0.006 over a  $T_{surf} = 500 - 400$  K range due to the emergence of hydrogen site blocking below  $T_{surf} = 500$  K. Above 500 K,  $S_0$  for CH<sub>4</sub> beams seeded in H<sub>2</sub> and He converged to nearly identical values at 550 K. This validates that any low-level steady-state coverage of H did not 1) affect the

reaction probability due to site blocking or 2) react with and lead to desorption of the methyl products of methane dissociation during the dose. Further details on these measurements and the analysis are found in Ref (32).

For CHD<sub>3</sub> doses the nozzle temperature,  $T_{nozzle}$ , was increased to temperatures between 550 - 900 ±1 K which produced molecules with  $E_{trans}$  ranging from 101-160 kJ/mol and FWHM energy distribution  $\Delta E_{trans}/E_{trans} \approx 5\%$  as measured through time-of-flight techniques. These measured values for the beams used are displayed in Table 4.1. For each of the selected  $E_{trans}$  values,  $S_0$  was determined for both laser-off,  $S_0^{Off}$ , and laser-on,  $S_0^{On}$ , conditions through King and Wells (K&W) reflectivity measurements (Section 2.4.1) by monitoring  $M/Z = 19$  amu during the experiment.

For optical excitation we pumped the CHD<sub>3</sub> molecular beam to the ( $\nu_1$ ,  $\nu=1$ ) symmetric C-H stretch via the R(1),  $\Delta K=0$  transition at 3005.538 cm<sup>-1</sup>. The infrared laser crossed the molecular beam path approximately 8 times within a multi-pass mirror setup. Each pass occurred at a slightly different angle with respect to the molecular beam path to ensure that the full Doppler shifted subset of CHD<sub>3</sub> molecules were excited.(30) The optically prepared molecules remained in the desired ro-vibrational state for the ca. 200  $\mu s$  flight time from the excitation region to the surface since the radiative lifetime of the gas phase C-H stretching state in the methane is on the order of many  $ms$ .(33) Spatially resolved Auger Electron Spectroscopy verified that the reactive flux of laser excited molecules was uniform across the Ni(111) surface. The eigen-state resolved sticking probabilities,  $S_0^{v'l}$ , reported in this paper are calculated as in Equation 4.1.

Nozzle temperature, $T_{nozzle}$ (K)	$\langle E_{trans} \rangle$ , kJ/mol	Stream velocity, $v_0$ (m/s)	Width parameter, $\alpha$ (m/s)
550	101.1	3240.00	174.31
600	112.3	3418.09	168.02
650	121.2	3547.60	191.51
700	130.7	3683.31	205.42
750	136.4	3760.72	216.91
900	160.4	4070.12	274.51

**Table 4.1** Measured CHD<sub>3</sub> translational energy and energy distributions as a function of  $T_{nozzle}$  measured through time-of-flight techniques.

$$S_0^{v_i} = \frac{S_0^{On} - S_0^{Off}}{f_{exc}} + S_0^{v=0} \quad \text{Equation 4.1}$$

The fraction of  $v_1, v=1$  excited molecules in the  $\text{CHD}_3$  molecular beam,  $f_{exc}$ , is a semi-empirically derived quantity. Due to relatively high nozzle temperatures used in this study there was significant rotational and vibrational state dilution of the ro-vibrational  $v''=0, J''=1$  ground state we excite from. While the  $\text{CHD}_3$  rotational degrees of freedom were significantly cooled during expansion through the nozzle, vibrational degrees of freedom were less affected due to the larger energy spacing between vibrational states. For  $\text{CHD}_3$  at  $T_{nozzle} = 300$  K there is minimal excited vibrational state population, with greater than 97% of the molecules existing in the  $v=0$  vibrational ground state. Significant vibrational state dilution of the  $\text{CHD}_3$  ground state occurs at a lower  $T_{nozzle}$  compared to  $\text{CH}_4$  due to the lower frequency normal modes in  $\text{CHD}_3$ . At the highest  $T_{nozzle} = 900$  K used in these experiments more than 63% of the molecules were thermally excited and only 37% remained in the  $v=0$  ground state. Rotational cooling is much more efficient, but is also limited to the highest values of  $T_{nozzle}$ . Details of our corrections for the ground rotational State Population appears in the supplemental information of Ref. (24). Combining these estimates of initial state population with our measurements of the extent of optical saturation of the pumping transition resulted in  $f_{exc}$  values ranging from 2-6% for the beam conditions used in this study.

Values of  $f_{exc}$  are limited by the fraction of molecules in the correct initial vibrational,  $f_{vib}$ , and rotational,  $f_{rot}$ , states along with the degree of optical saturation of the IR transition in the beam,  $f_{sat}$ , as demonstrated in Equation 4.2.

$$f_{exc} = f_{vib} \times f_{rot} \times f_{sat} \quad \text{Equation 4.2}$$

The procedure for determining  $f_{vib}$  and  $f_{rot}$  were reproduced from previous work performed by Killelea(31) with the general procedure outlined in Section 2.5.3 but will be briefly described below.

CHD<sub>3</sub> is an oblate symmetric top with  $C_{3v}$  symmetry and character table shown in Table 4.2. The methane molecules were pumped from the  $v = 0 \rightarrow 1$  vibrational state and  $J = 1 \rightarrow 2$  rotational state, therefore, the total number of available molecules for excitation are those molecules residing in the  $v''=0$  and  $J''=1$  states. The vibrational energy,  $E_{vib}$ , distribution was calculated for the six normal modes of CHD<sub>3</sub> (listed in Table 2.3), and all overtone combinations states, under each set of beam conditions as set by the vibrational temperature,  $T_{vib}$ . Since there was minimal vibrational cooling during expansion we define  $T_{vib} = T_{nozzle}$ . We verified that our thermocouple reading from the nozzle was representative of the gas temperature through time-of-flight measurements of a pure He molecular beam. Since He behaves like an ideal gas and does not possess any rotational or vibrational levels, its heat capacity is well defined, and its velocity can be predicted from  $T_{nozzle}$ .(34) The measured He velocities were within 2% of the predicted values, making us confident in our assumption that  $T_{vib} = T_{nozzle}$ .

Two quantum numbers describe the rotational state of CHD<sub>3</sub>: the rotational quantum number, J, and its projection onto the C<sub>3v</sub> molecular symmetry axis, K. Since CHD<sub>3</sub> is an oblate symmetric top, the symmetry axis is the c-axis (the inertial axis with the highest moment of inertia). The inertia constants of the a and b axis are identical. The energy of each J,K state,  $E_{J,K}$ , is calculated using Equation 4.3 with the constants in Table 4.3.(35)

$$E_{J,K} = B_0J(J + 1) + (C_0 - B_0)K^2 - D_JJ^2(J + 1)^2 - D_{JK}J(J + 1)K^2 - D_KK^4$$

Equation 4.3

CHD<sub>3</sub> has (2J+1)-fold space degeneracy but lacks the (2J+1) K-state degeneracy found in CH<sub>4</sub> due to the reduced symmetry of the C<sub>3v</sub> versus T<sub>d</sub> point group. Nuclear spin statistics are simpler for CHD<sub>3</sub> due to the presence of only two symmetry species, A and E. Their statistical weights are 11:8, respectively, as calculated with their spin weight,  $\epsilon_I$ , and number of levels,  $n_I$ , displayed in Table 4.4. Rotational cooling of CHD<sub>3</sub> preserves the nuclear spin state, and was presumed to be similar to the group's prior measurements in CH<sub>4</sub> molecular beams(31), which showed a linear relationship between  $T_{nozzle}$  and the rotational temperature,  $T_{rot}$ :

$$T_{rot} = 0.0247 \times T_{nozzle} \quad \text{Equation 4.4}$$

$C_{3v}$	E	$2C_3$	$3\sigma_v$	
$A_1$	1	1	1	$T_z$
$A_2$	1	1	-1	$R_z$
E	2	-1	0	$(T_x, T_y); (R_x, R_y)$

**Table 4.2**  $C_{3v}$  character table

Rotational Constant	Energy, $\text{cm}^{-1}$
$B_0$	3.27916
$C_0$	2.62896
$D_{0,J}$	4.945E-5
$D_{0,JK}$	-3.83E-5
$D_{0,K}$	1.38E-5

**Table 4.3** Rotational Constants for  $\text{CHD}_3$

Symmetry Species, $\Gamma$	Spin Weight, $\epsilon_{\Gamma}$	Number of Levels, $\eta_{\Gamma}$	$K$ state
A	$\frac{1}{3}(2I + 1)(4I^2 + 4I + 3)$	$\frac{2}{3}\left[1 + 2\cos\left(\frac{2\pi K}{3}\right)\right] : K \neq 0$ $K=0; \eta_{\Gamma}=1$	$K = 3n$
E	$\frac{8}{3}I(I + 1)(2I + 1)$	$\frac{2}{3}\left[1 - \cos\left(\frac{2\pi K}{3}\right)\right]$	$K = 3n \pm 1$

**Table 4.4** Equations for calculating the spin weights for the different symmetry species of CHD<sub>3</sub> and their associated  $K$  values.

The fraction of molecules in the  $J''=1, K''=0$  rotational state was calculated from the rotational state distribution at each  $T_{rot}$  value leading to approximately 14% of the  $\text{CHD}_3$  molecular beam being in the correct rotational state.

The last aspect of calculating  $f_{exc}$  involves the fraction of molecules that are saturated by the incident infrared beam,  $f_{sat}$ . We measured the power dependence saturation curve using the pyroelectric bolometer and found that saturation of the transition occurs at power  $P < 0.5$  W. This made us confident that the power available for experiments,  $P \approx 1$  W, was sufficient to achieve total saturation of the available molecules within the  $\text{CHD}_3$  beam. Furthermore, the use of linearly polarized light as the excitation source limited the total number of molecules that were excited to 50%, leading to  $f_{sat} = 0.50$ . Values of  $f_{vib(v=0)}$ ,  $T_{rot}$ ,  $f_{rot}$ , and the resulting  $f_{exc}$  used in the calculation of  $S_0^{v,l}$  are displayed in Table 4.5 and the effect of increasing  $T_n$  on  $f_{v=0}$ ,  $f_{rot}$ , and  $f_{exc}$  are shown graphically in Figure 4.1.

As mentioned above, knowing the ground state sticking probability,  $S_0^{v=0}$ , was necessary to compute the state resolved sticking probability,  $S_0^{v,l}$ , shown in Equation 4.1. A direct measurement of  $S_0^{v=0}$  was not possible at the experimental used  $E_{trans}$  values due to the high levels of vibrational population. Thermally populated vibrations increase the reactivity of the incident  $\text{CHD}_3$  molecules leading to  $S_0^{Off} > S_0^{v=0}$ . For the purpose of reported values appearing in the published paper(24) and here,  $S_0^{Off}$  was taken to be equivalent to  $S_0^{v=0}$ , but in actuality it represents the upper limit of  $S_0^{v=0}$ . Several different ways to obtain

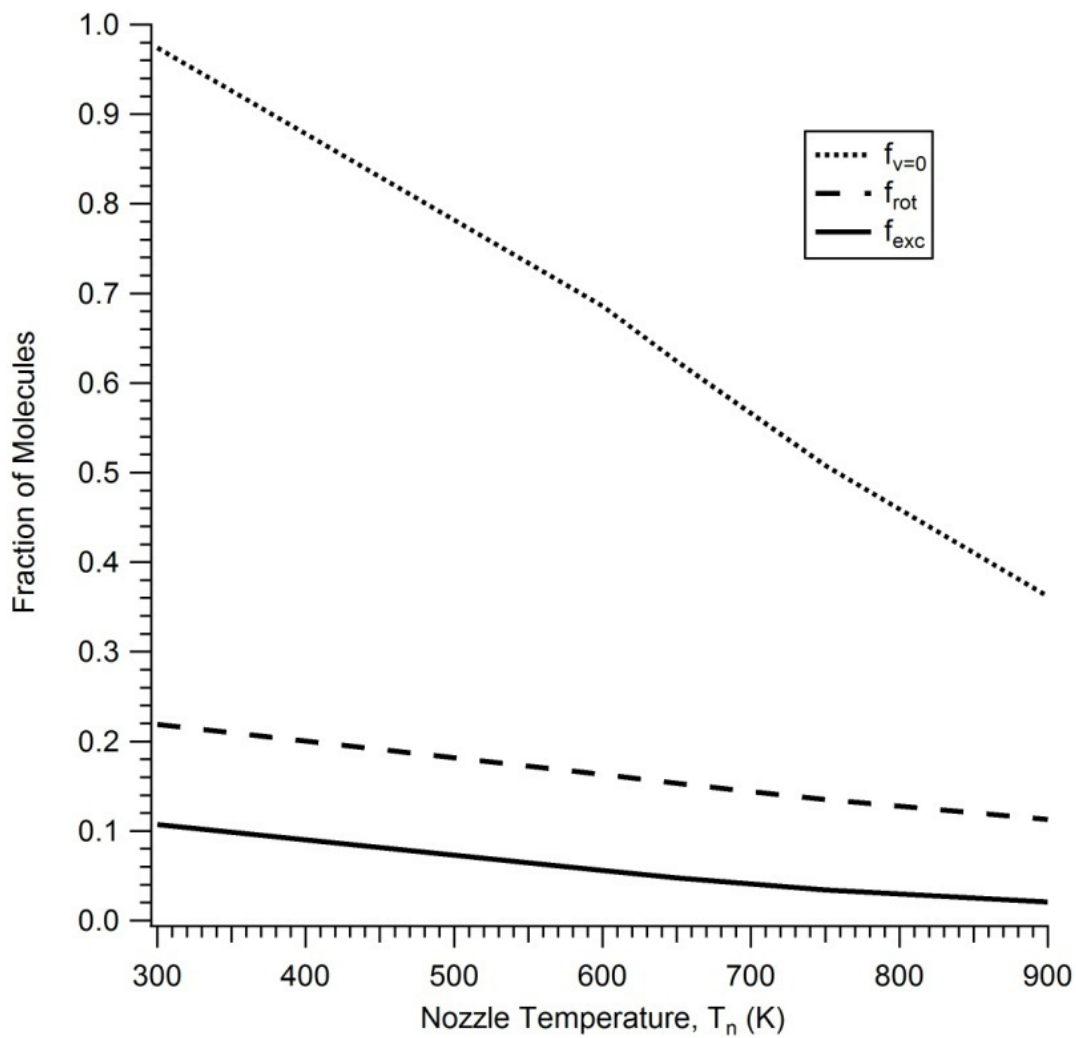


**Figure 4.1** Calculated fraction of  $\text{CHD}_3$  molecules in the  $v=0$  ground vibrational state,  $f_{v=0}$ , in the  $J=1$  rotational state,  $f_{rot}$ , and the resulting total number of molecules excited through laser absorption,  $f_{exc}$ .

$T_{nozzle}, \text{K}$	$f_{v=0}$	$T_{rot}, \text{K}$	$f_{rot}$	$f_{exc}$
300	0.974	7.4	0.219	0.107
600	0.686	14.8	0.163	0.0559
650	0.624	16.0	0.153	0.0477
700	0.566	17.3	0.144	0.0408
750	0.508	18.5	0.135	0.0343
900	0.362	22.2	0.113	0.0205

**Table 4.5** Calculated fraction of  $\text{CHD}_3$  molecules in the  $v=0$  vibrational ground state,  $f_{v=0}$ , rotational temperature,  $T_{rot}$ , fraction of molecules in the  $J=1$  rotational state,  $f_{rot}$ , and the resulting fraction of molecules excited by infrared absorption,  $f_{exc}$ , at the nozzle temperatures used in these experiments. The values for  $T_{nozzle} = 300 \text{ K}$  are included for comparison.

more accurate approximations of  $S_0^{v=0}$  were explored to ensure our reported values were not overly inflated by this assumption. Both of these methods involved using AIMD calculated values for  $S_0^{v=0}$  but to different degrees. In the first method,  $S_0^{v=0}$  values were calculated by multiplying the experimentally measured  $S_0^{Off}$  values by the AIMD computed ratio of  $S_0^{v=0} / S_0^{Off}$ . The reliance on AIMD values for this calculation requires the assumption that the calculations accurately capture the increased reactivity from the thermally populated  $\text{CHD}_3$  molecules. Alternatively, the  $S_0^{v=0}$  AIMD computed values were used in the calculation of  $S_0^{v1}$  with the experimentally measured  $S_0^{Off}$  and  $S_0^{On}$  values. These two latter methods produced similar results as taking  $S_0^{Off} = S_0^{v=0}$ , as stated above, and proved to fall within the error of replicate measurements of  $S_0^{Off}$  and  $S_0^{On}$ . In this way we were confident that our estimates of  $S_0^{v=0}$  were not significantly biasing our state-resolved  $S_0^{v1}$ .

Nattino et. al. performed the initial sticking probability calculations for  $S_0^{Off}$ ,  $S_0^{v1}$ , and  $S_0^{v=0}$  using AIMD simulations.(9, 20) The ab initio total-energy and molecular dynamics program VASP(21, 22) was used to calculate the forces with density functional theory (DFT) using a specific reaction parameter (SRP)(23, 36) functional. This functional is an adjustable exchange-correlation function which takes a weighted sum of two different functionals, PBE(37) and RPBE(38), with the mixing determined by iterative fitting of the experimental data. The overall functional,  $E_{xc}$ , is displayed in Equation 4.5. The last term,  $E_c^{vdW-DF}$ , is an additional term that describes the van der Waals forces present in the system.

$$E_{xc} = xE_X^{RPBE} + (1 - x)E_X^{PBE} + E_C^{vdW-DF} \quad \text{Equation 4.5}$$

The mixing parameter,  $x$ , was determined by fitting the first three points of the  $S_0^{Off}$  ( $E_{trans} = 101-121$  kJ/mol) sticking curve. At these energies the ground state population is dominated by  $v=0$  molecules, which should make the quasi-classical description valid. This led to an optimized mixing parameter of  $x = 0.32$ .

### 4.3 Results and Discussion

Initial sticking probability measurements were performed for both  $S_0^{Off}$  and  $S_0^{On}$  in triplicate and are summarized in Table 4.6. The reported error is derived from the replicate measurements for  $S_0^{Off}$  and the upper bound of  $S_0^{v1}$ . Since  $S_0^{v=0}$  is approximated to be equivalent to  $S_0^{Off}$  in the calculation of  $S_0^{v1}$  we expanded the lower bound of the error reported for  $S_0^{v1}$  to include the difference in the AIMD calculated value for  $S_0^{v=0}$  and the experimental value for  $S_0^{Off}$ . We are confident that this captures the error introduced with this assumption because  $S_0^{Off}$  represents an upper limit on  $S_0^{v=0}$  whereas the AIMD calculated value represents a lower limit.

The measured sticking values for both  $S_0^{Off}$  and  $S_0^{v1}$  increase smoothly over the  $E_{trans}$  range investigated and shows evidence of approaching an asymptote in reactivity at  $E_{trans} = 160$  kJ/mol. These data are presented in Figure 4.2 along with results at lower  $E_{trans}$  collected by Killelea(31) in 2007. The data by Killelea are over a strikingly similar  $T_{nozzle}$  range but used He as the carrier gas, leading to an overall slower  $CHD_3$  molecular beam in the 53 - 88 kJ/mol  $E_{trans}$  range. The detection method used by Killelea was bulk H/D titration with the surface temperature held at 90 K, well below the 550 K used in this study. Despite these differences the transition between the two data sets appears to be smooth with no large discontinuities. A major difference arises in how much the added quanta of the  $\nu_1$  vibration contributed to measured reactivity. Killelea observed that the added quanta enhanced reactivity by greater than 10-fold for the two

$E_{trans}$ , kJ/mol	$S_0^{Off}$	$S_0^{v1}$	$S_0^{Off}$ Error $2\sigma$	$S_0^{v1}$ Error* $2\sigma$
101.1	1.22E-02	-	6.70E-04	-
112.3	2.59E-02	9.90E-02	1.43E-04	1.09E-2 : 1.38E-2
121.2	4.55E-02	1.43E-01	7.76E-04	2.17E-2 : 2.89E-2
130.7	6.63E-02	1.96E-01	1.81E-03	4.88E-2 : 6.03E-2
136.4	9.71E-02	2.45E-01	2.13E-03	7.07E-2 : 7.23E-2
160.4	1.99E-04	4.42E-01	3.16E-03	2.06E-1 : 2.68E-1

\*The error for  $S_0^{v1}$  is reported for both the upper (first number in column) and lower bounds.

**Table 4.6** Measured initial sticking probabilities for  $\text{CHD}_3$  on Ni(111) at  $T_{surf}$  = 550 K. The error reported is  $2\sigma$  with explanation of how the error was calculated explained in the text.

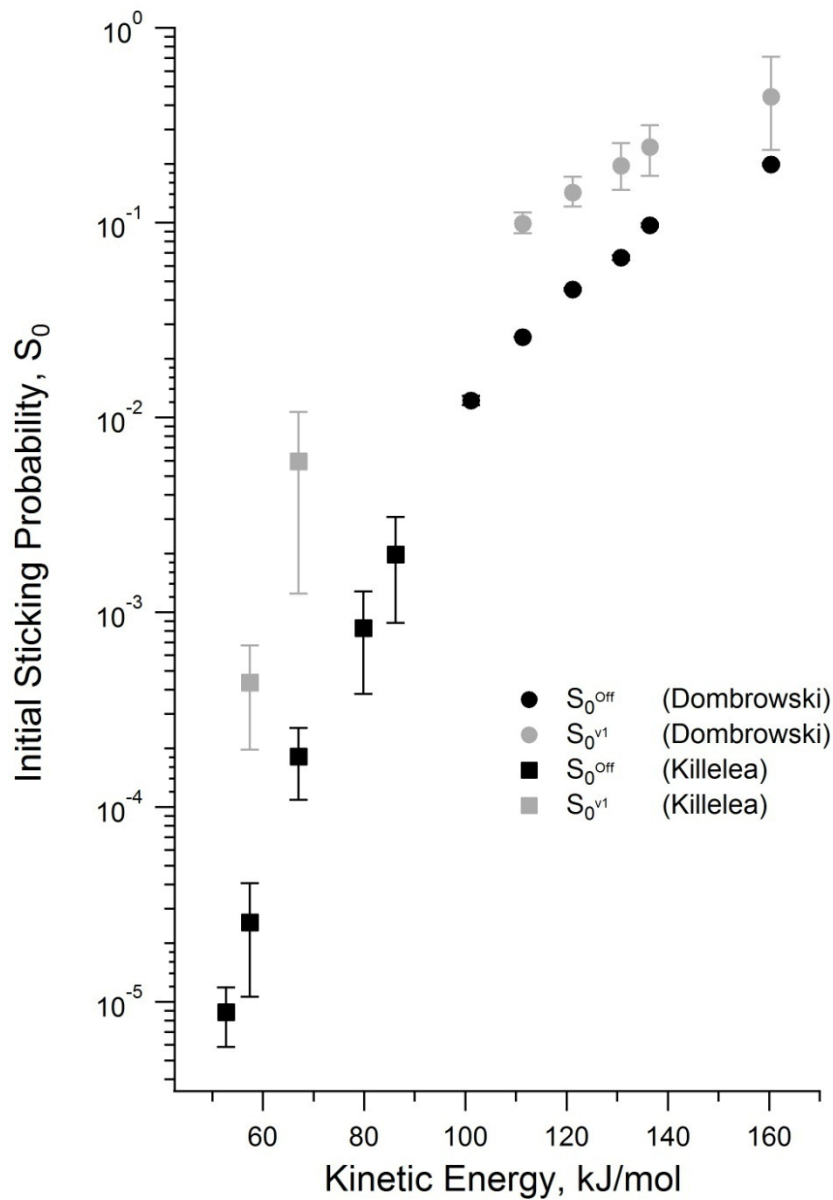


**Figure 4.2** Initial Sticking probability curves for  $\text{CHD}_3$  on Ni(111) for laser-off,  $S_0^{off}$ , and  $v_1 v=1$  state-resolved,  $S_0^{v1}$ , molecules. The squares are previous values recorded by Killelea and the circles are the data collected in this study as displayed in Table 4.6. Both data sets include  $2\sigma$  error bars.

kinetic energies where state resolved data was collected, while at the higher energy regime, reported here, enhancement due to the added  $\nu_1$  quanta was only 2-4 fold, decreasing with increasing  $E_{trans}$ . This is consistent with the location of the chemisorption barrier at approximately 97 kJ/mol.(39) Since the molecules are prepared with 36 kJ/mol of vibrational energy and at the lowest  $E_{trans} = 101$  kJ/mol that gives the molecules an average internal energy of 137 kJ/mol to overcome the chemisorption barrier. This excess in internal energy increases the number of favorable approach geometries and gives less preference for the added quanta of stretch vibration to enhance reactivity. Based on previous measurements for CH<sub>4</sub> reactivity on Ni(111)(32) at  $T_{surf} = 90 - 550$  K it is reasonable to assume that the sticking probability curve for CHD<sub>3</sub> at  $T_{surf} = 550$  K would diverge from the  $T_{surf} = 90$  K data collected by Killelea at lower  $E_{trans}$  values.

Figure 4.3 shows the same sticking probability curve as Figure 4.2 without the data from Killelea but includes the calculated sticking probability values generated by Nattino et al.(24) Additionally, the experimental data is fit to a generalized logistic, LGS, function displayed in Equation 4.6 where  $S_0(E_{trans})$  is the translational dependent initial sticking probability,  $A$  is the asymptotic reactivity,  $W$  is width of the transition,  $E_0$  is the inflection point of the reaction curve, and  $\nu$  describes the symmetry of the curve. The parameters used to fit the experimental determined  $S_0^{Off}$  and  $S_0^{vI}$  values for Equation 4.6 are compiled in Table 4.7.

$$S_0(E_{trans}) = A \div \left[ 1 + \nu \exp \left( -\frac{(E_{trans} - E_0)}{W} \right) \right]^{\frac{1}{\nu}} \quad \text{Equation 4.6}$$

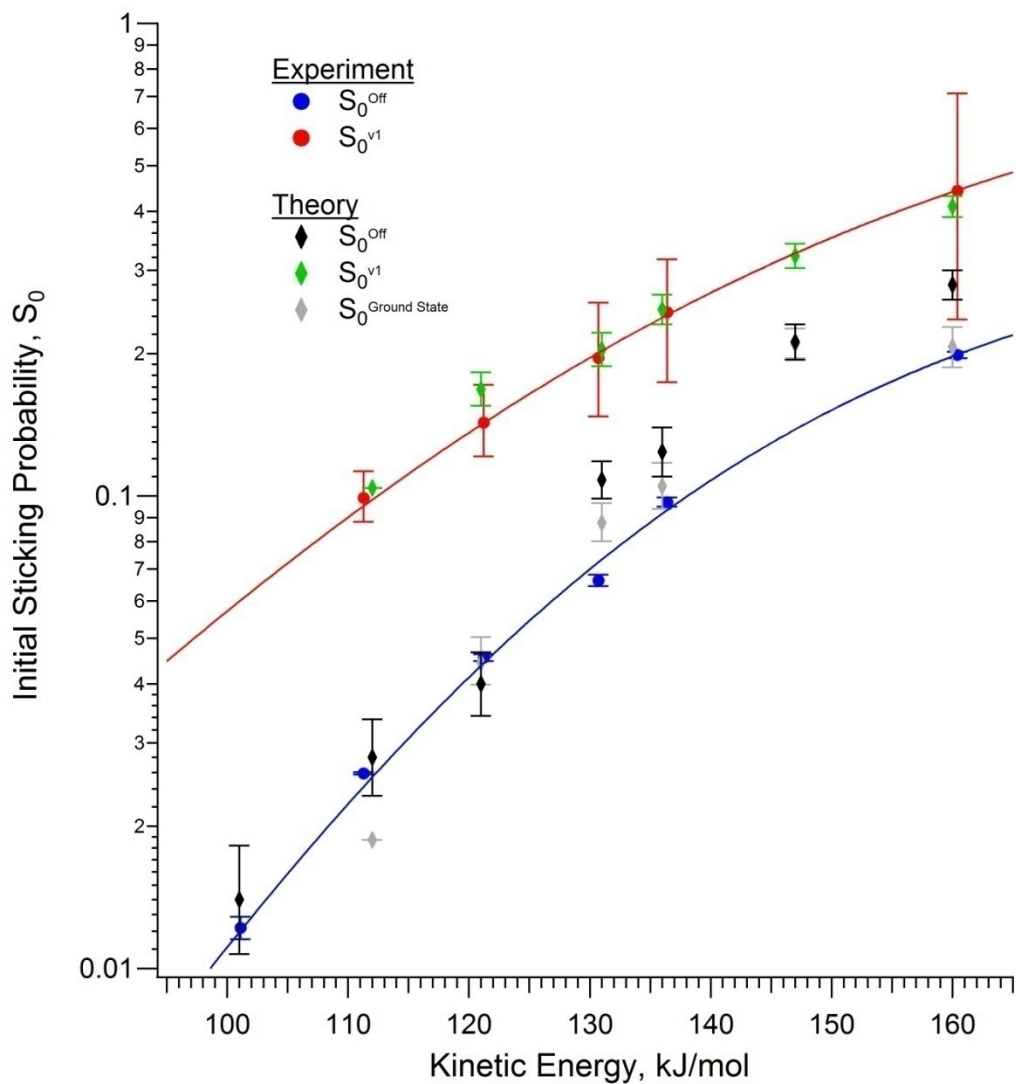


**Figure 4.3** Measured and AIMD calculated sticking probability curves for  $\text{CHD}_3$  on Ni(111). The error associated with theoretical values is expressed as  $1\sigma$ . The best fit lines are described by Equation 4.6 with the parameters outlined in Table 4.7.

Parameter	$S_0^{Off}$	$S_0^{v1}$
A	0.380	1.000
$E_0$ (kJ/mol)	152.7	159.6
W (kJ/mol)	25.5	34.2
$\nu$	0.407	0.437

**Table 4.7** Fitting parameters in Equation 4.6 used to fit experimental data in Figure 4.3.

There is excellent agreement between the measured and calculated values. This agreement is best for  $S_0^{v1}$  excited molecules and the first several  $S_0^{Off}$  points. The agreement is expected to be best for  $S_0^{Off}$  at lower  $E_{trans}$  because the SRP functional was constrained to those points. These points also represent the lowest nozzle temperatures used in the study where assumptions of  $f_{exc}$  were least impactful. At the higher  $E_{trans}$  values ( $T_n = 700 - 900$  K) the degree of thermally populated molecules increases rapidly. Properly modeling the energy contributions of thermally excited C-D bending vibrations within a classical mechanics model likely leads to the discrepancy between calculated and measured values of  $S_0^{Off}$ . The agreement with  $S_0^{v1}$  represents no more than a 4.5 kJ/mol shift, with an average of a 2.2 kJ/mol energy shift from experimental values. Since the reactivity of only a single vibrational mode ( $v_1, v=1$ ) was calculated there are fewer assumptions about the reactivity of the various thermally populated states present in  $S_0^{Off}$ , leading to a more accurate calculation of  $S_0^{vi}$ .

Nattino further validated the use of the weighted SRP functional by assessing the energy shift noted above for  $S_0^{v1}$ . Since four out of the five data points fall within 4.2 kJ/mol (1 kcal/mol) of the experimental values, and motivated by the classical hole model(36), the calculations describe experiment within chemical accuracy ( $\leq 1$  kcal/mol). Furthermore, Stouffer's Z-score test(40) was applied to the data to test whether the computed  $S_0^{v1}$  values are equal to the measured values. This test led to a value of  $p = 0.47$ , where any value less than 0.05 would be rejected.

Obtaining such close agreement between experimental and calculated values substantiates our treatment of the numerous degrees of freedom that impact reactivity. The accuracy in absolute barrier heights substantiates the SRP functional and the PES as derived from the converged DFT calculations. In future studies this approach can be applied and used to benchmark new electronic structure methods.

Another benefit of performing the calculations using AIMD methods is the ability to discern exactly where the reactive encounters of CHD<sub>3</sub> on the Ni(111) surface occur and contrast that to other low index metal surfaces. The reactive encounter distribution on Ni(111) was assessed for molecules possessing  $E_{trans} = 112$  kJ/mol ( $S_0 = 0.03$ ) and showed there was little preference for a single reaction site. In contrast, in the distribution observed for CHD<sub>3</sub> on Pt(111) a vast majority of the dissociative events occurred over the on-top site(9) for similar  $S_0$  at lower  $E_{trans} = 75$  kJ/mol. See Figure S13 found in the supplemental information of Ref. (24). This is an important factor to consider when treating the dynamical factors as the CHD<sub>3</sub> approaches the surface. The azimuthal  $\phi$ -rotation of the molecule with respect to the surface has been shown to have little impact for CH<sub>4</sub> dissociation on the on-top site of a host of metal surfaces.(39) Recently Shen et al. used a quantum dynamical model to describe CH<sub>4</sub> reactivity on Ni(111) and observed a strong dependence on both the impact site and the azimuthal  $\phi$  angle.(41)

## 4.4 Conclusion and Future Directions

The laser-off and state-resolved ( $v_1, v=1$ ) reactivity of  $\text{CHD}_3$  on Ni(111) was measured over the  $E_{\text{trans}} = 101 - 160$  kJ/mol regime at a constant surface temperature  $T_{\text{surf}} = 550$  K. The added quanta of C-H stretching vibration enhanced reactivity across the entire sticking curve and compared favorably to previous measurements for  $\text{CHD}_3$  reactivity on Ni(111).<sup>(31)</sup> The beam energies and surface temperature were chosen to ensure that molecules reacted through an "over-the-barrier" process with excess energy in the reaction coordinate, and the surface phonons behaved classically.

The experimental values were used in benchmark calculations performed by Nattino et al.<sup>(24)</sup> The SRP approach to DFT with an empirically derived mixing coefficient was coupled with AIMD to produce a quantitative and chemically accurate description of a polyatomic molecule reacting with a metal surface. The dynamical information obtained for this specific polyatomic molecule-surface reaction can be extended to future studies for the chemisorption of more complex gaseous reagents on metal surfaces. A recent publication by Migliorini et al. looks at the  $\text{CHD}_3 / \text{Pt}(111)$  and stepped Pt(211) systems using the same DFT derived potential, SRP functional, and mixing parameter to compare with experimentally measured sticking probabilities.<sup>(42)</sup> This is further validation that this method can be extended to other systems. Future work will continue to use this same approach for methane and its isotopologues on various crystalline metal surfaces to test how these dynamical factors transfer to similar systems. Due to the relative ease of collecting data in this high  $S_0$  regime through

K&W reflectivity modulation techniques recently developed and discussed in section 2.5.3., it would be advantageous to perform these experiments on the iridium single crystals and stepped nickel surfaces our group is currently interested in.

## 4.5 References

1. D. C. Clary, Quantum Dynamics of Chemical Reactions. *Science* **321**, 789-791 (2008).
2. M. Qiu, Z. Ren, L. Che, D. Dai, S. A. Harich, X. Wang, X. Yang, C. Xu, D. Xie, M. Gustafsson, R. T. Skodje, Z. Sun, D. H. Zhang, Observation of Feshbach Resonances in the  $F + H_2 \rightarrow HF + H$  Reaction. *Science* **311**, 1440-1443 (2006).
3. J. P. Perdew, A. Ruzsinszky, G. I. Csonka, O. A. Vydrov, G. E. Scuseria, L. A. Constantin, X. Zhou, K. Burke, Restoring the Density-Gradient Expansion for Exchange in Solids and Surfaces. *Physical Review Letters* **100**, 136406 (2008).
4. C. Filippi, S. B. Healy, P. Kratzer, E. Pehlke, M. Scheffler, Quantum Monte Carlo Calculations of  $\{\mathrm{H}\}_2$  Dissociation on Si(001). *Physical Review Letters* **89**, 166102 (2002).
5. F. Libisch, C. Huang, P. Liao, M. Pavone, E. A. Carter, Origin of the Energy Barrier to Chemical Reactions of  $\{\mathrm{O}\}_2$  on Al(111): Evidence for Charge Transfer, Not Spin Selection. *Physical Review Letters* **109**, 198303 (2012).
6. P. M. Hundt, B. Jiang, M. E. van Reijzen, H. Guo, R. D. Beck, Vibrationally Promoted Dissociation of Water on Ni(111). *Science* **344**, 504-507 (2014).
7. A. K. Tiwari, S. Nave, B. Jackson, Methane Dissociation on Ni(111): A New Understanding of the Lattice Effect. *Physical Review Letters* **103**, 253201 (2009).
8. B. Jiang, R. Liu, J. Li, D. Xie, M. Yang, H. Guo, Mode selectivity in methane dissociative chemisorption on Ni(111). *Chemical Science* **4**, 3249-3254 (2013).
9. F. Nattino, H. Ueta, H. Chadwick, M. E. van Reijzen, R. D. Beck, B. Jackson, M. C. van Hemert, G.-J. Kroes, Ab Initio Molecular Dynamics Calculations versus Quantum-State-Resolved Experiments on  $CHD_3 + Pt(111)$ : New Insights into a Prototypical Gas-Surface Reaction. *The Journal of Physical Chemistry Letters* **5**, 1294-1299 (2014).
10. V. L. Campbell, N. Chen, H. Guo, B. Jackson, A. L. Utz, Substrate Vibrations as Promoters of Chemical Reactivity on Metal Surfaces. *The Journal of Physical Chemistry A* **119**, 12434-12441 (2015).
11. S. Nave, A. K. Tiwari, B. Jackson, Dissociative Chemisorption of Methane on Ni and Pt Surfaces: Mode-Specific Chemistry and the Effects of Lattice Motion. *The Journal of Physical Chemistry A* **118**, 9615-9631 (2014).
12. X. Shen, J. Chen, Z. Zhang, K. Shao, D. H. Zhang, Methane dissociation on Ni(111): A fifteen-dimensional potential energy surface using neural network method. *The Journal of Chemical Physics* **143**, 144701 (2015).
13. B. Jiang, M. Yang, D. Xie, H. Guo, Quantum dynamics of polyatomic dissociative chemisorption on transition metal surfaces: mode specificity and bond selectivity. *Chemical Society Reviews* **45**, 3621-3640 (2016).
14. G.-J. Kroes, Toward a Database of Chemically Accurate Barrier Heights for Reactions of Molecules with Metal Surfaces. *The Journal of Physical Chemistry Letters* **6**, 4106-4114 (2015).

15. R. Peverati, D. G. Truhlar, Quest for a universal density functional: the accuracy of density functionals across a broad spectrum of databases in chemistry and physics. *Philosophical Transactions of the Royal Society A* **372**, (2014).
16. A. C. Luntz, J. Harris, CH<sub>4</sub> dissociation on metals: a quantum dynamics model. *Surface Science* **258**, 397-426 (1991).
17. G. Jones, J. G. Jakobsen, S. S. Shim, J. Kleis, M. P. Andersson, J. Rossmeisl, F. Abild-Pedersen, T. Bligaard, S. Helveg, B. Hinnemann, J. R. Rostrup-Nielsen, I. Chorkendorff, J. Sehested, J. K. Nørskov, First principles calculations and experimental insight into methane steam reforming over transition metal catalysts. *Journal of Catalysis* **259**, 147-160 (2008).
18. D. R. Killelea, V. L. Campbell, N. S. Shuman, A. L. Utz, Bond-Selective Control of a Heterogeneously Catalyzed Reaction. *Science* **319**, 790-793 (2008).
19. A. Krupski, Debye temperature of the Pb layers on Ni(111). *physica status solidi (b)* **243**, 467-472 (2006).
20. A. Groß, A. Dianat, Hydrogen Dissociation Dynamics on Precovered Pd Surfaces: Langmuir is Still Right. *Physical Review Letters* **98**, 206107 (2007).
21. G. Kresse, J. Furthmüller, Efficient iterative schemes for ab initio total-energy calculations using a plane-wave basis set. *Physical Review B* **54**, 11169-11186 (1996).
22. G. Kresse, D. Joubert, From ultrasoft pseudopotentials to the projector augmented-wave method. *Physical Review B* **59**, 1758-1775 (1999).
23. Y.-Y. Chuang, M. L. Radhakrishnan, P. L. Fast, C. J. Cramer, D. G. Truhlar, Direct Dynamics for Free Radical Kinetics in Solution: Solvent Effect on the Rate Constant for the Reaction of Methanol with Atomic Hydrogen. *The Journal of Physical Chemistry A* **103**, 4893-4909 (1999).
24. F. Nattino, D. Migliorini, G.-J. Kroes, E. Dombrowski, E. A. High, D. R. Killelea, A. L. Utz, Chemically Accurate Simulation of a Polyatomic Molecule-Metal Surface Reaction. *The Journal of Physical Chemistry Letters* **7**, 2402-2406 (2016).
25. L. B. F. Juurlink, D. R. Killelea, A. L. Utz, State-resolved probes of methane dissociation dynamics. *Progress in Surface Science* **84**, 69-134 (2009).
26. R. R. Smith, D. R. Killelea, D. F. DelSesto, A. L. Utz, Preference for Vibrational over Translational Energy in a Gas-Surface Reaction. *Science* **304**, 992-995 (2004).
27. R. D. Beck, A. L. Utz, in *Dynamics of Gas-Surface Interactions: Atomic-level Understanding of Scattering Processes at Surfaces*, R. Díez Muiño, Ed. (Springer, Berlin, Heidelberg, 2013), pp. 179-212.
28. L. B. F. Juurlink, P. R. McCabe, R. R. Smith, C. L. DiCologero, A. L. Utz, Eigenstate-Resolved Studies of Gas-Surface Reactivity: CH<sub>4</sub>(v<sub>3</sub>) Dissociation on Ni(100). *Physical Review Letters* **83**, 868-871 (1999).
29. P. R. McCabe, L. B. F. Juurlink, A. L. Utz, A molecular beam apparatus for eigenstate-resolved studies of gas-surface reactivity. *Review of Scientific Instruments* **71**, 42-53 (2000).
30. L. B. F. Juurlink, R. R. Smith, A. L. Utz, Controlling Surface Chemistry with Light: Spatially Resolved Deposition of Rovibrational-State-Selected Molecules. *The Journal of Physical Chemistry B* **104**, 3327-3336 (2000).

31. D. R. Killelea, PhD Thesis, Bond-Selective Control of a Gas-Surface Reaction, *Tufts University* (2007).
32. V. L. Campbell, PhD Thesis, State Resolved Measurement of Surface Temperature Dependence and Isotopically Selective Reactivity of Methane on Ni(111), *Tufts University* (2011).
33. P. Hess, C. B. Moore, Vibrational energy transfer in methane and methane-rare-gas mixtures. *The Journal of Chemical Physics* **65**, 2339-2344 (1976).
34. D. K. Bronnikov, D. V. Kalinin, V. D. Rusanov, Y. G. Filimonov, Y. G. Selivanov, J. C. Hilico, Spectroscopy and non-equilibrium distribution of vibrationally excited methane in a supersonic jet. *Journal of Quantitative Spectroscopy and Radiative Transfer* **60**, 1053-1068 (1998).
35. M. Lewerenz, M. Quack, Vibrational spectrum and potential energy surface of the CH chromophore in CHD<sub>3</sub>. *The Journal of Chemical Physics* **88**, 5408-5432 (1988).
36. C. Díaz, E. Pijper, R. A. Olsen, H. F. Busnengo, D. J. Auerbach, G. J. Kroes, Chemically Accurate Simulation of a Prototypical Surface Reaction: H<sub>2</sub> Dissociation on Cu(111). *Science* **326**, 832-834 (2009).
37. J. P. Perdew, K. Burke, M. Ernzerhof, Generalized Gradient Approximation Made Simple. *Physical Review Letters* **77**, 3865-3868 (1996).
38. B. Hammer, L. B. Hansen, J. K. Nørskov, Improved adsorption energetics within density-functional theory using revised Perdew-Burke-Ernzerhof functionals. *Physical Review B* **59**, 7413-7421 (1999).
39. S. Nave, A. K. Tiwari, B. Jackson, Methane dissociation and adsorption on Ni(111), Pt(111), Ni(100), Pt(100), and Pt(110)-(1×2): Energetic study. *The Journal of Chemical Physics* **132**, 054705 (2010).
40. S. A. S. Stouffer, E. A.; DeVinney, L. C.; Star, S. A.; William, R. M. Jr, *Studies in Social Psychology in World War II. Vol. I: The American Soldier: Adjustment During Army Life.* (Princeton University Press, Princeton, NJ, 1949).
41. X. Shen, Z. Zhang, D. H. Zhang, Communication: Methane dissociation on Ni(111) surface: Importance of azimuth and surface impact site. *The Journal of Chemical Physics* **144**, 101101 (2016).
42. D. Migliorini, H. Chadwick, F. Nattino, A. Gutiérrez-González, E. Dombrowski, E. A. High, H. Guo, A. L. Utz, B. Jackson, R. D. Beck, G.-J. Kroes, Surface Reaction Barriometry: Methane Dissociation on Flat and Stepped Transition-Metal Surfaces. *The Journal of Physical Chemistry Letters* **8**, 4177-4182 (2017).



# Chapter 5 : State-resolved reactivity ( $v_3, v=1$ ) of $\text{CH}_4$ on Ni(111) at elevated surface temperatures

## 5.1 Introduction

The dissociative chemisorption of methane on low index catalytically active metal surfaces has been scrutinized by experimental and theoretical studies over recent decades(1-5) for its role in the industrially relevant steam reforming of methane to produce hydrogen. Recent interest in the adsorption kinetics of methane on nickel also stems from the favorable conditions that exist for graphene growth.(6-10) The rate limiting(11) initial C-H bond cleavage is highly activated, and satisfactory reaction kinetics require elevated pressures and temperatures in excess of 900 K within reactors.(12, 13) Thermal activation for this reaction is driven by increased methane translation, vibrational and rotational populations, and surface phonon population.(14) Separating how the molecular and surface degrees of freedom that govern the complicated potential energy surface for dissociation on surfaces remains a major goal for surface scientists.

Supersonic molecular beam techniques measure methane's initial sticking probability on a clean surface,  $S_0$ , as a function of translational energy,  $E_{trans}$ , dependence for  $S_0$ . A direct dissociative mechanism ( $\log S_0 \propto E_{trans}$ ) dominates at high  $E_{trans}$ (15) on a range of low-index transition metal surfaces, and a precursor-

mediated mechanism ( $S_0 \propto \frac{1}{E_T}$ ) prevails at low  $E_{trans}$  on iridium(16-18) and platinum(19) surfaces, with no evidence of a precursor mechanism yet observed on nickel surfaces.

State-resolved studies coupling molecular beam techniques with direct infrared laser excitation of incident methane reagents permits quantification of state-resolved reaction probabilities,  $S_0^{vi}$ , for individual methane ro vibrational states. Methane dissociation has proven to be vibrational-mode specific.(20-23) Vibrational modes with similar energies activate dissociation to varying degrees, in some cases more than  $E_{trans}$ . The efficacy of individual vibrational modes is dependent on the chemical identity and the face of the low index surfaces studied. Efficacies on the (111) face of Ni, Pt, and Ir single crystals for the  $\nu_3, \nu=1$  C-H stretch vibration are measured as 1.25(20), 0.71(24), and 0.43(18), respectively, in accordance with the calculated C-H bond distance at the transition state.(25, 26) The efficacy for the same vibration is less,  $\eta(\nu_3) \approx 1$ , on Ni(100)(27) compared to Ni(111), further demonstrating that surface structure, even for the same metallic centers, plays a large role in how internal energy couples to the reaction coordinate. These techniques provide reaction probabilities for well-defined  $E_{trans}$ ,  $E_{vib}$ , and  $E_{rot}$  that span the range of energies present under thermal conditions. This level of experimental control is advantageous for rigorous theoretical description which has for the first time in recent history been able to fully account for all molecular degrees of freedom impacting methane dissociation on metal surfaces.

Previous work has primarily focused on how different vibrations of the gas-phase methane reagent affect dissociation, but thermally excited vibration of the metal surface can also affect reactivity. Near the  $E_{trans}$  energy threshold for reaction, surface atom vibrations can have a dramatic impact on reactivity.(28) More generally, increased surface temperature,  $T_{surf}$ , has been observed to promote CH<sub>4</sub> dissociation but the magnitude of the effect varies widely depending on the surface identity and gas conditions. Dissociative chemisorption, which proceeds through a direct, single collision mechanism, was initially thought to be largely insensitive to surface temperature due to the short interaction time inhibiting energy transfer between the surface and reacting molecule.(4) In contrast, reactions that were sensitive to  $T_{surf}$  were interpreted to proceed via a precursor-mediated mechanism in which energy for dissociation was supplied via energy exchange with a hot surface. This correlation has been proven insufficient in qualifying the reaction mechanism, and in fact,  $T_{surf}$  effects are observed on a host of metal surfaces that react through a direct mechanism. Large effects have been observed on Pt(111)(29, 30), Ir(111)(17), and Ru(0001)(31) but less so on the Ni(100)(15, 32) and Ni(111)(33) surfaces.

The surface oscillator model(11, 34) ascribed the observed surface temperature effects to the relative motion of the incoming reagent and recoil of the interacting surface atom, and invoked a thermally assisted tunneling mechanism to explain differences in reaction probability for CH<sub>4</sub> and CD<sub>4</sub>.(35) Carré et. al. extended the surface mass model(11) to CH<sub>4</sub> reactivity on Ni(111) across a wide range of surface temperatures(36) obtaining semi-quantitative

agreement with experiment but they were unable to accurately capture experimentally observed isotope effects. A statistical model assuming a physisorbed intermediate and statistical treatment of energetic coordinates has been developed but lacks the observed mode-specificity that appears to be ubiquitous in these surface reactions.<sup>(37)</sup> Electron hole-pair coupling can also have drastic effects on gaseous adsorption onto metallic surfaces (38, 39) but has been shown to have minimal effects on dissociative chemisorption for CH<sub>4</sub> on Ni(111) due to the short interaction time.<sup>(4)</sup>

Recent density functional theory (DFT) studies show that the transition state geometry of the methane-surface complex is heavily distorted upon adsorption to the on-top site of the reacting metal atom.<sup>(25, 26)</sup> On Ni(111), when the reaction complex is allowed to relax, the metal atom puckers above the surface plane by 0.25 Å at its minimum transition energy. As the surface atom displacement, denoted as  $Q$  by the authors, varies between +0.25 Å and -0.25 Å (beneath the surface plane), the barrier for dissociation is modulated by 20 kJ/mol. Therefore, variation of  $Q$ , of the interacting surface oscillator with the adsorbing methane molecule, provides better access to the transition state. The large masses involved in this system make it computationally expensive to calculate the effect on dissociation for a relaxing metal atom, however, a lattice-sudden model has proven to be effective since surface atom motion takes longer than the hyperthermal methane-surface interaction.<sup>(40)</sup> The vibrating metal atom has been modeled to have two energy-shifting effects on the minimum energy path for dissociation.<sup>(41)</sup> First, the distance from the surface,  $Z$ , for the transition state

complex is shifted away from the surface by an amount  $\alpha Q$ . Secondly, and more important for this discussion, the barrier for dissociation changes linearly by  $-\beta Q$ . The validity of this energy shifting technique has been verified (42) and tested for several molecule-surface systems, some of which are displayed in Table 5.1.

Campbell et al.(28) measured the initial sticking probability of methane in the ( $v_3, v=1$ ) vibrationally excited state from  $T_{surf} = 90 - 475$  K. At  $T_{surf} = 90$  K there was a sharp energetic threshold for the reaction where  $S_0^{v^3}$  dropped by a factor of approximately 200 in less than a 10 kJ/mol translational energy range. In the same  $E_{trans}$  range at 475 K surface temperature there was only a 5-fold decrease. The only difference between these two conditions was the surface phonon population. At 90 K, more than 99% of the surface oscillators are in the  $v=0,1$  states and at 550 K close to 60% are in vibrational states  $v>1$ .(43) By effectively freezing the surface motion at 90 K the lower energy pathways that involve Ni surface atom motion are eliminated. As the system was starved for energy in the  $E_{trans}$  coordinate there was an abrupt decrease in the number of molecules that had sufficient energy to overcome the reaction barrier. Above  $E_{trans} = 50$  kJ/mol they observed that the sticking probability curves converged and showed no greater than a 2-fold decrease in reactivity from 90 to 475 K. If one was only looking at the high energy regime they would also conclude that this reaction is insensitive to  $T_{surf}$ . That doesn't mean that the high energy regime lacks useful information. The majority of molecular beam experiments for

<b>System</b>	<b><math>\alpha</math></b>	<b><math>\beta</math> (eV / Å)</b>
CH <sub>4</sub> / Ni(111)	0.75	1.10
CH <sub>4</sub> / Pt(111)	0.83	0.95
H <sub>2</sub> O / Ni(111)	0.78	0.63

**Table 5.1** Surface coupling parameters calculated through DFT techniques.(41)

methane dissociation on Ni(111) focus on surface temperature lower than  $T_{surf} = 600$  K.(44, 45):(20, 21)

In the current study we extend the known range of  $S_0$  data for CH<sub>4</sub> on Ni(111) from  $T_{surf} = 500 - 1000$  K for laser off,  $S_0^{Off}$ , and eigen-state resolved ( $v_3, v=1$ ),  $S_0^{v_3}$ , sticking probabilities. A new experimental technique has been developed for these experiments that drastically decreases the time required for data acquisition, permits coverage-dependent measurements of reactivity, and increases the confidence in our reported values. In this technique, square wave modulation of the infrared laser excitation source during deposition combined with real-time uptake measurements using King and Wells molecular beam reflectivity, led to the simultaneous measurement of  $S_0^{Off}$  and  $S_0^{On}$ , and twenty or more replicate measurements of  $(S_0^{On} - S_0^{Off})$  during a single experiment as discussed further in Sections 2.5.3 and below.

## 5.2 Experimental Methods

The following experiments were performed in a supersonic molecular beam surface-scattering chamber(1, 3, 46, 47) with additional details of the design and implementation found in Refs. (48-51). Many of the methods presented here mimic our recent publication(52) and Section 4.2 of this thesis.

A 0.25% CH<sub>4</sub> in H<sub>2</sub> gas mix with a backing pressure of 40 PSIG was expanded continuously from a temperature-controlled molecular beam nozzle source maintained at temperature  $T_{nozzle}$ . Impurities in the gas stream were removed using a dry ice in acetone bath and gas polisher (Supelco Supel-Pure-O), effectively removing any CO, O<sub>2</sub>, H<sub>2</sub>O, and unsaturated hydrocarbons from the reactant gas. The nozzle source heated to temperatures ranging from 500 to 900 K produced a well-defined CH<sub>4</sub> beam with incident translational energies  $E_{trans}$  ranging from 96 to 167 kJ/mol with an energy spread  $\Delta E_{trans} / E_{trans} \approx 5\%$  as measured through time-of-flight mass spectrometry. The experimentally determined velocities and velocity spreads are displayed in Table 5.2. The CH<sub>4</sub> molecules impinged along the surface normal of a clean Ni(111) surface at temperatures ranging from  $T_{surf} = 500$  to 1000 K.

The Ni single crystal (Surface Preparation Laboratory) was polished to 0.1° of the (111) plane. The crystal was attached to a dry ice cooled XYZ-rotatable manipulator in the ultra-high vacuum (UHV) chamber (base pressure =  $1.0 \times 10^{-10}$  Torr) with the crystal temperature monitored using a Type-E

$T_{nozzle}$ , K	$\langle E_{trans} \rangle$ , kJ/mol	Stream velocity, $v_0$ (m/s)	Width parameter, $\alpha$ (m/s)
500	95.6	3456.59	197.60
600	114.0	3774.91	222.25
700	133.6	4086.12	278.27
900	166.5	4562.12	354.30

**Table 5.2** Methane beam conditions at the four  $E_{trans}$  values utilized in this study.

thermocouple spot welded to the top of the crystal. The crystal was cleaned each morning before experiments by heating to 1000 K for 30 seconds followed by  $Ar^+$  sputtering at 500 eV for 15 minutes and subsequent annealing to 1100 K for 45 minutes. The lack of sulfur, oxygen, and carbon after this cleaning cycle was verified through auger electron spectroscopy (VG Microtech, VG-100AX). No contaminants were detected after a one hour  $T_{nozzle} = 300$  K dose on the Ni(111) surface where contaminants stick but methane scatters non-dissociatively. This ensured that background gases or impurities in the feed gas did not contribute to the measured reactivity. Carbon was deposited on the surface during each experimental dose; therefore, after each dose  $T_{surf}$  was increased to 1000 K for 5 minutes to dissolve any remaining carbon into the Ni bulk.

We measured the initial sticking probability,  $S_0$ , on the clean Ni(111) surface for each pair of  $T_{nozzle}$  and  $T_{surf}$  with and without laser excitation of the incident  $CH_4$  beam, denoted as  $S_0^{On}$  (laser-on sticking probability) and  $S_0^{Off}$ , respectively. For  $S_0^{On}$  a narrow bandwidth ( $\Delta\nu < 1$  MHz) infrared laser intersected the incident  $CH_4$  molecules in a multi-pass mirror setup contained within the molecular beam apparatus. The laser path was fanned by nearly parallel mirrors to achieve complete saturation of the Doppler-shifted molecules that diverged from the center beam path to impact the surface near the edge. The  $CH_4$  molecules were excited from the  $v''=0, J''=1$ , to  $v'=1, J'=2$  of the  $\nu_3$  anti-symmetric C-H stretching mode via the R(1) transition at  $3038.485 \text{ cm}^{-1}$ . The measured  $S_0^{Off}$  values are averaged over all the thermally populated ro-vibrational states in  $CH_4$  at a given  $T_{nozzle}$ . Infrared absorption within the beam excites a fraction  $f_{exc}$  of the  $v''=0$

molecules to the excited vibrational state ( $v_3, v=1$ ), but the existing  $E_{vib}$  distribution remains for the molecules not excited by the laser. The difference between reaction probabilities with respect to laser excitation is then only caused by the molecules that are excited to the ( $v_3, v=1$ ) state.

We calculated the state-resolved initial sticking probability,  $S_0^{v_3}$ , using our measured values of  $S_0^{Off}$ ,  $S_0^{On}$ , and calculated  $f_{exc}$ , as shown in Equation 5.1.

$$S_0^{v_3=1} = \frac{S_0^{On} - S_0^{Off}}{f_{exc}} + S_0^{v=0} \quad \text{Eq. 5.1}$$

The value of  $S_0^{Off}$  is an upper limit to the  $v=0$  ground state sticking probability,  $S_0^{v=0}$ , and was used as an estimate for  $S_0^{v=0}$  in these experiments since it is not possible to access the selected  $E_{trans}$  values at low values of  $T_{nozzle}$ . The calculated values for  $f_{exc}$  under the various beam conditions are displayed in Table 5.3 with further explanation found in Refs. (52). The following sections describe the methods used to measure  $S_0^{Off}$  and  $S_0^{On}$ .

In prior studies from our group, the values for  $S_0^{Off}$  and  $S_0^{On}$  were most often measured independently in separate experimental doses or through time consuming AES mapping procedures. A new method developed for these experiments has led to an increased ease of data collection and fidelity. This method employed the basics of the King and Wells (K&W) molecular beam reflectivity technique(53) with addition of modulation of the infrared laser excitation source during deposition. An overview of the method is highlighted in

$T_{nozzle}, K$	$f_{v=0}$	$T_{rot}, K$	$f_{rot}$	$f_{exc}$
300	0.993	7.90	0.543	0.269
500	0.908	13.16	0.475	0.216
600	0.828	15.80	0.437	0.181
700	0.734	18.43	0.400	0.147
900	0.542	23.69	0.335	0.091

**Table 5.3** Calculated vibrational and rotational factors for determination of the fraction of excited molecules,  $f_{exc}$ . The factors for  $T_{nozzle} = 300$  K are included for comparison to a vibrationally cool beam.

Section 2.4.2 with examples from this specific data set, but the basics of how the experiments were performed is detailed here.

The K&W technique measures the partial pressure change for the reacting gas resulting from exposure to a surface (Fig. 2.5). Molecules that do not react scatter non-dissociatively and produce no change in the reagent pressure in the experimental chamber. For molecules that dissociate, there is a decrease in the measured pressure equal to the number of molecules that stick to the surface. The initial sticking probability is then the quotient of the molecules that react on the surface compared to the total number of molecules hitting the surface. The dissociation is monitored in real time, which allowed for the coverage depending sticking probability,  $S(\theta)$ , to be measured at the same time. For molecules that are excited by the laser to the  $\nu_3 \nu=1$  vibrational state there is a larger drop in pressure under the same energetic conditions. Instead of performing two measurements for  $S_0^{Off}$  and  $S_0^{On}$  the excitation laser source was modulated using an electro-mechanical shutter during deposition (Fig 2.6). The resulting K&W trace then had a square wave modulation in reactivity with the laser excited molecules having a lower measured pressure, as monitored by a QMS tuned to an  $m/z$  characteristic of methane, compared to the non-excited molecules. The shutter modulation drive signal was recorded in conjunction with the K&W QMS data for facile separation of the two conditions. K&W experiments that once led to a single measurement of either  $S_0^{Off}$  or  $S_0^{On}$  per experiment now produce upwards of 20 measurements in the same experimental dose. Since measurements of  $S_0^{Off}$  or  $S_0^{On}$  are made in rapid succession, this new method is also much less affected by slight variations in

molecular beam flux or QMS sensitivity that occur on timescales longer than two seconds.

There are several factors that affected the collection of this modulation data. The dissociation products for methane on Ni(111) are a methyl radical and H atom. At temperatures above 500 K, methyl completely dehydrogenates and surface hydrogen atoms recombinatively desorb, leaving behind surface-bound C. The solubility of carbon in nickel is relatively high(54), but the diffusion from surface into the bulk is an activated process. We find that this process turns on rapidly at temperatures around 700 K(55), the middle of our investigated temperature range. This led to two different regimes that impacted the shape of the K&W data. At temperatures at and above 800 K the surface carbon diffused into the bulk faster than it accumulated onto the surface. Therefore, when the Ni(111) surface was exposed to the methane beam there was a drop in pressure (molecules reacting) and that pressure drop remained constant with increasing exposure because the surface was perpetually “clean” due to rapid recombinative desorption of H, and dissolution of C into the Ni bulk. This allowed for  $S_0^{Off}$  and  $S_0^{On}$  to be collected over a constant  $S(\theta \approx 0)$  regime with no site blocking. At or below  $T_{surf} = 700$  K dissolution into the bulk slowed to become negligible, and essentially all C accumulated on the surface, resulting in a  $S(\theta)$  response that decreased with increasing C coverage. The cumulative C coverage at time  $t$ ,  $\theta(t)$ , was determined by integrating the incident methane flux (0.08 ML/s as measured) multiplied by the observed sticking probability from the K&W measurements during periods with and without laser excitation over the total time of deposition.

The sticking probability was then plotted against the calculated coverage values to produce  $S(\theta)^{On}$  and  $S(\theta)^{Off}$ .

The resulting plot of both  $S(\theta)^{On}$  and  $S(\theta)^{Off}$  were both linear with increasing coverage at temperature above 500 K, as shown in Figure 2.8. Given the dissociation process occupies at least two surface sites, this coverage dependence suggests that the C atoms aggregate into islands, during the dose. The Temkin isotherm(56), which provides a linear relationship between  $S(\theta)$  and  $\theta$  with the desired parameter,  $S_0$ , and the fitting parameter,  $\alpha_T$ , is an appropriate model.

$$S(\theta) = S_0 \times (1 - \alpha_T \theta) \quad \text{Equation 5.2}$$

The values for  $\alpha_T$  were determined for the  $S_0^{Off}$  dataset and the  $S_0^{On}$  was constrained to this value. This was valid because as carbon accumulated onto the surface there was an increasing insensitivity to the added  $v_3$ ,  $v=1$  quanta and both curves tended to the same x-intercept which is defined by  $\alpha_T$ . In this way, we were able to use the entire series of  $S(\theta)$  measurements to define the zero-coverage values of  $S_0^{Off}$  and  $S_0^{On}$ . Variance values were derived from the fit to Equation 5.2, which led to a significant increase in our confidence in reported values of  $S_0^{Off}$  and  $S_0^{On}$  due to the highly constrained fit. The IGOR program used to process the K&W data to produce the data presented below is included, and expanded upon, in Appendix B.

### 5.3 Results and Discussion

We plot  $S_0^{Off}$  and  $S_0^{v3}$  versus translational energy for all surface temperatures in Figure 5.1 (Table 5.4) with  $2\sigma$  (95% confidence limit) error bars. At each surface temperature methane reactivity increased with increasing  $E_{trans}$ , consistent with a direct dissociative mechanism. The addition of one quanta in the  $v_3$  vibrational mode enhanced reactivity across the entire energetic regime. The absolute differences between  $S_0^{Off}$  and  $S_0^{v3}$  were largest for the two middle  $E_{trans}$  values, 114 and 134 kJ/mol, with differences ranging between 7-10%. For 167 and 96 kJ/mol beams the difference in reactivity were slightly lower and range from 7-8% and 4-7%, respectively. The more striking comparison is between the relative change in  $S_0^{Off}$  and  $S_0^{v3}$ , displayed in Figure 5.2. At  $E_{trans} = 167$  kJ/mol,  $S_0^{v3}$  was about 20% greater than  $S_0^{Off}$  at all surface temperatures. As  $E_{trans}$ , and therefore the total energy available to the system decreases to 96 kJ/mol,  $S_0^{Off}$  drop nearly by a factor of 25, and  $v_3$  excitation begins to play a greater role in activating the reaction. At the lowest energy condition ( $E_{trans} = 96$  kJ/mol,  $T_{surf} = 500$  K)  $S_0^{v3}$  was about 400% greater than  $S_0^{Off}$  with intermediate conditions falling between these two cases. At all values of  $E_{trans}$  studied, the change in relative initial sticking probabilities is relatively insensitive to surface temperature. This implies that when methane energies ( $E_{trans} + E_{vib}$ ) exceed 100 kJ/mol and  $T_{surf} \geq 500$  K, the enhancement in  $S_0$  provided by  $v_3$  excitation is not strongly dependent on surface temperature.

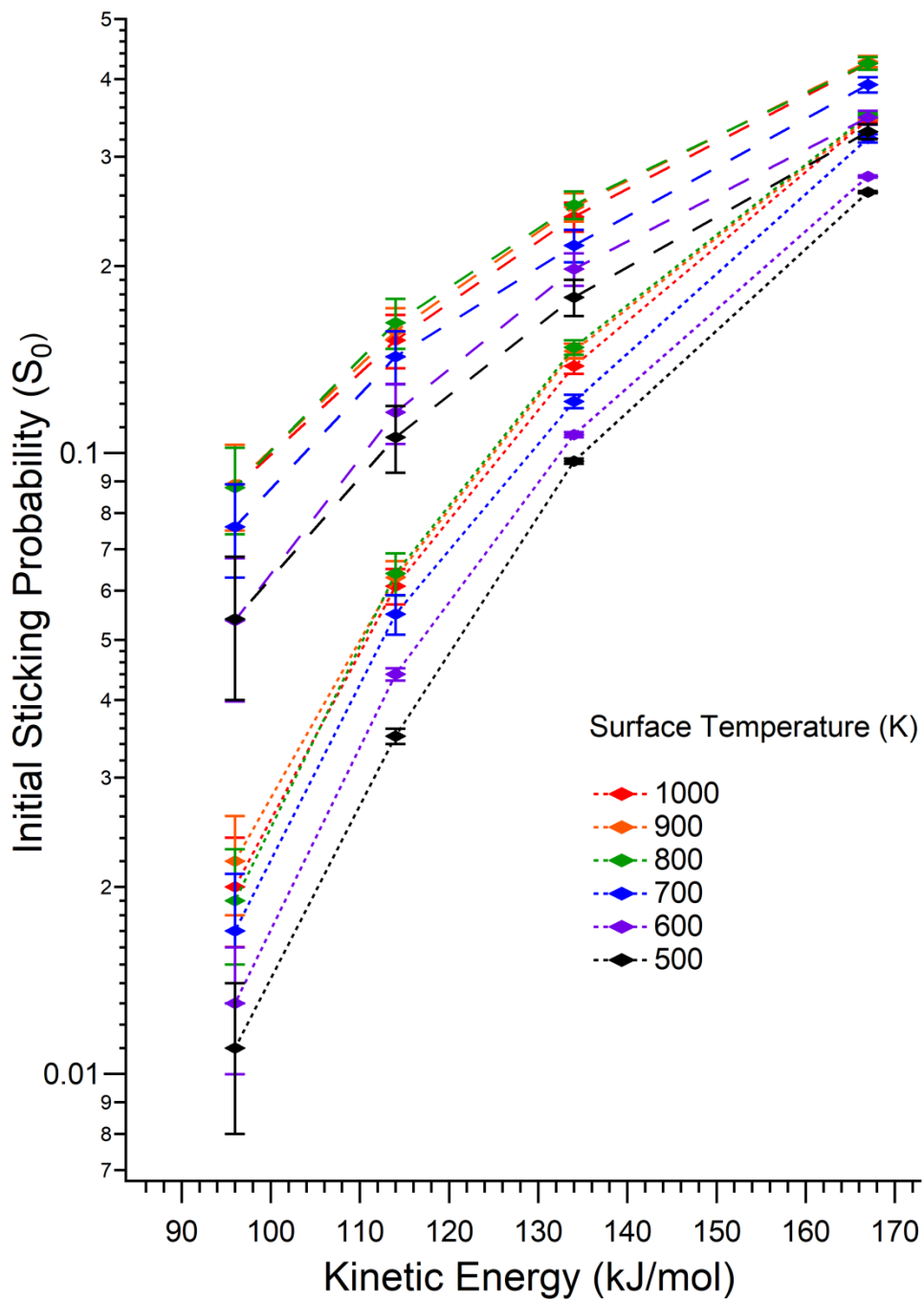


**Figure 5.1** Sticking probability curves for  $\text{CH}_4$  dissociating on Ni(111) surface at six different surface temperatures.  $S_0^{off}$  values are represented by dotted lines and  $S_0^{v3}$  by solid lines.

$T_{surf},$ K	$T_{nozzle},$ K	$S_0^{off}$	$S_0^{v_3, v=1}$	$2\sigma(OFF)$	$2\sigma(v_3)$
1000	900	0.344	0.424	0.003	0.010
	700	0.138	0.240	0.004	0.013
	600	0.061	0.152	0.004	0.015
	500	0.020	0.088	0.004	0.014
900	900	0.347	0.427	0.003	0.009
	700	0.146	0.249	0.004	0.013
	600	0.063	0.157	0.004	0.014
	500	0.022	0.089	0.004	0.014
800	900	0.350	0.424	0.003	0.010
	700	0.148	0.251	0.004	0.013
	600	0.064	0.162	0.005	0.015
	500	0.019	0.088	0.004	0.014
700	900	0.321	0.392	0.005	0.011
	700	0.121	0.216	0.003	0.013
	600	0.055	0.143	0.004	0.014
	500	0.017	0.076	0.004	0.013
600	900	0.279	0.349	0.001	0.009
	700	0.107	0.199	0.001	0.012
	600	0.044	0.117	0.001	0.013
	500	0.013	0.058	0.003	0.014
500	900	0.263	0.329	0.001	0.009
	700	0.097	0.178	0.001	0.012
	600	0.035	0.106	0.001	0.013
	500	0.011	0.054	0.003	0.014

**Table 5.4** Measured initial sticking probabilities for laser off,  $S_0^{off}$ , and state-resolved,  $S_0^{v_3}$ , CH<sub>4</sub> on Ni(111) and the calculated error.

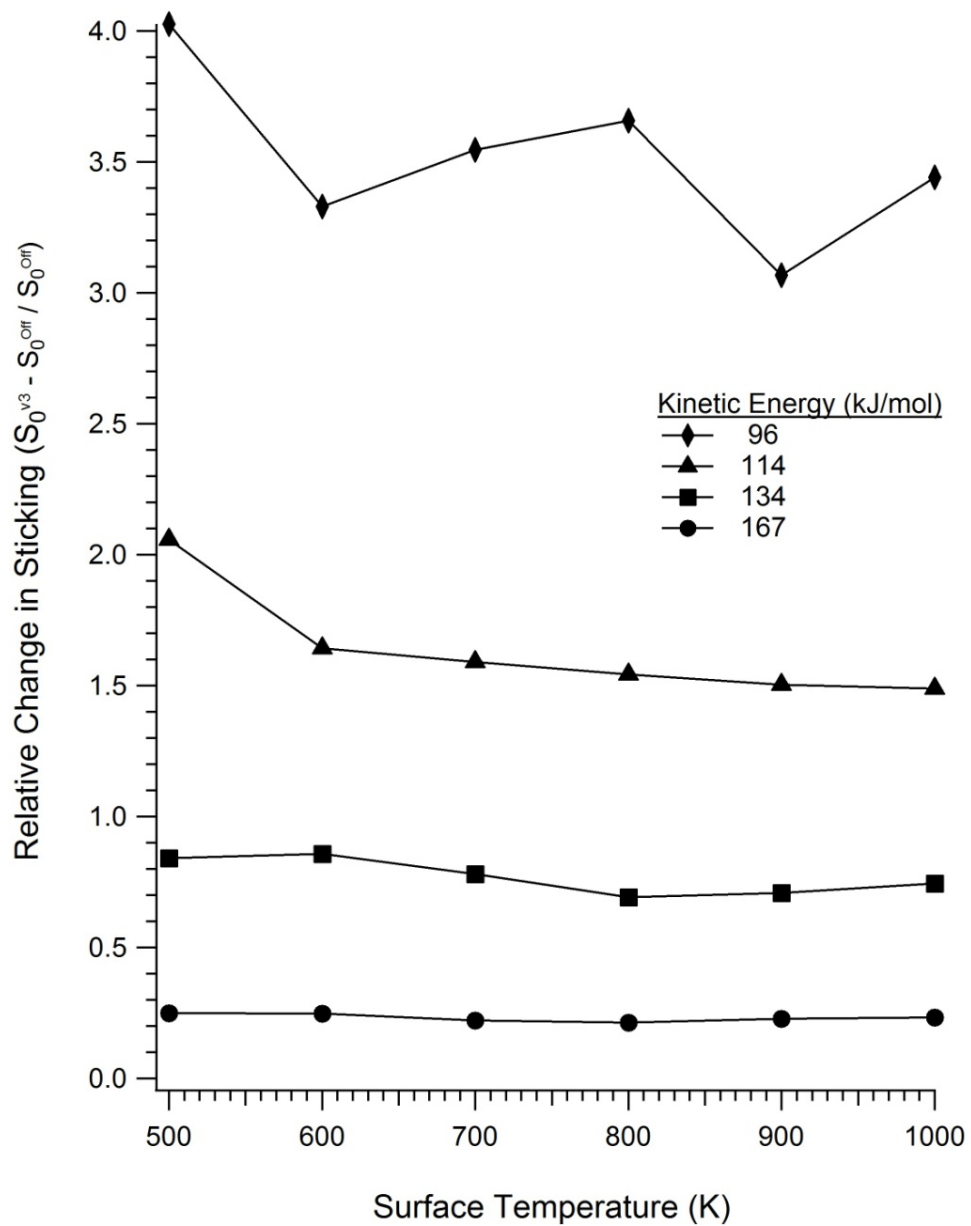


**Figure 5.2** Relative fractional change in  $S_0^{Off}$  and  $S_0^{v3}$  for the four  $E_{trans}$  from  $T_{surf} = 500 - 1000$  K.

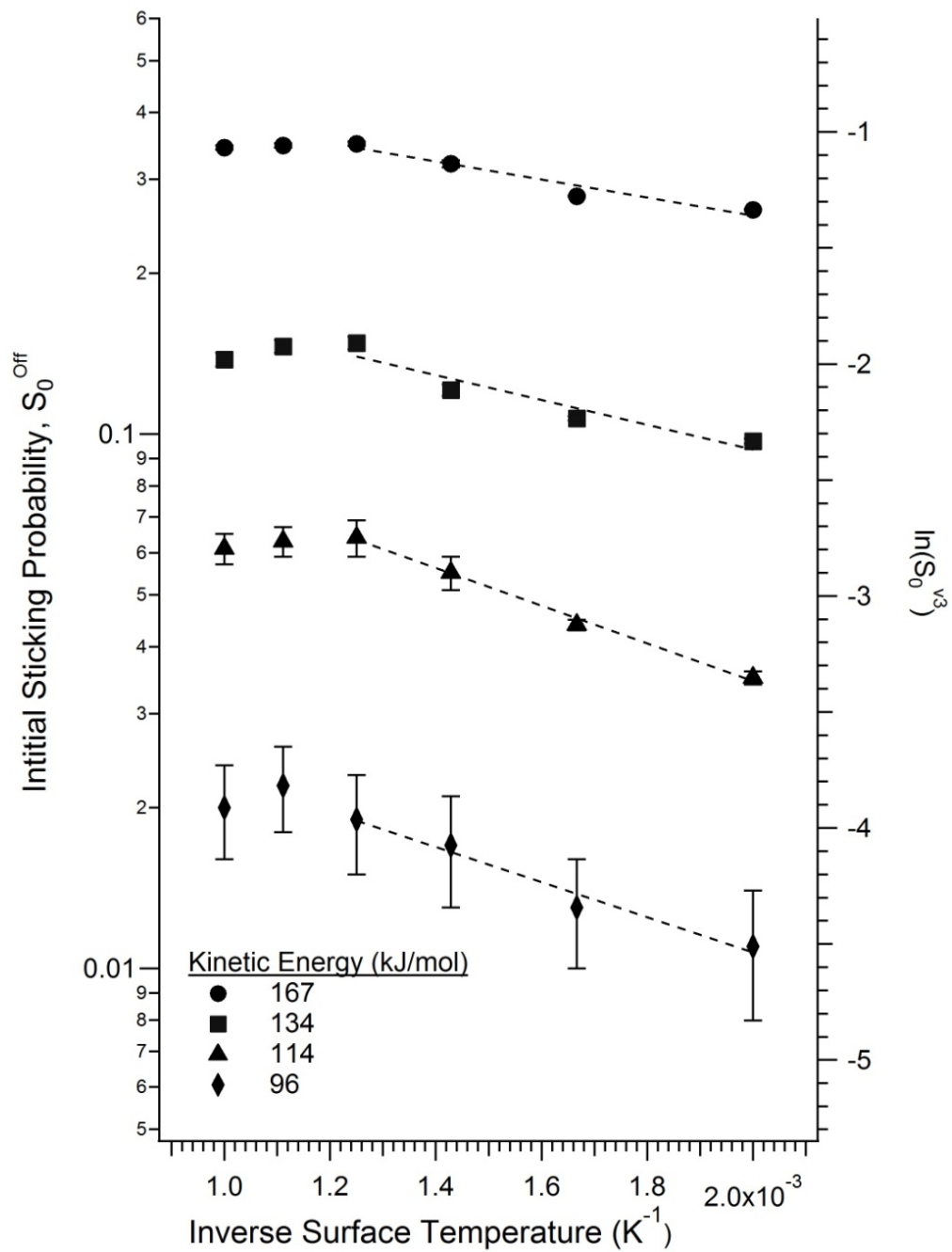


**Figure 5.3** Surface temperature dependence for laser-off initial methane sticking probability,  $S_0^{Off}$ , as a function of inverse surface temperature ( $K^{-1}$ ).

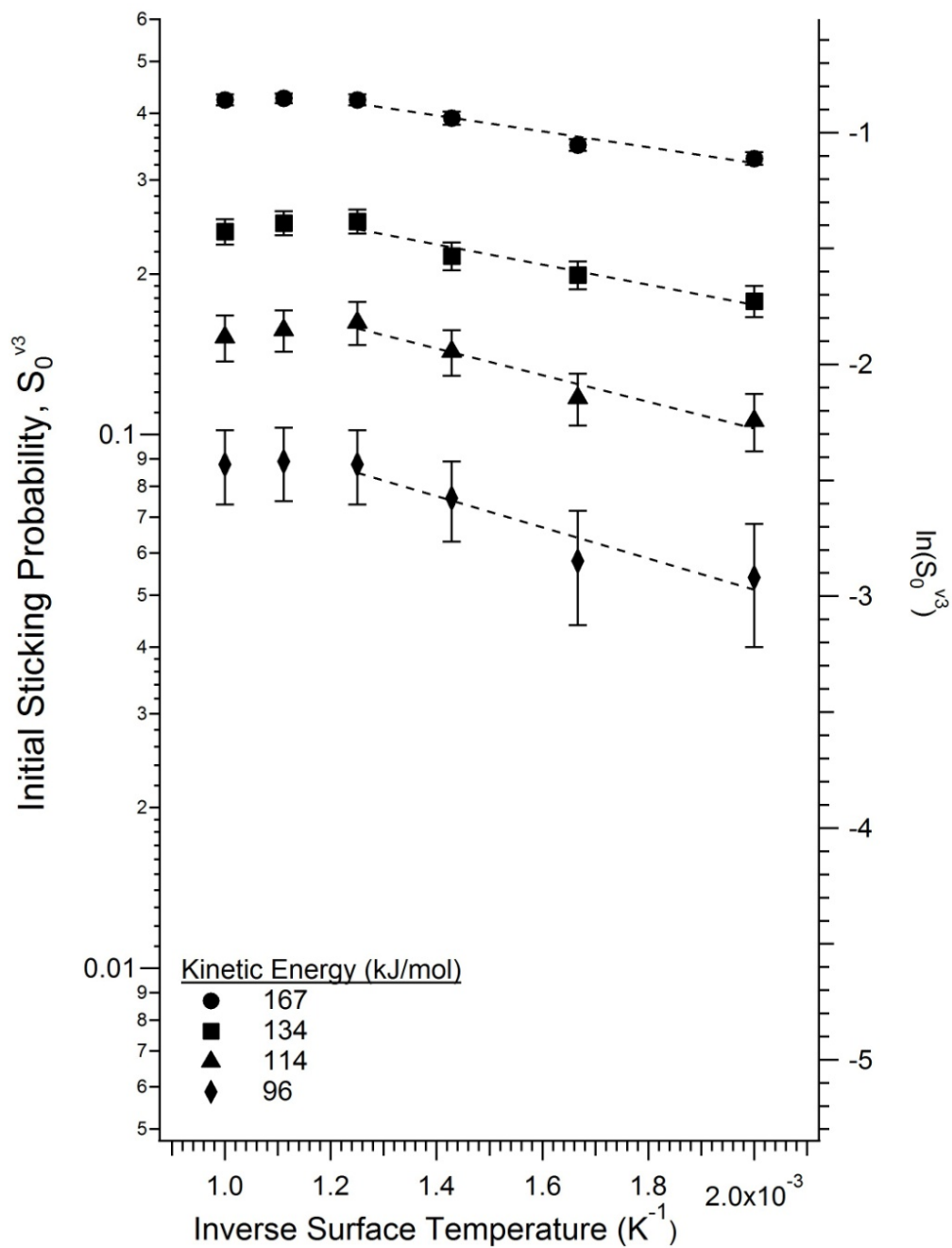


**Figure 5.4** Surface temperature dependence for state-resolved initial methane sticking probability,  $S_0^{v^3}$ , as a function of inverse surface temperature ( $K^{-1}$ ).

Unlike the situation for molecules whose energy is just above the energy threshold for reaction, at high total energy, surface temperature is less effective than  $E_{trans}$  or  $E_{vib}$  at promoting reaction under these energy-rich conditions. Plotting  $S_0^{Off}$  and  $S_0^{v3}$  against inverse  $T_{surf}$  produces the Arrhenius plots in Figures 5.3, and 5.4, respectively. For both  $S_0^{Off}$  and  $S_0^{v3}$  there was no significant change in the  $T_{surf} = 1000 - 800$  K range. Interestingly, there may be a slight decrease (mostly within the error bars) in  $S_0$  with *increasing*  $T_{surf}$ . While the decrease is small, this trend is observed across the majority of the four  $E_{trans}$  values for  $S_0^{Off}$  and  $S_0^{v3}$ . This also does not appear to be an artifact of how the experiments were performed. The surface temperature, 800 K, at which the reaction became insensitive to increasing temperature was constant across the entire range of  $E_{trans}$  and  $E_{vib}$  conditions. This leads us to believe that this effect is then not dependent on the methane internal energy during dissociation, but is purely a surface effect.

For  $T_{surf}$  from 700 - 500 K reactivity decreases linearly for every set of beam conditions. The best fit lines through this  $T_{surf}$  range are produced by fitting a straight line through  $\ln(S_0)$  versus inverse  $T_{surf}$ . The pre-exponential term,  $A$ , and activation energy,  $E_a$ , are extracted from the fit line as in Equation 5.3 and displayed in Table 5.5 for each  $E_{trans}$  value.

$$\ln[S_0(E_{trans}, T_{surf}, v_i)] = \ln(A) - \frac{E_a}{R} \left( \frac{1}{T_{surf}} \right) \quad \text{Equation 5.3}$$

Both the calculated activation energy and pre-exponential term increase with decreasing  $E_{trans}$  except for  $S_0^{Off}$  at  $E_{trans} = 114$  kJ/mol. Campbell(28) performed a similar analysis for  $T_{surf} = 90 - 300$  K and found that the activation energy

$E_{trans}$ , kJ mol <sup>-1</sup>	$S_0^{Off}$ Coefficients		$S_0^{v^3}$ Coefficients	
	Activation energy, kJ mol <sup>-1</sup>	Prefactor x10 <sup>3</sup> kJ/mol	Activation energy, kJ mol <sup>-1</sup>	Prefactor x10 <sup>3</sup> kJ/mol
167	3.24	1.79	2.85	1.56
134	4.45	3.66	3.61	2.40
114	6.74	5.73	4.79	3.08
96	6.30	20.5	5.60	5.08

**Table 5.5** Calculated coefficients from the best fit lines of  $S_0^{Off}$  (Figure 5.3) and  $S_0^{v^3}$  (Figure 5.4).

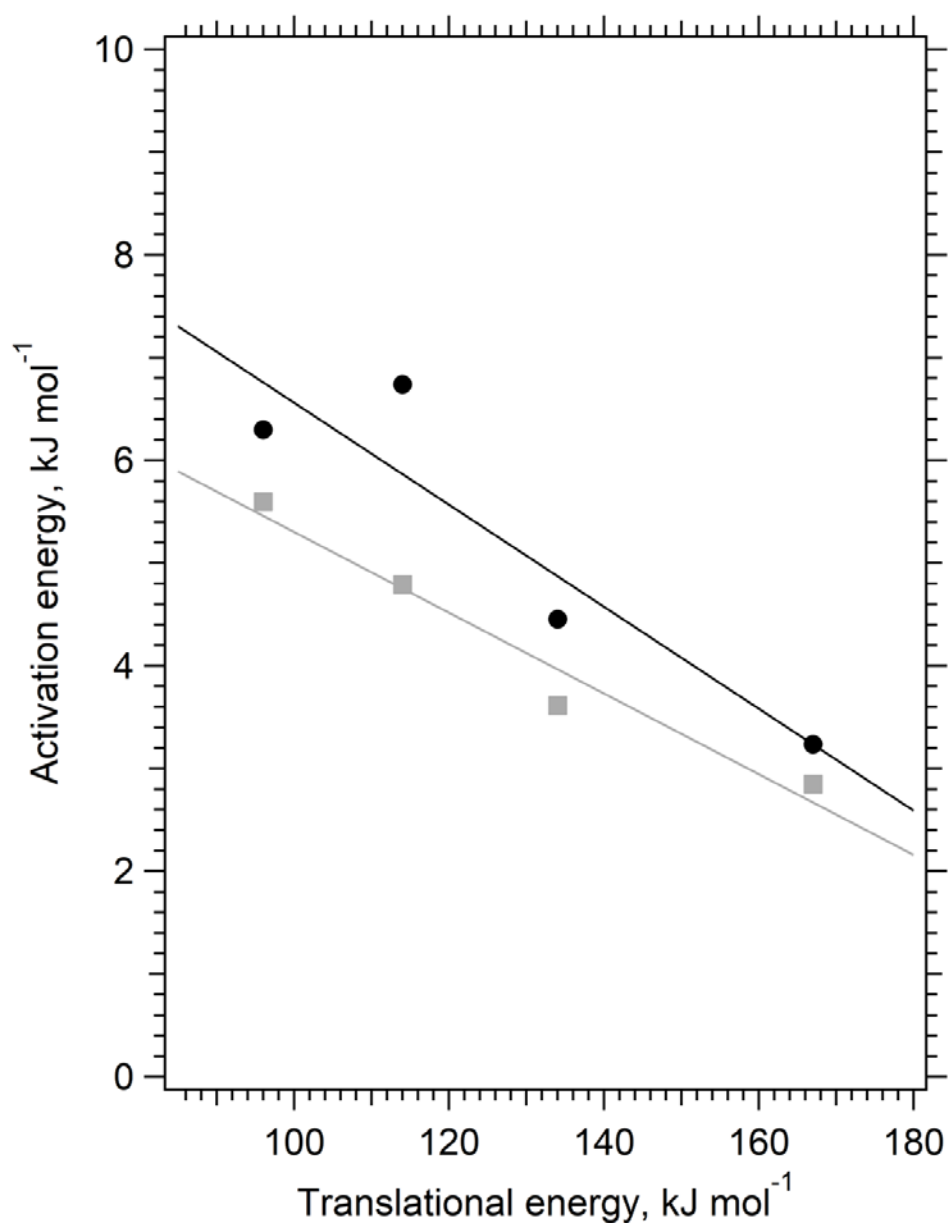


**Figure 5.5** Calculated activation energies for surface temperature activation for  $S_0^{Off}$  (■) and  $S_0^{v^3}$  (●).

changed from 8.6 to 2.0 kJ/mol from  $E_{trans} = 32.6 - 40$  kJ/mol, a 7.4 kJ/mol range. We observed a much smaller change; over a 71 kJ/mol range in  $E_{trans}$  we calculate a change of approximately 3 kJ/mol in activation energy. This plot is shown in Figure 5.5. This is not surprising given the large surface temperature effect they observed at 90 K.

Previous calculations(28) for CH<sub>4</sub> on Ni(111) in the  $T_{surf}=0 - 550$  K range suggested convergence of reaction probabilities by approx.  $E_{trans} = 95$  kJ/mol. This is contrary to our observations where a difference in reactivity is measured even at our highest  $E_{trans} = 168$  kJ/mol and up to  $T_{surf} = 700$  K. A key assumption in previous calculations forced the reaction to proceed over the most reactive adsorption site, the on-top site. Indeed, the calculated distribution of reactive encounters for CHD<sub>3</sub> on both Ni(111) and Pt(111) surfaces shows a majority occurring at the on-top site.(40) This assumption may break down under the experimental conditions here because the methane's total internal energy is far above the barrier for reaction. It is proposed that the surface temperature dependence at these high surface temperatures and methane internal energies is likely dominated by the next lowest barrier location on the surface, the bridge site, becoming active, rather than continued Arrhenius activation for a single barrier. The on-top site saturates at lower  $E_{trans}$  than the bridge site and loses much of its surface temperature dependence. The surface temperature dependence that we observe at higher  $E_{trans}$  is dominated by the bridge sites turning on.

## 5.4 Conclusions and Future Directions

The conversion of methane to hydrogen in industrial steam reforming reactors is carried out under high pressures and temperatures. Up until now there has been minimal experimental data for methane dissociation on single crystals under surface temperatures approaching those used in industrial settings. To assess methane dissociation under these conditions, state-resolved ( $v_3, v=1$ ) sticking probabilities for methane dissociating on Ni(111) were measured at high surface temperature,  $T_{surf} = 500 - 1000$  K. These experiments demonstrated that the initial (clean surface) methane dissociation probability was sensitive to surface temperatures up to 700 K but showed only small changes in reactivity from 800 – 1000 K for all  $E_{trans}$  and  $E_{vib}$  conditions. Carbon dissolution kinetics become important at these elevated temperatures and will be further discussed in Chapter 6. In fact, coverage-dependent sticking measurements, in combination with systematic variation in the reactive methane flux, can shed light on carbon dissolution kinetics that could play an important role in heterogeneous catalysis.

The K&W modulation technique outlined in this Chapter allowed the studies to be performed since reaction products do not remain on the surface for post-dose analysis at surface temperatures above 700 K. The method also has the potential to substantially decrease the time required to collect sticking data for future comparison. Currently a Ni(997) surface is being prepared in our experimental chamber and these experiments will be replicated on this stepped surface to assess how the surface temperature effects observed here compare to a stepped surface. In the future, it will be advantageous to collect data at  $T_{surf} >$

1000 K to determine if decrease in sticking with increasing  $T_{surf}$  becomes a significant factor in dissociation. Unfortunately, there is currently no known method to collect similar data for  $T_{surf} > 700$  K and  $S_0 < 1\%$ . At these surface temperatures on Ni(111) the reaction products do not persist on the surface, precluding the post-dose analysis techniques required when  $S_0$  is below the detection through K&W reflectivity.

A future paper in collaboration with theoretical calculations will look at how reactivity is affected at these elevated surface temperatures. It is apparent that the model for methane dissociation will have to include additional factors that both increase the surface temperature dependence from 500 – 700 K, but also address the insensitivity of the reaction to  $T_{surf}$  above 800 K.

## 5.5 References

1. L. B. F. Juurlink, D. R. Killelea, A. L. Utz, State-resolved probes of methane dissociation dynamics. *Progress in Surface Science* **84**, 69-134 (2009).
2. A. L. Utz, Mode selective chemistry at surfaces. *Current Opinion in Solid State and Materials Science* **13**, 4-12 (2009).
3. R. D. Beck, A. L. Utz, in *Dynamics of Gas-Surface Interactions: Atomic-Level Understanding of Scattering Processes at Surfaces*, R. Diéz Muiño, H. F. Busnengo, Eds. (Springer-Verlag, Berlin, 2013).
4. X. Luo, B. Jiang, J. I. Juaristi, M. Alducin, H. Guo, Electron-hole pair effects in methane dissociative chemisorption on Ni(111). *The Journal of Chemical Physics* **145**, 044704 (2016).
5. H. Chadwick, R. D. Beck, Quantum state resolved gas-surface reaction dynamics experiments: a tutorial review. *Chemical Society Reviews* **45**, 3576-3594 (2016).
6. A. A. Puretzy, I. A. Merkulov, C. M. Rouleau, G. Eres, D. B. Geohegan, Revealing the surface and bulk regimes of isothermal graphene nucleation and growth on Ni with in situ kinetic measurements and modeling. *Carbon* **79**, 256-264 (2014).
7. K. Li, C. He, M. Jiao, Y. Wang, Z. Wu, A first-principles study on the role of hydrogen in early stage of graphene growth during the CH<sub>4</sub> dissociation on Cu(1 1 1) and Ni(1 1 1) surfaces. *Carbon* **74**, 255-265 (2014).
8. L. Meng, Q. Sun, J. Wang, F. Ding, Molecular Dynamics Simulation of Chemical Vapor Deposition Graphene Growth on Ni (111) Surface. *The Journal of Physical Chemistry C* **116**, 6097-6102 (2012).
9. R. Wensch, R. Hübner, F. Munnik, S. Melkhanova, S. Gemming, G. Abrasonis, M. Krause, Nickel-enhanced graphitic ordering of carbon ad-atoms during physical vapor deposition. *Carbon* **100**, 656-663 (2016).
10. S. Chen, W. Xiong, Y. S. Zhou, Y. F. Lu, X. C. Zeng, An ab initio study of the nickel-catalyzed transformation of amorphous carbon into graphene in rapid thermal processing. *Nanoscale* **8**, 9746-9755 (2016).
11. A. C. Luntz, J. Harris, CH<sub>4</sub> dissociation on metals: a quantum dynamics model. *Surface Science* **258**, 397-426 (1991).
12. J. F. Xu, F. Froment, Methane steam reforming, methanation and water-gas shift: I. Intrinsic kinetics. *AIChE Journal* **35**, 88-96 (1989).
13. M. B. John R. Anderson, *Catalysis - Science and Technology*. Catalysis (Springer-Verlag Berlin Heidelberg, ed. 1, 1987), vol. 5.
14. H. Chadwick, R. D. Beck, Quantum State-Resolved Studies of Chemisorption Reactions. *Annual Review of Physical Chemistry* **68**, 39-61 (2017).
15. P. M. Holmblad, J. Wambach, I. Chorkendorff, Molecular beam study of dissociative sticking of methane on Ni(100). *The Journal of Chemical Physics* **102**, 8255-8263 (1995).

16. D. C. Seets, M. C. Wheeler, C. B. Mullins, Mechanism of the dissociative chemisorption of methane over Ir(110): trapping-mediated or direct? *Chemical Physics Letters* **266**, 431-436 (1997).
17. D. C. Seets, C. T. Reeves, B. A. Ferguson, M. C. Wheeler, C. B. Mullins, Dissociative chemisorption of methane on Ir(111): Evidence for direct and trapping-mediated mechanisms. *The Journal of Chemical Physics* **107**, 10229-10241 (1997).
18. E. Dombrowski, E. Peterson, D. Del Sesto, A. L. Utz, Precursor-mediated reactivity of vibrationally hot molecules: Methane activation on Ir(1 1 1). *Catalysis Today* **244**, 10-18 (2015).
19. A. V. Walker, D. A. King, Dynamics of the Dissociative Adsorption of Methane on Pt{110}(1x2). *Physical Review Letters* **82**, 5156-5159 (1999).
20. R. R. Smith, D. R. Killelea, D. F. DelSesto, A. L. Utz, Preference for Vibrational over Translational Energy in a Gas-Surface Reaction. *Science* **304**, 992-995 (2004).
21. L. B. F. Juurlink, R. R. Smith, D. R. Killelea, A. L. Utz, Comparative Study of C-H Stretch and Bend Vibrations in Methane Activation on Ni(100) and Ni(111). *Physical Review Letters* **94**, 208303 (2005).
22. R. D. Beck, P. Maroni, D. C. Papageorgopoulos, T. T. Dang, M. P. Schmid, T. R. Rizzo, Vibrational Mode-Specific Reaction of Methane on a Nickel Surface. *Science* **302**, 98-100 (2003).
23. P. Maroni, D. C. Papageorgopoulos, M. Sacchi, T. T. Dang, R. D. Beck, T. R. Rizzo, State-resolved gas-surface reactivity of methane in the symmetric C-H stretch vibration on Ni(100). *Physical Review Letters* **94**, 246104 (2005).
24. H. Ueta, L. Chen, R. D. Beck, I. Colon-Diaz, B. Jackson, Quantum state-resolved CH<sub>4</sub> dissociation on Pt(111): coverage dependent barrier heights from experiment and density functional theory. *Physical Chemistry Chemical Physics* **15**, 20526-20535 (2013).
25. G. Henkelman, H. Jónsson, Theoretical Calculations of Dissociative Adsorption of CH<sub>4</sub> on an Ir(111) Surface. *Physical Review Letters* **86**, 664-667 (2001).
26. S. Nave, B. Jackson, Methane dissociation on Ni(111) and Pt(111): Energetic and dynamical studies. *The Journal of Chemical Physics* **130**, 054701 (2009).
27. L. B. F. Juurlink, P. R. McCabe, R. R. Smith, C. L. DiCologero, A. L. Utz, Eigenstate-Resolved Studies of Gas-Surface Reactivity: CH<sub>4</sub>(v<sub>3</sub>) Dissociation on Ni(100). *Physical Review Letters* **83**, 868-871 (1999).
28. V. L. Campbell, N. Chen, H. Guo, B. Jackson, A. L. Utz, Substrate Vibrations as Promoters of Chemical Reactivity on Metal Surfaces. *The Journal of Physical Chemistry A* **119**, 12434-12441 (2015).
29. A. C. Luntz, D. S. Bethune, Activation of methane dissociation on a Pt(111) surface. *The Journal of Chemical Physics* **90**, 1274-1280 (1989).
30. H. Chadwick, A. Gutiérrez-González, R. D. Beck, Quantum state resolved molecular beam reflectivity measurements: CH<sub>4</sub> dissociation on Pt(111). *The Journal of Chemical Physics* **145**, 174707 (2016).

31. R. C. Egeberg, S. Ullmann, I. Alstrup, C. B. Mullins, I. Chorkendorff, Dissociation of CH<sub>4</sub> on Ni(1 1 1) and Ru(0 0 0 1). *Surface Science* **497**, 183-193 (2002).
32. A. C. Luntz, CH<sub>4</sub> dissociation on Ni(100): Comparison of a direct dynamical model to molecular beam experiments. *The Journal of Chemical Physics* **102**, 8264-8269 (1995).
33. M. B. Lee, Q. Y. Yang, S. T. Ceyer, Dynamics of the activated dissociative chemisorption of CH<sub>4</sub> and implication for the pressure gap in catalysis: A molecular beam–high resolution electron energy loss study. *The Journal of Chemical Physics* **87**, 2724-2741 (1987).
34. M. Hand, J. Harris, Recoil effects in surface dissociation. *The Journal of Chemical Physics* **92**, 7610-7617 (1990).
35. J. Harris, J. Simon, A. C. Luntz, C. B. Mullins, C. T. Rettner, Thermally assisted tunneling:  $\text{CH}_4$  dissociation on Pt(111). *Physical Review Letters* **67**, 652-655 (1991).
36. B. J. Marie-Noëlle Carré, Dissociative chemisorption of CH<sub>4</sub> on Ni: The role of molecular orientation. *The Journal of Chemical Physics* **108**, 3722-3730 (1998).
37. H. L. Abbott, A. Bukoski, I. Harrison, Microcanonical unimolecular rate theory at surfaces. II. Vibrational state resolved dissociative chemisorption of methane on Ni(100). *The Journal of Chemical Physics* **121**, 3792-3810 (2004).
38. Y. Huang, C. T. Rettner, D. J. Auerbach, A. M. Wodtke, Vibrational Promotion of Electron Transfer. *Science* **290**, 111-114 (2000).
39. O. Bünermann, H. Jiang, Y. Dorenkamp, A. Kandratsenka, S. Janke, D. J. Auerbach, A. M. Wodtke, Electron-hole pair excitation determines the mechanism of hydrogen atom adsorption. *Science*, (2015).
40. B. Jackson, F. Nattino, G.-J. Kroes, Dissociative chemisorption of methane on metal surfaces: Tests of dynamical assumptions using quantum models and ab initio molecular dynamics. *The Journal of Chemical Physics* **141**, 054102 (2014).
41. H. Guo, A. Farjamnia, B. Jackson, Effects of Lattice Motion on Dissociative Chemisorption: Toward a Rigorous Comparison of Theory with Molecular Beam Experiments. *The Journal of Physical Chemistry Letters* **7**, 4576-4584 (2016).
42. X. Shen, Z. Zhang, D. H. Zhang, CH<sub>4</sub> dissociation on Ni(111): a quantum dynamics study of lattice thermal motion. *Physical Chemistry Chemical Physics* **17**, 25499-25504 (2015).
43. V. L. Campbell, PhD Thesis, State Resolved Measurement of Surface Temperature Dependence and Isotopically Selective Reactivity of Methane on Ni(111), *Tufts University* (2011).
44. N. Chen, Y. Huang, A. L. Utz, State-Resolved Reactivity of Methane (v<sub>2</sub> + v<sub>4</sub>) on Ni(111). *The Journal of Physical Chemistry A* **117**, 6250-6255 (2013).
45. R. Bisson, M. Sacchi, T. T. Dang, B. Yoder, P. Maroni, R. D. Beck, State-Resolved Reactivity of CH<sub>4</sub>(2v<sub>3</sub>) on Pt(111) and Ni(111): Effects of

- Barrier Height and Transition State Location. *The Journal of Physical Chemistry A* **111**, 12679-12683 (2007).
46. R. R. Smith, D. R. Killelea, D. F. DelSesto, A. L. Utz, Preference for vibrational over translational energy in a gas-surface reaction. *Science* **304**, 992-995 (2004).
  47. D. R. Killelea, V. L. Campbell, N. S. Shuman, A. L. Utz, Bond-selective control of a heterogeneously catalyzed reaction. *Science* **319**, 790-793 (2008).
  48. L. B. F. Juurlink, P. R. McCabe, R. R. Smith, C. L. DiCologero, A. L. Utz, Eigenstate-Resolved Studies of Gas-Surface Reactivity: CH<sub>4</sub>(v<sub>3</sub>) Dissociation on Ni(100). *Phys.Rev.Lett.* **83**, 868-871 (1999).
  49. L. B. F. Juurlink, R. R. Smith, A. L. Utz, The role of rotational excitation in the activated dissociative chemisorption of vibrationally excited methane on Ni(100). *Faraday Discuss.* **117**, 147-160 (2000).
  50. L. B. F. Juurlink, R. R. Smith, A. L. Utz, Controlling Surface Chemistry with Light: Spatially Resolved Deposition of Rovibrational-State-Selected Molecules. *J.Phys.Chem.B* **104**, 3327-3336 (2000).
  51. P. R. McBabe, L. B. F. Juurlink, A. L. Utz, A molecular beam apparatus for eigenstate-resolved studies of gas-surface reactivity. *Rev.Sci.Instrum.* **71**, 42-53 (2000).
  52. F. Nattino, D. Migliorini, G.-J. Kroes, E. Dombrowski, E. A. High, D. R. Killelea, A. L. Utz, Chemically Accurate Simulation of a Polyatomic Molecule-Metal Surface Reaction. *The Journal of Physical Chemistry Letters* **7**, 2402-2406 (2016).
  53. D. A. King, M. G. Wells, Reaction mechanism in chemisorption kinetics. Nitrogen on the {100} plane of tungsten. . *Proc.R.Soc.London Ser.A* **339**, 245 (1974).
  54. J. J. Lander, H. E. Kern, A. L. Beach, Solubility and Diffusion Coefficient of Carbon in Nickel: Reaction Rates of Nickel-Carbon Alloys with Barium Oxide. *Journal of Applied Physics* **23**, 1305-1309 (1952).
  55. L. Baraton, Z. B. He, C. S. Lee, C. S. Cojocar, M. Châtelet, J.-L. Maurice, Y. H. Lee, D. Pribat, On the mechanisms of precipitation of graphene on nickel thin films. *EPL* **96**, 46003 (2011).
  56. R. I. Masel, *Principles of adsorption and reaction on solid surfaces*. Wiley series in chemical engineering (Wiley, New York, 1996), pp. xiv, 804 p.



# Chapter 6 : Carbon uptake into Ni(111) during CH<sub>4</sub> molecular beam deposition

## 6.1 Introduction

Understanding and predicting the catalytic activation of gaseous species on surfaces requires an intimate knowledge of the myriad processes that occur. The complexity of these systems is apparent with the ever increasing knowledge and literature base. Assumptions that an initially clean and well ordered surface remains as such throughout chemical deposition cannot be taken as fact. Simple adsorption kinetics leading to site blocking on a surface can neglect the importance of bulk and subsurface layer effects, which can often be non intuitive and highly system dependent. Introduction of a carbidic adsorbate can restructure even the most densely packed Ni(111) surface(1) and even more drastic structural changes involving dislocated rows(2, 3) or broad morphological changes in catalytic particles(4) have been observed during deposition. Surface atoms resulting from dissociative chemisorption of feedstock gases can migrate into the subsurface and bulk layers of the catalyst with implications for subsequent adsorption. The added subsurface atoms can alter the electronic structure of the surface(5, 6) or become a reactant itself,(7) emerging from the subsurface with more energy than the corresponding surface bound species. Vattuone *et. al.* proposed that the pressure gap that complicates the comparison of ultra-high

vacuum studies to real reactor conditions contains a "structure gap" in which the structure of the adsorbing metal can be vastly different between the two environments.(8)

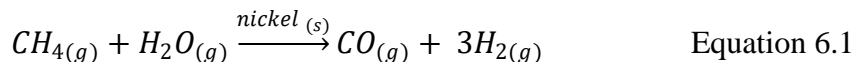
When starting with a clean surface, these effects can lead to an induction period while equilibrium, or at least a steady state, is established between the surface, subsurface, and bulk layers. This can also lead to oscillations in observed behavior for surface species as the individual layers are populated and depopulated based on their relative stabilities and concentration dependent diffusion rates.(9) The population of the subsurface can also be influenced by the incident energy ( $E_i$ ) of the reactant gas. For example, King and co-workers used a molecular beam source to dose O<sub>2</sub> onto Pt(100) with  $E_i = 0.5$  and 0.9 eV followed by temperature programmed desorption measurements. The lower  $E_i$  beam condition led to two desorption features at  $T_{surf} = 650$  and 680 K corresponding to surface bound O-atoms recombinatively desorbing, while increasing  $E_i$  led to a depopulation of these two features in favor of a desorption feature at 970 K, postulated to be from higher binding energy O-atoms in the subsurface layer.(10, 11) Unsurprisingly, incorporation of adsorbates into the subsurface and bulk layers is largely dependent on the surface identity and structure. Out of the four crystalline faces of Ag single crystals (100, 110, 410, 210) only the latter showed O-atom uptake into the subsurface layer as measured by high resolution electron energy loss spectroscopy (HREELS)(8) and X-ray photoelectron spectroscopy (XPS)(12). They proposed two pathways for possible incorporation into the subsurface: a) direct dissociation of O<sub>2</sub> and migration to the subsurface and b) the

dissolution of mobile O-atoms on the surface which are able to move to the lowest energy site to enter the subsurface. Both conditions were highly dependent on  $E_i$  and angle of incidence,  $\theta_i$ , with the latter mechanism showing a large dependence on surface bound O-atom coverage.

Subsurface species are both complicated to detect with current surface science techniques and to interpret for ultimate mechanistic understanding of the system. Studies of subsurface H atoms showed that these species are potent hydrogenation species for hydrogenating surface bound alkyl species, alkenes, and alkynes.(7, 13) Selective hydrogenation of alkynes to alkenes on metallic surfaces has been observed to proceed through an initial induction period where selectivity is low, resulting in mostly alkane products. Due to this induction period it was proposed that the accumulation of carbonaceous products on the surface is necessary for alkene production.(14, 15) Teschner *et. al.* studied the hydrogenation reaction for  $C_{2,4,5}$  alkynes on Pd foil with *in situ* high-pressure XPS looking specifically at the transition of selective alkene hydrogenation.(16) The non-selective induction period contained significantly less signal resulting from subsurface carbon (Pd-C, 335.6 eV) than the selective regime. Under pure  $H_2$  exposure there is significant uptake into the subsurface layers of Pd, forming Pd  $\beta$ -hydride. In the presence of surface bound carbon, however, the subsurface H-atoms are outcompeted by migratory C-atoms, depleting the subsurface layers of hydrogen. The subsurface H-atoms are less selective for single hydrogenation because they possess more energy as they emerge onto the surface. The carbon suppresses this reaction channel, leading to the high selectivity (>95%) for the

alkene product. Here is an example of *two* subsurface species competing and ultimately driving significant changes in the overall observed reaction.

The steam reforming of methane to produce hydrogen gas over a nickel catalyst (Eq. 6.1) is performed at high temperatures and pressures.



The reaction of CH<sub>4</sub> on single crystals has been heavily studied in the goal of understanding the initial rate-determining C-H bond cleavage event. The complete dehydrogenation of the methyl group proceeds rapidly upon adsorption at temperatures above 500 K, leaving a surface bound carbon. The solubility of carbon in nickel is high, approximately 0.5 at% at 1000 K.<sup>(17)</sup> Figure 6.1, reproduced from Ref. (17), demonstrates the sharp onset of solubility and even sharper onset of surface carbon diffusion with increasing  $T_{surf}$ . With the ultimate goal of steam reforming to convert surface bound carbon to CO<sub>(g)</sub> it is deleterious for carbon deposits to persist, leading to catalyst coking. The early studies into carbon deposition on nickel surfaces focused on minimizing the carbon accumulation on or into the nickel substrate.<sup>(18)</sup> More recently, the interest in the C/Ni system stems from its relative ease at producing well ordered graphene sheets and carbon nanotubes. That topic will be discussed in more detail; however, it is important to note some of the energetic and morphological changes that have been observed during carbon deposition on Ni surfaces.

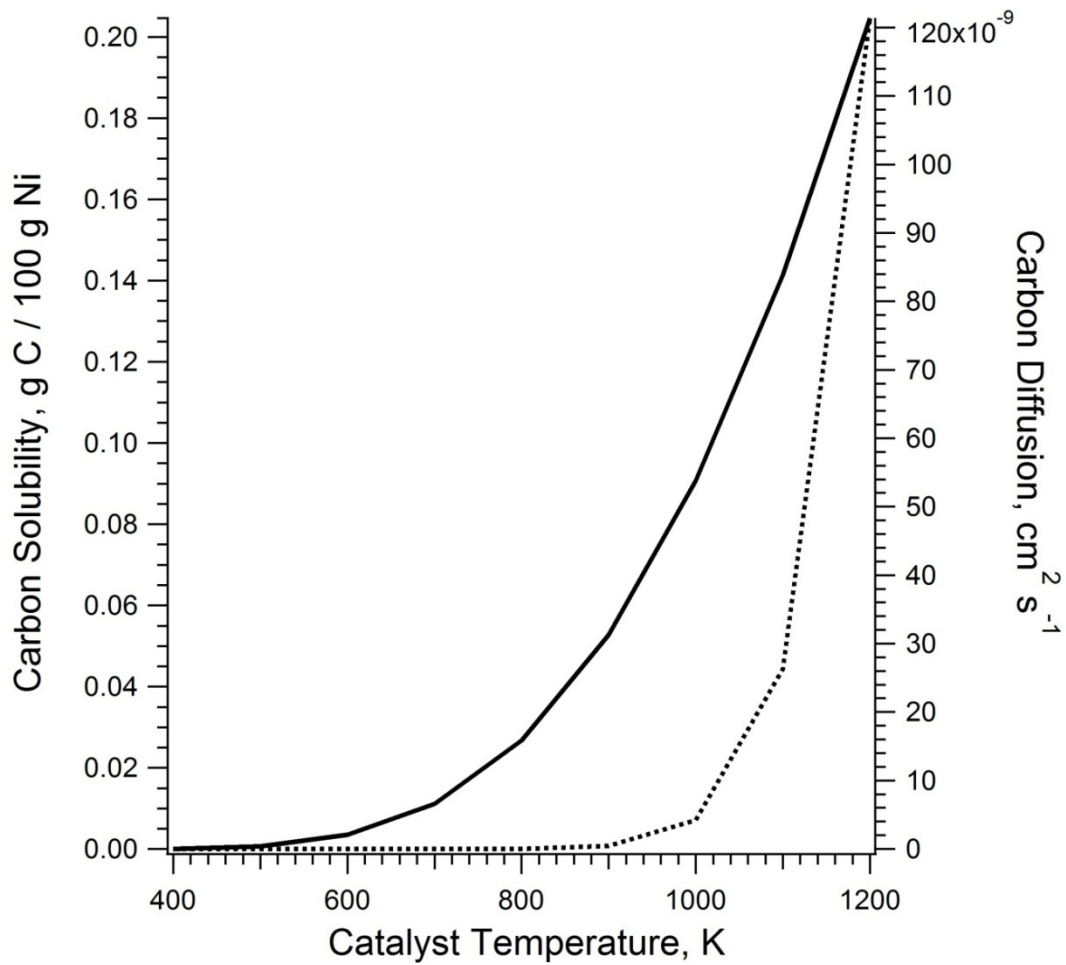


**Figure 6.1** Experimentally measured carbon solubility (left axis, solid line) and surface carbon diffusion (right axis, dotted line) reproduced from Ref. (17)

Previous density functional theory (DFT) calculations predict that carbon adsorption onto a Ni(111) surface can lead to formation of steps. This is the result of carbon adsorption to the step being more stable by 1.2 eV than on the terrace atoms, inducing the structural change.<sup>(19)</sup> The formation and adsorption onto the steps can lower the adsorption energy for the reacting hydrocarbon feed source and increase the diffusion barrier for carbon on the surface due to the highly stable step site. Additional DFT measurements explored the effect of subsurface carbon in the Ni(111) lattice on methane dissociation barriers, finding that the saturated subsurface leads to a 52 kJ/mol increase in activation energy (91 to 143 kJ/mol).<sup>(20)</sup> In the presence of subsurface carbon all the available adsorption sites are destabilized with respect to methane adsorption, however, the fcc site is preferentially destabilized by approximately 20 kJ/mol in relation to the other sites. Methane activation at the fcc site becomes much more endothermic, 77 kJ/mol compared to 6 kJ/mol on clean Ni(111), and results in the much higher dissociation barrier. This brings into question what exactly is happening on the surface during carbon deposition: at what temperatures and pressures is it likely that the subsurface is saturated with carbon without being transported into the bulk nickel lattice?

The interest in graphene synthesis on solid substrates has been increasing since the demonstration of its unique electronic properties in 2004.<sup>(21)</sup> The mechanical<sup>(22-24)</sup>, thermal<sup>(25-27)</sup>, and optical properties<sup>(28, 29)</sup> of graphene have shown its wide range of applicability for material science research. There are diverse methods for producing graphene but the most promising is transition

metal catalyzed chemical vapor deposition due to the low cost and quality of the synthesized graphene.(30-34) While a host of transition metals and their alloys have been explored,(35-37) by far the most common catalysts used are composed of Cu(38-45) and Ni(46-51). Graphene formed on these two surfaces differ significantly in both their morphology and time required for growth. On Cu substrates the solubility of carbon is extremely low and graphene growth leads to large areas of well ordered domains at high temperatures.(34) For Ni substrates the growth times and temperatures are significantly reduced due to the interplay of surface, subsurface, and bulk carbon concentrations. Li, X. *et. al.* used carbon isotope labeling to alternately deposit  $^{12}\text{C}$  and  $^{13}\text{C}$  from  $\text{CH}_4$  during graphene formation to compare the growth mechanisms on Cu and Ni.(52) Ni films showed a homogenous distribution of the two isotopes despite being introduced at periodic intervals, but the Cu substrate showed distinct domains of  $^{12}\text{C}$  and  $^{13}\text{C}$  within the graphene layer. The authors attributed this to the two different carbon sources available for growth on Ni but the Cu substrate only had surface bound carbon from  $\text{CH}_4$  dissociation and growth proceeded through addition to the edges of nucleated graphene sheets. On Ni the source for growth primarily comes from subsurface carbon precipitating onto the surface. Another important difference is the role of hydrogen in carbon kinetics on Cu and Ni. Li, K. *et. al.* used DFT to assess the observation that  $\text{CH}_4$  dehydrogenation is inhibited on Cu in the presence of excess  $\text{H}_{2(\text{g})}$ (53) but that process does not inhibit graphene growth on Ni(111).(54) They found that there needed to be more than 200 times the amount of  $\text{H}_{2(\text{g})}$  present to promote hydrogenation of the predominate intermediate,  $\text{CH}$ , to

CH<sub>3</sub> on Ni when compared to Cu.(55) At this point it is important to note the wide range of conditions that can affect graphene nucleation and proliferation on a surface, specifically for Ni as that is most applicable to the current study.

The first step for graphene formation is the deposition of carbon from a feedstock gas. The deposition can occur first and the substrate temperature changed, often cooled, to promote graphene formation through precipitation. In this scenario the total carbon concentration is unchanged after deposition is complete, but as temperature is changed, the non-equilibrium distribution of carbon throughout the lattice and on the surface drives growth. Akin to this approach a pulsed source can be used at a static substrate temperature so a well defined quantity of carbon is seeded into the substrate and the effect is monitored and replicated at different substrate temperatures.(56) The third approach, and the one employed here, is the continuous deposition of carbon until steady-state is established between the surface, subsurface, and bulk layers. These three approaches provide diverse but mutually important information about the system.

The equilibrium of carbon within the Ni surface, subsurface, and bulk is dependent on many factors. The identity of the carbon precursor can drastically change the rate of dissociative adsorption onto the surface. The overall addition of carbon onto the substrate is a product of the flux,  $F$ , and sticking probability,  $S_0$ , hereon termed “reactive flux”. Carbon precursors such as acetylene(57) and ethylene(58) react with ease on Ni surfaces and will exhibit much higher  $S_0$  values at lower energetic conditions than CH<sub>4</sub>, and also require less pressure to achieve an appreciable reactive flux.

In this study we use a supersonic molecular beam source to generate a methane molecular beam with large amounts of internal energy. The methane beam flux is altered by H<sub>2</sub> seeding with different amounts of enrichment to achieve total incident fluxes ranging from 0.05 to 0.39 ML/s. The uptake of CH<sub>4</sub> onto the surface is monitored *in situ* using quadrupole mass spectrometry (QMS) reflectivity techniques at a fixed surface temperature. As mentioned above there is a sharp transition for carbon solubility and diffusion in Ni that depends on surface temperature. Using the range of reactive flux conditions available the transition temperature for the onset of diffusion into the bulk is assessed.

## 6.2 Experimental Methods

A supersonic molecular beam surface scattering chamber(59) was used in the following studies to measure the initial sticking probability,  $S_0$ , and coverage dependent sticking probability,  $S(\theta)$ , of methane on Ni(111). The experiments performed here are similar to those reported in Chapter 5 but with different goals in mind. In Chapter 5 we examined the surface temperature dependence of  $S_0$  across a wide range of translational energies with and without laser excitation. In this chapter we explore how surface temperature governs the dissolution of the carbon products into the nickel bulk.

Two different CH<sub>4</sub> mixes seeded in H<sub>2</sub> (1%, 0.05%) were supersonically expanded through the nozzle orifice to produce well defined CH<sub>4</sub> beams. The nozzle temperature,  $T_{nozzle}$ , used for both mixes and all the data collected below was 900 K. A constant nozzle temperature was used for these studies to ensure that the only variable energetic coordinate was surface temperature,  $T_{surf}$ . The translational energies,  $E_{trans}$ , for both mixes at this temperature were measured through time-of-flight mass spectrometry. The  $E_{trans}$  values were similar, with the 1% and 0.05% possessing 161.4 and 172.6 kJ/mol of  $E_{trans}$ . Since  $T_{nozzle}$  was identical, the vibrational energies for both mixes were assumed to be identical due to the limited vibrational cooling during expansion. Therefore; the biggest difference between the 1% and 0.05% mixes was the incident flux, which was measured to be 0.39 and 0.05 ML/s, respectively. The different fluxes expanded the useful range of  $T_{surf}$  in which methane dissolution transitioned from no

observed dissolution, to complete dissolution. The same Ni(111) single crystal was used and cleaned using the same methods described in Chapter 5.

King and Wells (K&W) reflectivity techniques were used to measure  $S(\theta)$  over the  $T_{surf}$  range 685 – 850 K. The lower flux mix, 0.05%, was used for  $T_{surf} = 685 – 750$  K and the higher flux mix, 1%, was used from 750 – 850 K. The time dependent coverage was calculated from the K&W data by integrating the product of the measured sticking probability with methane flux values over the duration of the dose.

$$\theta(t) = \int_0^t S(t) \times flux \quad \text{Equation 6.2}$$

It is important to point out that the coverage values reported here do not necessarily represent surface coverage. Because surface carbon can diffuse into the nickel subsurface and bulk layers,  $\theta$  is actually the total amount of carbon deposited across these three areas.  $S(\theta)$  was then the measured reaction probability at each point in the K&W trace taken with the integrated coverage calculated in Equation 6.2. A typical K&W trace, in which the beam flag was removed at  $t \approx 115$  s, and the accumulated coverage, or total number of ML deposited, are shown in Figure 6.2. The sticking probability for this dose stayed relatively constant from  $t = 115$  to 200 seconds, and the resulting coverage increased linearly during this time. When  $S$  started to drop at  $t > 200$  s, the slope of  $\theta(t)$  also decreased because less carbon was being deposited per second.

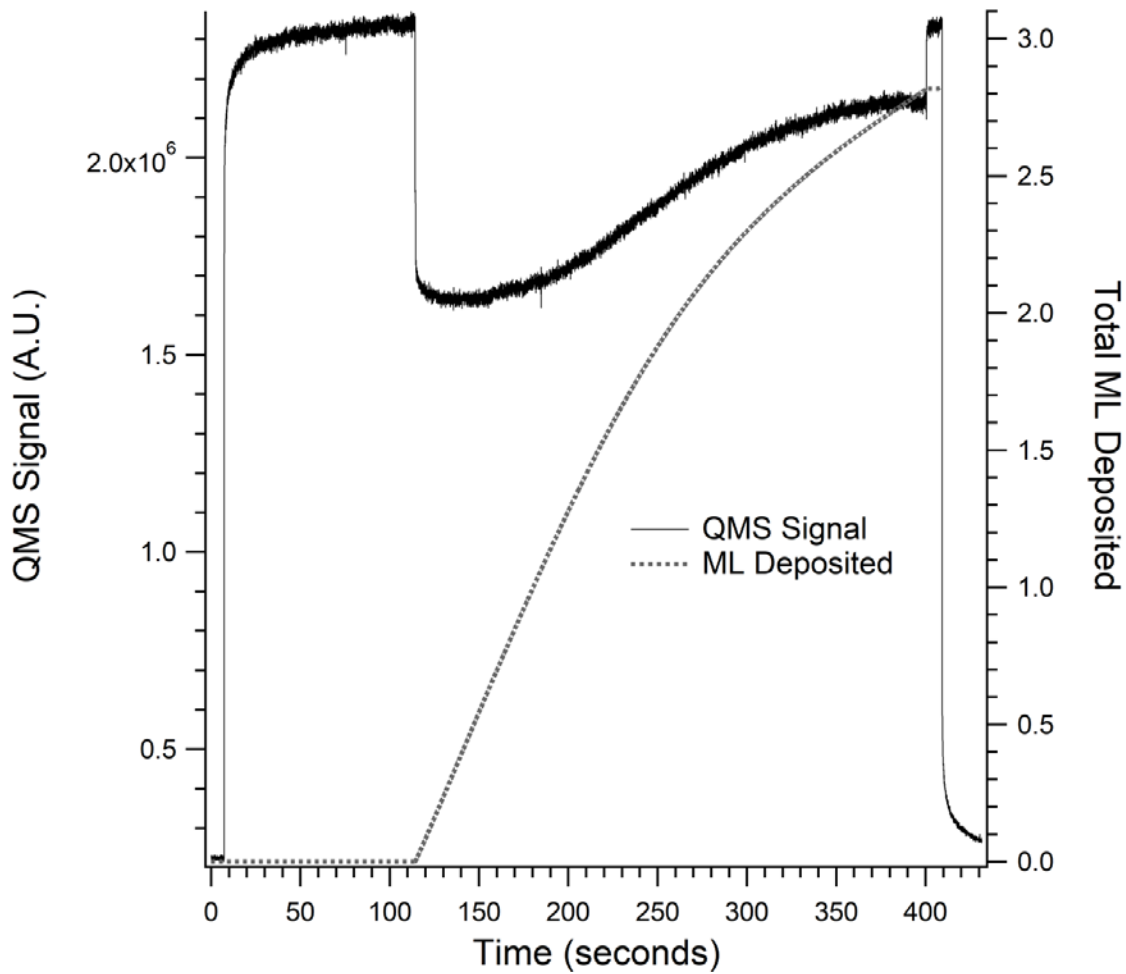


**Figure 6.2** Representative King and Wells reflectivity experiment for methane dissociation on Ni(111) at  $T_{nozzle} = 900$  K and  $T_{surf} = 725$  K for the lower flux (0.05 ML/s) molecular beam used in these experiments. The dotted line is the calculated carbon uptake resulting from methane dissociation.

Out of curiosity, several of the experimental doses were performed using the laser modulation techniques outlined in Chapter 5. It is not the goal of this Chapter to describe how that vibrational energy enhanced reactivity, and in fact it has no noticeable effect on the dissolution rates, but it is worth noting because there are a few interesting observations. For those experiments approximately 10% of the incident methane beam was excited to the ( $\nu_3$ ,  $\nu=1$ ) anti-symmetric C-H in methane. The laser was modulated using an electro-mechanical shutter and the same K&W experiment was performed as outlined above.

### 6.3 Results and Discussion

The raw King and Wells data for the uptake of CH<sub>4</sub> onto the Ni(111) surface is displayed in Figures 6.3 and 6.4. The former is for the more dilute methane mix over the  $T_{surf} = 685 - 750$  K range and the latter for the 1% mix over the  $T_{surf} = 785 - 850$  K range. There are evidently several processes occurring as surface temperature is increased.

Looking at the uptake curves in Figure 6.3, the lowest  $T_{surf} = 685$  K show that  $S_0$  begins decreasing nearly immediately after the shutter is opened, due to site blocking from carbon deposition. Figure 6.5 shows the coverage dependent values of  $S(\theta)$  plotted vs.  $\theta$ , and reactivity decreased linearly with increased carbon exposure (Figure 6.5) until approximately 50% of a monolayer was deposited. In contrast, in the  $T_{surf} = 700$  K trace in Figure 6.2, there was a short period where  $S$  was constant, or even increasing slightly, followed by a relatively linear decrease in sticking with increasing carbon deposition (not shown).  $S(\theta)$  at 700 K did not begin to decrease appreciably until 0.35 ML had been deposited, with a total of  $\approx 1$  ML deposited before a steady state reaction probability was reached. With  $T_{surf} = 750$  K substantially more carbon was deposited without any reduction in  $S(\theta)$  due to site blocking on the surface, and only a slow decrease in sticking is observed (45-35%) after 7 ML of carbon was dosed onto the nickel surface. The initial drop in the QMS signal, which corresponds to initial sticking probability,  $S_0$ , varies with  $T_{surf}$ . The values for  $S_0$  increased from about 0.25 to 0.45 as  $T_{surf}$  increased from 685 to 750 K, with the two intermediate temperatures

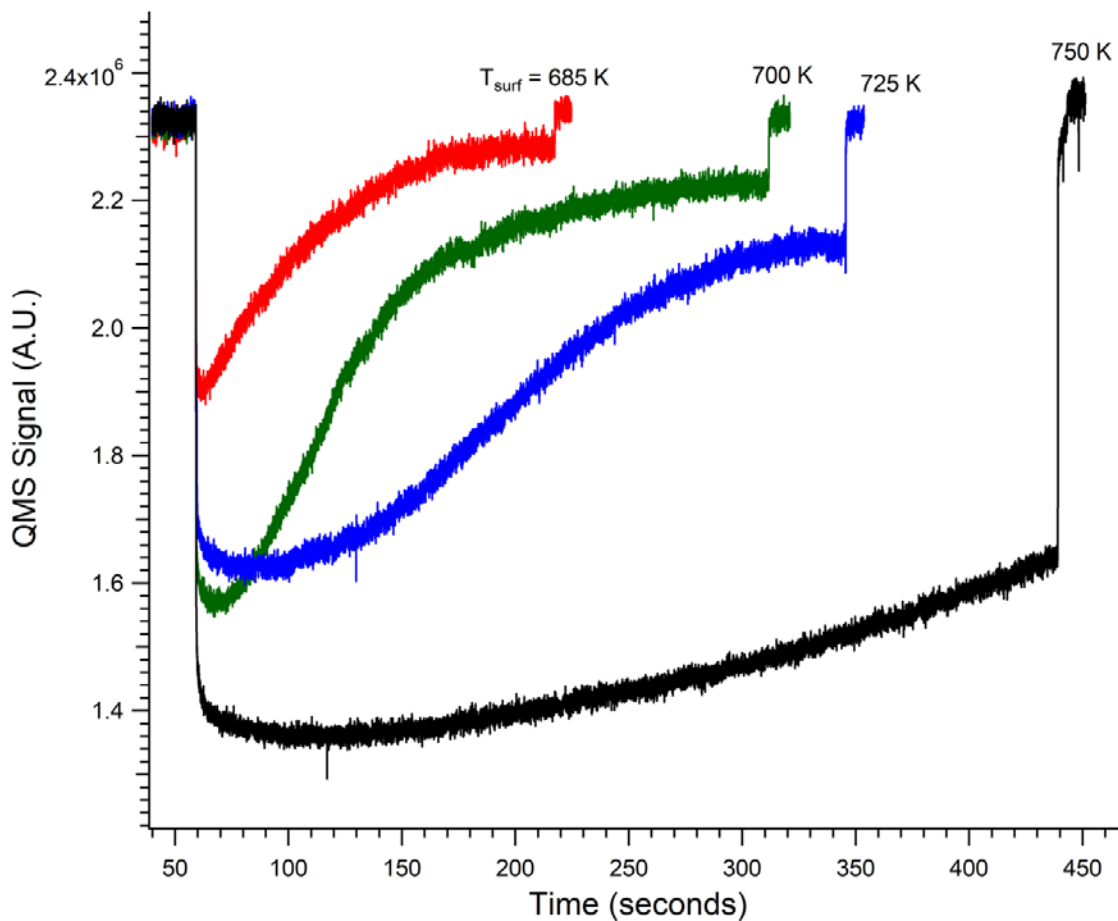


**Figure 6.3** King and Wells reflectivity measurements for  $\text{CH}_4$  on Ni(111) from  $T_{surf} = 685$  K to 750 K for the 0.05%  $\text{CH}_4/\text{H}_2$  molecular beam.

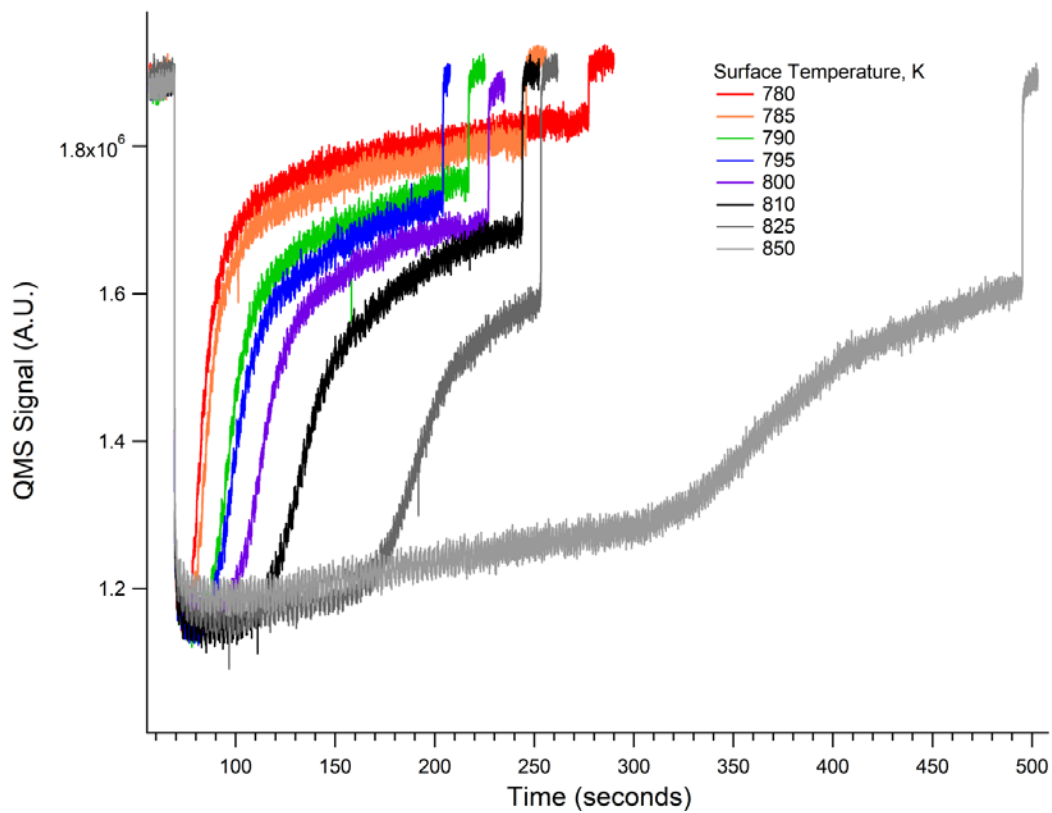


**Figure 6.4** King and Wells reflectivity measurements for CH<sub>4</sub> on Ni(111) from  $T_{surf} = 780$  K to 850 K for the 1% CH<sub>4</sub>/H<sub>2</sub> molecular beam.

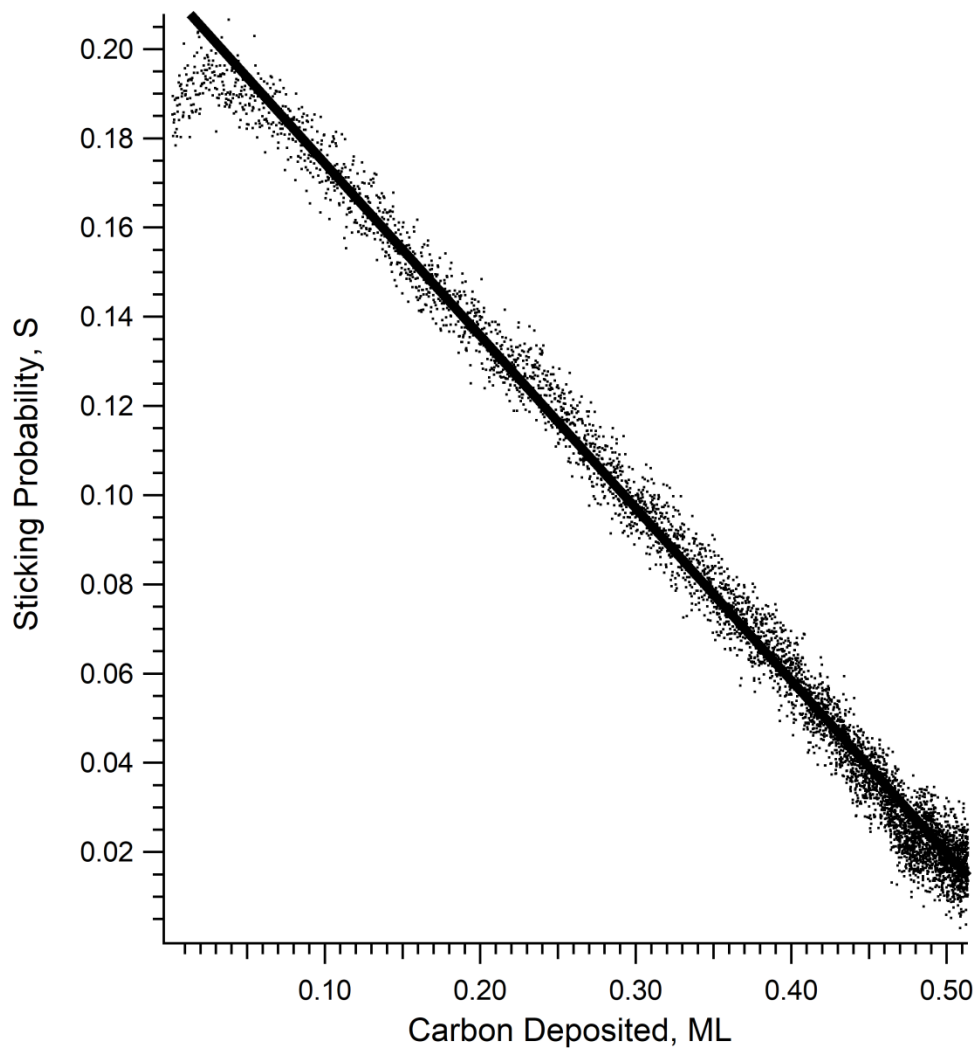


**Figure 6.5** Methane sticking probability as a function of total deposited carbon (ML) for the  $T_{surf} = 685$  K dose in Fig. 6.3.

showing similar reactivity. The sticking probabilities at steady state after carbon accumulation were also influenced by surface temperature, with more  $\text{CH}_4$  dissociation occurring at higher  $T_{surf}$  values. Multiplying the sticking probability at the steady state region by flux results in the steady state carbon accumulation, in ML/s. Overall surface temperature is observed to affect four factors for the lower flux mix: 1) initial sticking probability, 2) amount of carbon deposited before site blocking is observed, 3) total amount of carbon deposited until steady state is reached, 4) rate of steady state deposition. In these experiments, the incident reactive flux is relatively low, so there are, on average, many seconds during which a C reaction product could diffuse into the subsurface region and regenerate a reactive site before another methane impacts the surface at the same site. Next, we look at what happens when a higher incident flux beam decreases the time available between an initial reaction event and a subsequent methane-surface collision at that site.

The 1% methane/hydrogen beam has a nearly 10-fold higher reactive flux than the 0.05% beam, but very similar  $E_{trans}$ . This led to a much faster deposition rate where more than 15% of a ML was deposited per second at the beginning of each dose. At these beam energies and surface temperatures, the initial sticking probabilities,  $S_0$ , were nearly constant across the entire  $T_{surf} = 780 - 850$  K range. Therefore, the main difference in the traces in Figure 6.4 is the  $T_{surf}$  dependent C dissolution rate and its effect on subsequent methane dissociation and C deposition. The  $T_{surf} = 780$  K trace in Figure 6.4 shows nearly complete site

blocking within 25 seconds, with approximately 3 ML deposited before steady state was reached.

A series of K&W measurements were made for 5 K steps of  $T_{surf}$  from 785 K to 825 K, as shown in Figure 6.4. The overall shape of the K&W traces remains constant up to about 800 K. After the initial dip in QMS signal, which corresponds to reactivity on the bare surface, the QMS signal begins to rise as site blocking and other processes inhibit further sticking. After some time, the QMS signal approaches a quasi-steady-state value intermediate between full reflectivity ( $S(\theta) = 0$ ) and its initial value. Under these conditions, the reaction rate, as measured by the product of  $S(\theta)$  and incident flux, is equal to the dissolution rate of C leaving the surface. Figure 6.4 shows that this steady-state QMS signal, and the corresponding value of  $S(\theta)$ , as well as the amount of carbon deposited before steady state reactivity varies with surface temperature. The most significant change from  $T_{surf} = 780 - 800$  K was the change in  $S(\theta)$  as the system approached a steady state methane dissociation rate. Figure 6.6 shows the rate of carbon accumulation during this steady-state phase, which is assumed equal to the C dissolution rate, for every condition where a steady-state plateau in  $S(\theta)$  was reached. This was calculated simply by taking the average reaction probability across the plateau region multiplied by the incident flux. Note that measurements made with high- and low-flux beams yield identical dissolution kinetics, as they should. Also included in the plot are values obtained using the 0.25 CH<sub>4</sub>/H<sub>2</sub> mix used in Chapter 5 for comparison because that dataset included lower surface temperatures. At the lowest  $T_{surf}$  presented here, only  $9 \times 10^{-4}$  ML methane

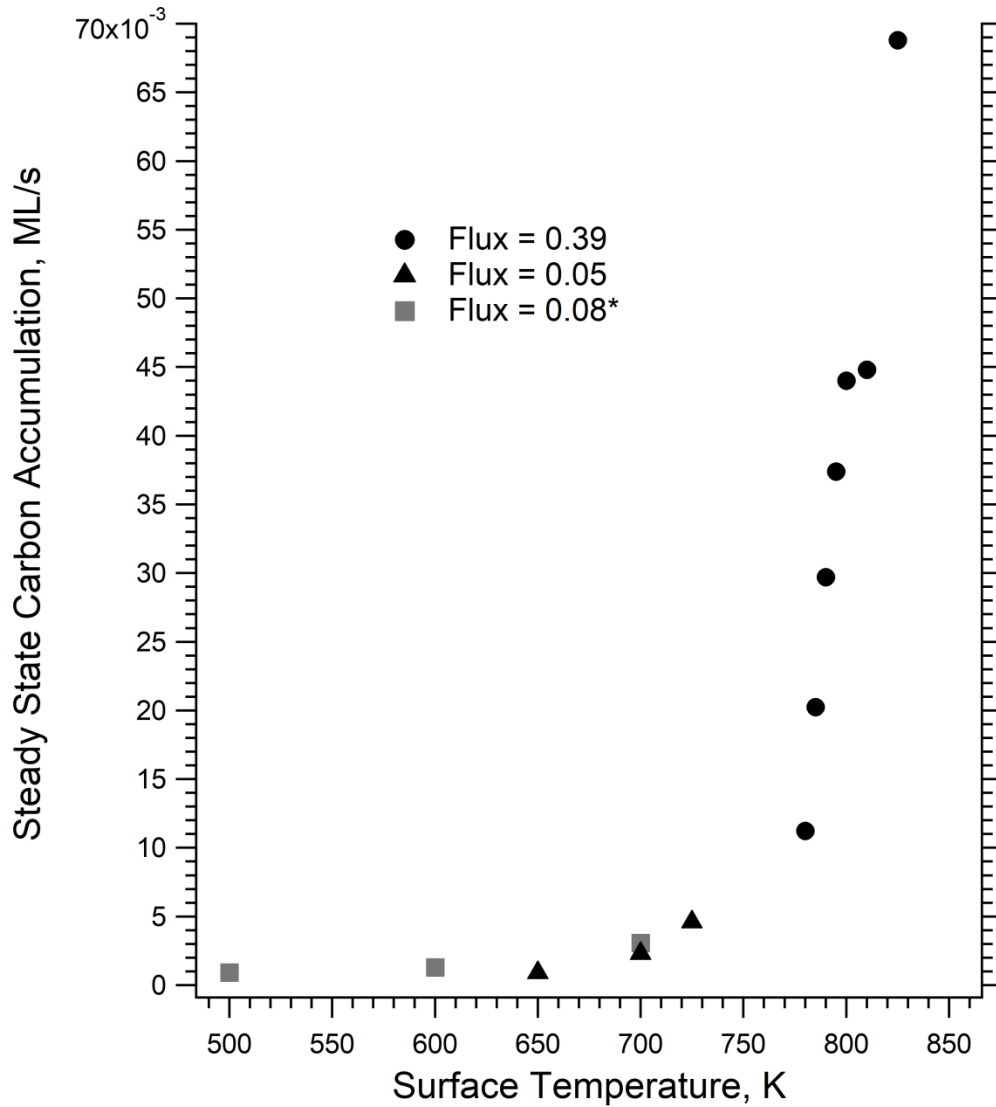


**Figure 6.6** Carbon accumulation rates at steady state on a carbon covered surface. The black markers are data collected with the 1% ( $\blacktriangle$ ) and 0.05% ( $\blacksquare$ )  $\text{CH}_4/\text{H}_2$  mixes. \*The data for flux = 0.08 ML/s with the 0.25%  $\text{CH}_4/\text{H}_2$  ( $\square$ ) mix presented in Chapter 5.

deposited per second on the carbon filled surface due to the extremely slow C absorption kinetics at this low surface temperature. This value increased rapidly for  $T_{surf} = 780 - 800$  K, increasing from 0.011 to 0.044 and reaching a maximum of 0.069 at  $T_{surf} = 825$  K. This highlights the rapid onset of carbon dissolution on the Ni(111) surface between 780 and 800 K. For  $T_{surf} = 850$  K there was no steady state reached; however, there was a linear decrease in sticking with increasing exposure and after approximately 250 seconds, or 40 ML of methane deposited, there was a more rapid transition in site blocking.

The amount of methane deposited onto the surface changed drastically from  $T_{surf} = 685 - 850$  K. Figure 6.7 summarizes the results collected across the entire temperature range, showing the calculated methane deposition in ML over the time of the dose. The dotted lines correspond to the 0.05% mix and solid lines the 1% mix. Over less than a 200 K range in surface temperature the same nickel crystal goes from being able to accommodate 0.5 ML to more than 50 ML. Qualitatively, this has been understood in our lab because we have been studying methane dissociation on Ni(111) for a long time.<sup>(60)</sup> Whenever we dose methane on the surface we flash the crystal and the carbon is no longer detectable, but I don't think we truly appreciated how readily the nickel dissolved the carbonaceous products. The first question that arises here is: where does the carbon go?

One possibility is that the carbon diffuses across the Ni(111) surface, finding unoccupied sites and freeing up the area where methane is deposited. Our chamber is equipped with a beam size selector. The experiments outlined above

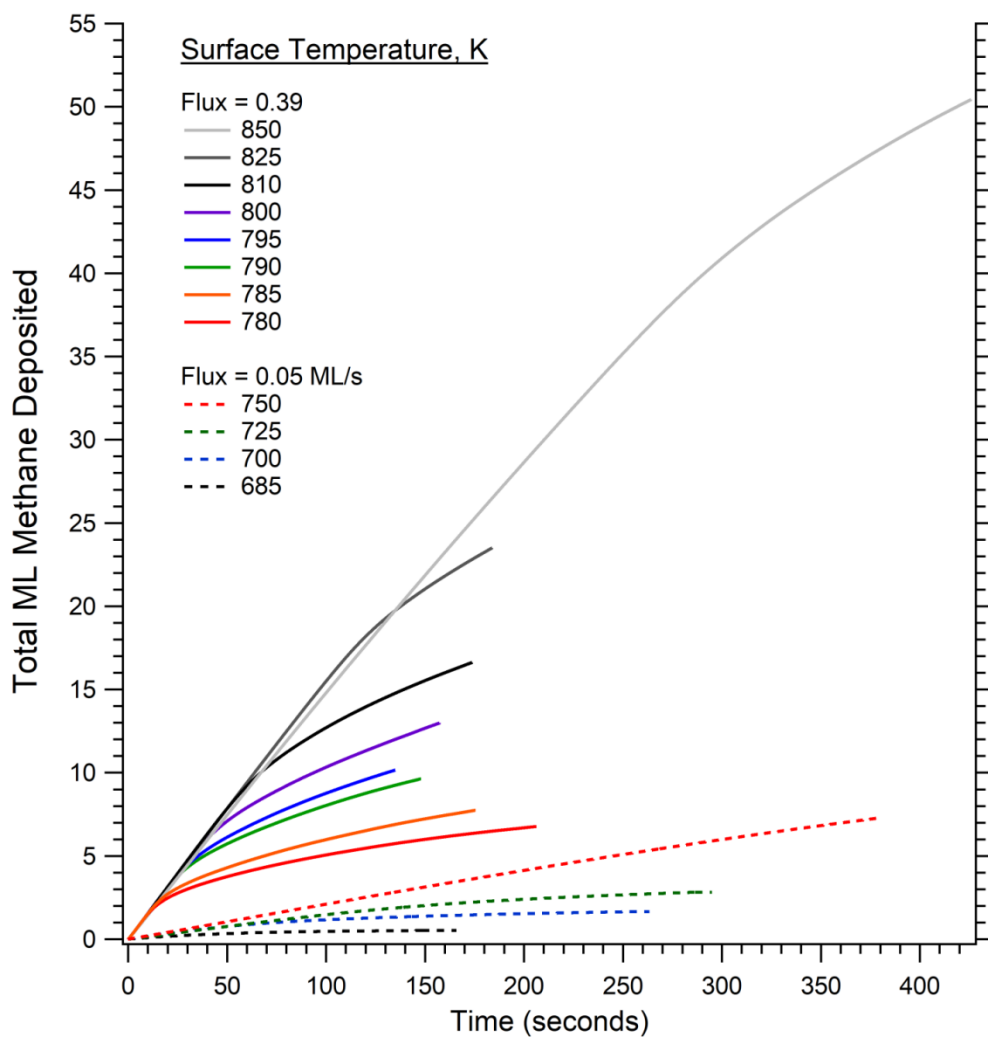


**Figure 6.7** Integrated methane accumulation on Ni(111) from  $T_{surf} = 685 - 850$  K for the two  $\text{CH}_4$  molecular beams used in this study.

were performed using the medium beam valve hole (MBVH) with a dose area of  $0.38 \text{ cm}^2$  on the crystal, corresponding to 49% of the total crystal area. The dose at  $T_{surf} = 780 \text{ K}$  was replicated for the small beam valve hole (SBVH) with a dose area of  $0.07 \text{ cm}^2$ , corresponding to an 8.4% overlap with the crystal surface. If there is spillover of carbon from the area being dosed, the MBVH condition should have less total carbon uptake than with the SBVH because there is less area to diffuse into. Figure 6.8 shows the results from these two doses. The two K&W traces fall nearly exactly on top of each other. Spillover does not appear to be a factor under these conditions.

An attempt was made to model the different processes for carbon accumulation on the surface based on the qualitative observations discussed above. An IGOR program included in Appendix C contains the start to that model; however, it was unable to reproduce the myriad experimental conditions. The general idea behind the model is to take the known amount of methane deposited onto the surface from experiment and allocate the resulting carbon product into different regions within the nickel lattice based on the prescribed surface temperature. The model is detailed graphically in Figure 6.9. The nickel lattice is separated into the subsurface and bulk regions. The methane molecule collides and reacts with the surface,  $k(c)$ , where the hydrogen atoms dissociate and recombinatively desorb. The surface carbon can then diffuse into the subsurface layer,  $k(+s)$ . The subsurface carbon can then diffuse into the bulk,  $k(b)$ , where it is never seen again (irreversible). These processes were based on the variable induction period where sticking did not change with exposure. In the

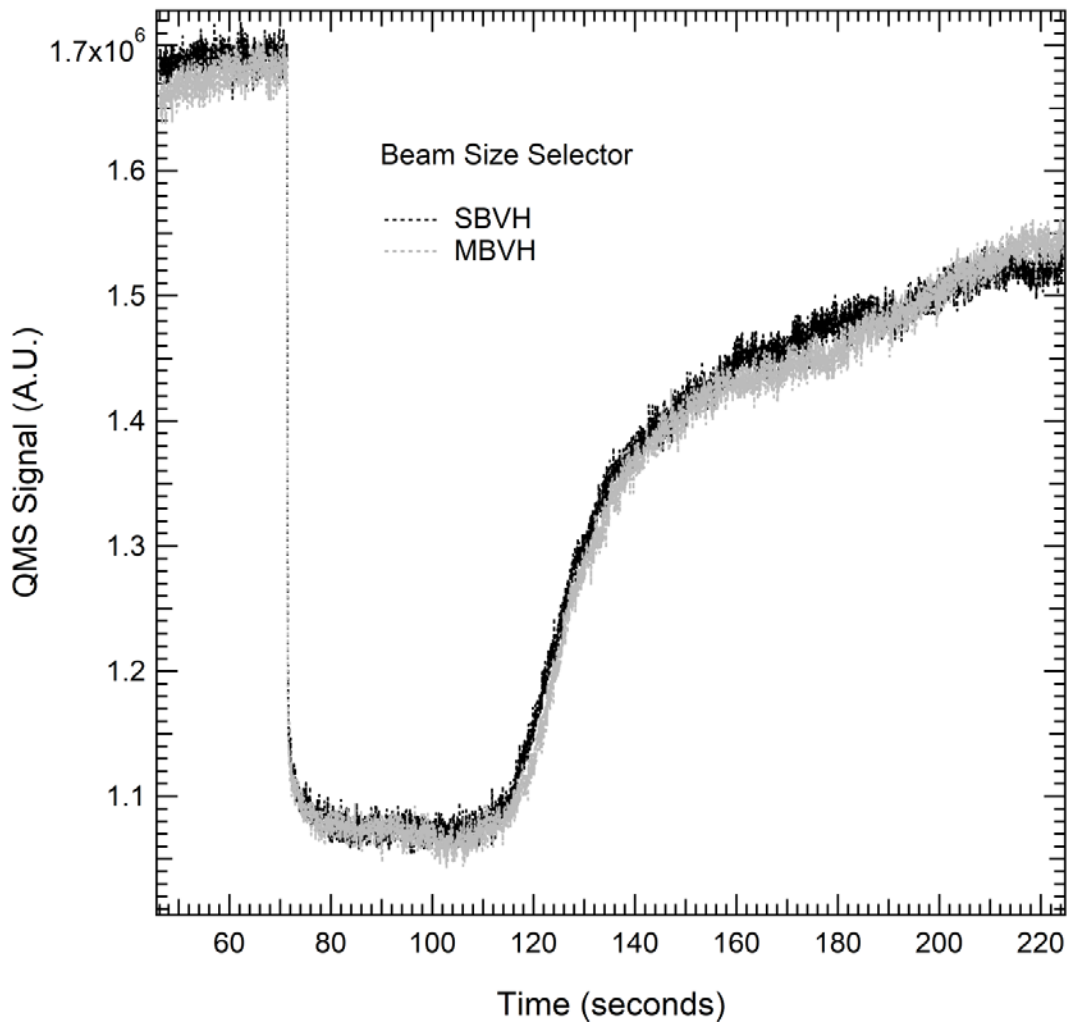


**Figure 6.8** Comparison of the K&W traces between the small beam valve hole (SBVH) and medium beam valve hole (MBVH) for the 1% CH<sub>4</sub>/H<sub>2</sub> mix at  $T_{surf} = 780$  K.

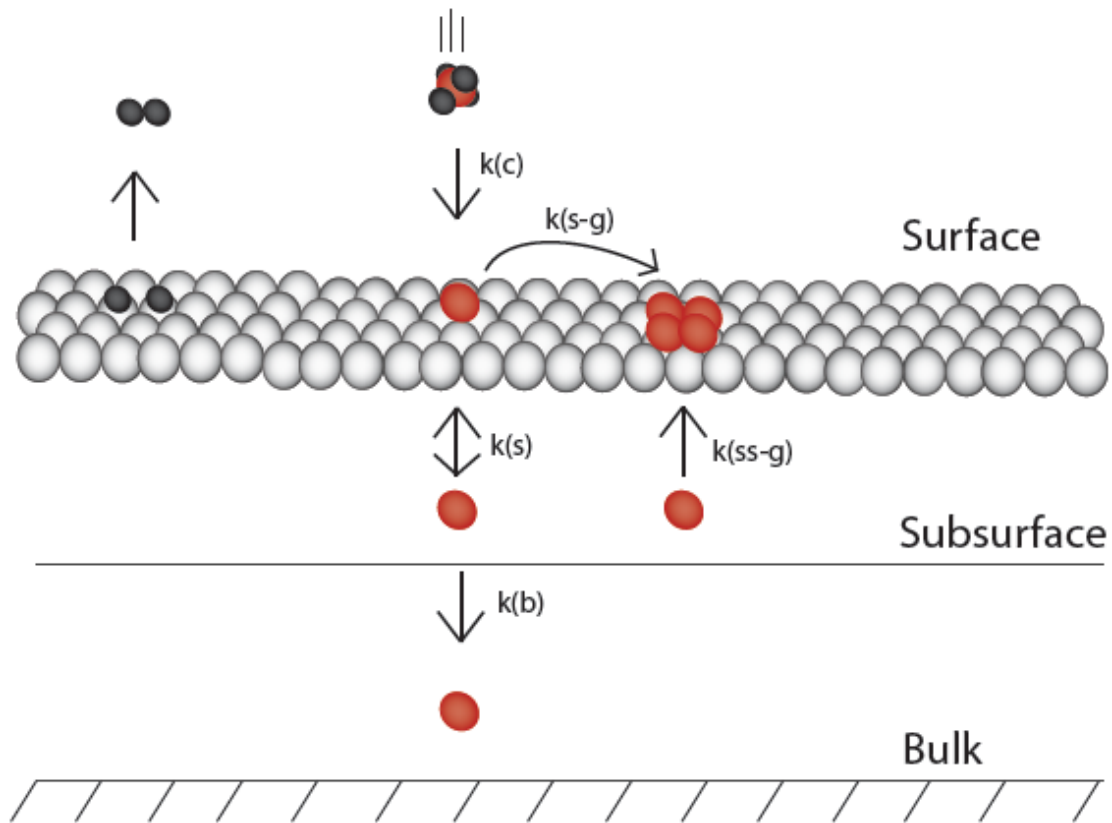


**Figure 6.9** Methane diffusion model into the Ni(111) subsurface and bulk from the surface. The methane molecule reacts on the surface [ $k(c)$ ] and diffuses into the subsurface [ $k(+s)$ ] where it can either diffuse back to onto the surface [ $k(-s)$ ] or into the bulk [ $k(b)$ ]. Graphene formation can proceed by aggregation on the surface [ $k(s-g)$ ] or as the carbon diffuses to the surface [ $k(ss-g)$ ].

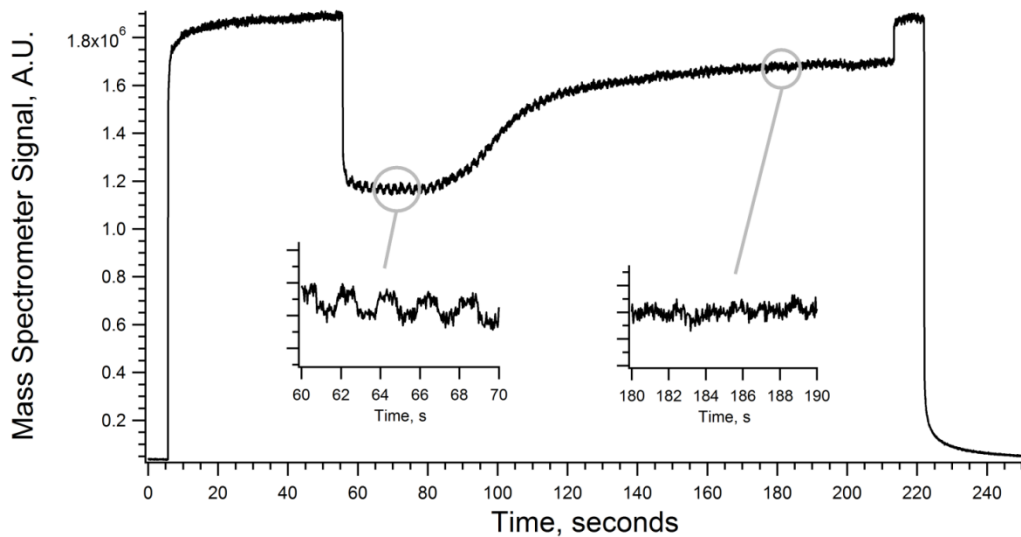


**Figure 6.10** King and Wells modulation experiment for CH<sub>4</sub> excited to the  $v_3$ ,  $v=1$  vibrational state. The insets demonstrate the change in sensitivity to the added vibration for a clean and carbon covered surface.

first 1-10's of seconds there was anywhere between 2 and 20 ML of methane deposition before there was accumulation on the surface that blocked sites. If the diffusion of carbon into the subsurface layer  $k(+s)$  is fast then the subsurface must be filled before surface accumulation occurs. Basically, it is the temperature dependent competition between transport from the surface to the subsurface and subsurface to the bulk. If diffusion into the bulk from the subsurface is slower than diffusion from the surface to the subsurface, then the subsurface will become filled and then carbon will accumulate on the surface and begin to inhibit further methane dissociation. As temperature is increased at the same  $k(c)$ , diffusion into the bulk becomes dominant, as demonstrated at  $T_{surf} = 850$  K. As surface coverage increases there is also the possibility of forming graphene.<sup>(46)</sup> Graphene stability on Ni(111) is higher than a lone bound carbon due to C-C bond interactions, making it more difficult to remove it from the surface. The model shown attempts to incorporate the ability of graphene to serve as a more stable sink for C on the surface by making it possible for graphene formation to come from surface aggregation,  $k(s-g)$ , or from carbon coming up from the subsurface,  $k(ss-g)$ . In the end, a simple transport model with a defined energy for C in each of these three locations – surface, subsurface, and bulk, does not capture the full range of experimental observations presented here. Additional processes and energetics are likely at play, and more work needs to be carried out to understand carbon migration in this system so these processes can be more accurately modeled.

Lastly, it was mentioned that laser modulation was performed for a few of these doses. The K&W laser modulation trace in Figure 6.9 demonstrates that

when sticking is high and methane is reacting on a “clean” surface the vibrationally excited molecules are more reactive. As site blocking increased, the reactivity for both the laser on and laser off beams decreased.

## 6.4 Conclusion and Future Directions

Methane dissociation on single crystals has been an area of great interest to surface scientists. Its application in the steam reforming of methane to produce hydrogen has been one of the main focuses. It is also a convenient system to study carbon dissolution kinetics when coupled with a molecular beam apparatus. Beam-surface experiments performed under ultra-high vacuum provide a clean environment where side reactions are minimized where the energetic molecules and high surface temperatures present under reactor conditions can be studied. Use of a molecular beam produces a well defined beam of reagents with a large reactive flux to the surface, removing the requirement for high pressures.

Methane molecular beam studies are most often carried out on the simplest surface without contaminants. In a reactor there is no such thing as a clean surface, subsurface, or bulk for a catalyst. In this study, we took a step away from the idealized system and studied the uptake of carbon into a Ni(111) surface. King and Wells experiments gave a direct measurement of carbon loading under precise reaction conditions. One of the difficulties now is to create a model to accurately describe exactly where that carbon is distributed throughout the lattice. A set of experiments that would be insightful would be to dose the surface with the beam until it is saturated. Then, block the deposition beam and wait varying amounts of time before re-introducing the beam to the crystal surface. This would allow the already deposited carbon to accommodate to the different lattice layers, and the subsequent deposition would give a readout on the current surface coverage if the function  $S(\theta)$  was known.

These experiments also lead to an interesting question: is it coincidence that methane dissociation becomes insensitive to changes in  $T_{surf}$  at the same temperature where carbon dissolution becomes active? There is clearly something going on with the surface above  $\sim 750$  K. He scattering experiments in this temperature regime (no studies were found at these high of temperatures) would provide some useful information about the morphological changes occurring to the surface atoms.

## 6.5 References

1. C. Klink, I. Stensgaard, F. Besenbacher, E. Lægsgaard, An STM study of carbon-induced structures on Ni(111): evidence for a carbide-phase clock reconstruction. *Surface Science* **342**, 250-260 (1995).
2. L. P. Nielsen, F. Besenbacher, E. Laegsgaard, I. Stensgaard, Nucleation and growth of a H-induced reconstruction of Ni(110). *Physical Review B* **44**, 13156-13159 (1991).
3. A. R. Alemozafar, R. J. Madix, Two-dimensional condensation anisotropic crystallization: H<sub>2</sub>/Ni(1 1 0). *Surface Science* **557**, 231-242 (2004).
4. P. L. Hansen, J. B. Wagner, S. Helveg, J. R. Rostrup-Nielsen, B. S. Clausen, H. Topsøe, Atom-Resolved Imaging of Dynamic Shape Changes in Supported Copper Nanocrystals. *Science* **295**, 2053-2055 (2002).
5. H. Bluhm, M. Hävecker, A. Knop-Gericke, E. Kleimenov, R. Schlögl, D. Teschner, V. I. Bukhtiyarov, D. F. Ogletree, M. Salmeron, Methanol Oxidation on a Copper Catalyst Investigated Using in Situ X-ray Photoelectron Spectroscopy. *The Journal of Physical Chemistry B* **108**, 14340-14347 (2004).
6. R. Blume, M. Havecker, S. Zafeirotos, D. Teschner, E. Vass, P. Schnorch, A. Knop-Gericke, R. Schlogl, S. Lizzit, P. Dudin, A. Barinov, M. Kiskinova, Monitoring in situ catalytically active states of Ru catalysts for different methanol oxidation pathways. *Physical Chemistry Chemical Physics* **9**, 3648-3657 (2007).
7. A. D. Johnson, S. P. Daley, A. L. Utz, S. T. Ceyer, The Chemistry of Bulk Hydrogen: Reaction of Hydrogen Embedded in Nickel with Adsorbed CH<sub>3</sub>. *Science* **257**, 223-225 (1992).
8. L. Vattuone, L. Savio, M. Rocca, Direct Access to Subsurface Sites in Gas-Surface  $\{\mathrm{O}\}_2/\mathrm{A}\{\mathrm{g}\}(210)$  Interactions using Supersonic Molecular Beams. *Physical Review Letters* **90**, 228302 (2003).
9. R. Imbihl, G. Ertl, Oscillatory Kinetics in Heterogeneous Catalysis. *Chemical Reviews* **95**, 697-733 (1995).
10. X. C. Guo, J. M. Bradley, A. Hopkinson, D. A. King, O<sub>2</sub> interaction with Pt{100}-hex-R0.7°: scattering, sticking and saturating. *Surface Science* **310**, 163-182 (1994).
11. J. M. Bradley, X. C. Guo, A. Hopkinson, D. A. King, A molecular beam investigation into the dynamics and kinetics of dissociative O<sub>2</sub> adsorption on Pt{100}-(1×1). *The Journal of Chemical Physics* **104**, 4283-4293 (1996).
12. L. Savio, A. Gerbi, L. Vattuone, A. Baraldi, G. Comelli, M. Rocca, Monitoring Super- and Subsurface Oxygen on Ag(210) by High Energy Resolution X-ray Photoelectron Spectroscopy: Subsurface Diffusion and Segregation. *The Journal of Physical Chemistry B* **110**, 942-947 (2006).
13. S. T. Ceyer, The Unique Chemistry of Hydrogen beneath the Surface: Catalytic Hydrogenation of Hydrocarbons. *Accounts of Chemical Research* **34**, 737-744 (2001).

14. Á. Molnár, A. Sárkány, M. Varga, Hydrogenation of carbon–carbon multiple bonds: chemo-, regio- and stereo-selectivity. *Journal of Molecular Catalysis A: Chemical* **173**, 185-221 (2001).
15. A. Borodziński, G. C. Bond, Selective Hydrogenation of Ethyne in Ethene-Rich Streams on Palladium Catalysts. Part 1. Effect of Changes to the Catalyst During Reaction. *Catalysis Reviews* **48**, 91-144 (2006).
16. D. Teschner, J. Borsodi, A. Wootsch, Z. Révay, M. Hävecker, A. Knop-Gericke, S. D. Jackson, R. Schlögl, The Roles of Subsurface Carbon and Hydrogen in Palladium-Catalyzed Alkyne Hydrogenation. *Science* **320**, 86-89 (2008).
17. J. J. Lander, H. E. Kern, A. L. Beach, Solubility and Diffusion Coefficient of Carbon in Nickel: Reaction Rates of Nickel-Carbon Alloys with Barium Oxide. *Journal of Applied Physics* **23**, 1305-1309 (1952).
18. L. S. Lobo, J. L. Figueiredo, C. A. Bernardo, Carbon formation and gasification on metals. Bulk diffusion mechanism: A reassessment. *Catalysis Today* **178**, 110-116 (2011).
19. H. S. Bengaard, J. K. Nørskov, J. Sehested, B. S. Clausen, L. P. Nielsen, A. M. Molenbroek, J. R. Rostrup-Nielsen, Steam Reforming and Graphite Formation on Ni Catalysts. *Journal of Catalysis* **209**, 365-384 (2002).
20. J. Xu, M. Saeys, First Principles Study of the Effect of Carbon and Boron on the Activity of a Ni Catalyst. *The Journal of Physical Chemistry C* **113**, 4099-4106 (2009).
21. K. S. Novoselov, A. K. Geim, S. V. Morozov, D. Jiang, Y. Zhang, S. V. Dubonos, I. V. Grigorieva, A. A. Firsov, Electric Field Effect in Atomically Thin Carbon Films. *Science* **306**, 666-669 (2004).
22. C. Lee, X. Wei, J. W. Kysar, J. Hone, Measurement of the Elastic Properties and Intrinsic Strength of Monolayer Graphene. *Science* **321**, 385-388 (2008).
23. J. S. Bunch, S. S. Verbridge, J. S. Alden, A. M. van der Zande, J. M. Parpia, H. G. Craighead, P. L. McEuen, Impermeable Atomic Membranes from Graphene Sheets. *Nano Letters* **8**, 2458-2462 (2008).
24. L. Zhu, J. Wang, T. Zhang, L. Ma, C. W. Lim, F. Ding, X. C. Zeng, Mechanically Robust Tri-Wing Graphene Nanoribbons with Tunable Electronic and Magnetic Properties. *Nano Letters* **10**, 494-498 (2010).
25. A. A. Balandin, S. Ghosh, W. Bao, I. Calizo, D. Teweldebrhan, F. Miao, C. N. Lau, Superior Thermal Conductivity of Single-Layer Graphene. *Nano Letters* **8**, 902-907 (2008).
26. N. Mingo, D. A. Broido, Carbon Nanotube Ballistic Thermal Conductance and Its Limits. *Physical Review Letters* **95**, 096105 (2005).
27. S. Ghosh, I. Calizo, D. Teweldebrhan, E. P. Pokatilov, D. L. Nika, A. A. Balandin, W. Bao, F. Miao, C. N. Lau, Extremely high thermal conductivity of graphene: Prospects for thermal management applications in nanoelectronic circuits. *Applied Physics Letters* **92**, 151911 (2008).
28. L. Yang, J. Deslippe, C.-H. Park, M. L. Cohen, S. G. Louie, Excitonic Effects on the Optical Response of Graphene and Bilayer Graphene. *Physical Review Letters* **103**, 186802 (2009).
29. Z. Chen, X.-Q. Wang, Stacking-dependent optical spectra and many-electron effects in bilayer graphene. *Physical Review B* **83**, 081405 (2011).
30. A. N. Obraztsov, Chemical vapour deposition: Making graphene on a large scale. *Nat Nano* **4**, 212-213 (2009).

31. J. Gao, J. Yip, J. Zhao, B. I. Yakobson, F. Ding, Graphene Nucleation on Transition Metal Surface: Structure Transformation and Role of the Metal Step Edge. *Journal of the American Chemical Society* **133**, 5009-5015 (2011).
32. D. Wei, Y. Liu, Controllable Synthesis of Graphene and Its Applications. *Advanced Materials* **22**, 3225-3241 (2010).
33. A. Reina, X. Jia, J. Ho, D. Nezich, H. Son, V. Bulovic, M. S. Dresselhaus, J. Kong, Large Area, Few-Layer Graphene Films on Arbitrary Substrates by Chemical Vapor Deposition. *Nano Letters* **9**, 30-35 (2009).
34. X. Li, W. Cai, J. An, S. Kim, J. Nah, D. Yang, R. Piner, A. Velamakanni, I. Jung, E. Tutuc, S. K. Banerjee, L. Colombo, R. S. Ruoff, Large-Area Synthesis of High-Quality and Uniform Graphene Films on Copper Foils. *Science* **324**, 1312-1314 (2009).
35. M. Batzill, The surface science of graphene: Metal interfaces, CVD synthesis, nanoribbons, chemical modifications, and defects. *Surface Science Reports* **67**, 83-115 (2012).
36. N. C. Bartelt, K. F. McCarty, Graphene growth on metal surfaces. *MRS Bulletin* **37**, 1158-1165 (2012).
37. C. Mattevi, H. Kim, M. Chhowalla, A review of chemical vapour deposition of graphene on copper. *Journal of Materials Chemistry* **21**, 3324-3334 (2011).
38. Y. Yao, Z. Li, Z. Lin, K.-S. Moon, J. Agar, C. Wong, Controlled Growth of Multilayer, Few-Layer, and Single-Layer Graphene on Metal Substrates. *The Journal of Physical Chemistry C* **115**, 5232-5238 (2011).
39. J. D. Wood, S. W. Schmucker, A. S. Lyons, E. Pop, J. W. Lyding, Effects of Polycrystalline Cu Substrate on Graphene Growth by Chemical Vapor Deposition. *Nano Letters* **11**, 4547-4554 (2011).
40. S. Nie, J. M. Wofford, N. C. Bartelt, O. D. Dubon, K. F. McCarty, Origin of the mosaicity in graphene grown on Cu(111). *Physical Review B* **84**, 155425 (2011).
41. S. W. Cranford, M. J. Buehler, Mechanical properties of graphyne. *Carbon* **49**, 4111-4121 (2011).
42. L. Gao, J. R. Guest, N. P. Guisinger, Epitaxial Graphene on Cu(111). *Nano Letters* **10**, 3512-3516 (2010).
43. A. Kumar, A. A. Voevodin, D. Zemlyanov, D. N. Zakharov, T. S. Fisher, Rapid synthesis of few-layer graphene over Cu foil. *Carbon* **50**, 1546-1553 (2012).
44. B. Hu, H. Ago, Y. Ito, K. Kawahara, M. Tsuji, E. Magome, K. Sumitani, N. Mizuta, K.-i. Ikeda, S. Mizuno, Epitaxial growth of large-area single-layer graphene over Cu(1 1 1)/sapphire by atmospheric pressure CVD. *Carbon* **50**, 57-65 (2012).
45. A. Guermoune, T. Chari, F. Popescu, S. S. Sabri, J. Guillemette, H. S. Skulason, T. Szkopek, M. Siaz, Chemical vapor deposition synthesis of graphene on copper with methanol, ethanol, and propanol precursors. *Carbon* **49**, 4204-4210 (2011).
46. J. Lahiri, T. Miller, L. Adamska, I. I. Oleynik, M. Batzill, Graphene Growth on Ni(111) by Transformation of a Surface Carbide. *Nano Letters* **11**, 518-522 (2011).

47. G. Alexander, K. Kurt, V. V. Denis, Dynamics of graphene growth on a metal surface: a time-dependent photoemission study. *New Journal of Physics* **11**, 073050 (2009).
48. D. Cheng, G. Barcaro, J.-C. Charlier, M. Hou, A. Fortunelli, Homogeneous Nucleation of Graphitic Nanostructures from Carbon Chains on Ni(111). *The Journal of Physical Chemistry C* **115**, 10537-10543 (2011).
49. M. Xu, D. Fujita, K. Sagisaka, E. Watanabe, N. Hanagata, Production of Extended Single-Layer Graphene. *ACS Nano* **5**, 1522-1528 (2011).
50. S. Hofmann, R. Sharma, C. Ducati, G. Du, C. Mattevi, C. Cepek, M. Cantoro, S. Pisana, A. Parvez, F. Cervantes-Sodi, A. C. Ferrari, R. Dunin-Borkowski, S. Lizzit, L. Petaccia, A. Goldoni, J. Robertson, In situ Observations of Catalyst Dynamics during Surface-Bound Carbon Nanotube Nucleation. *Nano Letters* **7**, 602-608 (2007).
51. R. S. Weatherup, B. C. Bayer, R. Blume, C. Ducati, C. Baehtz, R. Schlögl, S. Hofmann, In Situ Characterization of Alloy Catalysts for Low-Temperature Graphene Growth. *Nano Letters* **11**, 4154-4160 (2011).
52. X. Li, W. Cai, L. Colombo, R. S. Ruoff, Evolution of Graphene Growth on Ni and Cu by Carbon Isotope Labeling. *Nano Letters* **9**, 4268-4272 (2009).
53. B. Wu, D. Geng, Z. Xu, Y. Guo, L. Huang, Y. Xue, J. Chen, G. Yu, Y. Liu, Self-organized graphene crystal patterns. *NPG Asia Mater* **5**, e36 (2013).
54. M. Losurdo, M. M. Giangregorio, P. Capezzuto, G. Bruno, Graphene CVD growth on copper and nickel: role of hydrogen in kinetics and structure. *Physical Chemistry Chemical Physics* **13**, 20836-20843 (2011).
55. K. Li, C. He, M. Jiao, Y. Wang, Z. Wu, A first-principles study on the role of hydrogen in early stage of graphene growth during the CH<sub>4</sub> dissociation on Cu(1 1 1) and Ni(1 1 1) surfaces. *Carbon* **74**, 255-265 (2014).
56. A. A. Puzos, I. A. Merkulov, C. M. Rouleau, G. Eres, D. B. Geohegan, Revealing the surface and bulk regimes of isothermal graphene nucleation and growth on Ni with in situ kinetic measurements and modeling. *Carbon* **79**, 256-264 (2014).
57. L. S. T. Lobo, D. L., Complex Temperature Dependencies of the Rate of Carbon Deposition on Nickel. *Nature Physical Science* **234**, 15 (1971).
58. P. Trinsoutrot, H. Vergnes, B. Caussat, Three dimensional graphene synthesis on nickel foam by chemical vapor deposition from ethylene. *Materials Science and Engineering: B* **179**, 12-16 (2014).
59. L. B. F. Juurlink, PhD Thesis, Eigenstate-resolved measurements of methane dissociation on Ni(100), *Tufts University* (2000).
60. R. R. Smith, PhD Thesis, Rovibrational State-Resolved Studies of Methane Dissociation on Ni(111), *Tufts University* (2003).



# Appendix A

## LabVIEW Crystal Temperature Controller

### A.1 Overview

Control and monitoring of the crystal temperature was aided by the development of a new LabVIEW based PID controller. The previous generation of PID temperature controller(1) was adequate for precision control through the manipulation of adjustable potentiometers but lacked any graphical user interface (GUI). The advantages of switching to a computer controlled system are i) the elimination of integrated circuit components which are susceptible to failure, ii) facile switching between the type of thermocouple used for feedback monitoring, iii) real-time monitoring of the surface temperature over a long time period via the GUI and iv) rapid switching between temperature ramping parameters.

The general schematic for the new system is displayed in Figure A.1 but is exactly the same as before with the exception of replacing the PID controller with a computer. A thermocouple (E) spot welded to the top of the crystal provides a direct readout of the crystal temperature which is used as the process variable for the PID algorithm. The thermocouple signal passes through a thermocouple conditioner (D) before being fed into the data acquisition computer (DAC, A) through a 16-bit Measurement and Computer

analog to digital converter (B). A home-made 1% thoriated tungsten filament (F) placed approximately 5 mm from the rear face of the crystal is driven by a 0-10 A power supply (C) controlled by the DAC. A forward bias can be applied to the crystal via a 0-1000 V power supply (G) to achieve temperatures greater than 800 K.

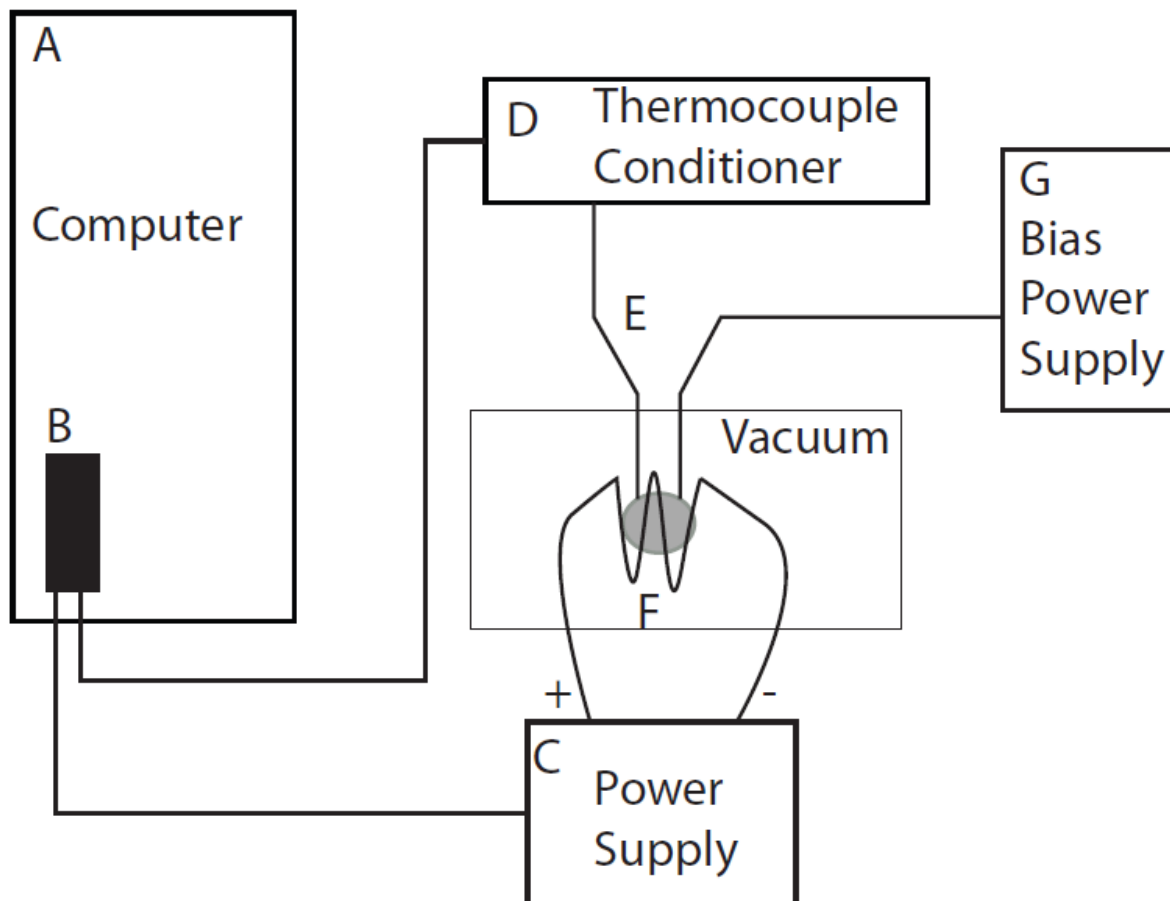


**Figure A. 1** Generalized schematic for crystal heater assembly with computerized control.

- A) Data acquisition computer, Windows PC running XP
- B) Measurement and Computing DAS1602/16 acquisition board
- C) Kepco Power Supply ATE 6-10M [0-6 V, 0-10 A]
- D) Intronic Power Isolated Thermocouple Conditioner
- E) Type-E thermocouple
- F) Filament, 1% thoriated tungsten
- G) Kepco Power Supply BHK 1000-0.2M

## A.2 General operation of PID controller

The program was written in LabVIEW version 7.1 along with Measurement and Computing's packaged VIs and Instacal for board configuration. The front panel for the PID controller is displayed in Figure A.2. The PID control variables in the upper left hand corner are empirically determined through iterative tuning. When the program was initially developed it appeared that there would need to be different settings for when the forward bias was on versus off. To date this is not a requirement and a single set of control variables is used for both conditions, however, the ease of switching between control variables through the LabVIEW based PID controller make this a seamless transition if required in the future.

There are three different modes of operation for this program. The first is in Manual mode where the filament drive voltage is directly controlled by a 0-10 V slider under "Manual Voltage Control". This is useful when the rate of temperature change is unimportant such as when the crystal is being set to a constant surface temperature,  $T_{surf}$ , for cleaning or experimental doses. It is important to slowly increase the voltage when in Manual mode to prevent large current spikes. The filament is especially susceptible to current spikes after prolonged periods of disuse. A good general rule of thumb is to increase 1 V over 1 second while observing the current output on the Kepco power supply (C). The second mode of

operation is when a constant temperature is desired. To achieve a constant temperature first ensure that the Manual/Ramp toggle is set to Manual. Input the desired temperature into one of the “Final Temp” fields under “Ramp Controls”. Next, move the toggle switch in the same area so that it is directed towards your desired “Final Temp”. Change the “Ramp Rate” field under the selected “Final Temp” field to a large value, e.g. 200. The ramp rate is unimportant here because we are just setting it to a constant temperature. Setting it to a high value ensure that the “Set Point” is equal to your Final Temp in a matter of seconds. Click the red “STOPPED” button and it will turn green and indicate “RUNNING”. At this point the Set Point trace to the right will start at the current  $T_{surf}$  and end at Final Temp. For example, if  $T_{surf} = 300$  K and the Final Temp is set at 900 K with a Ramp Rate of 200 K upon pressing STOPPED the Set Point will increase linearly from 300 to 900 K in 3 seconds. Performing this operation will have NO impact on the drive voltage because the Manual mode is selected. The Set Point value is only used when the Manual/Ramp toggle is in Ramp mode. Now that the Set Point is at the desired temperature increase the Manual Control Voltage, as described above, until the crystal temperature is at the Set Point value. At this point flip the toggle into Ramp mode; the PID control variables now define how the drive voltage responds to crystal temperature and the crystal temperature should rapidly approach the set point and remain within  $\pm 0.5$  K. For best results it is advised to slightly overshoot the desired temperature and

toggle into Ramp mode while the crystal temperature is still increasing. One danger in using these controls is the ability to over drive the filament current leading to damage of the filament or crystal. This is most likely to happen when the set point is significantly higher than the crystal temperature when switching into Ramp mode. This is a consequence of the PID algorithm trying its best to achieve the set point even if that means applying the full 10 V drive signal from the computer. After the desired amount of time has elapsed for cleaning or dosing the crystal temperature can be decreased by decreasing the Manual Control Voltage to zero and toggling to Manual mode allowing the crystal to cool without any applied heat from the filament. The last mode is used when a specific rate of crystal temperature increase is desired. First, start with the procedure for achieving a constant temperature and get the crystal temperature to the desired initial temperature. The toggle should be in Ramp mode at this point. In the other set point field that is not currently being used to hold the crystal at constant temperature input the desired Final Temp and Ramp Rate and ensure that the STOPPED button is not RUNNING. Once those fields are properly populated and the crystal is stable at the initial temperature the temperature ramp is ready to be initialized. Click the STOPPED button and quickly toggle the Ramp Controls toggle to point to the other set of ramp controls. Now the Set Point will linearly increase from the initial temperature to the final temperature based on the input ramp rate and the crystal temperature will mimic this ramp behavior. A

best practice here is to try this BEFORE you run the real experiment. The PID control variables are well tuned to achieve a constant temperature and may not be adequate for each individual ramp condition. If needed, tune the PID control variables and use the ability to rapidly toggle between two different PID control variables as discussed above. The most difficult regime to achieve a smooth ramp rate is at low temperatures where the drive voltage is initially very small. The crystal temperature can lag behind the set point by several degrees; if this is the case a larger P control variable can help lessen the lag.

The last feature in the front panel is the ability to add audible indicators at specified crystal temperatures. Experiments can become tedious, especially after several hundred repetitive experimental doses. If this is the case and your head is buried in a book or the latest internet meme set the appropriate toggles on the “Noise Indicators” section to ensure you don’t waste precious minutes being distracted while the crystal is ready to go!

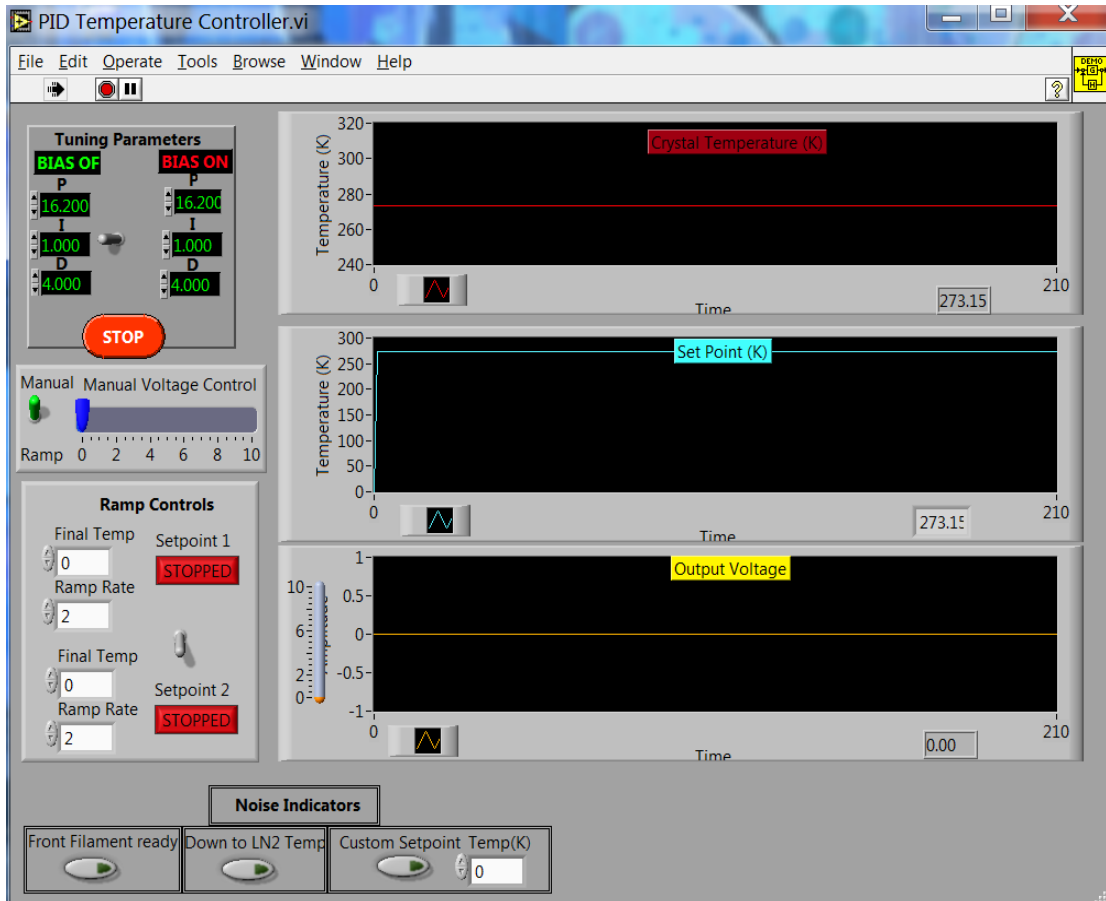
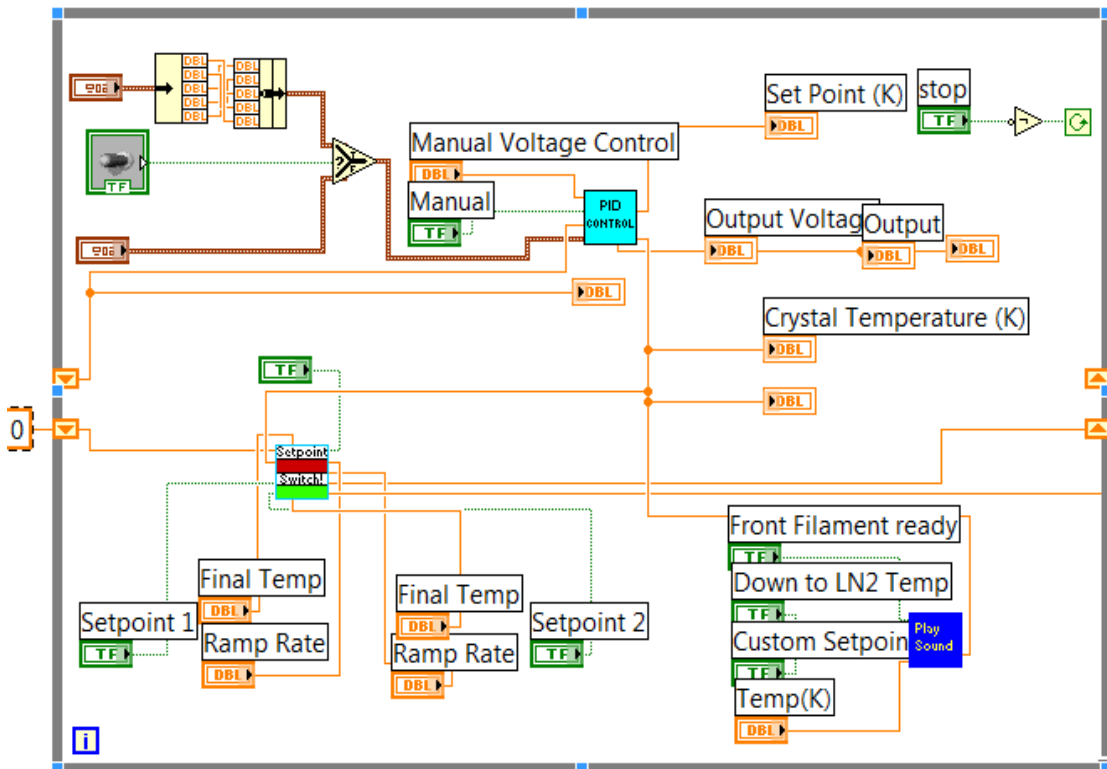


Figure A. 2 Front panel for “PID Temperature Controller.VI”



**Figure A. 3** Block diagram for “PID Temperature Controller.VI”

### A.3 LabVIEW Programming

LabVIEW programs are termed virtual instruments (VIs) and can contain multiple sub-routines within the same program. The three components to a LabVIEW program are the front panel where the user can make changes or view readouts, as in Figure A.2, the block diagram where components are connected to produce the proper programmatic flow, and the connector panel, where sub-routines pass variables between each other.

For the PID Temperature Controller described here there are a total of seven sub-routines and one front panel (PID Temperature Controller.VI). The programming hierarchy with the appropriate figure labels found in this section:

- PID Temperature Controller.vi Figure A.2,3
  - Simplified PID with normalized output.vi Figure A.4
    - Simple PID.vi Figure A.5
    - PID Temp reading.vi Figure A.6
      - Conv Type E, mV-K.vi Figure A.7
  - Switching between setpoints.vi Figure A.8
    - Setpoint Caclulator.vi Figure A.9
  - Play Sound.vi Figure A.10

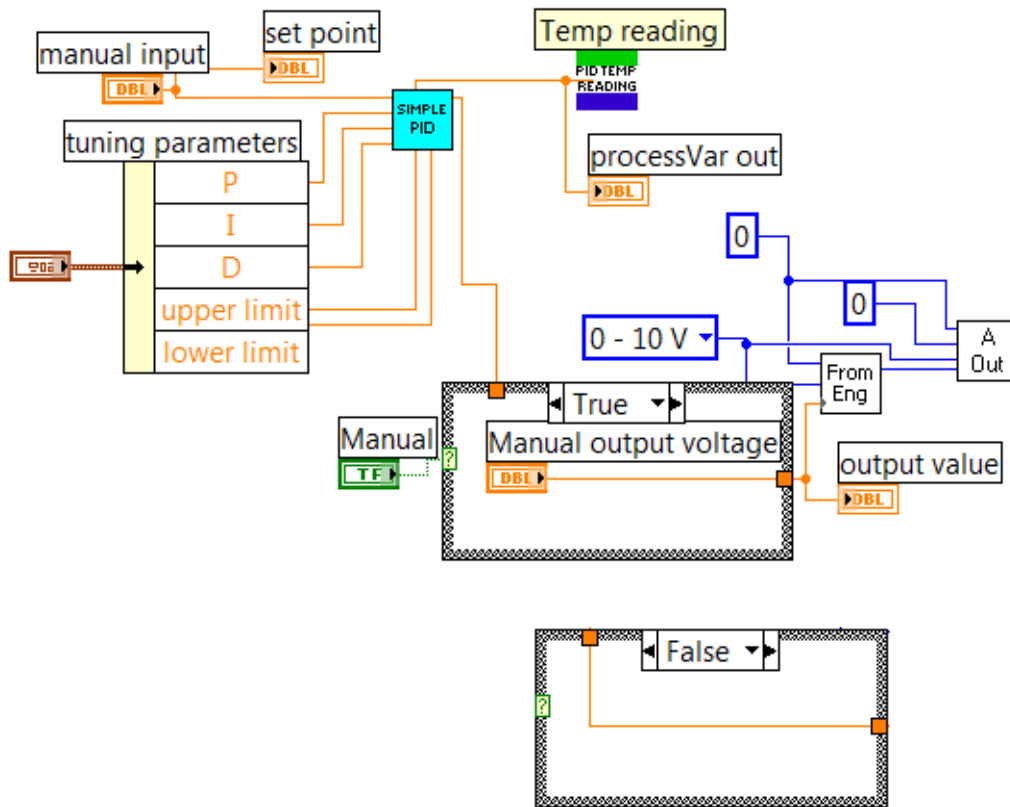


**Figure A. 4** Block diagram for “Simplified PID with normalized output.VI”

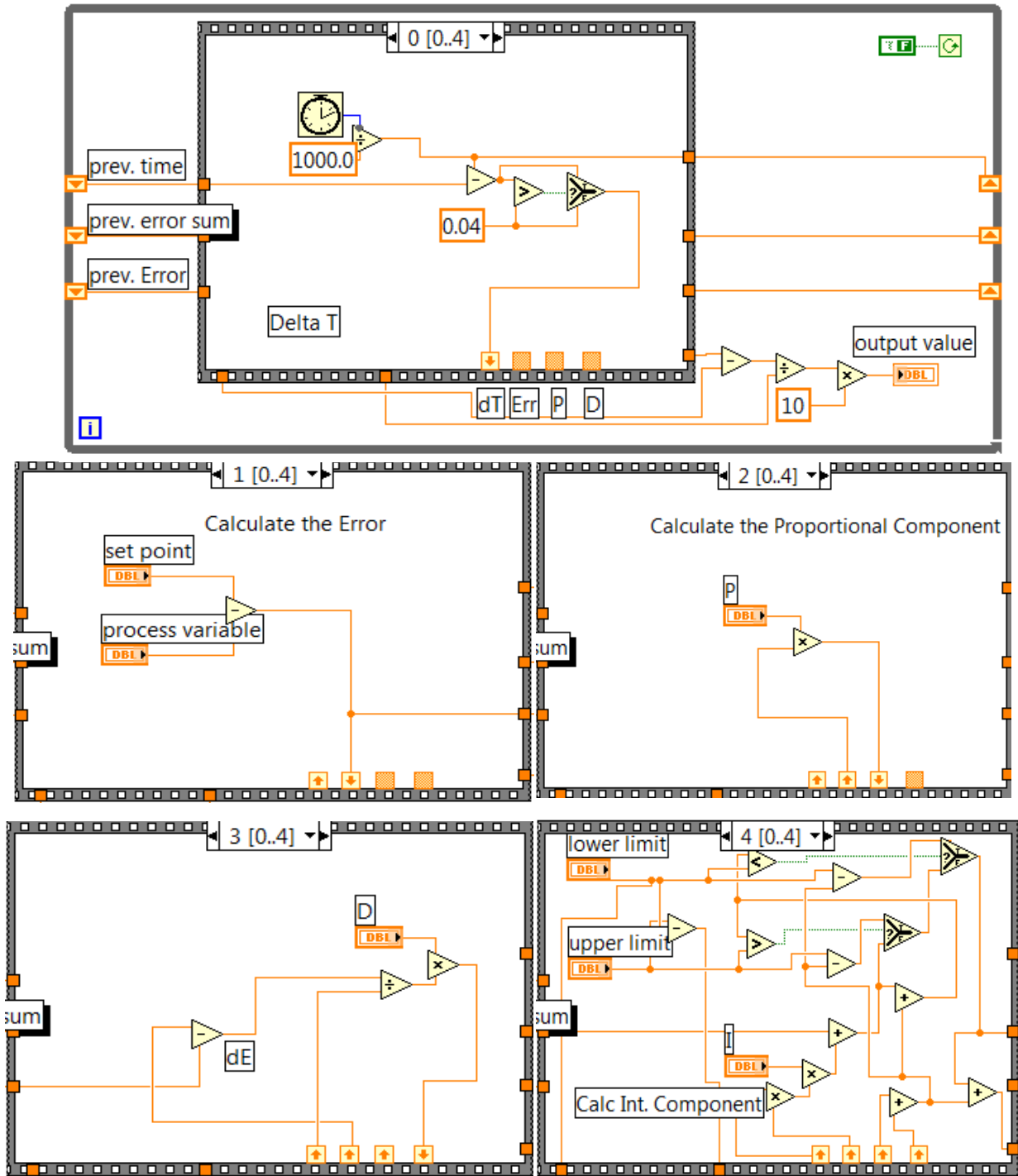


**Figure A. 5** Block diagram for “Simple PID.VI”

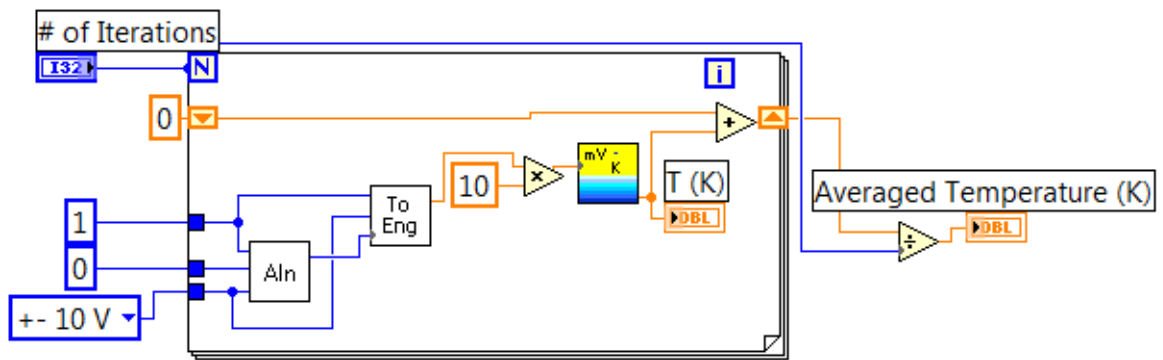


**Figure A. 6** Block diagram for “PID Temp reading.VI”

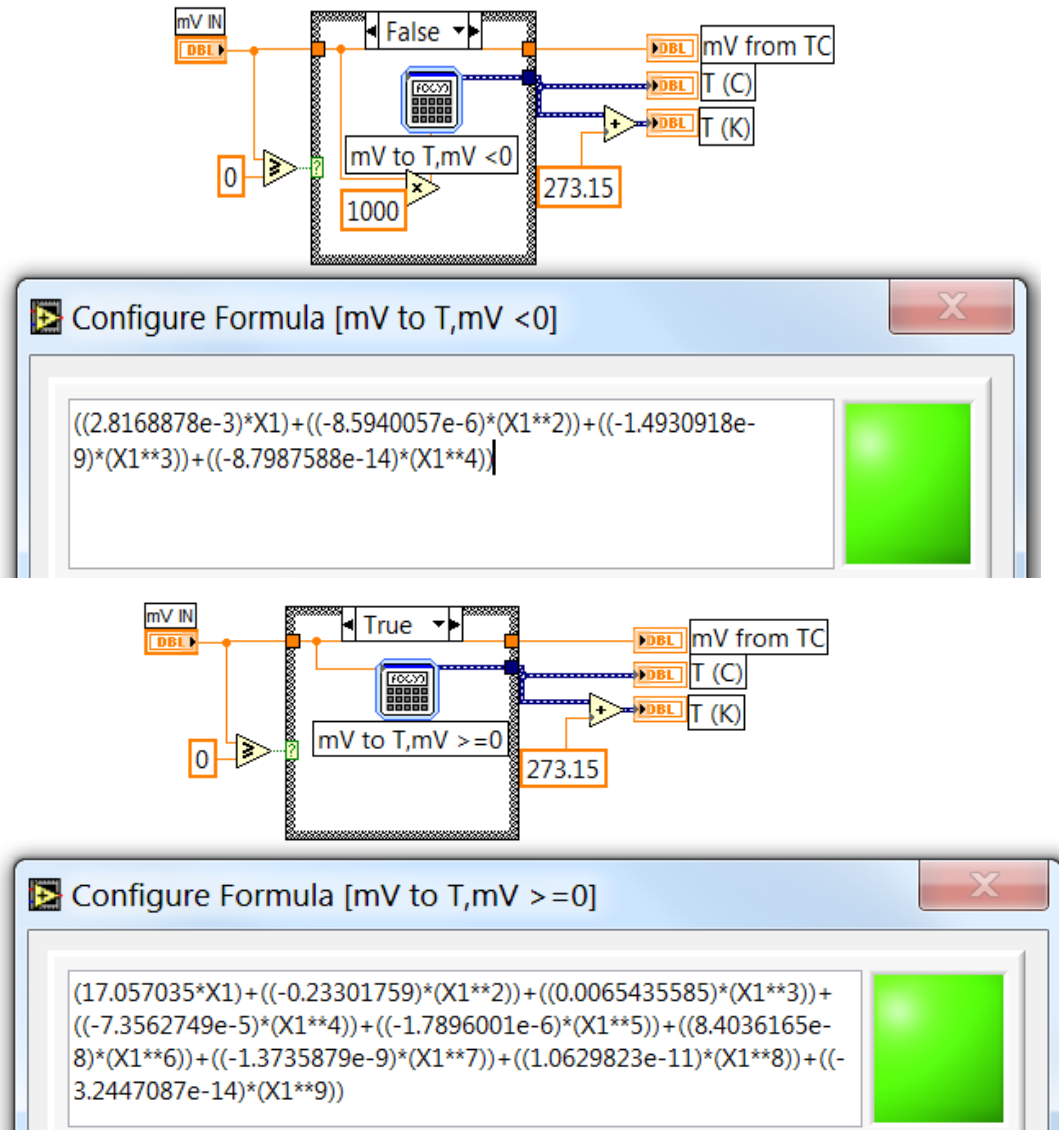


**Figure A. 7** Block diagram for “Conv Type E, mV-K.vi”

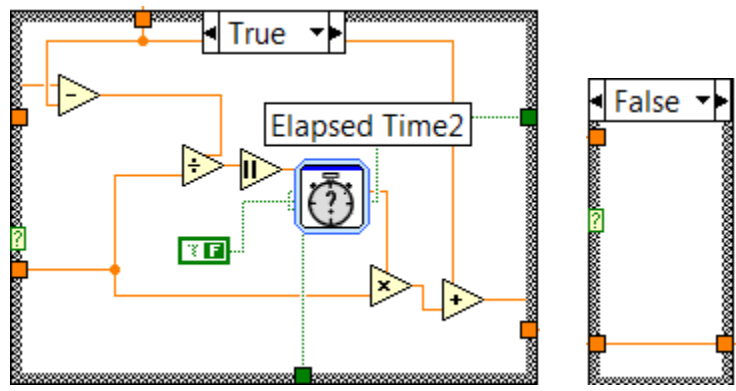
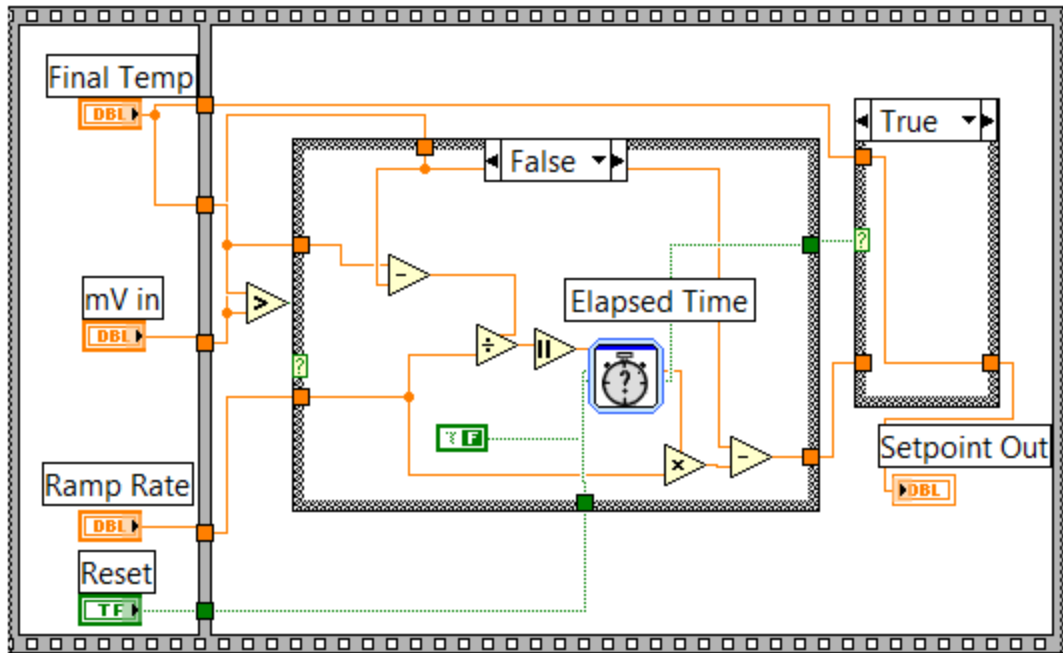


**Figure A. 8** Block diagram for "Setpoint Calculator.VI"

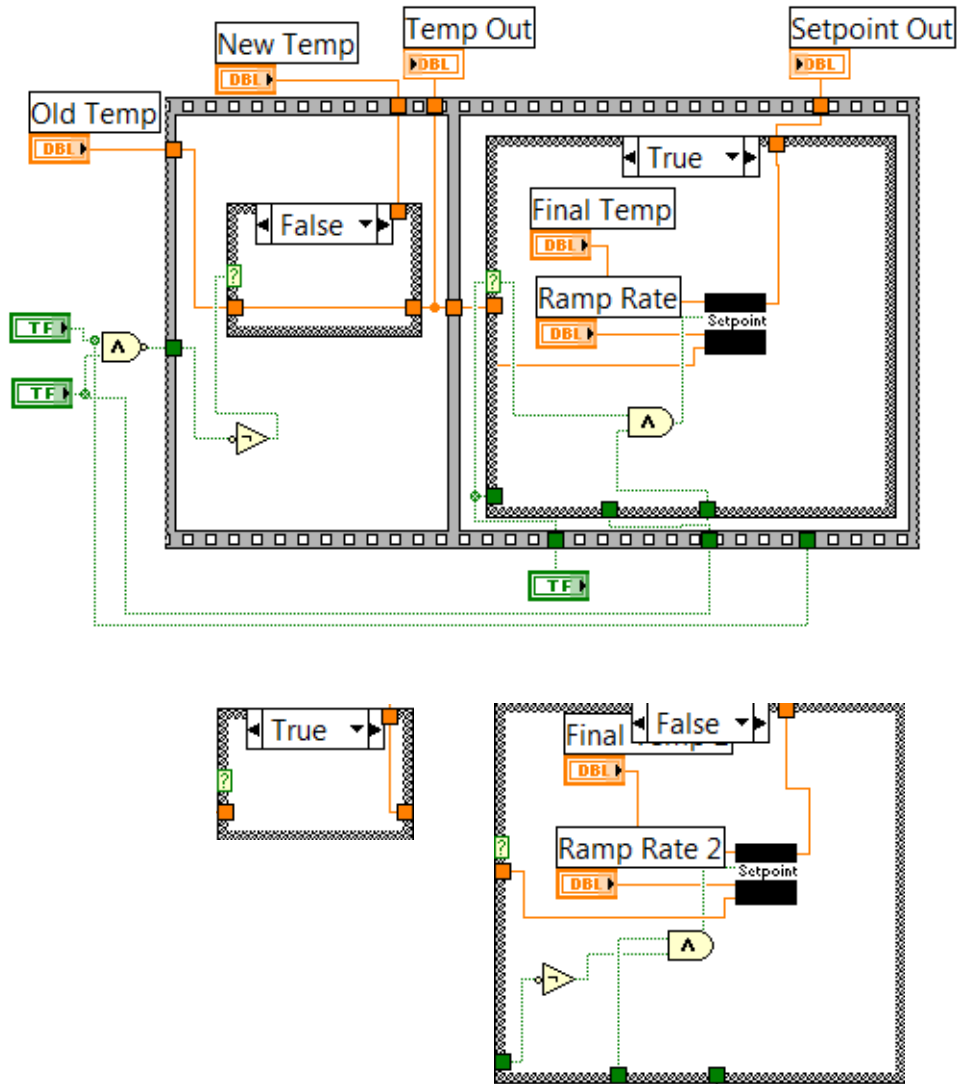


**Figure A. 9** Block diagram for “Switching between setpoints.VI”

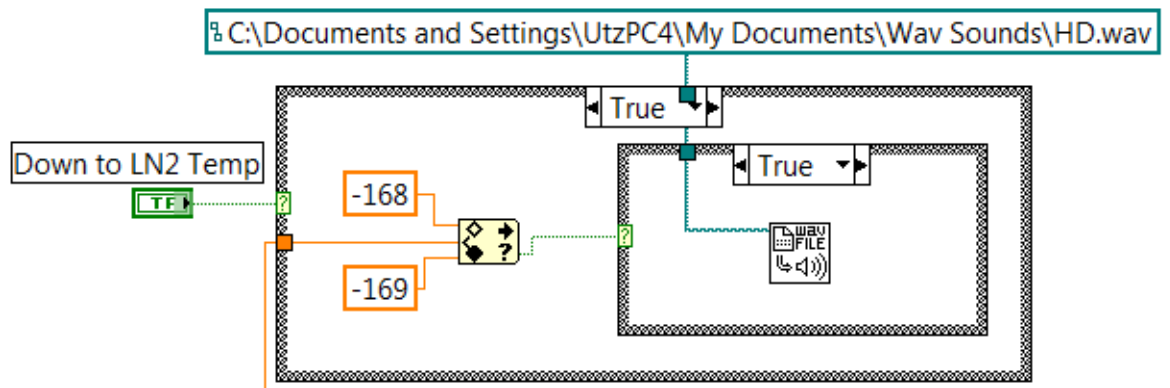


**Figure A. 10** Block diagram for “Play Sound.VI”

## A.4 References

1. R. R. Smith, PhD Thesis, Rovibrational State-Resolved Studies of Methane Dissociation on Ni(111), *Tufts University* (2003).



## Appendix B

### Igor - Modulation Fit walkthrough

#### B.1 General Overview

As discussed in Chapter 2 Section 2.4 2 and Chapter 4 a new method for simultaneous determination of the laser off,  $S_0^{Off}$ , and laser on,  $S_0^{On}$ , sticking probabilities has been developed. An Igor program was developed to process the large amounts of data collected using this method. The general experiment consists of collecting King and Wells (K&W) reflectivity data while modulating the molecular beam excitation source. The K&W acquisition program collects signal from the quadrupole mass spectrometer (QMS) and the shutter driver state (open/closed) to differentiate between the excited and non-excited molecules during the dose. The Modulation Fit Igor program calculates  $S_0^{Off}$  and  $S_0^{On}$  based on the shutter driver state and calculates the associated errors. The following section discusses the experimental procedure in greater detail, highlighting useful tips for performing these experiments. Next, use of the analysis program is discussed and the notable outputs from the program are discussed.

## B.2 Experimental Walkthrough

For a thorough walk-through of the experimental procedure see Section 2.4.2, the following is meant to guide a person using the same setup to produce data for analysis with the IGOR macro.

- 1) Warm the quadrupole mass spectrometer (QMS) filament up. Ensure that a steady baseline is achieved at the desired M/Z and approximate count rate. The best residuals are collected at  $\sim 2$  M counts and  $< 1$  mA of filament emission
- 2) Clean the crystal surface
- 3) Ensure that the cryostat and liquid nitrogen trap(s) for the diffusion pump(s) are full and have had time to reach equilibrium with the background gases within the chamber
- 4) Verify that the laser is locked to the desired transition and absorption within the beam is maximized
- 5) Set the laser shutter to the appropriate frequency
- 6) With the beam valve open, beam shutter closed, and beam flag blocking the beam, start the King and Wells (K&W) data acquisition program
- 7) Collect the baseline counts for 5-10 seconds
- 8) Open beam shutter and wait until the counts have stabilized (45-60 seconds total)
- 9) Remove the beam flag from blocking the crystal
- 10) Observe the response on the K&W program, allow the system to reach a steady state and remain there for 15-30 seconds
- 11) Block the crystal with the beam flag and wait 5-10 seconds
- 12) Close the beam shutter and stop program
  
- 13) Load the modulation fitting Igor program
- 14) Load the appropriate wave you wish to analyze
- 15) Open Table 1 and inspect the variables used in the function; the important one is Variables[0] which corresponds to the flux
- 16) Set cursors as shown in Figure B.1
- 17) Run macro "Place\_Cursors"
- 18) This will in effect generate all of the necessary waves for analysis and the graph shown in Figure B.2
- 19) Look at the generated Graph2 and pick between which points you want to use in the analysis
- 20) Place cursors as shown in Figure B.3

21) Run macro “Calculations”, the result being shown in Figure B.4 with explanation of outputs

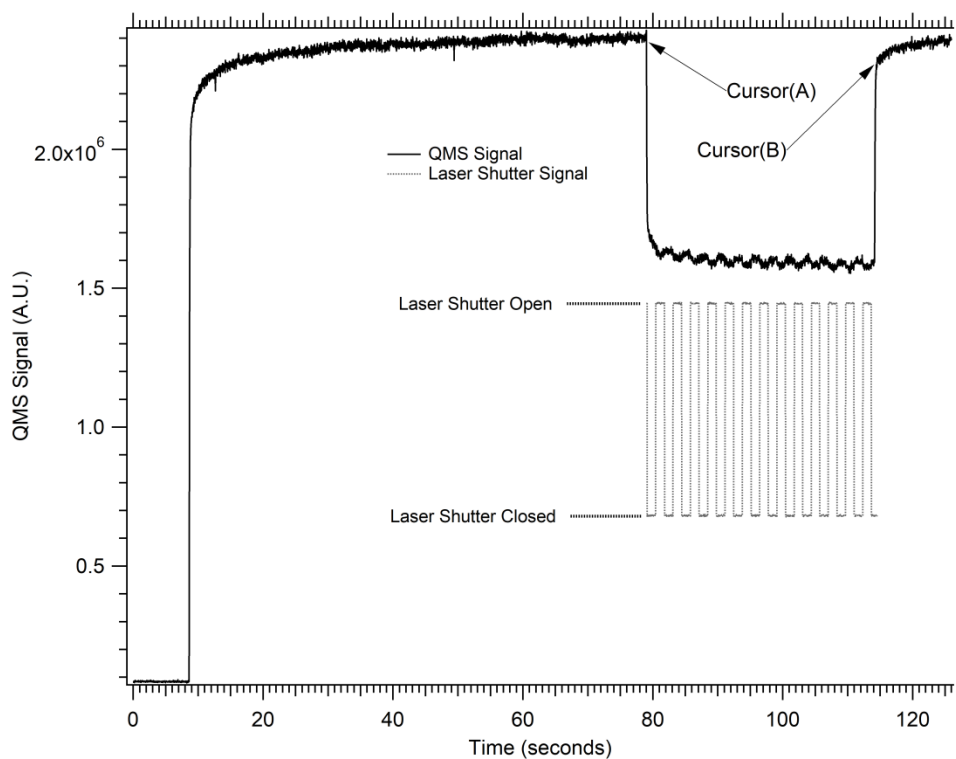


**Figure B. 1** King and Wells modulation experiment loaded into IGOR showing the correct cursor placement for “Place Cursors” macro.

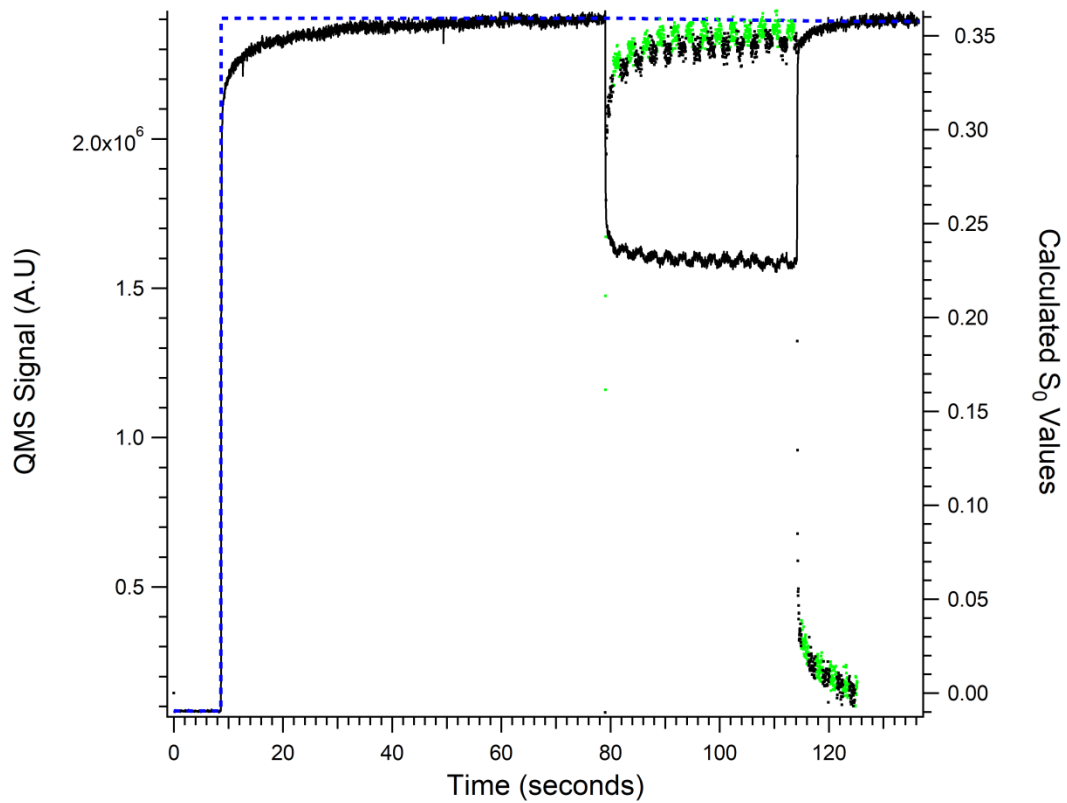


**Figure B. 2** Output from macro “Place Cursors” showing the calculated laser off (black dots) and laser on (green dots) sticking probabilities with axis on the right.

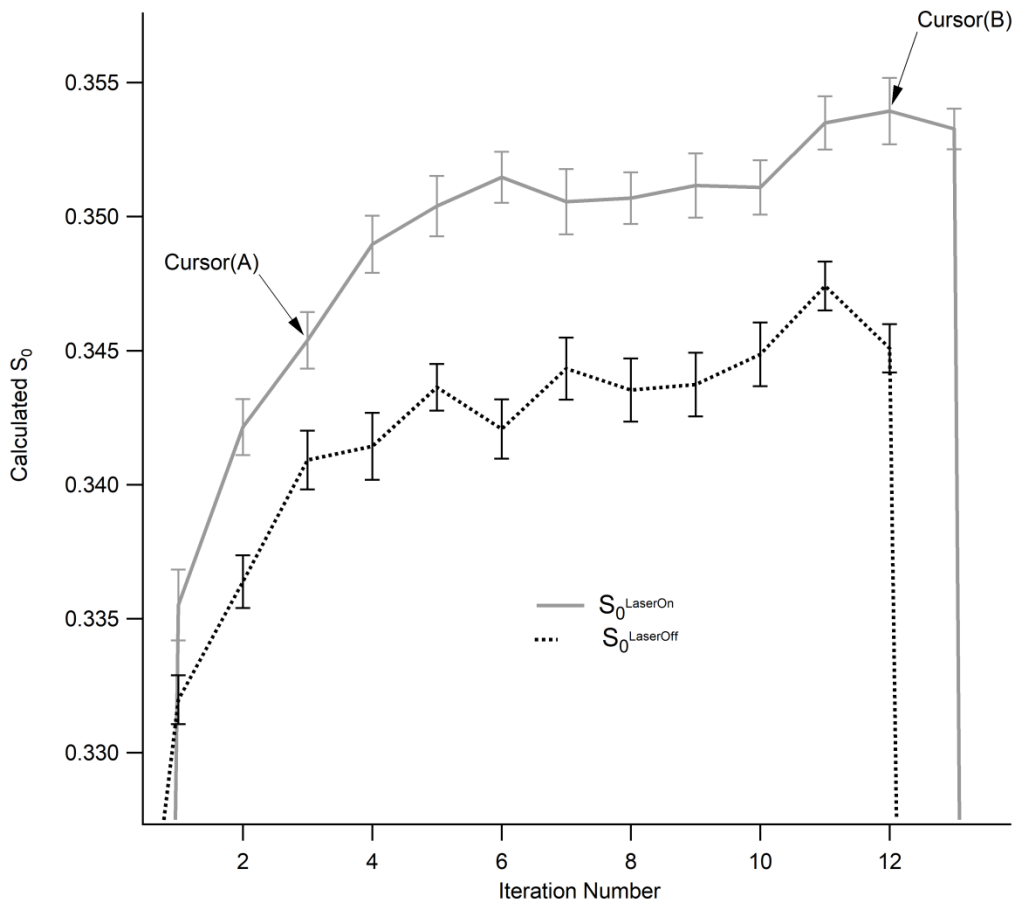
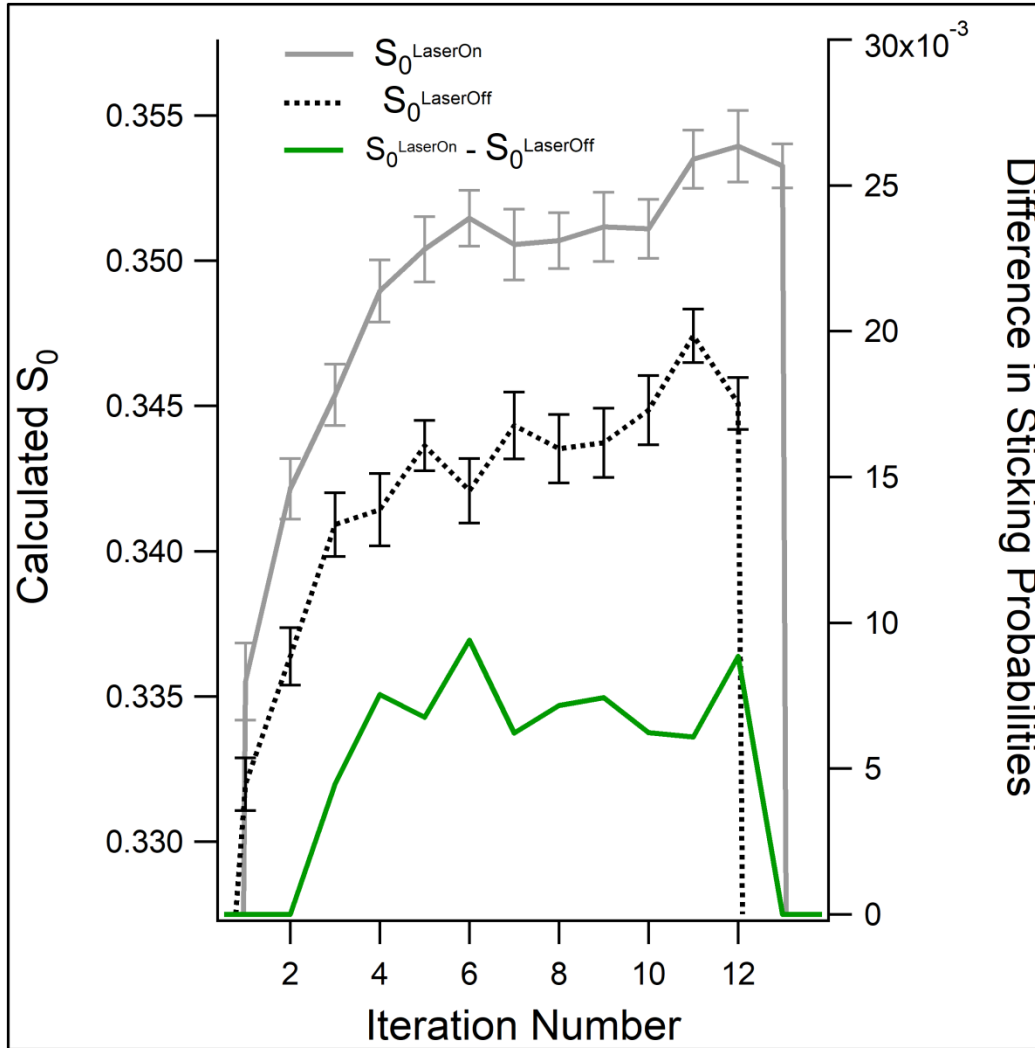


**Figure B. 3** Output from “Place Cursors Macro”. Also shown are the correct placement for the next macro “Calculations”. The iteration number corresponds to the shutter iteration for on/off measurements.



Results	Explanation
0.343701	Laser off Sticking
0.00218433	Laser off variance
0.00701377	Laser on - Laser off
0.00283902	Difference variance
9	N

**Figure B. 4** Output from “Calculations” macro. The table shows the outputs to use in calculations. The variance is reported as  $2\sigma$ .

### B.3 IGOR Code

```
#pragma rtGlobals=1          // Use modern global access method.

Macro Place_Cursors()
Modulation_Calcs()
END

Macro Calculations()
Do_calculations()
END

////////////////////////////////////
//////PRODUCE ALL OF THE FINAL NUMBERS FOR ANALYSIS////////
////////////////////////////////////

Function Do_calculations()
Wave Sticking_diff, Sticking_avg_On, Sticking_avg_Off, n_Off, n_On,
Sticking_std_Off, Sticking_std_On
variable i, numerator, denominator

Make /O/N=5 Results

//For pooled statistics on the laser off measurements
WaveStats/R=[pcsr(A),pcsr(B)] Sticking_avg_Off
Results[4] = pcsr(B) - pcsr(A)
Results[0] = V_avg

for(i=pcsr(A); i<(pcsr(B)+1); i+=1)
numerator = (n_Off[i] - 1) * Sticking_std_Off[i]^2 + numerator
denominator = (n_Off[i] - 1) + denominator
endfor
Results[1] = 2 * sqrt(numerator/denominator)

//For laser on error calculations
Sticking_diff = 0

for(i=pcsr(A); i<pcsr(B)+1; i+=1)
Sticking_diff[i] = Sticking_avg_On[i] - Sticking_avg_Off[i]
endfor

WaveStats/R=[pcsr(A),pcsr(B)] Sticking_diff
Results[2] = V_avg
Results[3] = 2 * V_sdev
```

```
//Make displays
•AppendToGraph/R Sticking_diff
•SetAxis right 0,*
•ModifyGraph rgb(Sticking_diff)=(65280,0,0)
•Legend/C/N=text0/J "\\s(Sticking_avg_On) Laser ON\r\\s(Sticking_avg_Off)
Laser OFF\r\\s(Sticking_diff) Difference"
•Display Sticking_Off vs Coverage_Off; AppendToGraph Sticking_On vs
Coverage_On
•ModifyGraph
mode=2,lsize=2,rgb(Sticking_Off)=(0,0,0),rgb(Sticking_On)=(0,65280,0)
•Label left "Sticking Probability";DelayUpdate
•Label bottom "Coverage (ML)"
Edit Results
End
```

```
////////////////////////////////////
```

```
Function Modulation_Calcs()
String input_wave_counts, input_wave_time
Wave Laser,Variables
Variable i,j,k,m,n,p
Variable flux, time_mod, initial_ON, initial_OFF, blocked_sites, E_ads, R, T,
C_Diff, dT
```

```
////////////////////////////////////
```

```
//////SETUP INPUT WAVES THROUGH
DIALOG////////////////////////////////////
```

```
////////////////////////////////////
```

```
    Prompt input_wave_counts, "Select Wave", popup
    WaveList("*sig_*",";","")
    DoPrompt "Input Wave", input_wave_counts
        if (V_flag != 0)
            return -1; // User canceled.
        endif
```

```
    Prompt input_wave_time, "Select Wave", popup
    WaveList("*Time_*",";","")
    DoPrompt "Input Wave", input_wave_time
        if (V_flag != 0)
            return -1; // User canceled.
        endif
```

```
Wave Counts = $input_wave_counts
Wave Timing = $input_wave_time
```

```
////////////////////////////////////
```

```

/////MAKING BASELINE FOR SUBTRACTION/////
/////

```

```

Make /O/N=3 Baseline_Bounds
Make /O/N=4 Topline_Bounds
Make /O/N=(numpnts(Counts)) Baseline
Make /O/N=(numpnts(Counts)) Baseline_Sub

```

```

//Average the initial points until the beam shutter opens (signal increases by 20%)
Baseline_Bounds[0]=0
for(i=0; Counts[i] < 1.2*Counts[0]; i+=1);
Baseline_Bounds[2] = Counts[i] + Baseline_Bounds[2]
endfor
Baseline_Bounds[2] = Baseline_Bounds[2]/i
Baseline_Bounds[1]=i
for(i=0; i<Baseline_Bounds[1]; i+=1);
Baseline[i] = Baseline_Bounds[2]
endfor

```

```

////Average the leading and tailing points of flag open / closed
Topline_Bounds[0]=pcsr(A)
Topline_Bounds[1]=pcsr(B)
Wavestats/R=[pcsr(A)-40,pcsr(A)]$input_wave_counts
Topline_Bounds[2]=V_Avg
Wavestats/R=[pcsr(B)+40,pcsr(B)]$input_wave_counts
Topline_Bounds[3]=V_Avg

```

```

//Populate Baseline with the proper values. This will help verify baselines are
valid.

```

```

for(i=Topline_Bounds[0]; i<Topline_Bounds[1]; i+=1);
Baseline[i] =Topline_Bounds[2] + (Timing[i] - Timing[Topline_Bounds[0]]) *
((Topline_Bounds[2] - Topline_Bounds[3])/(Timing[Topline_Bounds[0]]-
Timing[Topline_Bounds[1]]))
endfor
for(i=Baseline_Bounds[1]; i<Topline_Bounds[0]; i+=1);
Baseline[i] = Topline_Bounds[2]
endfor
for(i=Topline_Bounds[1]; i<(Topline_Bounds[1]+500); i+=1);
Baseline[i] = Topline_Bounds[3]
endfor
DeletePoints Topline_Bounds[1]+500, numpnts(Counts)-
Topline_Bounds[1]+500, Baseline
for(i=0; i<(numpnts(Counts)); i+=1);
    if(i>Topline_Bounds[0] && i<Topline_Bounds[1])
        Baseline_Sub[i] = Baseline[i] - Topline_Bounds[2]
    else

```

```

        Baseline_Sub[i] = 0
    endif
endfor

////////////////////////////////////////////////////////////////
//////MAKE LASER TRIGGER WAVES FOR
CALCS////////////////////////////////////////////////////////////////
////////////////////////////////////////////////////////////////

Make /O/N=(numpnts($input_wave_counts)) Laser_Mask //0 or 1, entire t axis
Make/O/N=500 Shutter_Signal //Stores the points of transition from ON/OFF
visa/versa

if(Laser[0]<0.1)
j=0
k=0
else(j=1,k=1)
endif

m=0

for(i=Topline_Bounds[0]; i<Topline_Bounds[1];i+=1);
    if(Laser[i]>0.1 && j ==0 && k==0)
        Shutter_Signal[m]=i
        j=1
        k=1 //start looking for an off measurement
        m+=1
    endif
        if(Laser[i]<0.1 && j ==1 && k==1)
            Shutter_Signal[m]=i
            j=0
            k=0 //start looking for an on measurement
            m+=1
        endif
    endif

    if(i>Topline_Bounds[0] && j==0)
        Laser_Mask[i]=0
    elseif(i>Topline_Bounds[0] && j==1)
        Laser_Mask[i]=1
    endif

endfor
Deletepoints m, 500-m, Shutter_Signal

////////////////////////////////////////////////////////////////

```

```

/////CALCULATING STICKING AND POPULATE APPROPRIATE ON/OFF
WAVES/////
/////

```

```

Make /O/N=(numpts($input_wave_counts)) Coverage_Off ,Coverage_On,
Sticking_Off, Sticking_On, Time_Off, Time_On, ML_Deposited_Exact
Make /O/N=(numpts(Shutter_Signal)/2) Sticking_avg_Off, Sticking_avg_On,
Sticking_std_Off, Sticking_std_On, Sticking_diff, n_Off, n_On
Variable s, u, x, y, v

```

```

s=0
u=0

```

```

for(i=Topline_Bounds[0]; i<Topline_Bounds[1];i+=1)
flux = Variables[0]
dT = Timing[i+1] - Timing[i]
ML_Deposited_Exact[i+1] = ML_Deposited_Exact[i] + flux * dt * (Baseline[i] -
Counts[i])/(Baseline[i] - Baseline_Bounds[2])

```

```

    if(Laser_Mask[i]==0)
        Sticking_Off[s] = (Baseline[i] - Counts[i])/(Topline_Bounds[2] -
Baseline_Bounds[2])
        Coverage_Off[s] = ML_Deposited_Exact[i+1]
        Time_Off[s] = Timing[i+1]
        s+=1
    elseif(Laser_Mask[i]==1)
        Sticking_On[u] = (Baseline[i] - Counts[i])/(Topline_Bounds[2] -
Baseline_Bounds[2])
        Coverage_On[u] = ML_Deposited_Exact[i+1]
        Time_On[u] = Timing[i+1]
        u+=1
    endif

```

```

endfor

```

```

u=0 //reset
s=0
y=0
n=0
v=0

```

```

if(Laser_Mask[Topline_Bounds[0]]==0)
    x=1
    else
        x=0
endif

```

```

for(i=Topline_Bounds[0]; i<Topline_Bounds[1]-75; u+=0)

    if(x==0 && i==Shutter_Signal[u])
        Make /O/N=(Shutter_Signal[u+1] - Shutter_Signal[u]) Temp_calcs
            for(i=Shutter_Signal[u]; i < Shutter_Signal[u+1]; i+=1)
                Temp_calcs[v] = (Baseline[i] - Counts[i])/(Topline_Bounds[2] -
Baseline_Bounds[2])
                v+=1
            endfor
            Sticking_avg_Off[y] = mean(Temp_calcs)
                for(v=0; v<numpnts(Temp_calcs); v+=1)
                    Temp_calcs[v] = (Temp_calcs[v] -
Sticking_avg_Off[y])^2
                endfor
                Sticking_std_Off[y] = 2 * sqrt(sum(Temp_calcs)) /
numpnts(Temp_calcs)
                n_Off[y] = numpnts(Temp_calcs)
                i=Shutter_Signal[u+1]
                x=1
                y+=1
                u+=1
                v=0
                DeletePoints 0, numpnts(Temp_calcs), Temp_calcs
        endif

        if(x==1 && i==Shutter_Signal[u])
            Make /O/N=(Shutter_Signal[u+1] - Shutter_Signal[u]) Temp_calcs
                for(i=Shutter_Signal[u]; i < Shutter_Signal[u+1]; i+=1)
                    Temp_calcs[v] = (Baseline[i] -
Counts[i])/(Topline_Bounds[2] - Baseline_Bounds[2])
                    v+=1
                endfor
                Sticking_avg_On[s] = mean(Temp_calcs)
                    for(v=0; v<numpnts(Temp_calcs); v+=1)
                        Temp_calcs[v] = (Temp_calcs[v] -
Sticking_avg_On[s])^2
                    endfor
                    Sticking_std_On[s] = 2 * sqrt(sum(Temp_calcs)) /
numpnts(Temp_calcs)
                    n_On[s] = numpnts(Temp_calcs)
                    i=Shutter_Signal[u+1]
                    x=0
                    s+=1
                    u+=1
                    v=0

```

```

DeletePoints 0, numpnts(Temp_calcs), Temp_calcs
endif

if(i!=Shutter_Signal[u])
i+=1
endif

endfor

////////////////////////////////////
//////MAKE DISPLAYS////////////////////////////////////
////////////////////////////////////

•AppendToGraph Baseline vs $input_wave_time
•AppendToGraph/R Sticking_On vs Time_On; AppendToGraph/R Sticking_Off
vs Time_Off
•ModifyGraph
rgb(Baseline)=(0,0,65280),mode(Sticking_On)=2,lsz(Sticking_On)=1.5;DelayU
pdate
•ModifyGraph
rgb(Sticking_On)=(0,65280,0),mode(Sticking_Off)=2;DelayUpdate
•ModifyGraph lsz(Sticking_Off)=1.5,rgb(Sticking_Off)=(0,0,0)
•Display Sticking_avg_On,Sticking_avg_Off
ModifyGraph
rgb(Sticking_avg_On)=(0,65280,0),rgb(Sticking_avg_Off)=(0,0,0);DelayUpdate
•ErrorBars Sticking_avg_On
Y,wave=(Sticking_std_On,Sticking_std_On);DelayUpdate
•ErrorBars Sticking_avg_Off Y,wave=(Sticking_std_Off,Sticking_std_Off)
•Label left "Sticking Probability";DelayUpdate
•Label bottom "Iteration Number"
ShowInfo

END

```

## Appendix C IGOR – Dissolution Startup

### C.1 General Overview

The results presented in Chapter 6 constitute a large data set across a wide range of reaction conditions. This made it difficult to analyze each individual component in an iterative manner to ultimately determine the model governing carbon dissolution. To aid in the analysis an IGOR program was developed that fit each set of conditions in the same program at the same time.

The program takes each individual “wave”, or experiment, along with the predefined constants and model for dissolution and fits the data. The model is discussed in Chapter 6 but it is necessary to point out a few features of the program. A front panel (Panel0), shown in Figure C.1, allows for user input to the IGOR modeling function. The arrows on the left of the panel correspond to the following energetic pathways:

S\_SS = Surface to subsurface

SS\_S = Subsurface to surface

SS\_B = Subsurface to bulk

S\_G = Surface to graphene

SS\_G = Subsurface to graphene

The Saturation Values input fields allow for the saturation coverage, in ML, to be changed for the surface and subsurface layers. The Functional Dependence fields are for changing the order of the reaction for a given step in the model. Figure C.1

is used to guide the user in defining the energies on Panel0. They basically correspond to the branching ratio for the different pathways with respect to  $E_A$ .

Figure C.3 demonstrates an example of an output from the fitting procedure. The program takes the amount of carbon deposited at time,  $t$ , that is a given from the experiment (pink dotted line,  $C_{\text{Experimental}}$ ) and first determines how much goes from the surface, where it is deposited, to the subsurface ( $S_{\text{SS}}$ ). It then allows that carbon to go into the bulk ( $SS_{\text{B}}$ ) or back onto the surface. The resulting carbon distribution is then allowed to form graphene through either aggregation on the surface ( $S_{\text{G}}$ ) or from carbon popping up from the subsurface ( $SS_{\text{G}}$ ). Then the next experimentally determined increment of carbon is added to the surface. If the amount of carbon added to the surface is larger than the saturation limit, this amount is skimmed off the top and added to a separate wave. This was done in this manner to limit the possible ways that adding carbon to the surface could essentially break the program, or create a condition that was unrealistic. In this way, the model could be verified because if there was no carbon skimmed off the top then the model was dealing with the deposited carbon properly. The trace  $C_{\text{Model}}$  (green dotted) corresponds to the total carbon deposited as calculated through the model; then, the amount of carbon skimmed off the top is the difference in  $C_{\text{Experimental}}$  vs.  $C_{\text{Model}}$ . This gave an easy visual verification if the input parameters were not close.

Lastly, Figure C.4 is a visual guide for the carbon coverage dependence for each of the processes. Since there is both an energetic barrier and dependence on carbon coverage the overall allocation from one layer into another is the

product of these two terms; essentially the product of values in Figure C.2 and C.4. Several different functional forms were experimented with but none were found to be satisfactory. The forms currently being used are based on an error function with best guesses used for the parameters based on the empirically observed response of the King and Wells traces. We observe that accumulation on the surface is rapid once it does start to happen so there was assumed to be some transition point where uptake on the surface was dominant compared to dissolution into the bulk. This also led to the inclusion of graphene formation since once graphene is formed it is much harder to remove and deactivation of the surface would occur rapidly once it started.

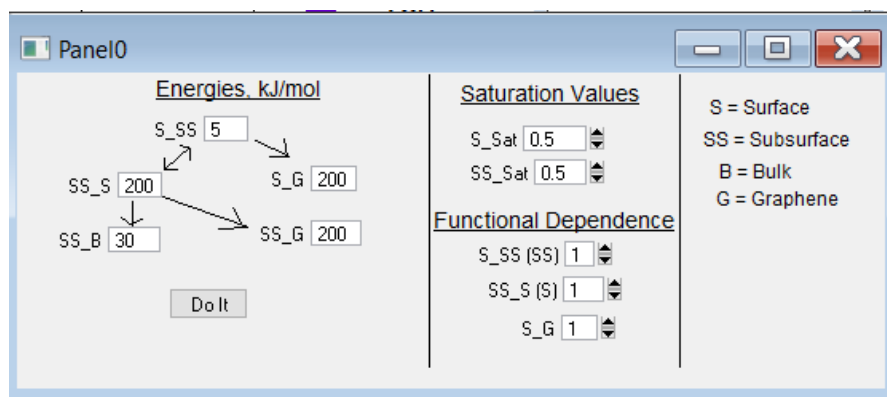


**Figure C. 1** Front panel for changing constants used in the model

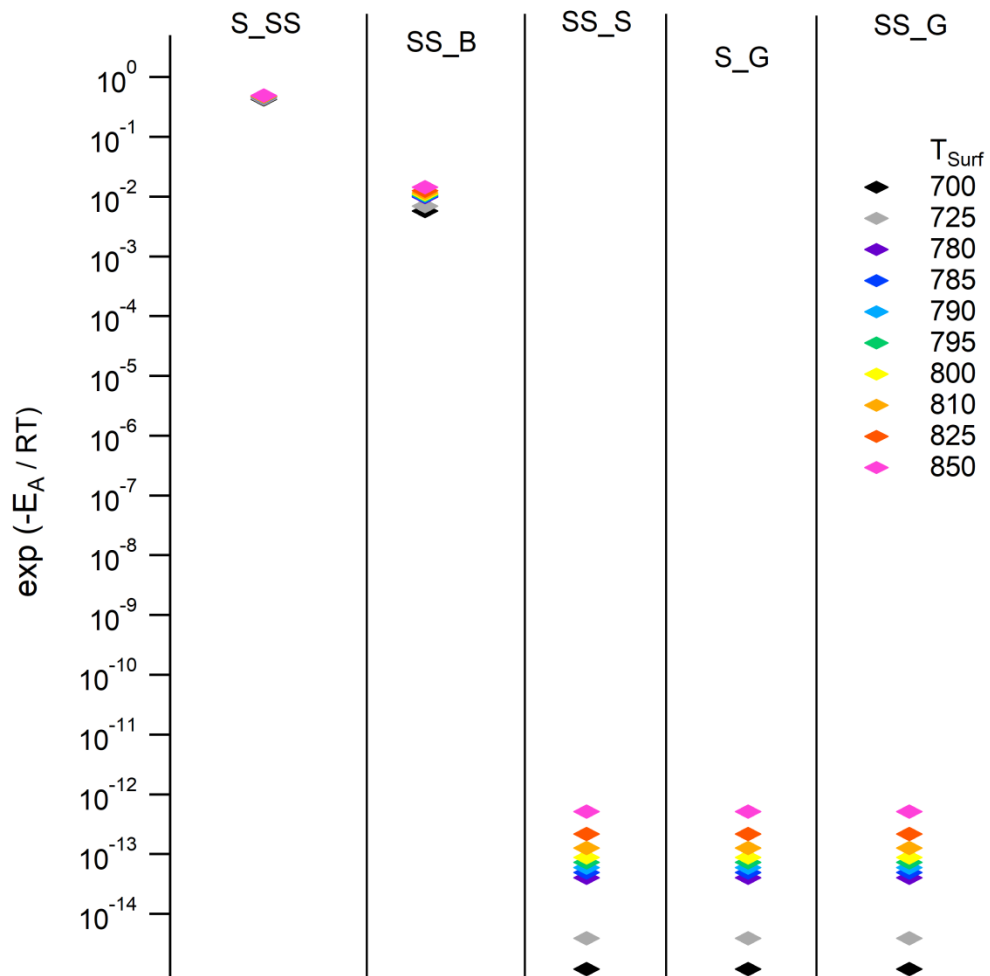


**Figure C. 2** Calculated energetic factors for the different processes impacting carbon allocation

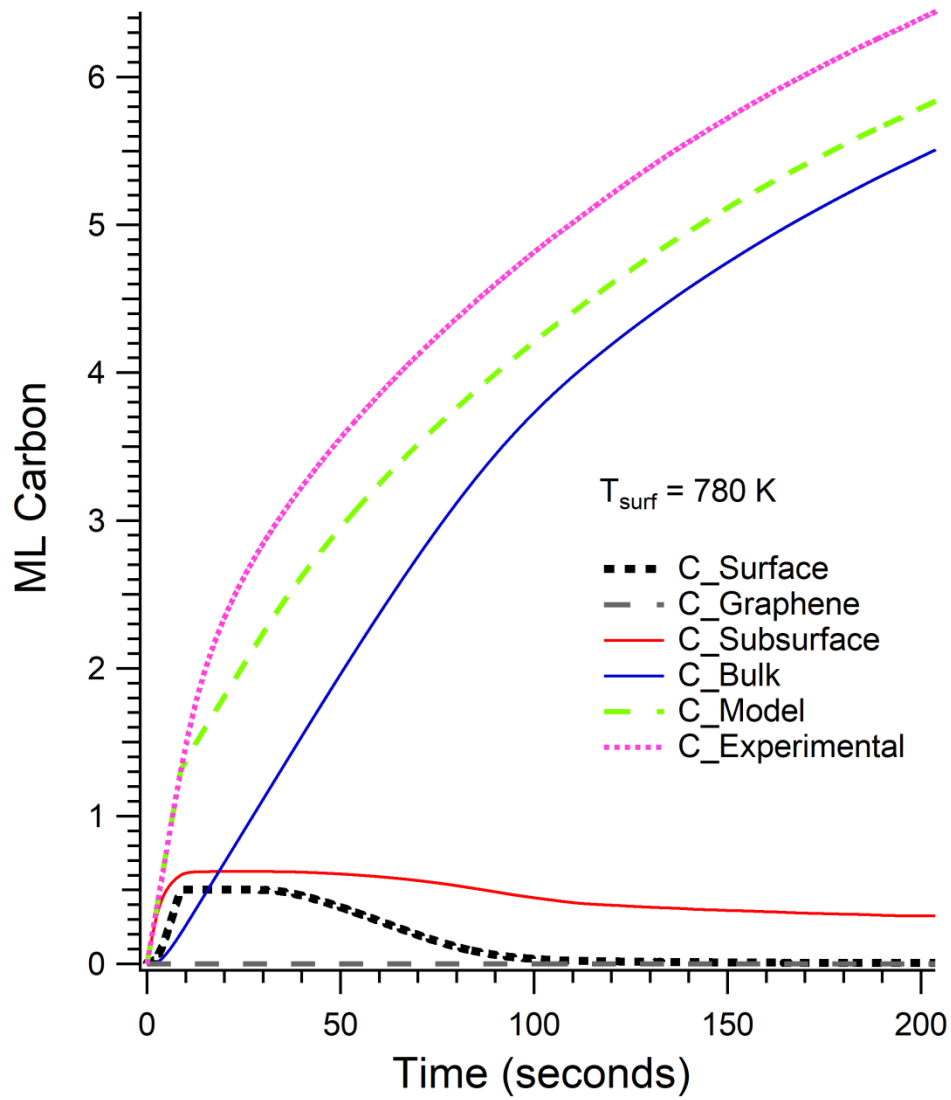


**Figure C. 3** An example of the output from the program. The legend shows which segment of the nickel lattice the carbon is allocated into. The wave C\_Experimental (pink, dotted) is calculated directly from the experimental data.

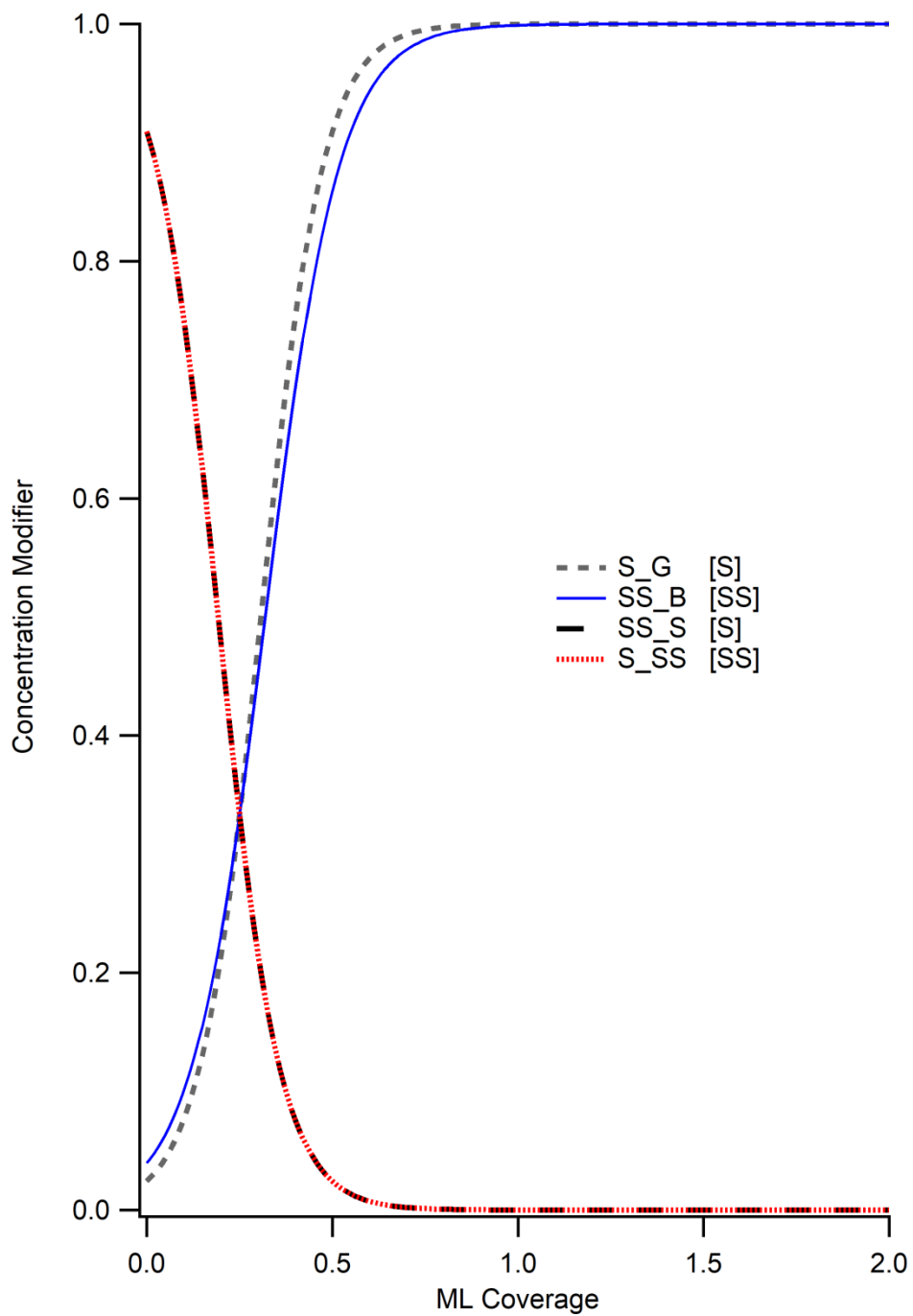


**Figure C. 4** Functional dependence for the different pathways on carbon concentrations in their respective layers

### C.3 Igor Code

```
#pragma rtGlobals=1          // Use modern global access method.

Function Diffusion_Fit()
wave Temperatures, Exp_Constants, w, C_Modeling
variable i, j, k, Kb, dT, S_Sat, SS_Sat, G_Sat
NVAR Flux

//////////DIFFERENT TEMPERATURE ITERATIONS//////////
for(i=0;i<numpts(Temperatures);i+=1)
//////CONSTANTS//////////
Kb = 8.314
dT = 0.03
S_Sat = Exp_Constants[6]
SS_Sat = Exp_Constants[7]
G_Sat = 0.5
//////////NAMING OF WAVES//////////
SVAR S_sticking
S_sticking = num2str(Temperatures[i]) + "_sticking"
SVAR S_time
S_time = num2str(Temperatures[i]) + "_time"
string S_Surface = "C_Surface_" + num2str(Temperatures[i])
string S_Subsurface = "C_Subsurface_" + num2str(Temperatures[i])
string S_Bulk = "C_Bulk_" + num2str(Temperatures[i])
string S_Graphene = "C_Graphene_" + num2str(Temperatures[i])
string S_Total = "C_Total_" + num2str(Temperatures[i])
string S_Deposited = "C_Deposited_" + num2str(Temperatures[i])
string S_Overflow = "C_Overflow_" + num2str(Temperatures[i])
string S_S_SS = "F_S_SS_" + num2str(Temperatures[i])
string S_SS_S = "F_SS_S_" + num2str(Temperatures[i])
string S_SS_B = "F_SS_B_" + num2str(Temperatures[i])
string S_S_G = "F_S_G_" + num2str(Temperatures[i])
string S_SS_G = "F_SS_G_" + num2str(Temperatures[i])
string Exponentials = "Exponentials_" + num2str(Temperatures[i])

Wave Counts = $S_sticking
Wave Timing = $S_time

Make /O/N=(numpts(Counts)) C_Surface = 0
Make /O/N=(numpts(Counts)) C_SubSurface = 0
Make /O/N=(numpts(Counts)) C_Bulk = 0
Make /O/N=(numpts(Counts)) C_Graphene = 0
Make /O/N=(numpts(Counts)) C_Total = 0
Make /O/N=(numpts(Counts)) C_Deposited = 0
```

```

Make /O/N=(numpnts(Counts)) C_Overflow = 0
Make /O/N=(numpnts(Counts)) C_S_Sat = 0
Make /O/N=(numpnts(Counts)) F_S_SS = 0
Make /O/N=(numpnts(Counts)) F_SS_S = 0
Make /O/N=(numpnts(Counts)) F_SS_B = 0
Make /O/N=(numpnts(Counts)) F_S_G = 0
Make /O/N=(numpnts(Counts)) F_SS_G = 0
Make /O/N=(numpnts(C_Modeling)) D_S_SS=0
Make /O/N=(numpnts(C_Modeling)) D_SS_S=0
Make /O/N=(numpnts(C_Modeling)) D_SS_B=0
Make /O/N=(numpnts(C_Modeling)) D_S_G=0
Make /O/N=5 W_Exponentials = 0

/////////////////////////////////INITIALIZE WAVES/////////////////////////////////
C_Surface[0] = Flux * dt * Counts[0]
C_Total[0] = C_Surface[0]
C_Deposited[0] = C_Surface[0]
C_S_Sat[0] = S_Sat
/////////////////////////////////FLUX DETERMINATION/////////////////////////////////
if(Temperatures[i] < 750)
    Flux = Exp_Constants[8]
elseif(Temperatures[i]>750)
    Flux = Exp_Constants[9]
endif
/////////////////////////////////MODEL FITTING/////////////////////////////////
for(j=1; j<numpnts(Counts); j+=1);

/////S_SS/////
F_S_SS[j] = (SS_Sat / (SS_Sat + exp(12*(C_SubSurface[j-1] - SS_Sat/2)))) ^
w[0] * C_Surface[j-1]*exp(-Exp_Constants[1]/(Kb*Temperatures[i]))

C_SubSurface[j] = C_SubSurface[j-1] + F_S_SS[j]

C_Surface[j] = C_Surface[j-1] - F_S_SS[j]

/////SS_S/////
F_SS_S[j] = (C_S_Sat[j-1] / (C_S_Sat[j-1] + exp(10*(C_Surface[j] - C_S_Sat[j-1]/2))))*C_SubSurface[j-1] ^ w[1] * exp(-
Exp_Constants[3]/(Kb*Temperatures[i]))

C_Surface[j] = C_Surface[j] + F_SS_S[j]

C_SubSurface[j] = C_SubSurface[j] - F_SS_S[j]

```

```

////////SS_B//////////
F_SS_B[j] = (SS_Sat / (SS_Sat + exp(-12*(C_SubSurface[j] -
(SS_Sat/2)))))*C_SubSurface[j]*exp(-Exp_Constants[2]/(Kb*Temperatures[i]))

C_Bulk[j] = C_Bulk[j-1] + F_SS_B[j]

C_SubSurface[j] = C_SubSurface[j] - F_SS_B[j]

////////S+SS_G//////////
F_S_G[j] = (G_Sat / (G_Sat + exp(-12*(C_Graphene[j-1] - G_Sat/2)))) *
C_Surface[j]*exp(-Exp_Constants[4]/(Kb*Temperatures[i]))

F_SS_G[j] = (G_Sat / (G_Sat + exp(-12*(C_Graphene[j-1] - G_Sat/2)))) *
C_SubSurface[j]*exp(-Exp_Constants[5]/(Kb*Temperatures[i]))

C_Graphene[j] = C_Graphene[j-1] + F_S_G[j] + F_SS_G[j]

C_Surface[j] = C_Surface[j] - F_S_G[j]

C_SubSurface[j] = C_SubSurface[j] - F_SS_G[j]

C_S_Sat[j] = C_S_Sat[j-1] - F_S_G[j] - F_SS_G[j]

////////++DOSE++//////////

C_Surface[j] = C_Surface[j] + (Counts[j] * Flux * dt)

//////////OVERFLOW//////////
if(C_Surface[j] > S_Sat)
    C_Overflow[j] = C_Overflow[j-1] + (C_Surface[j] - S_Sat)
    C_Surface[j] = S_Sat
    elseif(C_Surface<S_Sat)
        C_Overflow[j]=C_Overflow[j-1]
    elseif(C_Surface==S_Sat)
        C_Overflow[j]=C_Overflow[j-1]
endif

//////////SUMMATION//////////

C_Total[j] = C_Surface[j] + C_SubSurface[j] + C_Bulk[j] + C_Graphene[j]
C_Deposited[j] = C_Deposited[j-1] + Counts[j] * Flux * dt

endifor

//////////EXPONENTIALS//////////
W_Exponentials[0] = exp(-Exp_Constants[1]/(Kb*Temperatures[i]))

```

```

W_Exponentials[1] = exp(-Exp_Constants[2]/(Kb*Temperatures[i]))
W_Exponentials[2] = exp(-Exp_Constants[3]/(Kb*Temperatures[i]))
W_Exponentials[3] = exp(-Exp_Constants[4]/(Kb*Temperatures[i]))
W_Exponentials[4] = exp(-Exp_Constants[5]/(Kb*Temperatures[i]))

//////////CONCENTRATION DEPENDENCIES//////////CHANGE THIS
EVERYTIME.....//////////
for(k=0;k<numpnts(C_Modeling);k+=1)
D_S_SS[k] = (SS_Sat / (SS_Sat + exp(12*(C_Modeling[k] - (SS_Sat/2))))))
D_SS_B[k] = (SS_Sat / (SS_Sat + exp(-10*(C_Modeling[k] - (SS_Sat/2))))))
D_SS_S[k] = (S_Sat / (S_Sat + exp(12*(C_Modeling[k] - (S_Sat/2))))))
D_S_G[k] = (G_Sat / (G_Sat + exp(-12*(C_Modeling[k] - G_Sat/2))))
endfor

//////////WAVE POPULATION//////////
Make /O/N=5 $Exponentials = W_Exponentials
Make /O/N=(numpnts(Counts)) $S_Surface = C_Surface
Make /O/N=(numpnts(Counts)) $S_SubSurface = C_SubSurface
Make /O/N=(numpnts(Counts)) $S_Bulk = C_Bulk
Make /O/N=(numpnts(Counts)) $S_Graphene = C_Graphene
Make /O/N=(numpnts(Counts)) $S_Total = C_Total
Make /O/N=(numpnts(Counts)) $S_Deposited = C_Deposited
Make /O/N=(numpnts(Counts)) $S_S_SS = F_S_SS
Make /O/N=(numpnts(Counts)) $S_SS_B = F_SS_B
Make /O/N=(numpnts(Counts)) $S_SS_S = F_SS_S
Make /O/N=(numpnts(Counts)) $S_S_G = F_S_G
Make /O/N=(numpnts(Counts)) $S_SS_G = F_SS_G
Make /O/N=(numpnts(Counts)) $S_Overflow = C_Overflow

endfor

END

//////////
//////////BUTTON CONTROLS//////////
//////////
Function SetVarProc(ctrlName,varNum,varStr,varName) : SetVariableControl
    String ctrlName
    Variable varNum
    String varStr
    String varName
End

```

```

////////////////////////////////////////////////////////////////////////////////////////////////////////////////////////////////
////////////////////////////////////////////////////////////////////////////////////////////////////////////////////////////////
Function ButtonProc(ctrlName) : ButtonControl
    String ctrlName
    NVAR T_Surf, S_SS, SS_B, SS_S, S_G, SS_G, S_Sat, SS_Sat, w0, w1,
w2
    Wave EXP_Constants, w
    Exp_Constants[1] = S_SS*1000/////KJ to J/////
    Exp_Constants[2] = SS_B*1000
    Exp_Constants[3] = SS_S*1000
    Exp_Constants[4] = S_G*1000
    Exp_Constants[5] = SS_G*1000
    Exp_Constants[6] = S_Sat
    Exp_Constants[7] = SS_Sat
    Exp_Constants[8] = 0.047 //<750K      FLUXES
    Exp_Constants[9] = 0.39 //>750K
    w[0] = w0
    w[1] = w1
    w[2] = w2

    Diffusion_Fit()
End
////////////////////////////////////////////////////////////////////////////////////////////////////////////////////////////////
////////////////////////////////////////////////////////////////////////////////////////////////////////////////////////////////

```